Immersed Boundary Method for Cavitating and Biological Flows

Evangelos Stavropoulos - Vasilakis

Primary Supervisor: Prof. Manolis Gavaises

Secondary Supervisor: Dr. Phoevos Koukouvinis

CITY, University of London
School of Mathematics, Computer Science & Engineering
Department of Mechanical Engineering & Aeronautics

Thesis submitted towards the fulfilment of the requirements for the degree of
Doctor of Philosophy of CITY, University of London

London May 2020

To my grandfather, Antonis Vasilakis,
for his inspiring integrity and endeavours

iv

Declaration

I hereby declare that this thesis is the product of my own work, except where specific mention is made of a joint effort in the text, and that contributions from other authors or information derived from other sources are duly acknowledged in the references.

I confirm that the contents of this thesis are original and have not been submitted in whole or in part for consideration for any other degree or qualification in this, or any other university.

Evangelos Stavropoulos-Vasilakis, London May 2020

Abstract

The aim of the present work is the development of a computational tool to ease the numerical simulation of cavitating flows in domains of complex topology or with arbitrary moving boundaries. Within the framework of Computational Fluid Dynamics *(CFD)*, an Immersed Boundary *(IB)* Method has been developed. According to the IB methodology, the grid that discretises the computational domain does not need to conform to the geometry and the solid boundaries are modelled on a fixed canonical grid by alternations of the governing equations in their vicinity. This modelling strategy is beneficial in terms of both computational cost and numerical solution. The grid generation, which is a complex and time consuming process, is simplified as a regular canonical grid, non-conformal to the boundaries, can be used. In addition, when moving boundaries are present, a conformal grid would need to adapt or deform following the motion of boundaries, which would increase the computational cost of the simulations in the first case and affect the solution in the latter case; the use of IB method alleviates these issues. The developed method follows the direct-forcing approach, which simply adds to the governing equations a source term to account for the body force acting on the fluid. The simplicity of the method makes it suitable for complex flow regimes, including phase change, strong shocks and compressibility effects, as well as Fluid Structure Interaction *(FSI)*. Since cavitation dynamics regard a wide range of applications of engineering interest, from hydraulic machines to novel therapeutic techniques, the method is designed to be applicable in a wide range of flow regimes. Turbulent modelling and flow induced motion has been taken into account. The method has been successfully applied to cavitating and incompressible cases where conventional techniques are not easily or at all applicable. The shock-wave interaction with material interfaces is studied via the high-speed impact of a solid projectile on a water jet, which has been studied only experimentally before and only qualitative observations existed. The numerical investigation with the proposed methodology unveiled rich information regarding the physics of the impact, the resulting shock formation, cavitation development and interface instabilities initiation. Moreover, the methodology was applied on the thoroughly studied pulsatile flow through a bi-leaflet Mechanical Heart Valve, to provide additional information regarding shear stress development. The methodology aids an experimental campaign employing novel shear stress measuring techniques, carried out by our collaborators. The research work and the developed method described in the present Thesis, intend to set the foundations for more elaborate numerical investigations of highly complex problems of Fluid Dynamics.

Project's Contribution

The novelty of the present research work, is outlined by the attributes of the developed method and the problems that where addressed:

Simplicity of formulation The forcing method chosen benefits from the simple formulation and minimum changes of the solver. The calculation of the source term is a straightforward procedure, that avoids the complexities and the computational cost of other methodologies that involve multiple interpolation steps, adaptation of the computational stencil or geometrical alternation of the computational cells. Moreover, it is a highly "portable" numerical tool that can be coupled with different numerical flow solvers.

Range of Applicability The method is designed to address a wide range of applications. Special care is given on turbulence modelling within RANS framework. Also, apart from the prescribed movement, flow induced motion of the immersed boundary is taken into account. The method can be applied on flows of complex geometry, turbulent cavitating flows, as well as biological pulsatile flows of transition Reynolds number. When all the individual modelling features are put together, the method is able to deal with turbulent cavitating flows with Fluid Structure Interaction.

Cases studies With the developed method the simulation of problems which is prohibited with conventional CFD tools was made possible. The numerical investigation of the high-speed impact of a solid projectile on a water jet is made possible with the use of the proposed Immersed Boundary Method. Unprecedented detailed quantitative information about the physics of the impact, the developed shocks and cavitation, that where only captured qualitatively by experiments is provided. In addition, the method is applied on the wall shear stress study for the biological pulsatile flow through a bi-leaflet Mechanical Heart Valve. Although Immersed Boundary Methods is the standard approach in modelling prosthetic heart valves, the study aims to shed light in the shear stress distribution and to support the findings of a novel measurement technique developed by our collaborators.

x

Acknowledgements

Although working on a PhD is a very personal enterprise, it would be impossible, and probable meaningless, without the support, and sometimes joint effort, of many people.

First of all, I would like to express my gratitude towards to Prof. Manolis Gavaises, who accepted me in his research group and gave me the opportunity to undertake this PhD. I deeply appreciate his mentoring and look up to him for his intuition and scientific achievements. In addition, I am very grateful for the constant support of Dr. Phoevos Koukouvinis, who with extra care, patience and attention to detail would promptly aid me in my work and share his knowledge. I would like to thank them for trusting me.

Secondly, it goes without saying that these past 4 years were made easier by my colleagues and friends, who made the life in office A306 of College Building, pleasant and interesting. I would like to thank Nikos, Alvaro, Thodoris, Hesam, Georgia, Max, Carlos, Marco, Mithun and Milad for the time we spent in and out the office. I especially thank Nikos for the cooperation and support since day One in CITY, Alvaro for the life-prolonging laughs and Thodoris for his ever reassuring tone of voice. In addition I would like to thank Ilias, Homa, Yves and Andreas also for the scientific discussions, their curiosity and insights that helped me in my work. Special thanks go to Nikolas Chatziarsenis for his always prompt support through the administrative maze of the University life and his companionship in the frequent quests to the institute across the street.

In addition, I would like to thank Dr. Steffen Schmidt who hosted me in TUM and favoured me with his fellowship in scientific meetings and conferences.

I would like also to thank Qianhui Li and Prof. Bruecker for the collaboration on a joint research work, their insights and their effort.

The support of my friends and family was of utmost importance throughout this endeavour. If it were not for them and their emotional support I would not have made it.

At last, I would like to highlight my profound respect and admiration of the Academia and the people involved in scientific research and the educational process. It is a very creative, yet stressful and challenging, environment with fundamental purpose to widen our horizons. I have to attribute the spark of my desire to pursue this research study to the scientific and teaching staff of NTUA, where I completed my Diploma.

Contents

List of Figures

Chapter 1

Introduction

Contents

1.1 Background and Motivation

As *Immersed Boundary* methods are characterised those methods that lead to flow simulations on Cartesian grids, non-conformal to domain geometry. The term was first introduced to describe the method developed by Peskin [181], who studied the blood flow inside a heart on a simple non-conformal to the heart geometry Cartesian grid by simulating the effect of the immersed to the flow boundaries using external forces applied to the fluid.

Since then, this methodology has been studied thoroughly by many researchers and many alternations and improvements have been proposed, because it tackles the important issue of grid generation for complex geometries and facilitates the simulations with moving boundaries. Using this methodology, one does not generate a complex grid that conforms to the boundaries of the problem domain, but rather simulate the presence of these boundaries in the flow through modifications in the equations solved.

These methods provide simpler grid generation and easier complex geometry manipulation, resulting in smoother grids and therefore lowering the computational cost related to grid quality and transformations. The advantages of these methods over conformal grid approach, is becoming more clear when moving boundaries are present in the problem under consideration. In that case, following the conventional approach, the grid should adapt in every step to the modified domain, thus grid generation should take place in every step and as well as interpolation of the problem's variables from older to newer grids. Using immersed boundary method, the domain can be modified without change in the grid, thus the computational cost would drop significantly.

These exact advantages of immersed boundary methods in problems of moving geometries, act as the motivation for this study, where this approach is adopted to ease the simulations of demanding flows with moving boundaries, including solid to liquid impacts, cavitating flows through diesel injector during closing needle motion or bi-leaflet mechanical heart valve (MHV) operation.

The conventional strategy of generation of boundary-conforming grids for such problems, may become demanding and time consuming. When the numerical simulation involves moving parts with large displacements, common conformal grid strategies result in re-meshing of the entire domain in every time-step [97], or deforming the grid and adding or removing cell-layers when a desired cell size is reached [112]. In the case of marine propellers, to accommodate their rotational motion, either the entire computational domain would be rotated accordingly [11], or a multi-region mesh would be used, which lets the part of the grid that conforms with the propeller blades to slide with regards to the global domain [139]. Another approach of overset grids [224] (also known as Chimera grids), employs multiple overlapping grids, each one handling a separate geometrical feature, and relies on interpolating the solution between them. These techniques increase significantly the difficulty of the simulations and their computational cost.

Using conventional approaches, Koukouvinis et al. in [112] simulated the opening phase of the needle of a diesel injector, where the moving needle narrows the passages and the fluid is highly accelerated and the subsequent static pressure drop leads to cavitation. In order to simulate this motion, the mesh of the changing domain is adapted in every time step, by inflating and adding cell layers near the needle surface. This procedure requires an extremely complicated multi-block grid generation procedure as well as a sophisticated and computational expensive re-meshing technique during the entire simulation. The use of immersed boundary

method in the specific problem would result in a much simpler, static and more uniform mesh and less expensive simulation.

The *Chimera* method proposed by Steger et al. [213], employs *overset* grids conforming to the complex stationary, moving or deforming boundary. The governing equations are solved in both meshes and the solution is interpolated back and forth between the grids to enforce the coupling. Such methods have developed in close relation to aeronautic applications [38] and can achieve high-order of accuracy [195]. Applications may extend to Internal Combustion *(IC)* Engines [60] as well as to multiphase problems of free-surface in conjuction with Volume of Fluid *(VOF)* method [254]. Using immersed boundary methodology instead of Chimera, not only would simplify the mesh generation, but it would also avoid the grid-to-grid interpolation procedure and spatial dicretisation adaptation and eliminate their influence to the solution.

The present study focuses in the development of an immersed boundary method, for cavitaing flows with rigid immersed moving boundaries, within the framework of the open source OpenFOAM [68] toolbox. These flows are of demanding and complex nature, involving strong compressibility effects, non-trivial vapour and turbulent structures interaction, as well as should prove challenging for fluid structure coupling.

1.1.1 Applications of Cavitation

Cavitation is the phenomenon of vapour formation in liquids, due to pressure drop [69]. It is relevant to many engineering applications, as it may occur during the operation of hydraulic machines, ship propellers, injection systems of Internal Combustion Engines (ICE), as well as advanced rocket propulsion systems. The flow in hydraulic turbines [58] or Diesel injector nozzles [73] is severely and rapidly accelerated, static pressure may drop locally below saturation value and vapour cavities inception may be initiated, grow to a critical size and subsequently collapse violently. In these cases, cavitation is a side effect and regarded to be the source of erosion damage, noise or low efficiency of the mechanical devices. On the other hand, cavitation may prove beneficial when employed in non-invasive medical procedures for therapeutic purposes, like High Intensity Focused Ultrasound (HIFU) [94, 121, 143] used for *lithotripsy*.

Cavitation in engineering scales

Turbulent cavitating flows refer to various flow regimes encountered in industrial applications. The range of the cavitation and cavitation erosion application is vast; it includes, but is not limited to, marine propellers [11, 139], steam turbines [65], water turbines [189, 251], oil or fuel gear pumps [144], Diesel injection systems [57, 73, 112, 114, 156, 167–170, 249], as well as the high-speed flows of cryogenic fuels used in liquid rocket propulsion systems [230].

Modern and future emission standards demand increase of mixing and combustion process efficiency, in order to reduce the harmful by-products. In Diesel engines, these goals may be achieved by increasing the injection pressure. However, high compression ratios, above 15/1 and 20/1, may lead to severe acceleration of the fuel through injection nozzles risking cavitation formation [57]. Significant advances in cavitation research have been performed regarding the Diesel injection systems, via both experimental and numerical studies. Computational techniques have also been advanced alongside, allowing for more complex configurations or flow regimes to be studied. Giannadakis, Gavaises et Arcoumanis [73] performed simulations for the cavitating flow in Diesel nozzles at stationary needle lift, assisted by experiments. Kouk-

ouvinis et al. [112] conducted simulations including prescribed needle motion, which was set according to the lift profile, while eccentricity was neglected. Örley et al. [168, 169] investigated the primary break-up of the injected fuel in the combustion chamber revealing potential air entrainment in the nozzle and also accounted for needle lift dynamics, capturing a more realistic flow field. Naseri, Koukouvinis, Malgarinos et Gavaises [156] assessed the influence of viscoelasticity (a property of Diesel fuel additives) onto cloud and string cavitation, two mechanisms found in injection nozzles; it is observed that viscoelasticity may suppress small-scale features and stabilise cavities, reducing the intensity of cavitation cloud, however its effect depends on the orientation of the cavitating vortices inside the flow.

In addition, the link between cavitation and erosion and their effect on industrial applications is of high importance. Regarding experiments, material samples are exposed to multiple operating cycles, usually in extreme conditions, to evaluate erosion damage and material loss. Correlation of erosion patterns with cavitation formation can be revealed by juxtaposition of the experimental observations and of the detailed description of the flow field extracted from simulations. Dular and Coutier-Delgosha [54] study numerically and experimentally cavitation erosion on a metal hydrofoil, Gavaises, Koukouvinis et al. [70], investigate cloud cavitation formation and collapse in an axisymmetric apparatus developed for surface erosion acceleration tests, while Koukouvinis et al. [112] unveil cavitation and erosion patterns inside an Diesel injector's nozzle.

Liquid-to-solid Impacts

Liquid to solid impacts lead to shock wave release, which are reflected on material interfaces as rarefaction waves causing cavitation induction, growth and collapse in the liquid volume, with subsequent shock wave emission and potential erosion development on the solid.

Liquid impacts on solids regard physical problems of high engineering interest, as they are linked to erosion development [65] and eventual damage of mechanical structures and machines.

Cavitation formation and induced erosion can be realised during the impact of liquid droplets on steam-turbine blades [58], rain droplets impacting on airplanes [91] and wind-turbine blades [2]. Shock-wave interaction with material interfaces has been extensively demonstrated in e.g. underwater explosions [115] and spark/laser-generated bubbles [110], or the excitation of pre-existing nuclei by acoustic pulses [122].

Many experimental works on the mechanisms and the dynamics of liquid-to-liquids impacts [23, 163] or liquid-to-solid impacts [64], where solid compliance [66], deformation [8, 24, 30] or fracture [25] are also investigated, have established a solid understanding of the phenomena taking place, pinpointing cavitation formation due to pressure waves as one of the main causes of erosion. Moreover, shocks' interaction with liquid-gas interfaces has been thoroughly investigated and complex wave structures have been identified by numerous researchers [84, 86, 90, 96, 160, 164].

Such interactions between waves and interfaces have also applications in the medical and bioengineering fields [96]. For example, High Intensity Focused Ultrasound (HIFU) [94, 121, 143] is a non-invasive technique which relies on the production of strong pressure waves that induce the formation and collapse of cavities within tissues. The strong forced oscillations of such cavities lead to extreme localized heating and malignant tissue destruction (histotripsy) or the destruction of solid material, termed as stone (lithotripsy). Interactions of shock waves with soft matter and bubbles occur also in brain injuries caused during mild domestic explosions [121, 241]

and common head concussion accidents [161, 162] happening in everyday life. There are even animal species that have evolved to exploit the generation of shock waves through cavitation to stun or kill prey (snapping and mantis shrimps [111, 177]).

Mechanical Heart Valve Cavitation

A review of studies related to cavitation in bio-engineering applications, either as a side-effect or as a working functionality is presented by Brujan [29]. However, here we briefly mention the potential of cavitation formation in artificial heart valves.

Numerous research studies have been devoted in to unveiling and understanding the blood flow *(hemodynamics)* through prosthetic Mechanical Heart Valves (MHV), by means of both experiments, either *in vitro* or *in vivo*, and numerical simulations. Yoganathan et al. [248] and Sotiropoulos et Borazjani [208] present reviews of the state-of-the-art on MHV hemodynamics research, focusing mainly on computational investigations. The main characteristic of these flows, which serves as a motivation for the majority of studies, is the development of *non-physiological* flow patterns. These patterns include transition to turbulence and high-speed jetting, that encourage development of high shear stresses that can damage the blood cells.

Indications of potential cavitation induction during the operation of MHV have been pin-pointed by Kini et, [109], Lo et al. [133] and Graf et al. [79], however actual proof remains an open question. These studies have identified flow patterns favouring cavitation induction, during the operation of MHV or have observed cavitation induction in MHV mimicking devices. Cavitation in MHV not only leads to erosion of the metal surface but it may also be related to *hemolysis*, a chemical alternation of blood that can lead to *thrombosis*, through generation of severe shear stresses that can damage the blood cells.

The identified mechanisms that can initiate cavitation inception, according to Lo et al. [133], are namely *water hammer, squeeze flow, vortex and Venturi effects*. Tension and compression waves created on the closing phase of the valve, may lead to water hammer effect, as wall as squeeze effect due to closing gap between the leaflets and high-speed leakage jets, known as *Venturi effect*. However, the *vortex effect* is unclear whether is an important factor or not.

1.1.2 Applications of Immersed Boundary

Immersed Boundary *IB* methods, address a wide range of applications, regarding computational domains with either complex geometries and topologies or moving boundaries. In addition, they have been proven useful in various flow regimes and able to handle incompressible and compressible flows, multiphase flows with contact interfaces, heat transfer and turbulence. Finally, IB methods reportedly ease Fluid Structure Interaction *(FSI)* simulations [209], which may be relevant to a broad range of studies, spanning from the flow around flying insects, aquatic swimming, motion of humans, to cases of engineering interest like vortex induced vibrations and wind turbine farm flows.

As it has been already stated, the concept of IB methods originated from the investigation of incompressible blood flow within the contracting and expanding elastic boundaries of a model heart by Peskin [181]. IB methods are widely used in the numerical studies of biological flows. Gilmanov and Sotiropoulos [74, 75], Ge [47, 71, 72] and Borazjani [17, 19, 20, 22] have developed and utilised an ghost-cell IB method to study the incompressible blood flow through a mechanical heart valve, with either prescribed or induced by the flow motion. Borazjani et

5

al. [18] even combined the IB approach with a over-set methodology to account for the cardiac chamber contraction as well. Cristallo et al. [45] performed preliminary computations of the pulsatile flow through a static bi-leaflet heart valve, in semi-open position, in a axisymmetric aorta-mimicking channel, using a direct forcing IB method. Yang and Balaras [7, 245] also applied a direct forcing IB approach for Large Eddy Simulations *(LES)* computations of biological flows and studied the pulsatile flow through a model of arterial stenosis [7], at $Re = 1500$, and though a bi-leaflet mechanical heart valve in a axisymmetric aorta with prescribed motion [245], at $Re = 4000$. De Tullio et al. [228] employed a direct forcing IB method to study the flow through a bi-leaflet mechanical heart valve, with flow induced motion and a realistic aortic root geometry, which included the Valsalva sinuses. Moreover, they investigated the influence of the root geometry [49] on the flow, which is relevant to a surgical operation called *Bentall procedure* that replaces not only the valve, but the root (the sinuses) and the ascending part of the aorta as well.

Apart from the bio-engineering applications, the use of IB in particulate flows is a commonly accepted approach, according the review study of Deen et al. [52]. Uhlmann [229] developed a direct forcing IB method for incompressible particle flows, which is widely adopted. Municchi and Radl [153, 154] used a hybrid of direct forcing and Fictitious Domain *(FD)* IB method in momentum, heat and mass transfer studies of gas-particle suspensions (heterogeneous mixtures of particles in gas). Various studies used FD [219, 220, 234] or direct forcing IB methods [63] in problems of heat transfer in particulate flows .

Moreover, IB methodologies are utilised in cases of industrial interest, characterised by developed or transitional turbulent regimes and complex topologies. Fadlun et al. [59] and Cristallo and Verzicco [46] made use of direct forcing IB method to perform LES of the high Reynolds flow in an Internal Combustion *(IC)* engine's cylinder with a moving piston. Arienti et al. [4] studied the incompressible flow through a Diesel injector nozzle, with the aid of a level-set cut-cell Cartesian grid solver. Mochel et al. [149] performed Unsteady Reynolds Averaged Navier Stokes *(URANS)* simulations of the compressible high-Reynolds flow over a space launcher, adopting a direct forcing approach to account for complex geometrical details and lift the burden of grid generation.

Regarding cavitating flows, Battistoni et al. [9], Zhao et al. [253] as well as Örley et al. [167, 169, 170] employed a cut-cell IB methodology on the numerical prediction of cavitation inception in a Diesel injector with a moving needle. Recently, investigations of the cavitating flow around a moving underwater projectiles by Huang et al. [98] and Lee et al. [174], or around blunt bodies by Xu et al. [242, 243], also made use of cut-cell approach. On the other hand, a direct forcing method has been used by the authors' group to study cavitation induction in gear pumps by Mithun et al. [144] and during the closure of the claw of the pistol shrimp by Koukouvinis et al. [111].

Kadoch et al. [106] proposed a penalization method, in the framework of a pseudo-spectral solver, intended to be used for incompressible flows with scalar transport and mixing, which may concern various flows of industrial interest as chemical reactors, ventilation systems or atmospheric pollutant mixing. Cai et al. [35] studied wave energy harvesting using an IB method to model the semi-submerged heaving cylinder.

The IB approach facilitates the numerical investigation of, non-trivial and rather special problems of fluid dynamics. Gilmanov and Sotiropoulos [75], studied the flow induced by flapping insect wings or swimming fish. Vincent et al. [232] investigated hydroplaning flows

with the help of a FD method. These flows regard the loss of contact of automotive wheel tires with wet road, when the water depth in front of the tire generates enough pressure to overcome the vehicle's weight. Regarding aerodynamics, Grimberg and Farhat [82] used an *Embedded Boundary* method to simulate parachute inflation, relevant to state of the art aerospace development.

1.2   Computational Modelling of Cavitation

Multiphase Modelling   Multiphase flow modelling regards a wide range of applications. In depth analysis of modelling strategies and numerical methods for multiphase flows, can be found in the books of Städtke [212] and Prosperetti [184].

In order to model gas and liquid two-phase flows, one can either consider the two-fluid mixture as non-homogeneous or homogeneous. In the first case, the two fluids are described by separate set of balance equations, which model the the mass, momentum and energy conservation equations and phase-to-phase interactions by appropriate source terms. In the latter case, the two fluids are assumed to be in *mechanical* and *thermal* equilibrium, and can be described by a single set of conservation equations of a "pseudo-fluid" of average properties. The non-homogeneous mixture is a more accurate approximation of the physics of two-phase flow, as it stems from the large differences in state and transport properties between the gas and the liquid and considers the finite rate of interfacial transfer processes. The two fluids are described by a separate velocity, pressure and temperature fields; however the assumption of a single pressure field may be valid and simplifies the modelling. The precise description of the interface is required to correctly estimate the interfacial transfers; this is achieved by either correlating empirically the interface with local flow conditions or by explicitly advecting or tracking the interface. On the other hand, the homogeneous mixture approach relies on averaged flow properties and no longer needs the interface coupling. The mechanical and thermal equilibrium, means that the two fluids share the same velocity, pressure and temperature field. However, the transfer processes between the phases can be conducted with either infinite or finite rate.

Given that the interface can be described by a color or marker function, usually of a Heaviside form, the methods can be classified into methods that advect directly the interface function and those that advect point-markers from whom the interface function is constructed. The latter class of methods is dubbed *front-tracking*, and the interface can be described by a geometric surface shaped by the inter-connection of the marker points; the marker points are advected, most likely like Lagrangian particles and may carry additional information regarding the properties of the corresponding fluid or phase. The former category of methods, uses a transport equation to advect a scalar field that represents the interface function on the numerical background grid, where the equations of the single fluid are solved.

The Heaviside function (also known as step function) is well suited for distinguishing the different fluids or phases, by simply receiving non-zero value only in the region occupied by a specific fluid. The related interface would coincide with the sharp step of the Heaviside function and could be identified by the location where the derivative of the step function, the delta δ function, receives non-zero values. Therefore is a popular choice.

By simply advecting the interface function, through a transport equation within the framework of Finite Volumes, the solution most probably will be affected by *artificial diffusion*; the numerical solution of this transport equation is sensitive to the choice of numerical schemes. A remedy is found by using *Level-Set* or *Volume-Of-Fluid* (VOF) methods. According to the VOF method, the interface is *reconstructed* inside the computational cell, using Simple Line Interface Calculation *(SLIC)*, Piecewise Linear Interface Calculation *(PLIC)* or similar approach, where the interface in the cell is approximated by a straight line of specific orientation with regards the coordinate system or the flow direction. On the other hand, Level-Set method would assign to the interface function the signed normal distance of each cell from the interface; the fluids

would be distinguished by the positive or negative sign of the interface function, while the interface would be recognised by the zero value. As a consequence, Level-set method would provide a smooth and continuous field with a transitional zone between the fluids, while VOF method would result in a sharp interface. The VOF method though, is based on the mass conservation law and thus is more accurate that than the Level-set method.

Cavitation Modelling For simulations of cavitating flows, where liquid and gas-vapour phases exist, both modelling approaches, two-fluid, employing *interface-tracking*, and single-fluid, considering that the two phases compose a homogeneous mixture, can be used. However, the interface-tracking approach poses computational constrains regarding topological changes on the interface [184] and thus, it hardens the numerical modelling of phase change, as well the evolution of the vapour cavities, which often follow the cycle of abrupt initiation, growth and violent collapse. On the other hand, for a homogeneous mixture of liquid and vapour, the transfer process may be considered to happen in finite rate, where information about the interface is still need but can be implicitly extracted from the flow using a *interface-capturing* approach, or the mixture can be considered additionally in *thermodynamic* equilibrium and the rate of the transfer process infinite, following a Homogeneous Equilibrium Mixture *(HEM)* approach. Therefore, single-fluid computations are widely used.

Wang et al. [235] present a review of numerical methods employed on studies of attached, turbulent unsteady cavitating flows, where interface-tracking and homogeneous mixture models are summarised.

The HEM models, consider as working fluid, the homogeneous mixture of liquid and vapour, in mechanical, thermal and thermodynamic equilibrium, with varying density field; the modelling strategies differ regarding the definition of the density field [235]. The continuity and momentum equation may be coupled with a time-dependent differential equation linking pressure with density, a water-vapour state law for compressible fluids or a barotropic equation. For homogeneous mixture methods the Rayleigh-Plesset equation or a transport equation for vapour volume fraction may close the system of mass and momentum conservation equations.

Phase change is triggered when the static pressure is falling bellow vapour saturation pressure (for given conditions), taking into account the isentropic character of cavitating flows. However, a more "realistic" criterion would consider the principal stresses and therefore would be of differential form [235].

Recently, the need of multi-level cavitating modelling has arisen [235]. The accurate solution of bubble dynamics in microscopic scales should feed through filtering and probabilistic models a macro-scale flow solver with averaged quantities, for better capturing the physics of the cavitating flows.

The selection of numerical modelling strategy is dictated mainly by the application, the flow regime and the primary focus of the study. Since cavitation formation regards a wide range of applications and different types of cavitation have been identified for various flow regimes, numerous methodologies have been developed. For instance, in studies of cavitation formation over marine propellers incompressible solvers employing a homogeneous mixture approach with finite-rate mass transfer model can be used [11]. On the other hand, for Diesel injection applications, where effects of compressibility and wave-dynamics are important, compressible solvers employing HEM coupled with barotropic Equation of State seem more suitable [57].

Even for a single application, when the focus is shifted to specific aspects of the flow,

different models may be required. Leroux et al. [124], study the turbulent cavitating flow over a stationary hydrofoil, using a barotropic approach, while Ducoin et al. [53] and Huang et al. [97] use mass-transfer models, for the same hydrofoil, either stationary or in motion. According to rationale of the latter, cavitation and vortex dynamics are closely correlated and the *baroclinic torque*, which results from the miss-alignment of the pressure and density gradients, plays and important role. Barotropic models impose an alignment of these gradients, thus mass-transfer models are favoured for this application.

The most commonly used mass transfer models, are those of Kunz [117], Kubota [116], Singhal [207] and Merkle [142]. According to these models, an additional advection equation is solved for the vapour phase, in which sink/source terms are used to account for phase change. In their work, Ducoin et al. [53], present a comparative computational study between the latter three models, assisted by experiments. The turbulent cavitating flow over a stationary *NACA66* hydrofoil is simulated, for two distinctively different flow regimes, or quasi-steady sheet and unsteady sheet/cloud cavitation dynamics, and the performance of the models is assessed. The Merkle model was found to provide closer results to the experimental observations in both cases. Exploiting the findings of this study, Huang et al. [97] extend the research work to investigate the turbulent cavitating flow over a pitching *NACA 66* hydrofoil, using the Merkle model. The motion of the hydrofoil increases the complexity of the numerical computation, because the angle of attack reaches values past stall point and separation induced turbulent transition has to be account for. In addition, Koukouvinis et al. [112,113] utilise a generalisation of the Zwart-Gerber-Belamri [258] mass transfer model to investigate cavitation and erosion correlation for the flow through Diesel injector nozzles. Since an advection equation is solved for one phase, the location of the interface between the phases is known at every instant and thus, reconstruction may be applied to keep it sharp. Roohi et al. [188] employed a VOF approach to capture and reconstruct the liquid-vapour interface, coupled with different mass transfer models, to study cavitation regimes over a hydrofoil, and the results were in good agreement with experimental observations. However, it has to be noted that the aforementioned models involve empirical constants and therefore their applicability depends on correct tuning and thus, their performance might be situational.

On the other hand, the use of barotropic approach to link pressure and density fields and predict phase change, can lead to parameter-free formulations. According to this approach, thermodynamic closure for the governing equations can be achieved by neglecting thermal effects, not solving the energy equation but rather employing a piecewise with two or three sub-domains Equation of State *(EOS)*. Usually, the pure liquid phase is governed by *Tait* equation and the liquid-vapour mixture by a linearised EOS based on the speed of sound. In addition, pure vapour phase can either obey the linearised EOS of the liquid-vapour mixture or be treated as *perfect* gas, while possibly co-existing non-condesable gas is modelled by the *ideal* gas EOS. The liquid-vapour interface predicted by these methodologies is diffused, but this ensures a continuous variation of speed of sound between the two phases. Dular et Coutier-Delgosha [54] conduct a joint experimental and computational investigation of the turbulent cavitating flow over a circular leading edge symmetric hydrofoil, with special interest in erosion patterns; for the numerical simulations a barotropic cavitation model has been used successfully. Moreover, considering the cavitating flows through Diesel injector nozzles, Koukouvinis, Naseri et Gavaises [114] assess the performance of barotropic and mass-transfer models; non-significant discrepancies were found in the predictions of the two methodologies. Similar approach is

followed by Örley et al. [167–170], who study the cavitation inside injector nozzle, including needle motion, as well as they extend the single-fluid formulation into a two-phase method to account for non-condensable gas along with the liquid-vapour mixture and investigate cavitation in injection nozzles in conjunction with primary jet break-up. Although these methods do not capture a sharp interface, Ogloblina et al. [165] employ a barotropic cavitating model in the simulations of the collapse of bubble clusters; because of the fine spatial resolution this approach is able to resolve the interface implicitly.

The aforementioned studies, employing mass transfer and barotropic methodologies, regard computations on the Eulerian frame of reference. However, cavitating flows may be modelled in a Eulerian-Lagrangian formulation. Giannadakis, Gavaises et Arcoumanis [73] as well as Gavaises, Koukouvinis et al. [70] follow this approach. The liquid phase is solved on the *continuous* Eulerian reference frame while cavitation is considered as a discrete phase, comprised of *dispersed* gas/vapour bubbles, tracked on the Lagrangian frame of reference. Instead of resolving the kinematics and the dynamics of each individual bubble, the dispersed vapour phase is composed by *parcels* of identical bubbles, advected by the flow. A stochastic statistical approximation is employed to determine properties of the representative bubble parcels, while all bubbles one parcel evolve simultaneously according to single-bubble dynamics. The method is used to perform RANS simulations for the cavitating flow in Diesel nozzles [73], as well as RANS and LES simulations of the cloud cavitation formation and collapse in an axisymmetric apparatus developed for surface erosion acceleration tests [70]. Recently, Sou et al. [210] also presented a numerical investigation of cavitating flow over a step nozzle where cavitation bubbles were tracked in a Lagrangian way, however the trajectory and the dynamics of each bubble were calculated individually.

Turbulence Modelling for Cavitating Flows   Because cavitation induction regards a wide range of industrial applications and flows of engineering scales, the selection of strategy for the treatment of turbulence in the simulations is of high importance. The preferred approach is to solve for the mean flow and model small-scale spatial or temporal turbulent features by conducting Reynolds Averaged Navier Stokes *(RANS)* simulations. However, with the increase of computational resources, advanced numerical computations become more affordable and thus, Large Eddy Simulations *(LES)*, which resolve the entire range of turbulent scales, become an attractive and realistic alternative.

In their review, Wang et al. [235] apart from the physics of the attached turbulent cavitating flows and the alternative multiphase modelling methodologies, turbulence modelling is thoroughly discussed. Within the framework of RANS, the default eddy-viscosity models *(EVMs)*, suitable and widely used in engineering applications, seem to lack in capturing the dynamics of turbulent cavitating flows. These models, compared to Reynold stress models *(RSMs)*, exhibit less sensitive connection between turbulent stresses and streamline curvature, body forces and strong transport effects. Moreover, characteristics of the cavitating flows like the non-linear behaviour of the pressure-strain relation, the breakdown of turbulence scales in the liquid-vapour mixing region, as well as compressibility effects and reduced speed-of-sound values in the vapour regions, conflict with the turbulence modelling principles. The empirical constants present in EVNs, such as the popular two-equation $k - \omega$ and $k - \varepsilon$ models, need adjustment for non-equilibrium conditions found in such transient flows with swirl, adverse pressure gradients and recirculation.

From numerical tests on sheet cavitation, it is observed that standard EVMs underestimate the cavity length and give poor agreement with experiments regarding velocities and void-ratio within the cavity [44]. The standard models tend to generally over-predict the turbulent eddy viscosity inside the vapour region. Especially for sheet cavitation the high viscosity values towards the rear end of the cavity yield higher stresses that restrict the re-entrant jet [44, 53, 67, 124, 185]. The re-entrant jet is the principal mechanism of unsteady cavitation, that initiates from the downstream end of the cavity, develops underneath it and moves upstream to break the cavity cycle. The failure of the standard EVMs to capture the physics of the attached turbulent cavitating flows becomes more clear by the numerical work of Reboud et al. [185], which demonstrated that inviscid simulations give results closer to experimental findings than viscous computations employing standard $k - \varepsilon$ or $k - \varepsilon\ RNG$ models. To counteract this over-prediction, Reboud et al. [185] and Coutier-Delgosha, Patella et Reboud [67] proposed the introduction of a scaling function that takes in to account the compressibility of the mixture and reduces the turbulent viscosity in the mixture region. The *Reboud* correction is thereafter widely adopted and applied to the well-known two-equation models, $k - \varepsilon$, $k - \varepsilon\ RNG$, $k - \omega$, $k - \omega SST$ [43, 53, 54, 97, 124, 134].

On the other hand, LES computations applied to cavitating flows do not encounter similar modelling issues because even the small scale features are resolved. Koukouvinis, Naseri et Gavaises [114] perform a thorough assessment of turbulence modelling for the prediction of *incipient* and *developed* cavitation for flows inside Diesel injector nozzles. They consider RANS simulations, using $RNG\ k - \varepsilon$, *Realizable* $k - \varepsilon$ and $k - \omega\ SST$, *linear pressure-strain* Reynolds Stress Model (RSM), as well as LES computations with *WALE* model. The Reboud correction was also considered. It is found that either EVMs or RSM may not capture cavitation inception as they do not resolve low pressure existing in vortex cores, while prediction of unsteady cavitation leads to unphysically stable cavities and proves highly dependent on configuration. On the contrary, the LES computations predict correct flow field, vortical and vaporous structures, proper cavity shedding and associated instabilities. Following a slightly different approach, instead the traditional explicit subgrid-scales *(SGS)* model based LES, Egerer et al. [57], Örley et al. [167–170] propose the use of *implicit LES* to simulate the turbulent cavitating flow in Diesel injection systems. Implicit LES introduces turbulence modelling directly to the numerical discretisation of the conservation equations. Adaptive Local Deconvolution (ALDM) is used, which is a *non-linear* Finite Volume Method, capable of capturing pressure shocks and allowing pressure waves and turbulence to be propagated without numerical dissipation. However, these findings cannot reduce the significance and relevance of RANS computations to industrial applications; although the predictions may be found less accurate than those of LES, they consist of reliable and efficient numerical tools for engineers.

1.3 Immersed Boundary Methods

The Immersed Boundary Methods were first introduced by Peskin [181], who studied the incompressible blood flow inside the heart, by solving the flow equations on a Cartesian non-conformal mesh and adding a force term in the momentum equations representing the elastic boundaries of the heart, immersed in the global computational domain. According to studies of Mittal and Iaccarino [147] and Iaccarino and Verzicco [100], the Immersed Boundaries Methods can be classified into *indirect* boundary condition imposition by *continuous*, *discrete* forcing or *penalization* methods and *direct* boundary condition imposition by *ghost-cell* or *cut-cell* methods. A similar classification is followed by Sotiropoulos and Yang [209] who review the Immersed Boundary methods and applications in the context of Fluid Structure Interaction *(FSI)*. The methods are divided into *diffused interface*, corresponding to *indirect* methods, and *sharp interface*, corresponding to *direct* methods.

In the indirect methods, the *no-slip* boundary condition *(b.c.)* at the immersed body is imposed not by directly assigning the boundary value but rather by introducing a forcing term in the momentum equation that drives the solution to the desired value. According to the continuous approach, the forcing term is added in to the continuous form of the equations and therefore depends on the discretisation procedure, whereas for the discrete approach, the term is introduced after the discretisation. The method developed by Peskin [181] falls in the continuous approach and was targeted to problems with elastic boundaries. In the case of rigid boundaries however, the continuous forcing approach may result in stiff numerical schemes or lead to stability problems for highly unsteady flows [147], as it would require very large values of elastic modulus [119] or an iterative feedback forcing technique with high values of damping coefficients [77]. On the other hand, the discrete forcing approach, overcomes these issues for rigid bodies, by usually employing an initial prediction step where the momentum equations are solved neglecting the forcing term and the velocity estimation is used to evaluate the forcing term [15, 149, 229]. In these methods, the interface between the fluid and the solid region is *diffused* and occupies few computational cells in the vicinity of the surface of the immersed body.

In the direct methods, the desired *wall* boundary conditions for the immersed body are imposed by alternations in the numerical stencil on the computational cells in the vicinity of the immersed body interface. According the *ghost-cell* approach [19, 72, 136, 218], the boundary conditions are imposed on cell faces and nodes outside but in the immediate vicinity of the immersed body. The boundary condition values are calculated by means of interpolation between the b.c. point and its projection on the immersed body interface, with the use of artificial mirror and *ghost* points. On the contrary, the *cut-cell* methods [88, 102, 138, 170, 175, 198, 199] reconstruct the immersed boundary by altering the geometry and topology of the computational cells cut by the immersed body interface. The computational cells are divided into fluid and solid sub-cells by the intersecting immersed surface, which creates a new cell face upon which the boundary conditions are applied. The computational cells' topology therefore is altered, so that a regular hexahedral may become generic polyhedral, and the equations' dicretization is modified. These methods are considered to provide the most mathematically and geometrically accurate representation of the immersed body, as well as correct boundary condition imposition. In contrast to the *indirect* or *diffused interface* methods, they offer a sharp representation of the interface between the fluid and the solid.

The forcing methods usually involve a Lagrangian-Eulerian transformation [77, 119, 181, 229]

because the forcing term is evaluated on the Lagrangian points that represent the immersed boundary and then spread on the neighbouring Eulerian computational cells using a Dirac Delta function. The Lagrangian-Eulerian and the inverse transformations could become the bottle-neck of the numerical solution of the governing equations. Discrete forcing Immersed Boundary methods [15, 149] that evaluate the forcing term in the Eulerian frame and apply it to all the cells of the immersed body region, by-pass this issue. Moreover, in the *ghost-cell* or the forcing methodologies, the projection of the immersed boundary on the background mesh may result in a *stair-case* representation of the body as the partially covered cells are not considered as immersed boundary cells, which, in the case of moving immersed bodies, can lead to spurious oscillations that degrade the quality of the solution. This issue is overcome by simply considering even the partially covered cells in the forcing methods [15] or by employing the more complex, yet more accurate, *cut-cell* methods [199].

1.3.1 Indirect b.c. Imposition Methods

In order to present a comprehensive summary of the indirect boundary condition *(b. c.)* imposition Immersed boundary methods, let us consider the viscous incompressible momentum equation in the following vector form:

$$\frac{\partial \mathbf{u}}{\partial t} = \overbrace{-\mathbf{u} \cdot \nabla \mathbf{u} + \nu \nabla^2 \mathbf{u} - \frac{1}{\rho} \nabla p}^{rhs} + \mathbf{S} + \mathbf{f}_b \tag{1.1}$$

where $\mathbf{u}$ is the velocity vector, p is the pressure, ν, ρ are the kinematic viscosity and density of the fluid, $\mathbf{f}_b$ is the vector of body forces acted on the fluid and $\mathbf{S}$ is the vector of any additional momentum sources present in the domain.

Hereafter, and in the entirety of this text, the vectors in the equations are represented by bold fond. In addition, herein, the lower case letters refer to Eulerian frame of reference, while upper case refer to Lagrangian frame of reference (e.g. $\mathbf{x}_i$ the coordinates of ith Eulerian grid point and $\mathbf{X}_k$ of the kth Lagrangian point), unless explicitly otherwise stated.

The indirect b. c. Immersed Boundary methods presented herein, conclude in alternative formulations of the body forces $\mathbf{f}_b = \mathbf{f}_{Ib}(\mathbf{x}, \mathbf{u}, t)$, to account for the presence of the immersed body.

Continuous Forcing Methods

Peskin introduced the immersed boundary technique, to simulate the blood flow through a model heart, by calculating a force acting on the fluid by the elastic walls of the heart and adding it to the momentum equation. In his work [181], the flow is considered incompressible and solved on a Cartesian grid, while the immersed boundary is represented by a set of fibres tracked in a Lagrangian way. The force is calculated on the Lagrangian points $\mathbf{X}_k$, using an analogy to the spring force of Hooke's law. The force on the kth Lagrangian point is calculated with respect to its equilibrium position $\mathbf{X}_k^e$ as:

$$\mathbf{F}_k(t) = \mathcal{K} \cdot (\mathbf{X}_k(t) - \mathbf{X}_k^e) \tag{1.2}$$

Then, the forcing is spread from the immersed boundary Lagrangian points to the computational Eulerian grid ($\mathbf{X}_k \mapsto \mathbf{x}$). The Dirac $\delta(x)$ function is employed in the Lagrangian-Eulerian

$(\mathcal{L}_{L \mapsto E})$ transformation, in order to be localised in the vicinity of the immersed boundary points. The same interpolation function is used on the inverse $(\mathcal{L}_{L \mapsto E}^{-1})$ transformation, to estimate the velocity $\mathbf{V}_k$ of the immersed boundary points, from the fluid velocity field, and calculate their displacement. The $\mathcal{L}_{L \mapsto E}$ and $\mathcal{L}_{L \mapsto E}^{-1}$ transformations are expressed by the relations of 1.3a and 1.3b respectively.

$$\mathbf{f}_m(\mathbf{x}, t) = \sum_k \mathbf{F}_k(t) \cdot \delta(|\mathbf{x} - \mathbf{X}_k|) \tag{1.3a}$$

$$\frac{\partial \mathbf{X}_k}{\partial t} = \mathbf{V}_k = \int_{\Omega_f} \mathbf{u}(\mathbf{x}, t) \cdot \delta(\mathbf{x} - \mathbf{x}_k) gV \tag{1.3b}$$

This approach was adopted in the work of Lai and Peskin [119] and Griffith and Peskin [81] [80] and proved suitable for elastic boundaries. However, when used in case with rigid boundaries, it leads to stiff systems and stability constraints, therefore Goldstein et al. [78] proposed a feedback forcing method, to reduce oscillations and improve stability and boundary condition imposition. The source term they proposed for the momentum equation, has a form equivalent to the linear two-mode controller, popular in control system theory, using as error input signal the velocity $\mathbf{V}_k$ of the immersed boundary points $\mathbf{X}_k$, and consists of two parts, one integral and one linear part:

$$\mathbf{F}_k(t) = \alpha \cdot \int_0^t \mathbf{V}_k(t') dt' + \beta \cdot \mathbf{V}_k(t) \tag{1.4}$$

This approach can also be interpreted with the spring-damper system analogy, where the velocity oscillations are smoothed out and convergence is achieved much more quickly than with simple spring force, as shown in figure 1.1. More source terms could be added to simulate effects of turbulent drag as well as spacial and temporal derivatives. Saiki et Biringen [190], adopted the method of Goldstein and coupled with high-order Finite Different scheme to enhance the results' quality. Zhong et al. [255] also followed this feedback forcing approach for Fluid Structure Interaction problems of vortex induced vibrations.
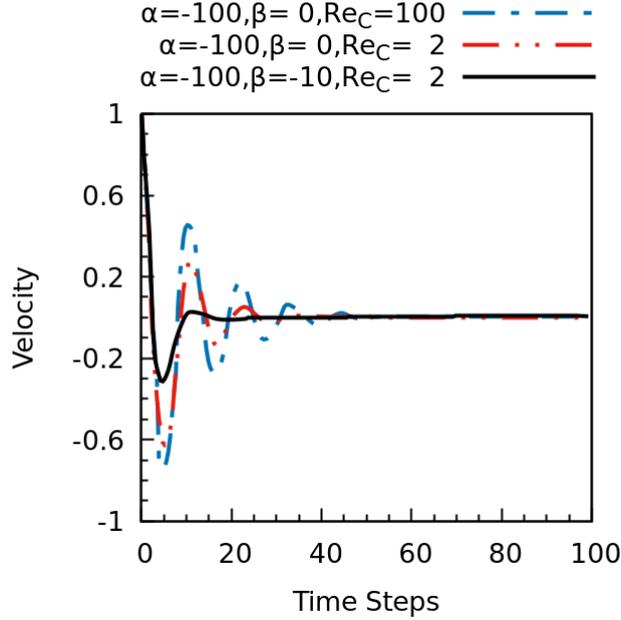
Figure 1.1: Time response of velocity u re-plotted from data presented in Goldstein et al. [77]. Apart from the dependence on the gain values α, β, the results are sensitive on the cell-level Reynolds Re_C, which measures influence of viscous forces and the cell size.

A similar continuous forcing methodology was proposed by Lima E Silva et al. [205], called Physical Virtual Model *(PVM)*. According to this method, a forcing term $\mathbf{F}(\mathbf{X})$ is calculated on the Lagrangian IB points explicitly from the flow variables of the previous time-step, using the interpolated Navier-Stokes equations $(\mathbf{f}(\mathbf{x}) \rightarrow \mathbf{F}(\mathbf{X}))$, accounting for acceleration, inertial, viscous and pressure forces, as in 1.5.

$$\mathbf{F}(\mathbf{X}_k) = \mathbf{F}_a(\mathbf{X}_k) + \mathbf{F}_i(\mathbf{X}_k) + \mathbf{F}_v(\mathbf{X}_k) + \mathbf{F}_p(\mathbf{X}_k) \tag{1.5}$$

where

$$\mathbf{F}_a(\mathbf{X}_k) = \rho \frac{\partial \mathbf{u}}{\partial t}(\mathbf{x}_k), \quad \mathbf{F}_i(\mathbf{X}_k) = \rho(\mathbf{u} \cdot \nabla)\mathbf{u}(\mathbf{x}_k), \quad \mathbf{F}_v(\mathbf{X}_k) = -\mu\nabla^2\mathbf{u}(\mathbf{x}_k), \quad \mathbf{F}_a(\mathbf{X}_k) = \nabla p(\mathbf{x}_k)$$

The forcing is then distributed on the Eulerian grid via the Dirac $\delta(x)$ function, added to the momentum equation and discretised along with the other terms, using a finite differences scheme.

In any of the aforementioned methodologies, the forcing term is introduced in the equations and discretised along them. However, the exact Dirac Delta function can not be used in the numerical computations; rather it is approximated by a smoothing distribution $\delta(|\mathbf{x}_i - \mathbf{x}_s|)$, which tends to diffuse the immersed boundary interface. The choice of the distribution function is essential to these methods as it affects greatly the order of accuracy, and many alternatives have been proposed by researchers [13,80,81,119,127,181,190]. Indicatively, the discrete Delta function $\delta(|\mathbf{x}_i - \mathbf{x}_s|) = \delta(r)$, was formulated as in relation 1.6a by Peskin [181], while Saiki et Biringen [190] proposed the approximation of 1.6b and Beyer et LeVeque [13] introduced the form of 1.6c. Moreover, the technique of distributing the forcing term using a discrete Delta function, may be used in direct forcing methodologies as well; as such, the method of

Pinelli, Favier et al. [182] employed the Delta function given by 1.6d. In the aforementioned relations, r measures the distance between Eulerian grid point $\mathbf{x}_i$ and Lagrangian IB point $\mathbf{x}_s$ and h defines the radius of the interpolation stencil. Figure 1.2 visualises these distributions, for $h = dx$.

$$\delta_P(r) = \frac{1}{h} \begin{cases} (1 + cos(\pi r/2h))/4, & r \leq 2h, \\ 0, & \text{otherwise} \end{cases} \tag{1.6a}$$

$$\delta_S(r) = \frac{1}{h} \begin{cases} (2h + r)/4h^2, & r \leq 2h, \\ 0, & \text{otherwise} \end{cases} \tag{1.6b}$$

$$\delta_B(r) = \frac{1}{h} \begin{cases} 1 - (r/h)^2, & r \leq h, \\ 2 - 3r/h + (r/h)^2, & h < r \leq 2h, \\ 0, & \text{otherwise} \end{cases} \tag{1.6c}$$

$$\delta_F(r) = \frac{1}{h} \begin{cases} \left(1 + \sqrt{-3\left(\frac{r}{h}\right)^2 + 1}\right)/3, & |r| \leq 0.5h \\ \left(5 - 3\left|\frac{r}{h}\right| - \sqrt{-3\left(1 - \left|\frac{r}{h}\right|\right)^2 + 1}\right)/6, & 0.5h < |r| \leq 1.5h \\ 0, & \text{otherwise} \end{cases} \tag{1.6d}$$
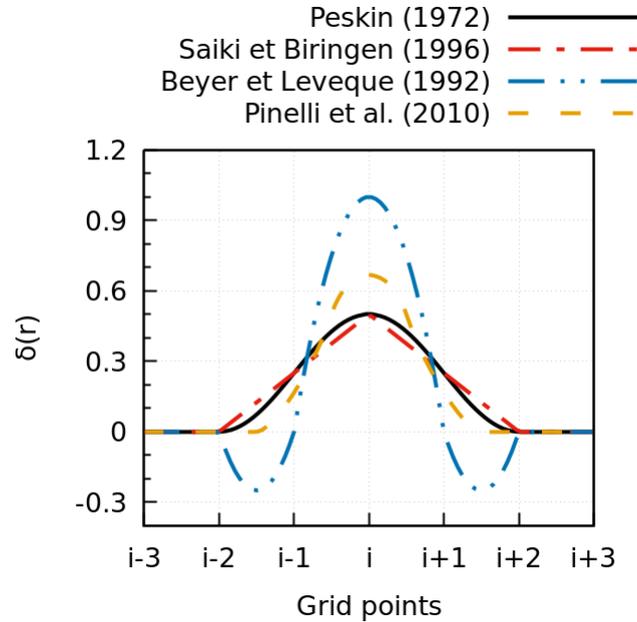
Figure 1.2: Plot of different discrete Delta functions $\delta(x)$, proposed by Peskin [181], Saiki et Biringen [190] and Beyer et LeVeque [13], as well as Pinelli et al. [182], for the Lagrangian-Eulerian and Eulerian-Lagrangian transformations.

Penalization and Fictitious Domain Methods

In this category fall the methods that are based in the idea that the immersed to the flow solid body can be seen as a porous medium with permeability tending to zero. Thus, the Navier-Stokes/Brinkman equations are considered, where the body force term of 1.1, is calculated as:

$$\mathbf{f}_{Ib} = -\frac{1}{\eta_u}(\chi\mathbf{u}) \tag{1.7}$$

with η_u being the permeability, sufficiently small for the solid region, and χ the color function that defines the solid region and localises the penalty imposition. Characteristic examples are the methods developed by Khadra et al. [107], Kadoch et al. [106] and Wachs et al. [234].

Khadra et al. [107] presented a finite volume Fictitious Domain *(FD)* / Penalization method for incompressible and viscous flows. A *Darcy drag*-like term is added in the momentum equations to account for porous or solid media, according to their permeability. Also the boundary conditions in their generalised form (as in 1.8) are linked with the governing equations through the addition of volumetric source terms. The final dimensionless form of the body force term of the equations 1.1, may be given by 1.9.

$$-\frac{\partial\phi}{\partial\mathbf{n}} = \alpha_\phi(\phi - \phi_\infty) + \phi_g, \ \phi_g: \text{ desired b.c. value} \tag{1.8}$$

$$\mathbf{f}_{Ib} = -\frac{\mathbf{u}}{ReDaK} - \beta_\mathbf{u}(\mathbf{u} + \mathbf{u}_\infty) - \phi_\mathbf{u} \tag{1.9}$$

where $Da = K_0/L_0^2$ is the *Darcy number*, defined as the ratio of reference permeability over the square of the length scale, $\beta_\mathbf{u} = \alpha_\mathbf{u}/\epsilon$, with $\epsilon = \mathcal{O}(h)$ the characteristic length of the order of the grid step size h, and K the permeability of the medium. For the fluid it is $K_f \to +\infty$ and $K_s \to 0^+$ for the solid. For Dirichlet b.c. $\alpha_\mathbf{u} \to +\infty \Rightarrow \beta_\mathbf{u} \to +\infty$

However, in this approach, if the center point of a cell lies in the domain occupied by the immersed boundary, the solid body permeability is assigned to the cell and therefore the interphase between the fluid and the solid coincides with the interface of the computational cells. That would lead to the *stair-case* representation of the immersed boundary, which in their study, Khadra et al. [107] counterbalanced by the use of local mesh refinement.

Kadoch et al. [106] developed a penalization method for a pseudo-spectral solver, intended to be used for incompressible flows with scalar transport and mixing. Therefore apart from the equations governing the fluid motion 1.1, in their penalised form, an additional scalar transport equation is considered. For the transport of a passive scalar θ, let be temperature or concentration, with κ annotating the diffusivity, the penalised advection-diffusion equation is given by 1.10. This *flux-based volume penalization* method can be used not only for Dirichlet, but for Neumann and Robin boundary conditions as well and was further generalised by Sakurai et al. [191] to account for *inhomogeneous Neumann* boundary conditions too.

$$\frac{\partial\theta}{\partial t} + ((1-\chi)\mathbf{u})\cdot\nabla\theta = \nabla\left((\kappa(1-\chi) + \eta_\theta\chi)\nabla\theta\right) \tag{1.10}$$

With regards to *multiphase* flows, Vincent et al. [232] applied a penalizing fictitious domain (FD) approach on two-phase flows with moving solids. The solid is also treated as a separate phase, thus the domain is divided in phase specific subdomains according to *phase functions*

$c_i(\mathbf{x}, t) \in [0, 1]$, $i = s, l, g$ for each phase (s: solid, l: liquid, g: gas).The incompressible Navier-Stokes equations are solved for the fluid domain, accounting for surface tension, along with a advection equation for the phase function c_i. In addition, an augmented Lagrangian method is used to deal with high density and viscosity ratio on the free-surface and avoid spurious and parasitic currents, by penalizing the advection terms of the momentum equation.

In order to achieve a more accurate representation of the solid interface, Wachs et al. [234] developed a finite volume *(FV)* Distributed Lagrange Multiplier/Fictitious Domain *(DLM/FD)* method with a second order accurate reconstruction of the boundary, using cubic quadratic basis functions, widely used in finite element methods. The quadratic interpolation functions however, require a large interpolation stencil of 9 points in two dimensional and 27 in three dimensional simulations. The forcing density function is calculated explicitly and in order to avoid any instabilities a smoothing operation is carried out.

Penalty method are developed within the framework of finite-elements formulation by Glowinski et al. [76], Joly et al. [105], Burman et al. [31], Zhou [256], whereas Shirokoff et al. [204] implement a penalizing finite-differences scheme. Another alternative is presented by Pepona and Favier [180], who couple a penalizing Immersed Boundary method, treating the body as a porous medium, with a Lattice Boltzmann method for moving bodies.

Direct Forcing Methods

The basis of Direct Forcing IB methods is often attributed to the works of Mohd-Yusof [150,151] and Fadlun et al. [59]. However, the work of Uhlmann [229] represents a milestone in the development of these methodologies. Mohd-Yusof [150, 151] proposed a IB method, in the framework of a Spectral solver, where the forcing term added in the momentum equations 1.1 is calculated as the sum of the Right Hand Side *(RHS)* terms, explicitly from velocity and pressure values of the previous time step, as in relation 1.11.

$$\mathbf{f}_b^{n+1} = \frac{\mathbf{u}^d - \mathbf{u}^n}{\Delta t} - \mathbf{rhs}^n = \frac{\mathbf{u}^d - \mathbf{u}^n}{\Delta t} + (\mathbf{u}^n \cdot \nabla)\mathbf{u}^n + \nabla p^n - \nu \nabla^2 \mathbf{u}^n \tag{1.11}$$

Fadlun et al. [59], developed a finite differences solver based on the direct forcing approach of Mohd-Yusof and tested against feedback forcing. Fadlun considered three different reconstructions of the interface between solid and fluid region, because the governing equations were discretised on a staggered grid and it was not guaranteed that the definition position of the components of the forcing and the velocity vectors would coincide. According to the first approach the immersed boundary is represented in a *stair-case* manner and the forcing term would be defined on the position of the velocity components, resulting in applying three different b.c. on three different points. According to the second approach, the forcing would be applied to the points closest to the boundary and a weighting factor, estimated as the *solid* volume fraction, would be applied to it. According to the third approach, a linear interpolation is used to calculate the *target* velocity $\mathbf{u}^d$ on the points near the boundary, therefore imposing a specific velocity profile over the boundary. The latter approach is found the most accurate, although it may require explicit grid refinement near the boundary to achieve high spatial density. Moreover, the treatment of the internal cells (i.e. the grid cells entirely covered by the IB), is discussed. Although the external flow solution is found independent of the internal flow field, when using the direct forcing approach, three different treatments are assessed. According to the first, the forcing is applied without smoothing on the internal cells as well,

imposing a constant velocity distribution which adapts the pressure accordingly. According to the second treatment, the internal cells receive no forcing and the flow develops freely. Finally, according the third approach, which is essential for spectral codes, the velocity on the internal cells adjacent to the boundary is reversed by continuing the linear profile from the exterior region.

The method proposed by Fadlun et al. [59] is widely adopted and applied on complicated flow simulations. It facilitates the demanding Large Eddy Simulations *(LES)* or Direct Numerical Simulations *(DNS)* computations of turbulent or transitioning flows performed by Cristallo and Verzicco [45, 46], Balaras [6, 7, 245] with either static or moving boundaries, as well as within the FSI framework by De Tullio et al. [49, 228].

Uhlmann [229] proposed a *fractional step* direct forcing Immersed Boundary Method for incompressible flows, with application on particle flows. The method is integrated in a 3-step Runge-Kutta solver, which employs pressure-velocity coupling through the Poisson pressure correction equation. The forcing term is evaluated using the intermediate velocity field and the convective, pressure and viscous terms extracted from a first momentum prediction step, which ignores the IB forcing. In other words, from the incompressible laminar momentum equations 1.1, the RHS terms of the momentum equation are used to extract an preliminary estimation of the velocity 1.12, which is then used to evaluate the forcing term 2.24. The forcing term and the preliminary velocity are then used to correct the velocity through a Helmholtz equation 1.14 and then estimate the pseudo-pressure 1.15 which advances the velocity and pressure in time. However, this methodology requires $\mathcal{L}_{L\mapsto E}$ transformations, using the discretised Dirac Delta function 1.6a proposed by Peskin [181]. The forcing term is first evaluated on the Lagrangian points representing the IB particle and then spread on the background Eulerian grid.

$$\tilde{\mathbf{u}} = \mathbf{u}^{k-1} + \mathbf{rhs}^{k-1/2} \cdot \Delta t, \text{ at iter. k in time-step } t_{n+1} \tag{1.12}$$

$$\mathbf{f}_{Ib}^{k} = \mathcal{L}_{L\mapsto E} \left\{ \left(\frac{\mathbf{U}^d - \tilde{\mathbf{U}}}{\Delta t} \right) \right\}, \quad \text{with } \tilde{\mathbf{U}} = \mathcal{L}_{L\mapsto E}^{-1} \{\tilde{\mathbf{u}}\} \tag{1.13}$$

$$\nabla^2 \mathbf{u}^* - \frac{\mathbf{u}^*}{\alpha_k \nu \Delta t} = -\frac{1}{\alpha_k \nu} \left(\frac{\tilde{\mathbf{u}}}{\Delta t} + \mathbf{f}_{Ib}^{k} \right) + \nabla^2 \mathbf{u}^{k-1} \tag{1.14}$$

$$\nabla^2 \phi^k = \frac{\nabla \cdot \mathbf{u}^*}{2\alpha_k \Delta t} \tag{1.15}$$

The method proposed by Uhlmann [229] is widely adopted by researchers. Feng and Michaelides [63] also employed a similar to Uhlmann's [229] direct-forcing IB approach on Direct Numerical Simulations *(DNS)* of heat transfer in particulate flows. The forcing term is applied on the interface cells in order to enforce the non-slip condition, as well as on the internal cells of the particles, to impose rigidity constraint. In addition to the source term for the momentum equations, a source term is formulated in a similar manner, explicitly from the values of the previous step, for the energy transfer equation, to impose the temperature of the particle as a boundary condition. In addition, Pinelli, Favier et al. [182], Cai, Favier et al. [32–34] and Cai et al. [35] adopted a direct forcing method that follows the same rationale as Uhlmann's approach [229], with a fractional-step calculation of the forcing term. However, a different approximation of the Dirac function, with three-steps presented in 1.6d, is employed to handle the Euler-Langrange transformations. Constant, Favier et al. [42] implemented the

method of Pinelli, Favier et al. [182] within the framework of finite volume methods and integrate it within the PISO algorithm, developing a new solver within `OpenFOAM`. Favier, Pinelli et al. [62] coupled the forcing IB approach proposed for Navier-Stokes equations by Pinelli, Favier et al. [182] with a Lattice Boltzmann method, for Fluid Structure Interaction simulations of slender bodies.

Riahi, Favier et al. [186] extended the previous works of fractional step forcing [32–35, 42, 182, 229] on compressible flows. Apart from determining a source term for the momentum equation to impose Dirichlet b.c. on the velocity field, an additional source term may be derived to impose the Neumann boundary condition on the pressure field over the IB interface. It is demonstrated that by taking into account that the pressure gradient can be decomposed on the normal and the tangential to the IB surface components, as in 1.16, and that on the normal to the IB surface direction should be zero, $\nabla P^d \cdot \mathbf{e}_{nIb} = 0$, a pressure correction term can be formulated manipulating the RHS terms of the momentum equation. Following the fractional-step approach and by considering $-\phi^{\,n+1/2} + \nabla p^{\,n+1/2} \cdot \mathbf{e}_{tIb} \approx -\alpha_s(\rho_L\mathbf{u})^*$, an alternative forcing term can be formulated 1.17. As the source terms are defined on the Lagrangian IB points, a three-step discrete Delta function 1.6d is then used to distribute the forcing on the Eulerian grid.

$$\nabla P^{n+1/2} = \nabla P^{n+1/2} \cdot \mathbf{e}_{nIb} + \nabla P^{n+1/2} \cdot \mathbf{e}_{tIb} \tag{1.16}$$

$$\begin{aligned} \mathbf{f}_{Ib}^{n+1/2} &= \alpha_s(\rho_L\mathbf{u})^d - \mathbf{rhs} \\ \Rightarrow \mathbf{f}_{Ib}^{n+1/2} &= \alpha_s(\rho_L\mathbf{u})^d - \phi^{n+1/2} + \nabla p^{n+1/2} \\ \Rightarrow \mathbf{f}_{Ib}^{n+1/2} &= \alpha_s\left((\rho_L\mathbf{u})^d - (\rho_L\mathbf{u})^*\right) - \left(\nabla p^d - \nabla p^{n+1/2}\right) \cdot \mathbf{e}_{nIb} \end{aligned} \tag{1.17}$$

Blais et al. [15] developed a methodology for incompressible flows, inspired by the *penalization* methods, where the a forcing term is coupled with pressure-correction PISO algorithm. The forcing term evolves in every new time-step from the value of the previous, throughput the iterative process using under-relaxation. The forcing term $\mathbf{f}_{Ib}$ is calculated by 1.18, using the under-relaxation factor $\alpha \in [0,1]$ and is applied on every cell in the region covered or intersected by the body using the *solid fraction* β. The solid fraction is calculated as the *boolean* sum of the cell points (vertices and center) in the solid region 1.19. This methodology adopts the *stair-case* approach and does not follow a Eulerian-Lagrangian representation or calculation of the forcing term and thus avoids the cumbersome interpolation steps. By using the *stair-case* approach, the projected volume of the IB on the background Eulerian mesh does not coincide with the actual volume of the determined by the closed surface mesh, and thus a volume correction is applied to the *halo-layer*. In every time-step m, a prediction step is carried out for the momentum equation, including the forcing term, and an velocity estimate $\mathbf{u}^{m*}$ is extracted. Then, the PISO loop commences with a Rhie-Chow interpolation that is applied (neglecting pressure gradient and IB forcing) to get a corrected value of the velocity $\mathbf{u}^{m**}$. Then, the pressure correction equation is solved using $\mathbf{u}^{m**}$ and $\mathbf{f}_{Ib}^{m*}$, and finally the velocity and then IB forcing term are updated ($\mathbf{u}^{m***}$ and $\mathbf{u}^{m***}$) and the algorithm continues to the next PISO iteration.

$$\mathbf{f}_{Ib}^{m***} = \mathbf{f}_{Ib}^{m*} + \frac{\alpha\beta}{\Delta t}\left(\mathbf{u}_{Ib}^m - \mathbf{u}^{m***}\right), \text{ for every time-step m} \tag{1.18}$$

$$\beta_i = \frac{N_{v,i}^{in} + N_{c,i}^{in} \cdot N_{v,i}^{tot}}{2N_{v,i}^{tot}}, \text{ for every grid cell i} \tag{1.19}$$

Based on the work of Blais et al. [15] and Wachs [234], Municchi and Radl [153, 154] presented a combined Immersed Boundary and Fictitious Domain method, for application on gas-particle suspension flows. In the framework of CFD-DEM *(CFD-Discrete Elements Method)*, where the particle kinematics are tracked and resolved, an Eulerian-Lagrangian approach is followed and for cases where the the particle sizes are smaller than the grid cell size, the governing equations contain unclosed terms and the approach is labelled as Particle-Unresolved Euler-Lagrange approach *(PU-EL)*. In their work, Municchi and Radl employed a multi-scale IB-FD approach that derives the needed closures for the fully resolved equations, from Particle-Resolved Euler-Lagrange *(PR-EL)* simulations or Particle-Resolved Direct Numerical Simulation *(PR-DNS)*, if no turbulence model is used. They developed a hybrid method were a forcing term is added on the dimensionless momentum and energy transport equations. The forcing term for the momentum equation is calculated throughout the PISO-IB loop as in the work of Blais [15], and is acting on the computational grid cells cut by the IB surface *(surface cells)*. An additional correction term acting on the computational grid cells covered by the IB solid particle, is added to ensure that no flow occurs inside the IB region. Moreover, a boundary layer reconstruction procedure is carried out in order to evaluate the values to be imposed on the surface cells. A source term is also used in the energy equation, which is calculated explicitly from the previous step. The imposed values are calculated by interpolation between the IB surface value and the neighbour grid cell values, as in the work of Wachs [234]. The order of the interpolation depends on the radius of the interpolation stencil, which tends to zero order when the stencil becomes so narrow to include only the IB surface point and results in a penalty function, as the regular fictitious domain methods.

Mochel et al. [149] employed a fractional step direct forcing IB approach as well, in conjunction with the compressible Unsteady Reynolds Averaged Navier Stokes *(URANS)* equations for high-Reynolds turbulent flows. Apart from the momentum equation, the turbulent model's equation are adapted by introducing a similar source term to impose the desired b.c. on the turbulent viscosity.

1.3.2 Direct b.c. Imposition Methods

Ghost-cell Methods

The *ghost-cell* methodologies impose boundary conditions (b.c.) on cell faces and nodes outside but in the immediate vicinity of the immersed body. The boundary values are calculated by means of interpolation between the b.c. point and its projection on the immersed body interface, with the use of artificial mirror *ghost* points. In the case of a linear interpolation function, the values of the ghost points are calculated by 1.20, where d_* represent distances.

$$\mathbf{u}_{gc} = \mathbf{u}_p - \frac{d_p + d_{gc}}{d_p}(\mathbf{u}_p - \mathbf{u}_{Ib}) \tag{1.20}$$

Gilmanov and Sotiropoulos [74] proposed initially a ghost-cell method for a finite differences scheme on staggered grid and a linear interpolation scheme to reconstruct the solution near the body. The method was then improved into a hybrid Cartesian/Immersed Boundary Method

[75] by discretising the equations on a hybrid staggered/non-staggered grid and incorporating a quadratic interpolation scheme. The nodes of the Cartesian background grid are categorised in to fluid, IB and solid nodes, regarding their position with respect to the triangulated surface *tri-surface* representing the IB body. As IB are labelled the nodes that lay outside but in the immediate vicinity of the IB tri-surface. The governing equations are solved on the fluid nodes, with boundary conditions imposed on the IB nodes and the solid nodes completely blanked out. The boundary conditions on the IB nodes are determined using interpolation. For both velocity and pressure, Dirichlet boundary conditions are determined on the IB nodes, as a linear interpolation between the surface value and the fluid value, on the line defined by the IB node and the nearest point of the tri-surface. The standard Neumann boundary condition for the spatial gradient $\nabla_{\mathbf{x}} p$ of the pressure field, is transformed into Dirichlet boundary condition for its normal to the IB surface component. The method is capable of treating immersed bodies defined by convex closed surfaces, thick or thin, as well as completely open surfaces, because of the way the boundary condition are defined on the grid point near the solid interface. This highlights an important advantage of the ghost-cell over the forcing methods.

The method was adopted and further enhanced to accommodate prescribed solid motion by Ge [71, 72] and Dasi [47]. Borazjani, Sotiropoulos et al. [10, 17, 19–22] applied the method on FSI simulations, with both non-deformable and deformable solids, and also combined it with an over-set approach [18] to perform computations on more complicated domains with multiple moving boundaries.

Takahashi et al. [218] employed a *ghost-cell* approach to study the compressible turbulent supersonic flow over 2D cylinders, where shocks (discontinuities) are present. A signed distance of the cells from the immersed boundary is used as a level-set function to categorize the computational cells as fluid cells, ghost-cells or solid cells. Ghost cells are considered those for which $0 \geq d_{gc} \geq -2\sqrt{2}\delta x$, with δx being the spatial resolution. Therefore the b.c. values are imposed on the cell centres of the cells *inside* the solid region but in the immediate vicinity to the interface. To estimate the b.c. values of the primitive variables on the ghost cells, an *image* point is used in fluid region, on the edge of a probe that extends from the ghost cell through the immersed boundary along the normal to the IB interface. The length of the probe is chosen $d_p = 1.75\delta x$ and the values of the variable on the image point are calculated by bilinear interpolation from the surrounding fluid cells. To impose the Dirichlet b.c. for the velocity, the velocity on the ghost cell is calculated by linear extrapolation 1.20 and to impose the Neumann b.c. for the pressure and density fields, the ghost cell values are assumed equal to the values of the image point.

Luo et al. [136] used a *ghost-cell* IB method, for problems of heat transfer in compressible flows, within a sixth-order finite-difference framework. To maintain the same order of accuracy, three layers of *ghost points* are used and the rest of the grid points laying in the solid region are disregard. A bilinear for 2D, or tri-linear for 3D, interpolation scheme is used to calculate the fluid properties on the mirror points from the neighbouring fluid points. The boundary condition for a variable ϕ can be expressed in the generic form of 1.21, involving the normal to the wall gradient $\partial\phi/\partial\mathbf{n}$. Apart from the usual *Dirichlet* ($\alpha = 0$, $\beta = 1$) and *Neumann* ($\alpha = 1$, $\beta = 0$) boundary conditions, the use of the ghost-cell approach facilitates the formulation of *Robin* (mixed, $\alpha, \beta \neq 0$) boundary conditions as well. The ghost-points value ϕ_G for *Dirichlet* and *Neumann* b.c. are calculated with respect to IB surface and mirror points values by 1.22 and 1.23 (using 2 mirror points) respectively; for *Dirichlet* b.c. the boundary value of the field

is known and for *Neumann* b.c. the value of the gradient of the field is known on the boundary, while for *Robin* b.c. both values are needed to get estimations on the ghost-points from 1.21 using two mirror points.

$$\alpha \frac{\partial \phi}{\partial \mathbf{n}} + \beta \phi = \phi_G, \ \ \phi_G: \text{ desired b.c. value} \tag{1.21}$$

$$\phi_G = 2\phi_{Ib} - \phi_M \tag{1.22}$$

$$\phi_G = \frac{(\phi_{M1} + \phi_{M2})}{2} - \frac{(d_{M1,Ib} + d_{G,Ib})}{2} \left(\frac{\partial \phi}{\partial n} \right)_{Ib} + \frac{(d_{M2,Ib} + d_{G,Ib})}{2(d_{M2,Ib} - d_{M1,Ib})}(\phi_1 - \phi_2) \tag{1.23}$$

Cut-Cell Methods

According the *cut-cell* methods, the background computational mesh, which is usually a canonical Cartesian grid, is directly cut by the surface representing the immersed boundary. The computational cells intersected by the IB representation are split into *live* and *dead* parts; the control volume is altered to take into account only the *live* fluid part into the solution, while the *dead* solid part is disregarded. Berger [12] presents a comprehensive but generic summary of cut-cell methodologies; the motivation and the advantages of this class of methods are discussed.

The main feature of cut-cell methods is the alternation of governing equations' integration procedure in the new control volume of the cut-cells and the computation of the fluxes on the segmented IB surface face. Moreover, the main, well known, issue of these methods is the *small cell stability* problem. When cut-cell method is employed, arbitrary small cells may appear during the numerical solution, that impose strict time-step constrains. When, in addition, the immersed body is moving, spurious oscillations appear in the pressure field [138, 198, 199], that deteriorate the quality of the simulations.

Seo et Mittal [199] attributed the noise in the flow solution, and the spurious oscillations of pressure field, to the spatial discontinuity of pressure over the IB interface and the temporal discontinuity of velocity field; in forcing methodologies, spreading and smoothing the source term diminishes these problems. Meinke et al. [138] confirmed this observation and successfully treated spurious oscillations by introducing smooth transition functions to the discretisation near the IB boundary.

To tackle the *small cell* stability issue, either *cell-merging* and *cell-linking* or *flux redistribution* can be performed. According the first approach, used by [88, 199], if the volume of the cut-cell is smaller than a certain threshold, it is merged with the neighbour cell; this approach is useful when the boundary is moving, however it may cause further instabilities. According to the second approach, employed in [138, 198], the flux difference for a small cell is scaled by its "volume-fraction", which represents the fluid part of the cell, and then the rest of the flux is distributed to the neighbouring cells. The redistribution is usually done via volume-weighting or density-weighting. A hybrid technique, that couples these two approaches is also found in the work of Örley et al. [170].

The representation of the immersed surface on the computational grid and the approximation of the intersection of the cutting surface with the cut-cell and the subsequent new cell face,

is another important aspect of the method. Schneiders et al. [198] and Meinke et al. [138] used a level-set singed distance function $\phi_s(\mathbf{x})$ to *"implicitly"* determine the solid boundary: $\phi_s < 0$ denotes the solid area, $\phi_s > 0$ the fluid area and the solid boundary is the isosurface of $\phi_s = 0$. A piecewise linear approximation of the solid boundary is constructed by the level-set function values stored on the cell centers. The location of the cut is estimated linearly by the interpolated level-set values on the cell vertices. A level-set function is also used by Pasquariello et al. [175], Castiglioni et al. [37], Thari, Pasquariello et al. [221]. Hartman et al. [88], James et al. [102], employed a piecewise linear representation of the boundary surfaces, as well. On the contrary, Seo and Mittal [199] and Örley et al. [170], represented the immersed boundary with a triangulated mesh. The precise edge and face cuts are determined and the segmented solid surfaces are reconstructed by triangulation. This approach ensures more accurate definition of the the new volume of the cut-cell and improves the quality of the results.

In addition, different approaches have been proposed for the calculation of the derivatives of the flow variables on the centres of the cut-cells. Hartman et al. [88] employed a linear least-squares method to compute the derivatives in the cut-cells. Johnson et al. [104] made use of *spline functions* to represent the variables within the cell volumes; in this way, the derivatives of the variables are continuous throughout the entire domain and on cut-cells the variables are well defined on cut-faces.

For viscous flows, where boundary layers are present, and the cell size should follow a progressive expansion over the wall or, more generally, the cell size is a function of the normal distance from the wall, few methodologies propose the geometric alternation of the cell nodes near the boundary and the cancellation of cut-cells. However, wall functions have been proposed in conjunction with cut-cell approach by Capizzano [36].

1.3.3   IB methods for Multiphase Flows

Many studies can be found in literature regarding multi-phase simulations with immersed boundary techniques, with applications especially on incompressible flows. Two-phase problems may regard droplets and bubble dynamics, free surface and wave interaction with structures and obstacles and may concern naval, micro fluids, internal combustion and biological applications.

For a scalar field α, representing temperature or concentration of a component in a mixture, the generic form of the transport equation governing its distribution in space and evolution along with the flow, taking into account advection, diffusion and any sources, is given by 1.24a. In the case of two-phase flows of immiscible fluids, the diffusion is not accounted for and the transport equation for the volume fraction of the secondary fluid takes the form of 1.24b.

$$\frac{\partial \rho \alpha}{\partial t} + \nabla \cdot (\mathbf{u} \rho \alpha) - \nabla \cdot (\mathcal{D} \rho \nabla \alpha) = S \tag{1.24a}$$

$$\frac{\partial \alpha}{\partial t} + \nabla \cdot (\mathbf{u} \alpha) = 0 \tag{1.24b}$$

On solid wall boundaries, for conformal grids, Neumann boundary conditions are set for the volume fraction in the transport equation, to impose the gradient value across the interface. Usually, the value of this gradient is set to zero, which physically corresponds to a contact angle of 90°; however advanced modelling alternatives considering contact line or triple point (gas-liquid-solid) dynamics, set different values. On the other hand, fluxes, that directly affect

the advection of the volume fraction, are governed by the momentum equation, where zero normal and tangential velocities value are imposed on walls, in the form of Dirichlet boundary conditions. On Immersed Boundaries, where velocities are set or driven by direct forcing, special care must be taken for the volume fraction field. Numerous approaches can be found in the literature.

Shen and Chan [201–203] implemented a direct forcing IB method, where the IB force is calculated as a difference of the velocity field from the body velocity in the area enclosed by the immersed surface, but no special treatment for the liquid volume fraction is applied in the transport equation and only fully submerged structures that do not interact with free-surface are considered. Sanders [194] and Peng [179] also developed direct forcing IB methodologies where no special treatment for the VOF transport equation is presented and no free-surface problems are considered. Liu, Wu et al. [132] used a penalized momentum equation with an additional volumetric source term coupled with a unmodified VOF transport equation for the secondary phase. Lin, San-Yih et al [131] implemented a direct forcing immersed boundary method with no special treatment for the VOF transport equation and the volume fraction field which they apply on free-surface and particle interaction problems (particle crossing free-surface).

Sun and Sakai [215] applied a direct forcing IB approach and consider the contact angle on the walls $\mathbf{n}_\phi \cdot (-\mathbf{n}_{Ib}) = cos\theta$, where $\theta = \pi/2$ is usually set. This condition corresponds to a zero-gradient b.c. for the volume fraction ϕ: $\nabla_{Ib}\phi = 0$. The advection of the interface in performed in the entire computational domain, but then a dilation or extension step is carried out. According to the former, a 3×3 stencil is used to update the ϕ values as a mean average of the neighbours for all fluid cells. According to the latter, a additional transport equation is solved iteratively for the solid cells, with the use of a pseudo-time step $dt_{ext} = dx$ and a pseudo-velocity $\mathbf{u}_{ext} = -\mathbf{n}_B$. However, both approaches lead to slight mass errors as the VOF advection is no longer conservative. As a remedy, Sun and Sakai periodically reset volume fractions by subtracting mean error in the interface cells.

Zhang [252] used a similar direct forcing approach for the source term in the momentum equation, but used a solid volume fraction function to mark the immersed boundary region, which plays an active role in the liquid transport equation, as after performing the advection step, the solid volume fraction is subtracted from the liquid volume fraction. That way, the free-surface is ensured to coincide with the solid interface. Malvandi [137] employed a simpler approach, as the solid density is taken into account both for the momentum forcing source term and the density balance. No special treatment for the volume fractions is needed as the liquid advection is controlled by the density spacial distribution.

Pengzhi Lin [130] implemented a labelled as *cut-cell* approach, which consists of a penalization procedure based on the cells' *openness*, coupled with a volume-of-fluid (VOF) method for free surface tracking. Instead of modifying the computational cells, a mask-solid volume fraction function is used to distinguish the solid from the fluid areas and to multiply the momentum equation so as it is only solved in the fluid area; this method is dubbed Partial Cell Treatment *(PCT)*. Therefore fluxes are calculated only in the fluid unmasked area and in the solid cells velocity is set to zero. A cut-off limit for the solid volume fraction function is used to avoid instabilities. For moving solids, an additional source term is calculated and inserted to the pressure Poisson equation. Regarding, treatment of the free-surface in the vicinity of the immersed body, the VOF function is defined on the remaining open fluid volume after

the penalization is performed Wu, Chu et al. [240] solved also a penalized momentum equation, following the PCT approach. Horgue [95] added a penalization term in the momentum equation for the velocity and a pressure correction term to ensure no pressure jumps on the solid interface. This approach has similarities to porous media penalization. For the secondary phase transport equation, the volume fraction values are explicitly set to a prescribed value inside the solid area. Kadoch [106] followed a penalizing approach for the momentum equation that treats the solid as porous media with a very small permeability, and extended it to the transport equation of the secondary fluid, by multiplying the advection and diffusion term with the fluid volume fraction and adding an artificial diffusion term for the solid region scaled with a *permeability* constant.

Yang [246] implemented a sharp interface IB/level-set method for wave structure interaction problems. IB forcing term is added on nodes near the IB surface and a level-set function ϕ is used to account for the two-phase flow, where the ϕ field represents the distance from the two-phase interface. For the interaction of free-surface with the immersed solid, a contact angle b.c. is formulated as $\mathbf{n}_\phi \cdot \mathbf{n}_{Ib} = -cos\theta$, where $\mathbf{n}_{Ib}$ is the outward normal direction to the IB surface, $\mathbf{n}_\phi$ the normal to the level-set function and θ the contact angle. From there, a Neumann b.c. is derived for the level-set function $\partial\phi/\partial t = -cos\theta$. This approach extends the fluid inside the solid area. This explicit modification of ϕ leads to slightly changed volume fractions.

Patel [178] implemented a different IB approach, by directly changing the computational stencil of the discretised momentum equation near and inside the solid, applying no-slip b.c. This approach seems similar to ghost-cell methods. In addition, for the VOF transport equation, contact line dynamics are considered for the cells on the interface. A smoothing procedure is used and the VOF field is extended into the IB region by solving an artificial transport equation.

Alternative approaches are also considered by researchers that do not use the conventional VOF or Level-Set logic. Vire [233] implemented a continuous forcing term to represent immersed boundaries but used a different set of flow equations for each phase and an advection equation for the fluid concentration, while modelling free-surface as a boundary condition. Angot [3] implemented a penalty-projection method for multiphase flows, according to which solid boundaries are modelled using a *fictitious domain* approach, where viscosity tends to infinity in the solid region. Li, Favier et al. [129] combined a Lattice Bolzmann method with an Immersed Boundary representation for both single or multi fluid flows, where the flow equations are solved in a Lagrangian framework and no transport equation is used to capture the interface between the phases. Nishida [158], used a different approach where the transport equation for the advected phase is not solved, but rather a phase-field equation instead. According this approach, fluid free energy is minimized to find the equilibrium interface. Source terms are inserted in the phase-field equations, applying a zero-gradient b.c. for the volume fraction on the immersed boundaries.

1.3.4 Turbulence modelling for IB Methods

When modelling turbulence, the numerical tools for the turbulent variables may have to be adjusted to take into account the presence of the IB body. Iaccarino and Verzicco [100] present a comprehensive overview of applications of IB Methods on turbulent flows.

Fadlun et al. [59], Balaras [6] and Cristallo and Verzico [46] are among the first to investigate the use of LES in conjunction with a direct forcing IB method, on flows of moderately

high Reynolds number. Such computations may regard a wide range of applications, from industrial to biological cases. Studies of incompressible flow inside a Internal Combustion *(IC)* cylinder/piston assembly at $Re = 2000$ [46, 59], on the wake of road vehicle at $Re = 20000$ up to $Re = 100000$ [46], through a channel with wavy wall at $Re = 6760$ [6, 46], as well as the pulsatile flow through a model of arterial stenosis at $Re = 1500$ [7] or through a bi-leaflet mechanical heart valve at $Re = 4000 - 6000$ [46, 245], are carried out using IB methodologies.

In most of these cases, a dynamic Smagorinsky model was used to estimate the stress tensor, based on the filter length and a coefficient dynamically determined by the flow field. As the Reynolds number increases, higher near-wall resolution is needed to resolve the flow structures within LES, and modelling may be required. Since the grid is not conforming to the IB boundary, the normal to the wall direction is uncertain and the modelling becomes non-trivial.

Although Fadlun et al. [59] did not mention any particular treatment near the IB, Balaras [6] assigned on the forcing nodes a boundary condition for turbulent viscosity ν_t, linearising it over the interface in similar manner as the velocity. The assigned ν_t b.c. is just an approximation of the proper value, but the error in the cases studied was estimated to be negligible. Cristallo and Verzicco [46] presented a potential remedy, by solving a differential equation for the viscous stresses on the external nodes adjacent to the IB, to create a *"layer"* and provide boundary conditions for LES.

More recently, Vincent et al. [232] applied a penalizing fictitious domain (FD) approach on two-phase flows with moving solids. More precisely, they investigated *hydroplaning* of vehicle tires on wet road. They employed an LES approach to account for turbulence, using a combination of Smagorinsky and Turbulence Kinetic Energy *(TKE)* models. Although this model is developed for single-phase flows and considers the sub-scale turbulent interaction of water and air as negligible, it was thought sufficient of the specific application, as the interfacial scales were large enough in the area of interest.

Although IB methods seem popular with LES and DNS computations, Cristallo and Verzicco [46] highlighted the implications arising the use of IB boundaries in cases of highly turbulent flows. Despite the fact that IB methods seem well suited for LES computations involving complicated geometries, their application is limited in flows of low and moderate Reynolds numbers. Such flows may regard biological flows. In contrast, as the Reynolds number increases the spatial resolution for capturing the smallest turbulent scales becomes drastically demanding. The subsequent increasing computational cost, in conjunction with accuracy issues arising from the lack of the ability to control the grid cell growth near to the immersed boundary, makes the IB coupling with LES less appealing. For high-Reynolds flows of large scales and industrial interest, like aeronautical applications, the Reynolds Averaged Navier Stokes *(RANS)* approach, employing turbulence models, may be more favourable.

Mochel et al. [149] implemented a direct-forcing IB method for compressible turbulent flows of high-Reynolds and use Spalart-Allmaras model in Unsteady RANS *(URANS)* and Detached Eddy Simulation *(DES)* approach. Apart from altering the momentum equation to account for the presence of the immersed body and impose no-slip condition on the boundary, they adapt the turbulence model equations. Following the same approach as for the momentum equations, where a volumetric IB forcing term is added, a source term is added in the transfer equation of the turbulence viscosity to impose the respective boundary condition. Also Grimberg and Farhat [82] used an *Embedded Boundary* method to simulate supersonic parachute inflation,

within an FSI approach, using a URANS solver in conjunction with Spalart-Allmaras turbulence model. Their work mainly focused on the solution algorithm of the Eikonal equation which computes the wall distance; however the proposed approach was adjusted for non-body conforming Eulerian grids, where the boundary condition for the Eikonal equation is enforced in the region of the immersed surface. Recently, Abalakin et al. [1] have performed Improved Delayed Detached Eddy Simulations *(IDDES)* for the turbulent flow around a cylinder at $Re = 3900$, employing a penalization IB method, and found good agreement with conventional body-fitted grid computations.

1.4 Open Challenges

From the literature review presented in the previous sections, it is evident that numerous computational methods have been developed to address a broad range of applications of multiphase flows and fluid and solid interactions.

It is evident that Immersed Boundary Methods have been employed for computational studies of various flow regimes and physical problems. However, the applications of IB methods on cavitating flows is limited. Considering the complex industrial applications of those flows, with moving geometries and potentially wide range of length scales that is difficult to be accommodated by conformal grids, it could be anticipated that such methods would be widely used. The use of IB methods for simulations of fuel injection cycles with moving needle [9, 167, 169, 170, 253] or of the operation of fuel gear pumps [144], clearly showcase the practical benefits of these methods.

The use of IB methods on cavitating flows widens the range of physical problems that can be studied. Given the undeniable ease of FSI studies by IB methods [209], similar approach could be employed in cavitating flows of industrial interest. Cavitation is a known source of noise and vibrations; an FSI numerical investigation of the link between cavitation and induced vibrations of rigid or deformable bodies could be achieved by modelling the bodies as Immersed Boundaries. In this framework, the system of propeller and rudder could be studied. In addition, as the interest of cavitating flows shifts to medical or bio-engineering applications, IB methods could prove useful in the numerical investigation of drug delivery or tissue damage by collapsing vapour bubbles. The IB methods are capable to handle complex geometries, large boundary displacements and topology changes.

On the other hand, although numerous IB methods are proposed, each has specific advantages and disadvantages and it is not easy to conclude which is the best. The choice of the method depends upon the application, in addition to the numerical complexity and computational cost this choice entails. Although the cut-cell approach enforces strict mass, momentum and energy conservation and thus, is considered the most accurate amongst the IB methods [170], it can suffer form *small cell instabilities* and calls for cumbersome topological manipulations. As an indication, the computational cost of computing intersections of a triangulated IB surface, comprised by M elements, with the computational cells and finding or creating the *cut-cells*, on a $N \times N \times N$ Cartesian grid that follows a tree-based data structure, is estimated at the order of $\mathcal{O}(N^2 \cdot M \cdot logM)$ [12]. On the contrary, ghost-cell approach requires a large number of interpolations that can be a bottleneck for the computations [136, 154] and its accuracy may depend on both the resolution of the IB representation and the background grid. Moreover, in ghost-cell methodologies, the projection of the immersed boundary on the background mesh may result in a *stair-case* representation of the body where the partially covered cells are not considered, which would lead to spurious oscillations [199], in the case of moving immersed bodies. Such numerical implications may be prohibiting for computations of complex turbulent multiphase flows with violent phase change.

The use of a forcing IB approach, would alleviate the obstacles from the computationally expensive manipulations related to cut-cells or ghost-cells methodologies. The use of a continuous color function to localise the forcing, which accounts for the partially covered cells, would also overpass the *stair-case* problem. Therefore, it becomes apparent that the use of *direct forcing* Immersed Boundary approach for cavitating flows should be investigated.

1.5 Objectives

The objective of the present research work is to develop an Immersed Boundary Method cavitating flows, suitable for addressing a wide range of applications, with main focus on computational problems of engineering scales.

The developed method is following the direct forcing approach because of its simplicity in implementation and robustness. The presence of solid boundary is modelled simply by the addition of a source term in the momentum equations, which is straightforward and fast to estimate. Complications arising from interpolations or special treatments of the computational cells cut by the immersed surface should be avoided. In addition, the forcing approach should provide a smoother solution, which may be important for cavitating flows with strong pressure variations.

The developed tool is coupled with multiphase flow solvers, employing the barotropic Equation of State to account for phase change. This is done mainly because the barotropic solvers are considered more suitable for the problems under consideration. In addition, using a interface-tracking or interface-capturing approach would increase the complexity of the numerics and would probably call for special treatment of the advection equation, the interface representation or the phase-change mechanism in the IB region.

Moreover, special care is taken to address turbulence modelling, within the framework of RANS. Well-known and widely used turbulence models should be adapted to account for the presence of an immersed solid wall, as it has been demonstrated by the literature. This regards applications of engineering interest, where turbulence modelling in an affordable computational cost is of high importance.

The method aims to be employed in studies of turbulent cavitating flows. In this category fall primarily flows of industrial interest including Diesel injection systems and gear pumps, for which RANS simulations is the standard approach. On the other hand, lately the focus is shifted towards bio-engineering applications of cavitation, such as heart valves, tissue damage and drug delivery, where LES or DNS computations are more suitable. In addition, the developed method may address cases of predominantly academic interest, involving complex configurations or delicate laboratory experiments, where conventional techniques fail. Thus, the proposed Immersed Boundary method is designed to deal with this wide range of applications and flow regimes and accommodate complicated physical processes, namely cavitation development, turbulence development and large deformations of the computational domain, by either prescribed or induced by the flow motion of the boundaries.

The tool is developed within the framework of the open source OpenFOAM [68] toolbox.

1.6 Outline

The thesis is structured in five chapters.

First, the numerical method is presented and explained in detail. Then, three chapters with computational works follow. Finally, the last chapter is dedicated to an assessment of the findings and the conclusions of the present research work.

Regarding the computational studies, they are divided in three parts, each composing an individual chapter. The first part, comprising Chapter 3, offers an evaluation of the performance of the developed method, and validates it against well known test cases; various flow regimes are considered with increasing complexity to assess the different features of the method. The second, presented in Chapter 4, illustrates most clearly the benefits of Immersed Boundary approach; an unprecedented numerical investigation delivers detailed information about the flow dynamics of the high-speed impact of a solid onto a water jet, unveiling rich physics, including shock structures, cavitation formation and interface instabilities. This problem has been only studied experimentally before and simulations with conventional tools would be computationally prohibited or even impossible. The last part, in Chapter 5, focuses on biological flows. The flow through a model aorta, featuring a 180° bend and including Valsalva mimicking sinuses and three arterial bifurcations, to closer replicate the geometry of a natural aorta, is studied. The focus is shed on wall shear stresses and the development of a non-physiological flow through a bi-leaflet Mechanical Heart Valve. The herein developed Immersed Boundary method is employed to model the valve, in a incompressible framework accounting for flow induced leaflet motion.

Finally, additional information regarding the implementation of the method, as well as an assessment of its performance in undeformable solid body Fluid Structure Interaction problems can be found in the Appendices.

Chapter 2

Numerical Method

Contents

In the present Thesis, a direct forcing Immersed Boundary *(IB)* method is developed for the Navier-Stokes equations, within the framework of the Finite Volume *(FV)* method. The direct forcing approach is chosen as it provides a simple and straightforward implementation and is applicable, with minimum modifications, in different flow regimes, namely incompressible, compressible and multiphase, as presented in chapter 1.

The IB method is developed to be applied in turbulent cavitating flows with moving geometrical parts. The cavitating flows are characterised by highly compressible phenomena, with large ratio of acoustic impedance between the liquid and the vapour phases and strong shock waves generated by vapour cavities' implosion. Moreover, flows where the immersed body's motion is induced by the flow field, in a Fluid Structure Interaction *(FSI)* concept between fluid and un-deformable solid, are considered. The developed direct forcing Immersed Boundary method is designed to handle these challenging flow conditions.

The method is implemented within the framework of *OpenFOAM*, an open source Finite Volume Computational Fluid Dynamics *(CFD)* toolbox.

The objective of this chapter is to present the developed Immersed Boundary method.

2.1 Governing Equations

In the present work, *turbulent, multiphase, cavitating* flows, of viscous Newtonian fluids, are considered. Such flows are governed by the *Navier-Stokes* (NS) equations. The Navier-Stokes equations, which express the momentum conservation 2.1a, along with the the continuity equation, which express the mass conservation 2.1b, and the energy equation, which expresses the energy conservation 2.1c, define a system of differential equations that describe the motion of the fluid. The Navier-Stokes equations can be seen as a direct application of Newton's second law into fluid mechanics and refer to forces equilibrium. Therefore, strictly speaking, the Navier-Stokes equations are the momentum conservation equations. However often the term is used to refer to the complete system of differential equations 2.1.

$$\frac{\partial \rho \mathbf{u}}{\partial t} + \nabla \cdot (\rho \mathbf{u}\mathbf{u}) = -\nabla p - \nabla \cdot \tilde{\tau} + \mathbf{S} \tag{2.1a}$$

$$\frac{\partial \rho}{\partial t} + \nabla \cdot \rho \mathbf{u} = 0 \tag{2.1b}$$

$$\frac{\partial \rho e_t}{\partial t} + \nabla \cdot (\rho e_t \mathbf{u}) = -\nabla p \mathbf{u} + \nabla(\tilde{\tau}\mathbf{u}) + \nabla \mathbf{q} + \mathbf{S} \cdot \mathbf{u} \tag{2.1c}$$

where

$\mathbf{u}$ is the velocity vector

ρ is the density of the fluid (or mixture of fluids)

p is the static pressure

$\tilde{\tau}$ is the stress tensor

$\mathbf{S}$ regroups the source terms of the momentum eq. representing volumetric forces (e.g. gravity)

e_t is the total energy

$\mathbf{q}$ denotes the heat-fluxes

To close this system of differential equations, an Equation of State *(EoS)* 2.2 is used to link the thermodynamic properties of the fluid, namely the density ρ with the pressure p and the temperature θ.

$$\rho = f(p, \theta) \tag{2.2}$$

For the viscous Newtonian fluids, the stress tensor $\tilde{\tau}$ is linear function of the strain rate tensor $\tilde{s}$ and the dynamic viscosity μ, which in turn depends on the temperature. The strain rate tensor is calculated by 2.3 and the stress tensor is evaluated by relation 2.4.

$$s_{ij} = \frac{1}{2}\left[\frac{\partial u_i}{\partial x_j} + \frac{\partial u_j}{\partial x_i}\right], \ i, j, k = 1, 2, 3 \tag{2.3}$$

$$\tau_{ij} = 2\mu(\theta)\left(s_{ij} - \frac{1}{3}s_{kk}\delta_{ij}\right), \ i, j, k = 1, 2, 3 \tag{2.4}$$

Substituting the expression of the strain rate 2.3 into the relation 2.4 for the stress tensor, the final expression of the viscous stress tensor for the Newtonian fluids is yielded 2.5, which in vector form reads as in 2.6.

$$\tau_{ij} = \mu(\theta)\left(\left(\frac{\partial u_i}{\partial x_j}\frac{\partial u_j}{\partial x_i}\right) - \frac{2}{3}\frac{\partial u_k}{\partial x_k}\delta_{ij}\right), \ i, j, k = 1, 2, 3 \tag{2.5}$$

$$\tilde{\tau} = \mu(\theta)\left(\left(\nabla\mathbf{u} + \nabla\mathbf{u}^T\right) - \frac{2}{3}\nabla\cdot\mathbf{u}\tilde{\mathbf{I}}\right) \tag{2.6}$$

where δ_{ij} is the *Kronecker delta*:

$$\delta_{ij} = \begin{cases} 0, & \text{if } i \neq j \\ 1, & \text{if } i = j \end{cases}$$

and $\tilde{\mathbf{I}}$ the identity matrix:

$$I_{ij} = \delta_{ij} \Leftrightarrow \tilde{\mathbf{I}} = \begin{bmatrix} 1 & 0 & 0 \\ 0 & 1 & 0 \\ 0 & 0 & 1 \end{bmatrix}$$

The governing system of equations can be simplified when the liquid is assumed incompressible or isothermal, which often hold true for the case of liquids, including water and blood. Moreover, for turbulent flows, turbulent fluctuations of the flow quantities should be modelled, therefore alternations to the existing equations or addition of new equations to the system my be required. Finally, when dealing with multiphase flows, additional considerations are needed for the treatment of the different phases and the interactions between them. For cavitating flows, *phase-change* has to be modelled, when the fluid can pass from liquid to gas phases and back again, as an abrupt and rapid process.

The aforementioned considerations towards the derivation of the final form of the governing equations are presented on the following subsections.

2.1.1 Incompressible NS

For an incompressible flow, the density is regarded constant and not depending on temperature or pressure changes. The temporal derivative of the density field equals to zero, and the continuity equations is simplified into a relationship for the divergence of velocity field. In addition, if the flow is regarded iso-thermal, there is no thermal energy transfer or temperature variations. Therefore the EoS and energy equation can be disregarded and the flow is determined simply by solving only the continuity 2.1b and momentum 2.1a equations.

The incompressible NS correspond to the system of differential equations of 2.7.

$$\nabla\mathbf{u} = 0 \tag{2.7a}$$

$$\rho\frac{\partial\mathbf{u}}{\partial t} + \rho\nabla\mathbf{u}\mathbf{u} = -\nabla p - \nabla\cdot\tilde{\tau} + \mathbf{S} \tag{2.7b}$$

35

Taking into account the continuity equation that imposes a divergent free velocity field, the viscous stress tensor $\tilde{\tau}$ results in the form of 2.8.

$$\tilde{\tau} = \mu \left(\nabla \mathbf{u} + \nabla \mathbf{u}^T \right) \tag{2.8}$$

In the case of biological flows the working fluid is usually considered incompressible and isothermal. More precisely, in *hemodynamics*, the study of blood flows, the working fluid (blood) is treated as incompressible Newtonian fluid, which is acceptable when the flow in large blood vessels is considered [226]. The temperature changes are also negligible and the temperature effects on density can be assumed insignificant, which is often the case.

2.1.2 Reynolds-Averaged Navier-Stokes

In the present work, moderate or high Reynolds turbulent flows are considered. The use of Direct Numerical Simulations *(DNS)* to resolve all the turbulent scales, is feasible for moderate Reynolds numbers and is a common approach for biological flows. However it is not applicable to cavitating flows of industrial applications at engineering scales. For simulating turbulent flows, the *Reynolds-Averaged Navier-Stokes* (RANS) approach is employed.

According to this approach, the governing Navier-Stokes equations are time-averaged, so as the flow at any given time-instant can be described by turbulent fluctuations over an average flow field. In other words, the flow quantities (velocity, pressure, energy) can be decomposed in to an average value (bar) and a fluctuation (prime):

$$\phi(\mathbf{x}, t) = \bar{\phi}(\mathbf{x}, t) + \phi'(\mathbf{x}, t)$$

The time-averaged value, over a temporal window T, is computed as:

$$\bar{\phi}(\mathbf{x}, t) = \frac{1}{T} \int\limits_{t}^{t+T} \phi(\mathbf{x}, t) \mathrm{d}t$$

Without loss of generality, referring to the case of incompressible flow for the sake of simplicity, the Reynolds-Averaged Navier-Stokes equations are derived from 2.7, by first decomposing the flow variables into mean and fluctuating parts, and then time-averaging the equations. This process, following some algebraic operations, yields the unsteady RANS equations of 2.9. For a step-by-step formulation, the reader is referred to Appendix **??**.

$$\nabla \cdot \bar{\mathbf{u}} = 0 \tag{2.9a}$$

$$\rho \frac{\partial \bar{\mathbf{u}}}{\partial t} + \rho \nabla \cdot (\bar{\mathbf{u}} \bar{\mathbf{u}}) = -\nabla \bar{p} - \nabla \cdot \left(\bar{\tilde{\tau}} + \tilde{\tau}_R \right) + \mathbf{S} \tag{2.9b}$$

where $\tilde{\tau}_R = -\rho \overline{\mathbf{u}' \mathbf{u}'}$ is the *Reynolds stresses* tensor, which is composed by the averaged product of the fluctuating components of the velocity field. The values of this tensor introduce six additional unknowns to the system of the equations and therefore cannot be determined by it. The closure of the system is provided by modelling this tensor and estimating its components using *turbulent models*. The turbulent models will be discussed in a following separate section.

2.1.3 Cavitation Modelling

In order to model cavitating flows, a *Homogeneous Equilibrium Mixture* approach is followed. The flow is considered as a mixture of two phases, the liquid and the vapour, which is treated as a single fluid. The two phases are considered to be in mechanical and thermodynamic equilibrium and are treated as a homogeneous mixture with single pressure and velocity fields. The mixture composition, and therefore its properties, are function of the vapour volume fraction α_v. The density and viscosity of the mixture are estimated from the weighted average of the equivalent liquid *(l)* and vapour *(v)* properties, as in 2.10a and 2.10b.

$$\rho = (1 - \alpha_v)\rho_{l,sat} + \alpha_v\rho_{v,sat} \tag{2.10a}$$
$$\mu = (1 - \alpha_v)\mu_l + \alpha_v\mu_v \tag{2.10b}$$

The flow is considered iso-thermal and governed by the barotropic law. Therefore the energy equation 2.1c is disregarded and not solved. The density is linked to the pressure through the barotropic Equation of State 2.11, using the compressibility of the mixture ψ.

From the different models available for the calculation of the ψ, the Wallis model is chosen, which is expressed by the formula 2.12. The compressibility of each phase is calculated as the inverse of the speed of sound squared $1/c^2$.

$$\rho = \psi p + (1 - \alpha_v)\rho_{L,0} - ((\alpha_v\psi_v + (1 - \alpha_v)\psi_l) - \psi)\, p_{sat} \tag{2.11}$$

$$\psi = (\alpha_v\rho_{v,sat} + (1 - \alpha_v)\rho_{l,sat}) \cdot \left(\frac{\alpha_v\psi_v}{\rho_{v,sat}} + \frac{(1 - \alpha_v)\psi_l}{\rho_{l,sat}}\right) \tag{2.12}$$

The vapour volume fraction, at any given time instant is calculated by relation 2.13 and an additional volume fraction transport equation is **not** required, as in many multiphase algorithms employing a Volume of Fluid *(VOF)* approach.

$$\alpha_v = \frac{\rho - \rho_{v,sat}}{\rho_{l,sat} - \rho_{v,sat}} \tag{2.13}$$

2.1.4 Velocity-Pressure Coupling Algorithm

Within the framework of `OpenFOAM` [68], pressure-based solvers, both incompressible and compressible, widely use an iterative pressure-correction algorithm called `PIMPLE` [93].

The `PIMPLE` algorithm is a combination of the Pressure Implicit with Splitting of Operators *(PISO)* [101] and the Semi-Implicit Method for Pressure Linked Equations *(SIMPLE)* [176] algorithms. It can be seen as an iterative PISO algorithm, which searches for a steady-state solution in each time step using under-relaxation, and therefore allows the use of larger time-steps than PISO. PIMPLE also achieves better and faster convergence compared to PISO, which is an important advantage for highly transient flows and will be exploited in cases involving moving geometries.

For incompressible flows the PIMPLE algorithm is implemented by `pimpleFoam` solver. The momentum equation 2.7b is first solved and then the PISO loop is called of a predefined number of iterations, where the pressure correction equation 2.14 is solved. Intermediate pressure and

velocity values are relaxed and the procedure is repeated until convergence criteria are satisfied or the maximum *outer* iterations are reached. If the maximum *outer* iterations are set to 1, the algorithm is operating in PISO mode.

$$\Delta p = \Delta \mathbf{u}\mathbf{u} \tag{2.14}$$

For cavitating cases, the `cavitatingFoam` solver is used, which is a compressible pressure-based solver, employing the *(HEM)* approach and following a PIMPLE based iterative pressure correction algorithm.

Introducing the barotropic EOS 2.11 into the continuity equation 2.1b, the pressure-correction equation 2.15 is extracted. The algorithm, in every (outer) iteration, solves the momentum equation 2.1b, then performs pressure-correction via 2.15 in the PISO loop and then updates ρ, α_v and ψ by 2.11, 2.13 and 2.12 respectively, until convergence is reached.

$$\frac{\partial \psi p}{\partial t} - (\rho_{l,0} + (\psi_l - \psi_v)p_{sat}) \frac{\partial \alpha_v}{\partial t} - \frac{\partial \psi}{\partial t}p_{sat} + \nabla \cdot \rho \mathbf{u} = 0 \tag{2.15}$$

The `cavitatingFoam` sovler has been used by Akira Sou et al. [14] for the case of a cavitating flow over a step nozzle and the results were compared to experimental measurements. The good agreement between the numerical and experimental data serves as a good validation case for the solver.

For the advancement in time, when using implicit pressure-correction algorithms 1$^{\text{rst}}$ order accurate Euler or 2$^{\text{nd}}$ order Crank-Nicolson time schemes have been employed; the latter is more appropriate for highly transient turbulent or cavitating cases. The time-step in the simulations is controlled by the Courant-Friedrichs-Lewy (CFL) condition, expressed by 2.16, which adjusts the time-step according to the maximum velocity in the computational domain. The PISO algorithm ensures accurate results with $Co_{max} \leq 1$, while with the PIMPLE algorithm even higher values can be reached without deteriorating the quality of the results or negative consequences on convergence.

$$Co_= max \left(\Delta t \cdot \Sigma_{faces} |\phi_i|/2V \right) \leq Co_{max} \tag{2.16}$$

For cavitating flows, an additional constraint is added, due to the variation of the Mach number between the liquid and vapour phases, which is expressed by the *acoustic* Courant number, defined by relation 2.17 using the compressibility. The maximum value may be in the order of 2 or 5, while even a value of 10 can be used in some cases. This constraint further decreases the time-step.

$$Co^{ac} = max \left(\Delta t / \left(2V\sqrt{\psi} \right) \right) \leq Co_{max}^{ac} \tag{2.17}$$

2.2 Turbulence Modelling

Within the framework of RANS simulations, the treatment of turbulent flows reduces to the computation of the Reynolds stresses tensor $\tilde{\tau}_R$ in the NS. This tensor is holds six additional unknowns that cannot be solved for by the NS equations and therefore is modelled.

Herein, the Reynolds stresses are modelled using the Boussinesq assumption 2.18, which relates the velocity fluctuations' stresses $\overline{\mathbf{u}'\mathbf{u}'}$ with the velocity gradients $\nabla\mathbf{u}$, the turbulent eddy

viscosity μ_{turb} and the turbulent kinetic energy k. The turbulent viscosity μ_{turb} is estimated by the turbulent model and the turbulent kinetic energy is evaluated as $k = \overline{\mathbf{u'u'}}/2$. The relation of the Boussinesq assumption for incompressible flows reduces to 2.19.

$$\tilde{\tau}_R = -\rho \cdot \overline{\mathbf{u'u'}} = \mu_{turb} \cdot \left(\nabla\overline{\mathbf{u}} + \nabla\overline{\mathbf{u}}^T\right) - \frac{2}{3}\left(\rho k + \mu_{turb}\nabla\cdot\mathbf{u}\right)\tilde{\mathbf{I}} \tag{2.18}$$

$$\tau_R = -\rho \cdot \overline{\mathbf{u'u'}} = \mu_{turb} \cdot \left(\nabla\overline{\mathbf{u}} + \nabla\overline{\mathbf{u}}^T\right) - \frac{2}{3}\rho k\mathbf{I} \tag{2.19}$$

The turbulent eddy viscosity is calculated based on an estimation of a turbulent velocity scale $\mathcal{U}$ and a turbulent length scale $\mathcal{L}$, as $\mu_{turb} \propto \mathcal{U} \cdot \mathcal{L}$. These scales are estimated by the turbulence models.

In the present work, the low-Re $k - \omega$ SST [141] has been mainly employed, but the use of *Spallar-Allmaras* [211] has been also assessed. Both have been modified for multiphase flows, incorporating the Reboud correction [67, 185], to account for variation in density and viscosity. This approach is a common practise in simulations of cavitating flows using the two-equations $k - \varepsilon$ and $k - \omega$ family of models [43, 53, 67]. On the contrary, the single-equation *Spallar-Allmaras* model, which is very popular for external aerodynamic flows, is not widely used in multiphase and cavitating flows. In addition, the applicability of the four-equation $k - \omega$ $SSTLM$ model, for capturing turbulent transition phenomena, proposed by Menter et al. [140], within the framework of the IB method has also been assessed.

The low-Re $k - \omega$ SST, which is widely used in numerous application of engineering scale, solves two additional transport equations for the turbulent kinetic energy k, eq. 2.20a, and the specific dissipation rate ω, eq. 2.20b, and uses them to provide an estimation of the turbulent viscosity ν_{turb} by 2.20c.

$$\frac{\partial\rho k}{\partial t} + \nabla\cdot(\rho\mathbf{u}k) = \nabla\cdot((\mu + \sigma_k\mu_{turb})\nabla k) + \overbrace{P_k - \beta^*\rho k\omega}^{S^k} \tag{2.20a}$$

$$\frac{\partial\rho\omega}{\partial t} + \nabla\cdot(\rho\mathbf{u}\omega) = \nabla\cdot((\mu + \sigma_k\mu_{turb})\nabla\omega) + \underbrace{\frac{\gamma\omega}{k}P_k - \beta^*\rho\omega^2 + 2(1 - F_1)\sigma_{\omega,2}\frac{\rho}{\omega}\nabla k\nabla\omega}_{S_\omega} \tag{2.20b}$$

$$\nu_{turb} = \frac{\alpha_1 k}{max\left(\alpha_1\omega, \sqrt{2}S_t F_2\right)} \tag{2.20c}$$

The $k - \omega$ $SSTLM$ model, solves two additional to the aforementioned k and ω transport equations, in order to capture regions where the flow transitions to turbulent regime. The *intermittency* γ, which triggers the turbulent kinetic energy production, and the *momentum thickness Reynolds* number $Re_{\theta t}$, which controls the onset transition, are introduced. They are estimated by 2.21a and 2.21b respectively.

$$\frac{\partial\rho\gamma}{\partial t} + \nabla\cdot(\rho\mathbf{u}\gamma) = \nabla\cdot\left((\mu + \frac{\mu_{turb}}{\sigma_\gamma})\nabla\gamma\right)\overbrace{+ P_\gamma - E_\gamma}^{S_\gamma} \tag{2.21a}$$

$$\frac{\partial\rho\hat{R}e_{\theta t}}{\partial t} + \nabla\cdot\left(\rho\mathbf{u}\hat{R}e_{\theta t}\right) = \nabla\cdot\left(\sigma_{\theta t}(\mu + \mu_{turb})\nabla\hat{R}e_{\theta t}\right) + \underbrace{P_{\theta t}}_{S_{\theta t}} \tag{2.21b}$$

The terms highlighted as S_* are treated as source terms. The models introduce a lot of parameters and empirical constants, to make it suitable for treatment of near wall regions *(low-Re)*. For expressions and the values of these parameters, which escape the scope of the current work, the reader is referred to the original journal articles of Menter [141] and Menter et al. [140], as well as the on-line Turbulent Modelling resource of NASA [155].

Finally, the one-equation *Spalart-Allmaras* model, solves the single transport equation 2.22a for the pseudo-viscosity $\tilde{\nu}$ and estimates the turbulent dynamic viscosity ν_{turb} from 2.22b.

$$\frac{\partial \tilde{\nu}}{\partial t} + \mathbf{u}\nabla\tilde{\nu} = \frac{1}{\sigma}\left[\nabla\cdot((\nu+\tilde{\nu})\nabla\tilde{\nu}) + c_{b2}\left(\nabla\tilde{\nu}\right)^2\right] \overbrace{+ c_{b1}(1-f_{t2})\tilde{S}\tilde{\nu} - \left[c_{w1}f_w - \frac{c_{b1}}{\kappa^2}f_{t2}\right]\left(\frac{\tilde{\nu}}{d}\right)^2}^{S_{\tilde{\nu}}}$$

(2.22a)

$$\nu_{turb} = f_{\nu 1}\tilde{\nu} = \frac{\chi^3}{\chi^3 + c_{\nu 1}^3}\tilde{\nu}, \text{ where: } \chi = \frac{\tilde{\nu}}{\nu}$$

(2.22b)

Similarly, the values and the expressions of the parameters can be found in the journal paper of and Spalart and Allmaras [211], the on-line Turbulent Modelling resource of NASA [155], as well as in the theoretical CFD manuals [152].

According to the Reboud correction, turbulent models provide an estimate for the turbulent dynamic viscosity ν_{turb} and then the turbulent eddy viscosity is computed as $\mu_{turb} = f(\rho)\cdot\nu_{turb}$, where the density function $f(\rho)$ is given by 2.23 and takes into account the spatial variation of the mixture's density.

$$f(\rho) = \rho_v + \left(\frac{\rho_v - \rho}{\rho_v - \rho_l}\right)^n \cdot (\rho_l - \rho_v), \ n = 10$$

(2.23)

In the implemented algorithms the turbulent transport equations are solved at the end of the time-step, after the pressure-correction iterations.

2.3 Immersed Boundary Forcing Term

The immersed solid boundary is represented by a surface mesh and a *continuous* color function, dubbed as the *IB mask*, is used to indicate the region of the computational domain enclosed by this surface. The color function (*IB mask*) receives values between 0 for *fluid cells* and 1 for *solid cells*. The modelling of the immersed solid boundary on the computational domain is achieved by the addition of a *forcing* term, a volumetric source term, in the momentum equations.

The forcing source term, seen in 2.24, is computed as the difference of the fluid velocity $\mathbf{u}_{fluid}$ from the IB solid velocity $\mathbf{u}_{Ib}$, divided by the time-step. It is designed to drive the solution of the momentum equation to the desired velocity value in the IB region, imposing a no-slip condition. To localise the application of the source term on the computational cells in the IB region, the forcing term is multiplied by the *IB mask* $\alpha_{IB,}$.

$$\mathbf{f}_{IB} = \alpha_{IB} \cdot \frac{\mathbf{u}_{Ib} - \mathbf{u}_{fluid}}{\Delta t} \ , \quad \alpha_{IB} \in [0,1]$$

(2.24)

In various direct forcing IB method reported in the literature, the forcing is applied only on the interface cells. Moreover, the forcing is first computed on the Lagrangian points defining the IB interface, and then is interpolated in the nearby cells. In contrast, in the herein proposed methodology, as the IB mask receives values in the (continuous) range $[0, 1]$, the forcing is applied on the interface as well as the internal to the solid area computational cells. In addition, the forcing is directly computed on the computational cells, where the solid velocity $\mathbf{u}_{Ib}$ is defined, and therefore the cumbersome interpolation procedure is avoided. The definition of the solid velocity $\mathbf{u}_{Ib}$ is discussed on the next section.

If this forcing term is formulated explicitly, using the velocity value of the previous time-step or iteration, can receive large values, which can lead to very stiff equations. This holds true especially for the cavitating flows, when the time-step tends to reach values of $10^{-8}s$, limited by high velocities or large deviation of the Mach number between the liquid and vapour phases. In order to tackle this difficulty, the IB source term can be treated implicitly by being linearised [16, 152], following Taylor expansion, as:

$$f_{Ib,k}(u_k)^t = f_{Ib,k}(u_k)^{t-1} + \frac{\partial f_{Ib,k}}{\partial u_k} \cdot (u_k^t - u_k^{t-1}), \ \ k = x, y, z$$

with regards to the time step t. Alternative approaches could employ *fractional step splitting* algorithms [126, 223], where the splits the homogeneous and inhomogeneous parts of the differential equations, or upwinding techniques [187].

As the IB methodology is combined with a pressure-correction algorithm, the forcing term should be updated in every pressure-correction iteration. Therefore for every intermediate step n within each time step t, the forcing term is calculated by 2.25.

$$f_{Ib,k}(u_k)^n = f_{Ib,k}(u_k)^{t-1} + \frac{\partial f_{Ib,k}}{\partial u_k} \cdot \left(u_k^n - u_k^{t-1}\right), \ \ k = x, y, z \tag{2.25}$$

2.3.1 IB Motion and Velocity

The solid velocity $\mathbf{u}_{Ib}$, which constitutes the desired boundary condition and is used in 2.24 for the computation of the forcing term, is defined directly for the computational cells. The computational cells in the IB region are considered as part of the solid body and their *solid velocity* is evaluated with respect to the velocity of the *center of gravity G_{Ib}* of the immersed boundary.

The immersed boundary is regarded as undeformable rigid body. Therefore, all the points of the solid have the same translational velocity, the velocity of the center of gravity G_{Ib} of the IB. On the other hand the angular velocity of each point of the solid depends on its position relative to the G_{Ib}. A geometric representation is given in figure 2.1. As a result, for each grid cell C_j in the solid region, the (imposed) solid velocity is given with respect to the position vector $\mathbf{r}_j = \overrightarrow{G_{Ib}C_j}$ by 2.26.

$$\mathbf{u}_{Ib,j} = \mathbf{u}_G + \mathbf{r}_j \times \omega_G \tag{2.26}$$

The motion of the immersed boundary can be pre-described but also be induced by the flow, making our method capable of with Fluid-Structure Interaction *(FSI)* simulations.
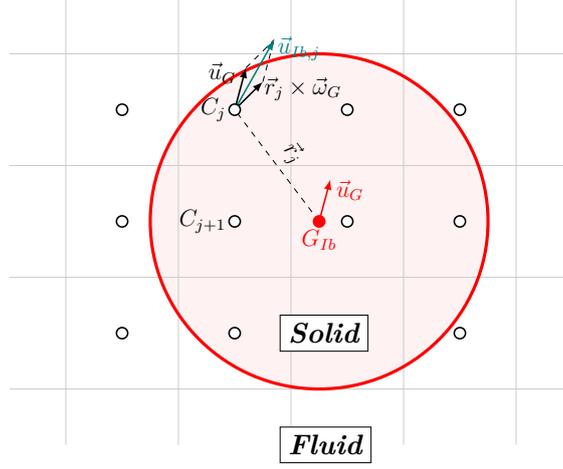
Figure 2.1: Solid body velocity estimation for cells in the Immersed Boundary region.

For FSI computations, an ODE solver is used to solve the *M-C-K* dynamic system 2.27, which defines the motion of a rigid body with six degrees of freedom *(6 d.o.f.)*, three translations $\mathbf{x} = (x, y, z)$ and three rotations $\theta = (\theta_x, \theta_y, \theta_z)$.

$$m \cdot \frac{\partial^2 \mathbf{x}}{\partial t^2} + c \cdot \frac{\partial \mathbf{x}}{\partial t} + k \cdot \mathbf{x} = \mathbf{F}_{ext} \tag{2.27a}$$

$$\tilde{\mathbf{I}}_R \cdot \frac{\partial^2 \theta}{\partial t^2} = \mathbf{M}_{ext} \tag{2.27b}$$

with

m the mass of the body

$\zeta = c/m$ the structural damping ratio

k the spring coefficient

$\tilde{\mathbf{I}}_R$ the moment of inertia matrix with respect to the center of rotation R

$\mathbf{F}_{ext}$ and $\mathbf{M}_{ext}$ the vectors of the external forces and moments

The solid motion solver, receives as an input from the fluid solver the forces acting on the immersed body, and returns the displacement of the center of gravity of the immersed boundary. However a *loose coupling* approach is followed, because the ODE is not solved simultaneously with the Navier-Stokes equations, but at the beginning of each time step, using the forces of the previous time step.

2.3.2 IB Mask Estimation

The immersed boundary is represented by a surface (*IB surface*), which is superimposed onto the computational grid and devides it into *fluid* and *solid* regions, as illustrated in figure 2.2a.

The color function (*IB mask*) representing the *solid region*, corresponds to the *solid volume fraction* of the cells. The mask can be seen as the ratio of the cell volume covered by the IB surface over the total cell volume and thus receives values between 0 for *fluid cells* and 1 for *solid cells*. The same procedure is used by Koukouvinis et al. [111] and Mithun, Koukouvinis et al. [144].
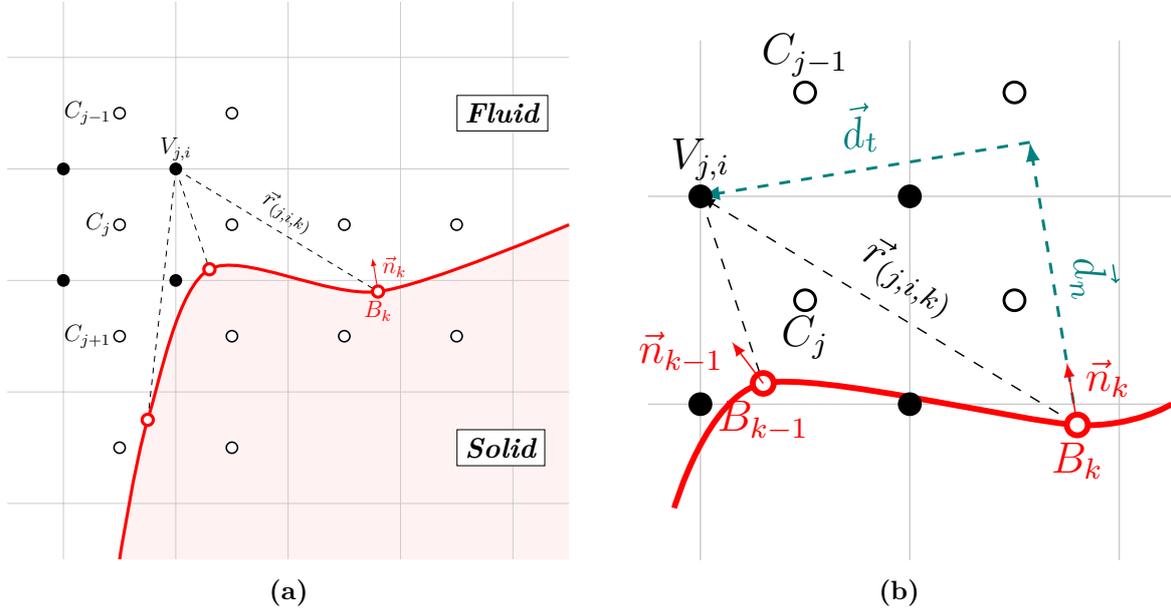
Figure 2.2: Representation of immersed boundary onto computational grid (left) and calculation of vertex distance from IB surface's nodes (right). The IB surface is represented by the solid red curve.

To estimate the cell volume enclosed in the *solid* region, for each vertex of the cell, the distance from the IB surface is calculated. The distance d_{ij} of each vertex is computed as a signed scalar, indicating whether the vertex lies inside ($d_{ij} < 0$) or outside ($d_{ij} > 0$) the area enclosed by the IB surface. As a result, the the vertices laying in the *fluid* region can easily be filtered out by keeping only the negative values ($min(d_{ij}, 0)$). The sum of the distance d_{ij} of the vertices in the *solid* region is used as a measure of the enclosed cell volume. Therefore, for each of the N_c cells of the domain with N_v vertices, the mask α_j is calculated as the ratio of the sum of the distance of the enclosed vertices over the the sum of the norms of the distances of all vertices. The mask is given by the relation 2.28.

$$\alpha_j = \frac{\displaystyle\sum_{i=1}^{N_v} \mid min(d_{ij}, 0) \mid}{\displaystyle\sum_{i=1}^{N_v} \mid d_{ij} \mid}, \quad j \in [1, N_c] \tag{2.28}$$

For each vertex, the distance from the IB surface is estimated as the minimum of the distance of the vertex from each of the points of the IB surface. More precisely, the distance is calculated as the orthogonal projection of the distance vector $\mathbf{r}_{ij,k}$ between the vertex V_i, of cell C_j, and the IB point B_k, on the normal $\mathbf{n}_{Ib,k}$ of the IB surface defined on the IB point. The procedure is expressed by relation 2.29 and illustrated in figure 2.2b, where the distance

vector $\mathbf{r}_{ij,k}$ is decomposed into a parallel and an orthogonal to the IB normal $\mathbf{n}_{Ib,k}$ component: $\mathbf{d}_t \perp \mathbf{n}, \mathbf{d}_n \parallel \mathbf{n}, \Rightarrow \mathbf{d}_t \perp \mathbf{d}_n$.

$$d_{ij} = min(d_n) = min\left(\mathbf{r}_{ij,k} \cdot \mathbf{n}_{Ib,k}\right), \quad \mathbf{r}_{ij,k} = \overrightarrow{B_k V_{ij}}, \quad i \in [1, N_c], \ j \in [1, N_v], \ k \in [1, N_{Ib}]$$
(2.29)

An indicative example is given in figure 2.3, where the triangulated surface mesh representing an immersed solid cylinder and the equivalent IB mask, calculated following the procedure presented above, are shown.

(a) IB surface (STL) **(b)** IbMask
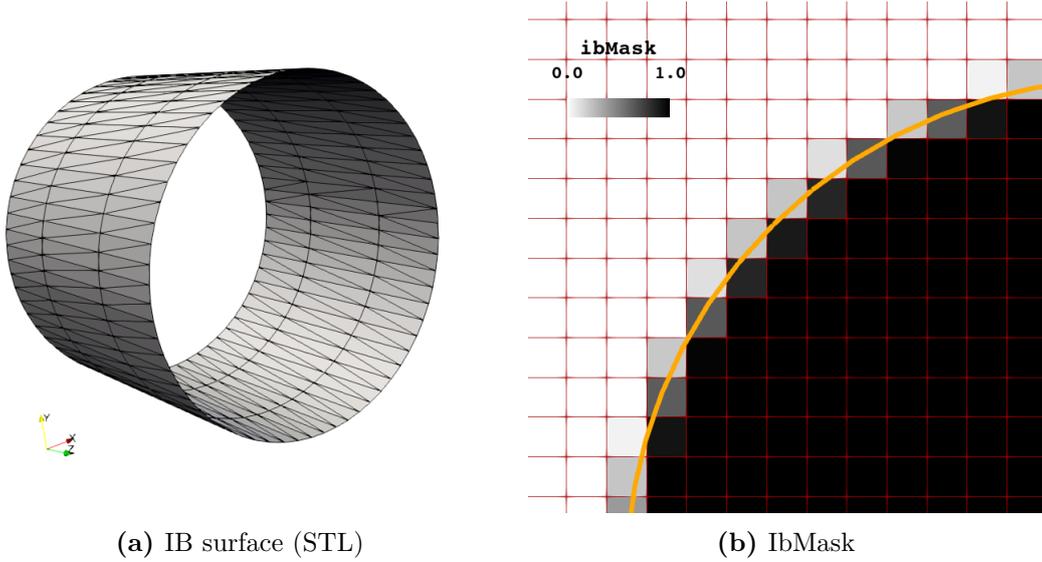
Figure 2.3: IB representation. The IB surface is read from an STL file (left), as a triangulated surface, and is translated into a solid volume fraction field on the computational grid (right).

2.3.3 Wall Treatment for Turbulence Modelling

Regular turbulence models can be used in conjunction with the proposed Immersed Boundary Method, with slight modifications.

Firstly, the wall distance y is altered to take into account the presence of the immersed solid. The distance $y_{wall,Ib}$ of every cell center from the IB surface is calculated and then the wall distance is estimated as the minimum between the $y_{wall,Ib}$ and the conventional y_{wall}, in a similar way presented by Mochel et al. [149]. This procedure is expressed by 2.30 and illustrated in figure 2.4.

$$y'_{wall} = min(y_{wall}, y_{wall,Ib})$$
(2.30)

Secondly, an additional term is added to the source terms S_* of the transport equations of the turbulent variables presented in section 2.2. This term is formulated with the same reasoning and in an similar way as 2.24, in order to drive the solving variable to a constant value inside the solid area, respecting the boundary conditions of the model in use.

In the case of $k - \omega \ SST$, the boundary conditions for the turbulent kinetic energy and the specific dissipation are set according to Wilcox [237] to $k_{wall} = 0 \ m^2 s^{-2}$ and $\omega_{wall} \to \infty$,

(a) Conformal wall distance   **(b)** IB wall distance   **(c)** Adapted wall distance
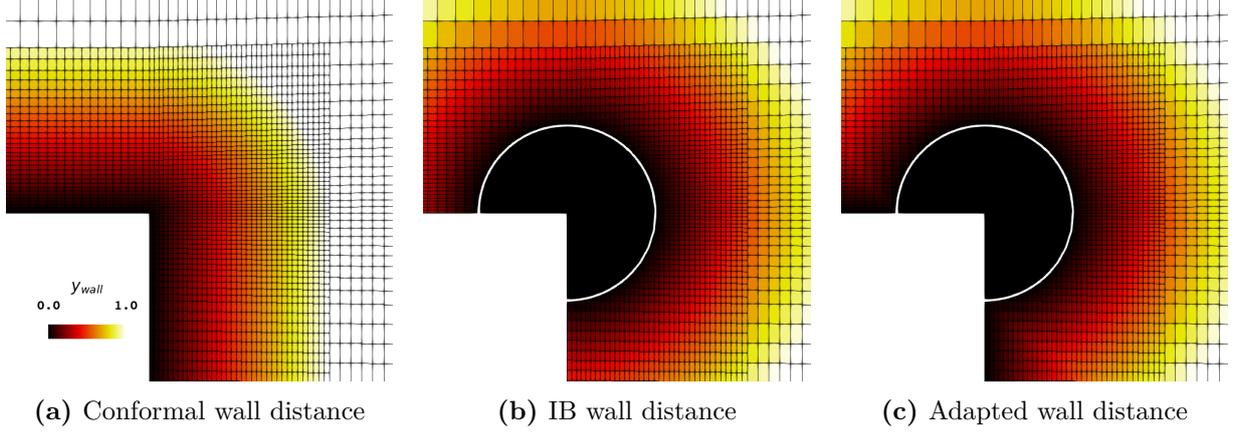
Figure 2.4: Adaptation of wall distance from the lower boundary of the computational domain, to account for the cylinder near the wall, represented as an immersed boundary.

practically $\omega_{wall} = 10^{15}\ s^{-1}$. In the case of Spalart-Allmaras model, the turbulent viscotisy in the area of the body sould tend to zero, so the boundary condition of the *pseudo-viscosity* $\tilde{\nu}_{wall} = 0$. The source terms are given by 2.31 and 2.32 respectively.

$$S'_k = S_k + \frac{k_{wall} - k}{\Delta t}, \qquad S'_\omega = S_\omega + \frac{\omega_{wall} - \omega}{\Delta t} \tag{2.31}$$

$$S'_{\tilde{\nu}} = S_{\tilde{\nu}} + \frac{\tilde{\nu}_{wall} - \tilde{\nu}}{\Delta t} \tag{2.32}$$

Therefore, taking the one-equation Spalart-Allmaras model as an indicative example, the transport equation of pseudo-viscosity 2.22a, after the introduction of the altered source term, will read as in 2.33.

$$\frac{\partial \tilde{\nu}}{\partial t} + \mathbf{u}\nabla\tilde{\nu} = \frac{1}{\sigma}\left[\nabla \cdot ((\nu + \tilde{\nu})\nabla\tilde{\nu}) + c_{b2}(\nabla\tilde{\nu})^2\right] + \overbrace{c_{b1}(1 - f_{t2})\tilde{S}\tilde{\nu} - \left[c_{w1}f_w - \frac{c_{b1}}{\kappa^2}f_{t2}\right]\left(\frac{\tilde{\nu}}{d}\right)^2 + \frac{\tilde{\nu}_{wall} - \tilde{\nu}}{\Delta t}}^{S'_{\tilde{\nu}}} \tag{2.33}$$

Chapter 3

Preliminary Computational Studies: Validation of the Method

Contents

This chapter is dedicated to the validation of the developed Immersed Boundary method against well documented benchmark cases. The validation is performed against numerical and experimental results extracted from the literature. The assessment of the method starts from simple incompressible flows in low Reynolds and then builds up in complexity to finally treat turbulent cavitating flows at high Reynolds. Initially, the method is employed on incompressible laminar flows around stationary or moving cylinders, which are standard tests to demonstrate the capabilities of similar methods. Then the turbulence modelling is tested on a well-known example of turbulent flow over a back-facing step in a channel at moderate Reynolds number. Finally the method is applied on the study of cavitating cases of rotating model propellers and stationary or pitching hydrofoils. This long and diverse validation process aims to demonstrate that the proposed method is capable of treating complex turbulent cavitating flows with moving boundaries and can be used on applications of industrial interest.

3.1 Incompressible Flows

3.1.1 Incompressible Flow over Cylinders

As an initial step for the validation of the herein proposed Immersed Boundary method, the incompressible flows over stationary and moving cylinders, at a low Reynolds number of $Re = U_{max} \cdot D/\nu = 100$, are considered.

These well documented flows are characterised by the Karman vortex street that develops on the wake of the cylinder, which depends on the Reynolds number of the flow and exhibits a specific Strouhal number $St = f \cdot D/U$ based on the vortex shedding frequency f.

Flow over Stationary Cylinder

The incompressible laminar flow, at $Re = 100$, past a circular cylinder, modelled by the herein proposed IB method, is simulated. The working liquid was chosen to be air, with density $\rho = 1.22 kg/m^3$ and kinematic viscosity $\nu = 1.57 \cdot 10^{-5} m^2/s$.

The case set-up, consists of a computational domain with dimensions $Lx = 55D \times Ly = 35D$, which is discretised using a canonical orthogonal grid. Telescopic refinement is used in order to control the resolution of the uniform grid in an area of $-1.5D \leq x \leq 1.5D$ and $-1.5D \leq y \leq 1.5D$ around the cylinder. The three meshes achieve resolution of $\delta x = \delta y = 5\%D$ (coarse), $\delta x = \delta y = 2.5\%D$ (medium) and $\delta x = \delta y = 1.25\%D$ (fine), with respect to the diameter of the cylinder D. The representation of the interface of the immersed boundary on the background mesh is illustrated in figure 3.1, which shows the computed IB mask *(solid volume fraction)* for the three different grids.

The inlet is placed on the left boundary of the domain, and fixed pressure outlet on the right boundary of the domain. Zero gradient boundary conditions are applied for the velocity on top and bottom boundaries. All simulations lasted for dimensionless time $t = t \cdot U/D = 360$ and the time-step was adjusted so that the Courant-Friedrichs-Lewy *(CFL)* condition of $Co_{max} = u\Delta t/\Delta x \leq 0.5$ was respected.

A visualisation of the flow is shown in figure 3.2, where the velocity and off-plane vorticity contours are plotted. The vortex street is visible and the expected pattern of the two successively shed counter-rotating vortices is well captured. Drag $C_D = 2f_x/(\rho D_{cyl}U^2)$ and lift $C_L = 2f_y/(\rho D_{cyl}U^2)$ coefficients are also well estimated, with regards to values reported in the literature, as seen in table 3.1.

	C_D	C_L	St
Sun [216]	1.367 ± 0.01	± 0.348	1.64
Lima [205]	1.39	-	0.16
De Palma [171]	1.32	± 0.331	0.163
Present IB 5%D	1.45	± 0.2	0.1389
Present IB 2.5%D	1.39	± 0.275	0.1469
Present IB 1.25%D	1.35	± 0.3	0.1523
Present Conf.	1.3	± 0.25	0.1417

Table 3.1: Force coefficients and Strouhal number for flow past stationary cylinder at Re=100.

(a) Coarse   **(b)** Medium   **(c)** Fine
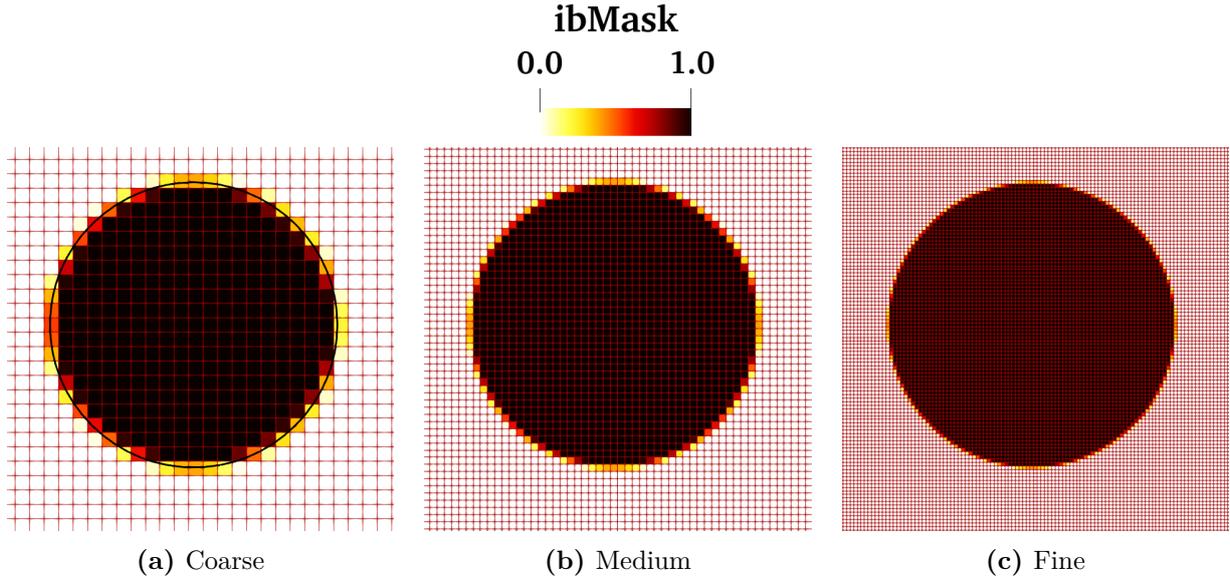
Figure 3.1: *IbMask* field for the representation of a immersed cylinder on three different canonical grids. The cell edge for the coarse grid *(a)* is $5\%D_{cyl}$, for the medium grid *(b)* is $2.5\%D_{cyl}$ and for the fine grid *(c)* is $1.25\%D_{cyl}$.

(a)   **(b)**
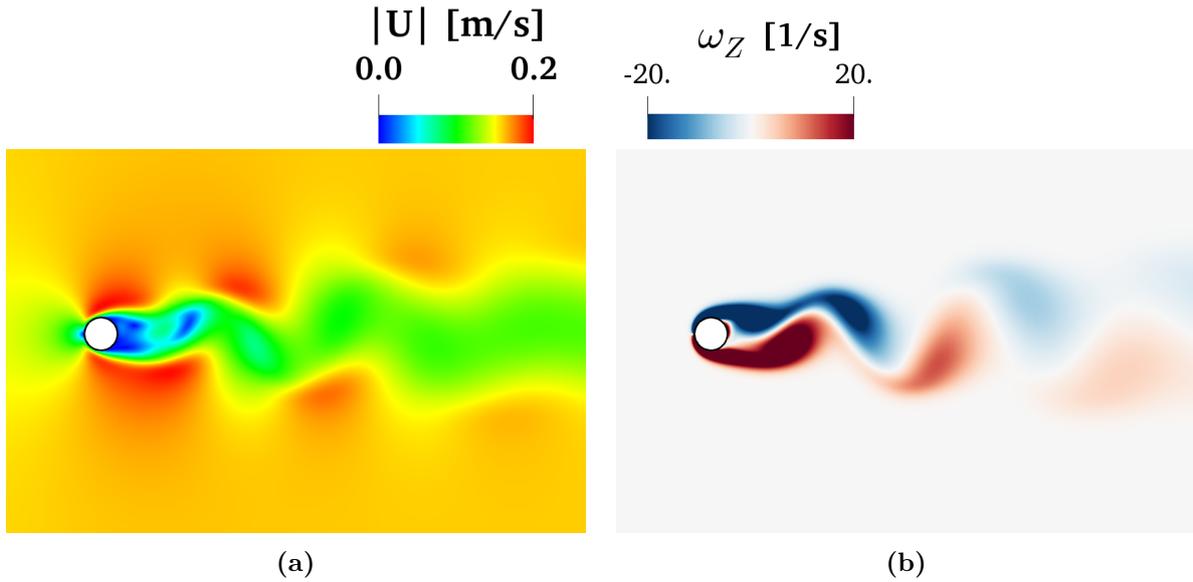
Figure 3.2: Velocity magnitude *(a)* and off-plane vorticity component *(b)* incompressible for flow past stationary cylinder at Re=100.

Oscillating Cylinder in Fluid at Rest

The oscillation of a cylinder in a fluid at rest is simulated using the Immersed Boundary method presented, in order to assess the method's capability to handle moving boundaries. Apart from the Reynolds number, this case is characterised also by the Keulegan–Carpenter number $KC = U_{max}/(f \cdot D)$, where U_{max} refers to the maximum velocity and f the frequency of the oscillation of the cylinder. The motion of the cylinder is described by a harmonic function $x(t) = -A sin(2\pi f t)$, with $A = KC/2\pi$ the amplitude of the oscillation.

The computations are carried out using air as the surrounding fluid and choosing $Re = 100$, and $KC = 5$, resulting in a Strouhal number $St = 0.2$, to match the experimental data available from Dütsch [56], which serve as reference for many researchers. The computation run for 8 oscillating periods and three different meshes are used to determine the mesh influence on the results. In addition, the IB method results are compared to simulations applying an Over-Set mesh technique, where the cylinder Over-Set mesh conforms to the solid cylinder boundary.

A $55D_{cyl} \times 35D_{cyl}$ domain is discretised using canonical orthogonal grid; telescopic refinement is used in order to achieve the desired resolution in a square region $[-3D_{cyl}, 3D_{cyl}]$, centered on the equilibrium point of the cylinder's oscillation. The three meshes yield a cell edge of $5\%D_{cyl}$ (coarse), $2.5\%D_{cyl}$ (medium) and $1.25\%D_{cyl}$ (fine), in the refined region near the cylinder.

In figure 3.3, the velocity components are plotted for three different phases of the oscillation and on four different cross sections along the oscillation path of the cylinder,for the three meshes, in order to assess the influence of spatial discretisation on the numerical results. The small deviation of the velocity profiles indicate that the immersed boundary method is mesh independent.
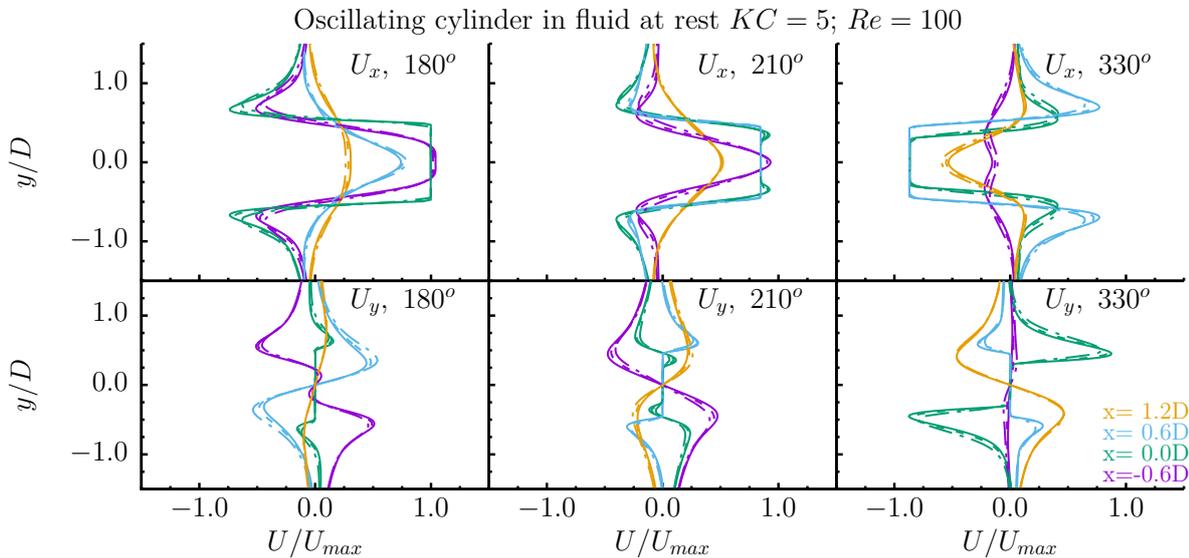
Figure 3.3: Mesh dependence of in-line (top) and cross (bottom) velocity for Immersed Boundary simulations of cylinder oscillation in air at rest, at $Re = 100$ and $KC = 5$, at four different cross-sections: coarse $(- \cdot -)$, medium $(- - -)$, fine (continuous line).

In figure 3.4 the Immersed Boundary method is compared to the experimental data of Dütsch [56], and to an *Over-Set mesh* methodology, available in `OpenFoam+` [166]. According to the Over-Set mesh approach, two grids are created, one background that does not take into account the moving cylinder and one smaller around the cylinder, which conforms to the geometry; an interpolation procedure is defined to communicate field values between the two meshes. The *medium* mesh is used for both numerical simulations. The predicted velocity profiles exhibit a good agreement for the two computational methods, as well as with the experimental data, although some peak values are not captured.

Finally, the drag coefficient over the length of the cylinder, computed as $C_D = 2f_x/(\rho D_{cyl}U^2)$, is plotted for the *IB* method, the Over-Set mesh and the experiments, in figure 3.5, where *IB*
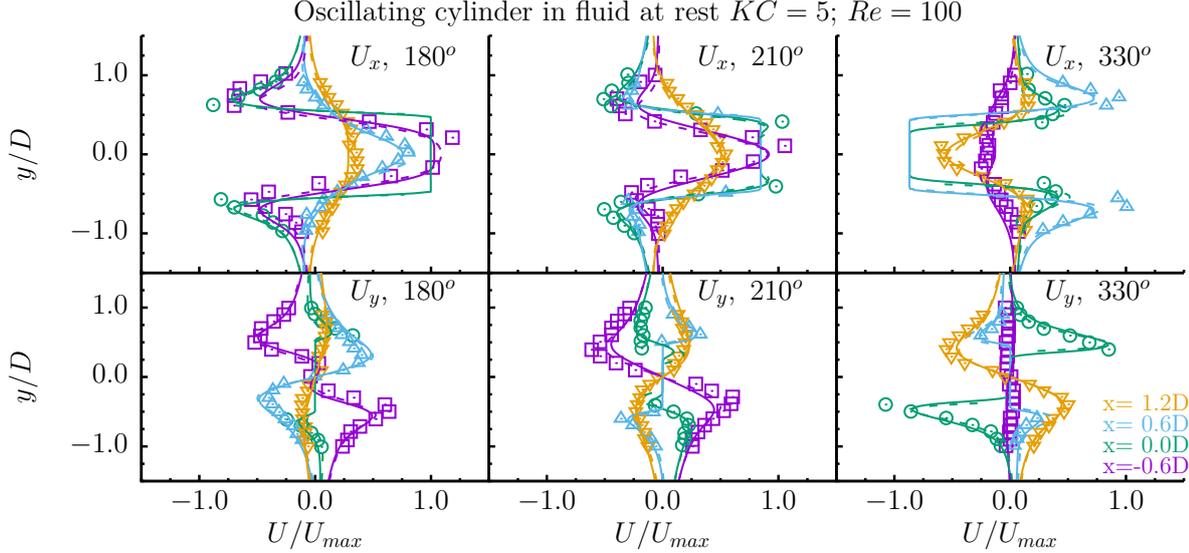
Figure 3.4: Comparison of in-line (top) and cross (bottom) velocity profiles for Immersed Boundary simulations *(continuous line)* of cylinder oscillation in air at rest, $Re = 100$ and $KC = 5$, to Over-Set mesh computations *(dashed line)* and Dütsch et al. [56] experimental data *(symbols)*, at four different cross-sections.

simulations for the three different meshes are compared in 3.5a for $dt = 0.5ms$ and for three different time steps using the medium mesh in figure 3.5b. Both methods produce results that coincide with experimental data. However, it can be observed that the Over-Set curve has a lot of spikes, whereas the IB curves are smoother. If the Over-Set method was to be used in the framework of a flow-induced motion for the cylinder, these spikes might result in non-convergent simulation and highly unsteady motion. In contrast, the IB method seems more suitable for such complicated fluid-structure interaction problems.

For the IB curve, the smoothness is influenced by the spacial and temporal resolution. A coarser grid yields weak force spikes in some parts of the oscillation, probably because the immersed body representation is not accurate enough. On the other hand, a larger time-step provides a smoother curve. The time step and minimum cell size control the percentage of a masked (solid) cell to be revealed and of an unmasked (fluid) cell to be covered by the immersed body as it moves and therefore affects the unsteadiness of the forcing source term.

Flow past Oscillating Cylinder

The next benchmark case considered to assess the performance of the proposed Immersed Boundary method is the case of an incompressible flow development over an in-line oscillating cylinder. The current Finite Volume IB method simulation results are compared with the numerical data of Hurlbut et al. [99], obtained using the Finite Difference approach.

The computations of Hurlbut et al. [99] were performed on a fixed grid, conforming to the cylinder surface. The oscillating motion of the cylinder was taken into account using a non-inertial coordinate transformation, where the velocity of the fluid is divided in to two components: one relative to the moving cylinder $(\mathbf{U}_f)$ and one relative to the inertial frame of reference $(\mathbf{U}_r)$. The latter is calculated as a function of time, representing the oscillation of
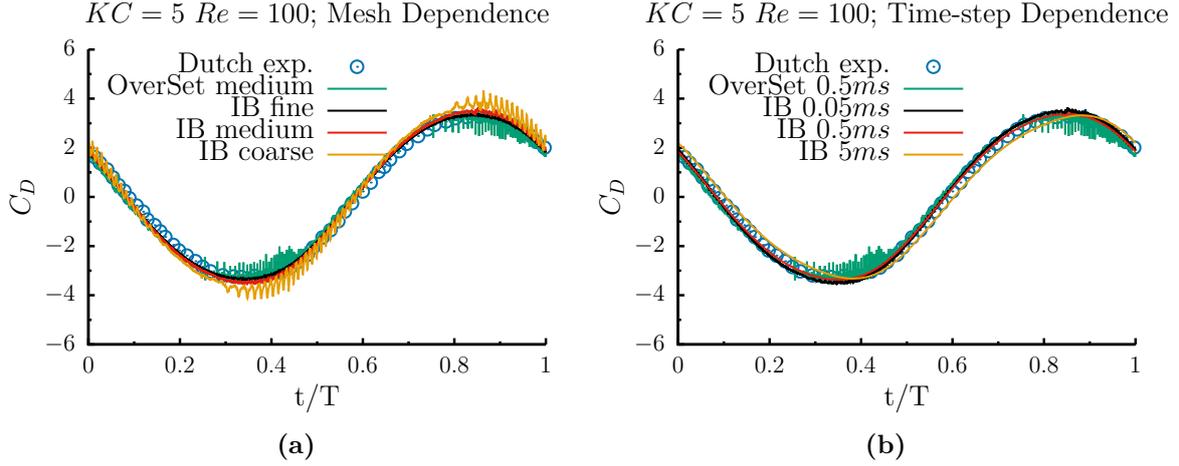
Figure 3.5: Comparison of drag coefficient for Immersed Boundary simulations with the three different meshes *(a)* and three different time steps *(b)*, to the computation of the Over-Set mesh technique (using the fine mesh) and the experimental data of Dütsch et al. [56].

the cylinder.

The cylinder is initially stationary, exposed in a flow of $Re = 100$, until a periodic vortex shedding is achieved. Then, it starts to oscillate at a frequency twice as the Strouhal number of the vortex shedding, which is calculated as $St_q = f_q U_{\inf}/D_{cyl} = 0.166$, where f_q the vortex shedding frequency; this is in agreement with the literature [171,205,216]. According to Hurlbut et al. [99], at such an oscillation frequency, phase locking is observed which increases the drag and maximizes the lift coefficient.

As in the previous case, air is chosen as the medium and the velocity of the cylinder is described by the equation $u_c(t) = 2\pi f_c A cos(2\pi f t)$, with the amplitude of the oscillation subject to the constrain of $KC = 5$ and $f_c = 2f_q$, where f_c the oscillation frequency of the cylinder.

The computational domain is chosen to be $L = 55D_{cyl}$ in length and $H = 35D_{cyl}$ in height, and discretised by an orthogonal Cartesian grid, which makes use of telescopic refinement near the cylinder and along the vortex street, to yield square cells with edge length of $\delta x = \delta y = 1\% D_{cyl}$.

Comparison of the drag (C_D) and lift (C_L) coefficient, extracted from the IB simulations, against the conformal grid computational data of Hurlbut et al. [99], show excellent agreement, as illustrated in figure 3.6. The current IB method provides accurate results and greatly simplifies the computational procedure compared to the numerical setup of Hurlbut et al. [99]

3.1.2 Incompressible Turbulent Flow over Backfacing Step

In order to test and validate the treatment of turbulent modelling by the presented Immersed Boundary method, a widely accepted benchmark case of the flow over a back-facing step [5, 85, 108, 120], at a Reynolds number of $Re = 69610$, is studied. The present numerical simulation results are compared to the experimental data provided by Kim [108].

The case consists of the incompressible flow of air ($\rho = 1.88553 \ kg/m^3$, $\mu = 1.83698 \cdot 10^{-5} \ kg/ms$) in a channel, over a back-facing step. The total height of the channel is $H_{Total} =$
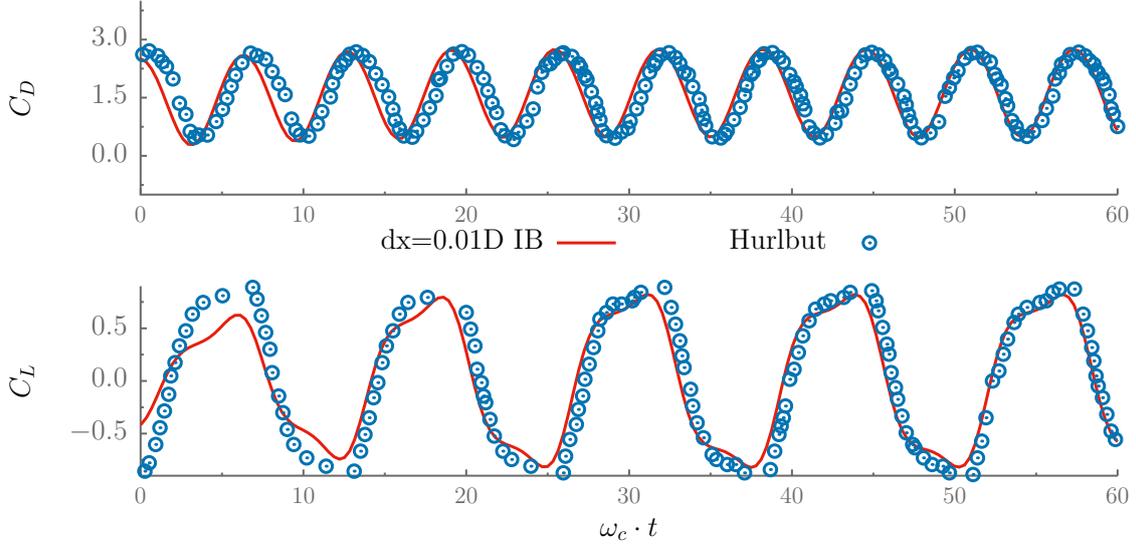
Figure 3.6: Flow over oscillating cylinder at $Re = 100$. Comparison of Lift (top) and Drag (bottom) coefficient for Immersed Boundary simulations *(lines)* to conformal grid computational data of Hurlbut et al. [99] *(symbols)*. The cylinder oscillates at a frequency two times greater than the vortex shedding frequency, $f_c = 2 \cdot f_q = St_q \cdot U_{inf}/D_c$.

$3h$, where h the height of the step. The step extends $L_1 = 4h$ downstream the inlet. The outlet is placed $L_2 = 61.4h$ downstream the step. The domain, which can be seen in figure 3.7a, matches the configuration reported by [85], who simulated the same flow using curvilinear grids. The step is represented as an Immersed Boundary, as seen in figure 3.7b.

(a) Domain

(b) Mesh
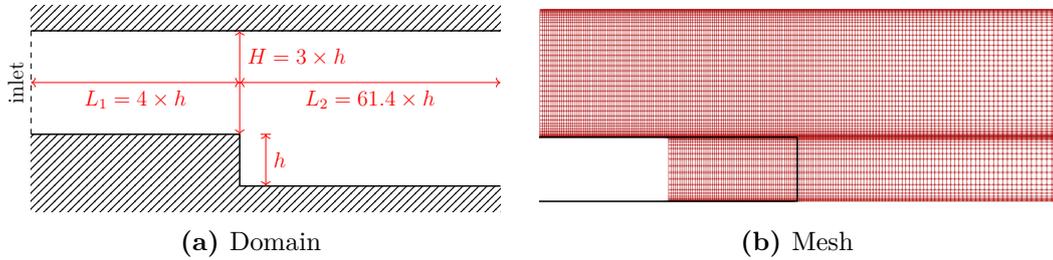
Figure 3.7: Computational domain (a) and mesh with IB surface (b) for back-facing step case. Geometric expansion of the cell height is used to refine the canonical orthogonal mesh near the wall and the top side of the step and achieve the desired y^+ value.

Unsteady Reynolds-Averaged (URANS) computations are carried out and the $k - \omega SST$ turbulent model is used. In addition to IB simulations, conformal grid simulations are also performed. Thus the performance of the IB method is evaluated, with respect to the accuracy of solver.

The conformal grid yielded $y^+ = 40$ near the wall. For the IB simulations, two different grids where used; a coarse achieving $y^+ = 40$, similar to the conformal grid, and a fine reaching $y^+ = 10$. When using an Immersed Boundary, is not trivial to determine the height of the first cell over the (immersed) wall, as the grid generally does not conform to the solid wall and the normal to the boundary direction does not coincide with the cell height. Therefore the y^+

serves rather as an indication of the grid resolution than an absolute characteristic measure of the turbulent modelling. In this particular case however, the computational cells are aligned with the immersed wall, therefore the y^+ retains its physical significance.

In figures 3.8 and 3.9, the profiles of turbulence kinetic energy *(TKE)* and in-line velocity *(U_x)* respectively, along different vertical sections downstream of the step, are plotted. The numerical results of the IB method are compared to the conformal grid results and the experimental data from [108]. Good agreement is found between the two numerical methods and the deviation of both from the experimental results is small. Moreover, the Immersed Boundary computations' results prove independent of the grid resolution over the step. However, both numerical methods do not capture accurately the velocity profile in the recirculation region (first four sections in figure 3.9), as well as they both underestimate the maxima of the curves. In addition, small differences are observed in the distributions of turbulent kinetic energy between the IB method and the conformal grid simulation, as the IB method overestimates turbulence near to the step (first two sections in figure 3.8).

Finally, the pressure recuperation along the lower wall of the channel, downstream of the step is presented in figure 3.10), where the pressure coefficient with respect to the minimum value is plotted. Although until a distance of $3h$ away from the step the numerical results are close to the experimental, they deviate significantly thereafter. However, the IB results are close to those of the conformal grid.

This deviation may be linked to the two-dimensional setup of the computations, in contrast to the three-dimensional nature of the flow, or to the limitations of RANS approach, as reported by Sohn [118].
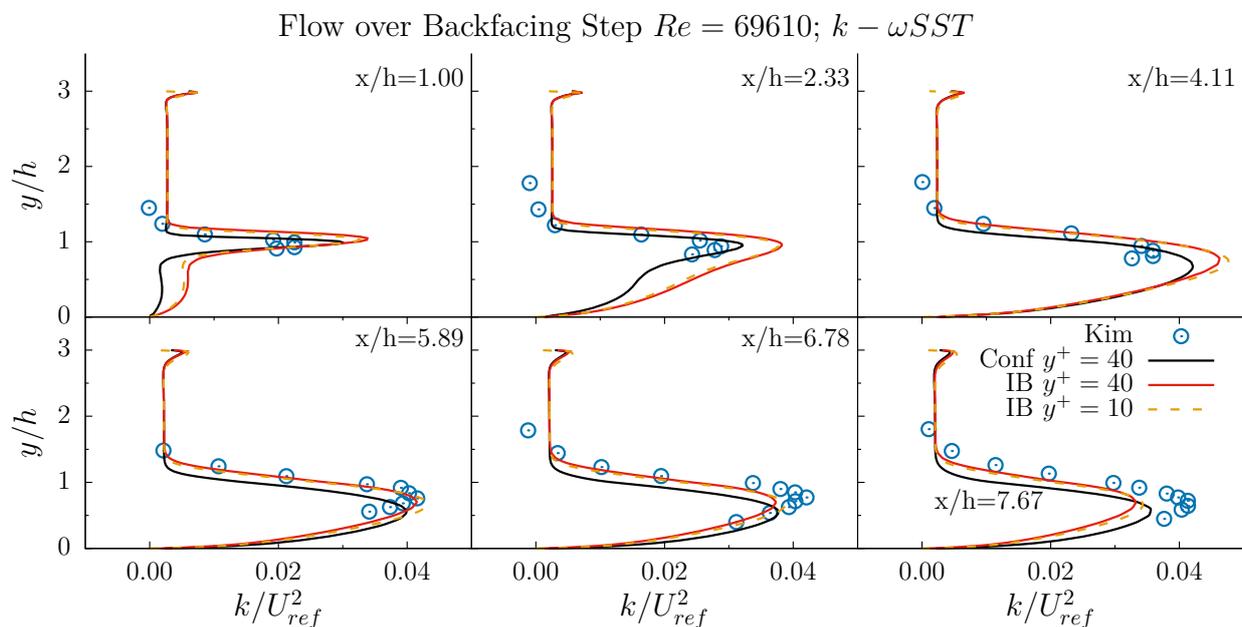
Figure 3.8: Flow over back-facing step. Turbulent Kinetic Energy vertical distribution on six different positions along the channel. Immersed Boundary results for coarse *(red line)* and fine mesh *(dash orange line)* compared to conformal grid computations *(black line)* and experimental data of Kim et al. [108] *(symbols)*.
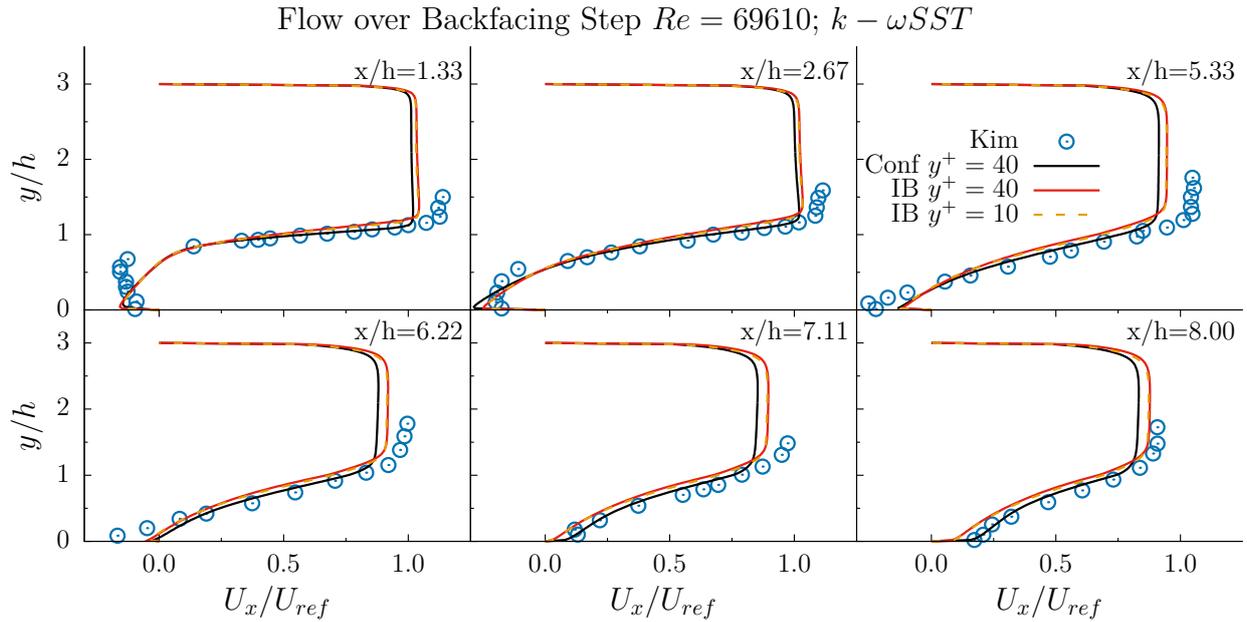
Figure 3.9: Flow over back-facing step. In-line velocity profile on six different positions along the channel. Immersed Boundary results for coarse *(red line)* and fine mesh *(dash orange line)* compared to conformal grid computations *(black line)* and experimental data of Kim et al. [108] *(symbols)*.
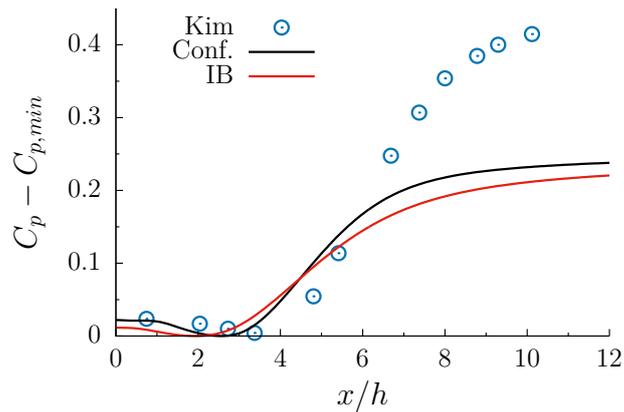
Figure 3.10: Flow over back-facing step. Pressure recuperation along the channel, after the step. Immersed Boundary results *(dashed line)* compared to conformal grid computations *(continuous line)* and experimental data of Kim et al. *(symbols)*.

3.2 Cavitating Flows

Following the benchmark incompressible cases, with moving or stationary immersed bodies, laminar or turbulent regimes, the present Immersed Boundary method is applied onto cavitating flows. At first the case of cavitation induced by a rotating cross immersed into stationary water is simulated, which could be seen as a case of an idealised propeller. Then, the method is used on fully turbulent cavitating flows past stationary or moving hydrofoils in a channel.

3.2.1 Cavitation Induction by Rotating Cross

As a first benchmark case, the cavitation induction by the rotation of a solid cross in water is considered. The initially idle cross is placed in water at rest and at the beginning of the simulation is instantaneously started to rotate at a constant angular velocity. The motion of the solid accelerates the surrounding stationary liquid and induces cavitation.

This test case was studied by Örley et al. [170] to validate their cut cell immersed boundary method against a simulation using a Arbitrary Lagrangian-Eulerian formulation *(ALE)*(with conformal to the geometry grid). In the present study, an additional simulation with a conformal to the cross geometry grid, employing a sliding mesh approach using Arbitrary Mesh Interface *(AMI)* [61] method, is carried out in order to compare with the developed Immersed Boundary method.

The cross consists of a circular hub with diameter $d_{hub} = 0.2\ m$ and two bars of the same thickness $w_{bar} = 0.1\ m$ but different length, $l_1 = 1.0\ m$ and $l_2 = 0.5\ m$. The study is two-dimensional. As computational domain is chosen a square with edge length $L_{sq} = 600\ l_1$ and is discretised by a canonical Cartesian grid. Three different mesh resolutions are used, as in [170], one with 10 cells (coarse mesh) along the thickness of the bars w_{bar}, one with 20 cells (medium mesh) and one with 40 cells (fine mesh). Several levels of telescopic refinement are used to achieve the desired resolution in an area $2\ l_1 \times 2\ l_1$ around the center of the hub of the cross.

The initial ambient pressure is set to $p_{init} = 1\ bar$, the liquid is initially at rest and the angular velocity of the cross is $\omega = 20\ rad/s$ around the axis perpendicular to the plane. The density of the liquid water is $\rho_L = 998.16\ kg/m^3$ and for the saturated vapour $\rho_V = 0.017312\ kg/m^3$, while the saturation pressure is set $p_{SAT} = 2339\ Pa$. The Wallis formula is used for the mixture's compressibility calculation.

As the cross starts to move, the ambient liquid is abruptly accelerated, pressure drops along the cross surface, small vapour structures are formed and strong pressure waves are emitted radially away from the solid boundary, visible in figure 3.11. These waves get superimposed while travelling away resulting in a complex pressure field. These initial vapour structures will then collapse and as the velocity field is developed, cavitation will be induced on the path of the cross, on the top of the long bars and near the convex surface of the hub. As these vapour structures collapse, new strong pressure waves are emitted towards the far field, as it can be seen in the sequence plots of figure 3.12.

Comparison of the vorticity contours for the different meshes and the AMI simulation, presented in figure 3.13, show that mesh resolution affects greatly the sharpness of the contours, with different structures visible on the finer mesh, which leads also to different vapour structures. In addition, the conformal mesh simulation (AMI approach) exhibit different vorticity and vapour structures than the IB computations, and capture weak vapour formation near the convex surface of the hub.
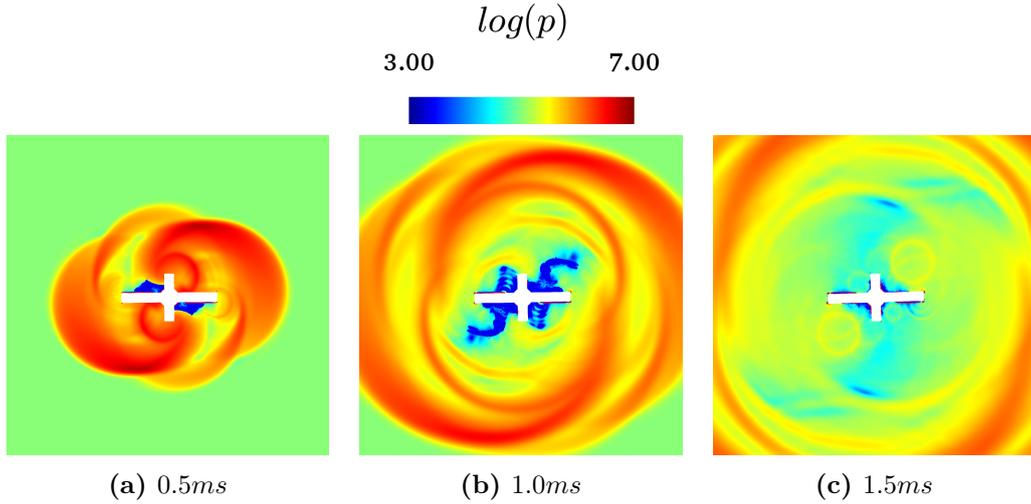
Figure 3.11: Pressure contours in logarithmic scale (*common logarithm $log_{10}(\cdot)$*), at the initial stages of the rotation of the cross inside initially stationary water. The time instances are extracted for the fine *(40 cells)* mesh. One complete rotation lasts $314ms$. Vapour volume fraction of 1% iso-line is plotted with red.
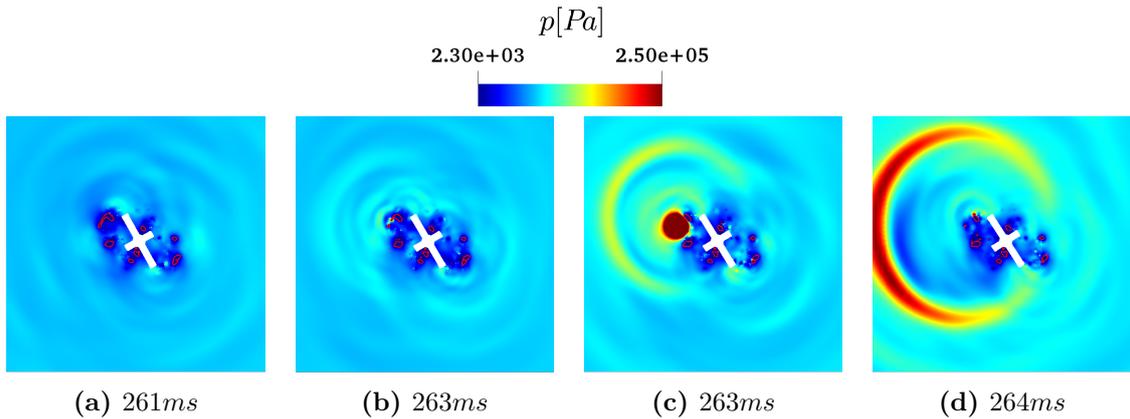
Figure 3.12: Pressure contours in logarithmic scale (*common logarithm $log_{10}(\cdot)$*), at the later stages of the rotation of the cross inside initially stationary water. The time instances are extracted for the medium *(20 cells)* mesh. One complete rotation lasts $314ms$. Vapour volume fraction of 1% iso-line is plotted with red.

The total amount of vapour created during one full rotation of the cross is plotted in figure 3.14, for the different grids, the AMI approach as well as the cut cell (for the three meshes) and the ALE simulations (for an equivalent to the medium mesh) reported by Örley et al. [170]. It can be seen that the current IB method, for the medium grid, although it results in a curve that follows closely the respective medium grid computation with cut cells of [170] but reaches a larger maximum, predicts greater vapour creation, than all the other computations. Finer grid resolution enhances the vapour creation, as expected. In addition, it can be observed that the conformal grid simulations give different predictions, which might be linked to the different solvers or barotropic models used.

The velocity magnitude contours, plotted in figure 3.15 for three phases of the oscillation,

57

for the computation with the medium grid, differ slightly from the AMI simulation, whereas the vapour structures show greater deviation. The difference becomes more apparent for the 360° degrees, where the velocity contous, the vapour distribution, and therefore the velocity streamlines, show significant differences.

Although differences can be noted between the IB and the AMI simulations, the current immersed boundary method proves adequate and suitable for treating cavitating flows with moving boundaries. The physics is captured, including pressure waves and vapour creation, growth and collapse.

(a) IB coarse   **(b)** IB medium   **(c)** IB fine   **(d)** AMI medium
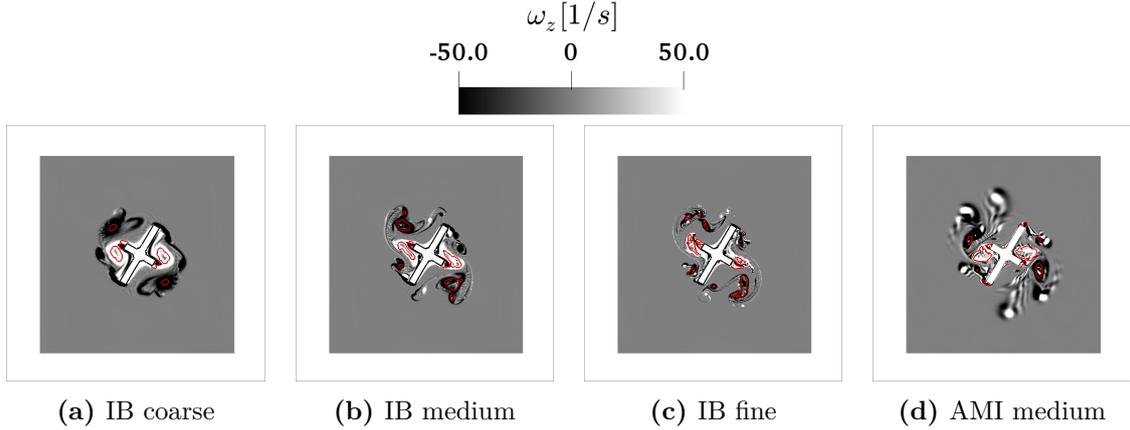
Figure 3.13: Vorticity contours for rotating cross in water at rest, at 240°. Current *direct forcing* Immersed Boundary method simulations for coarse *(a)*, medium *(b)* and fine mesh *(c)* are compared to sliding mesh computations *(d)* using AMI technique. Vapour volume fraction of 1% iso-line is plotted with red.

(a)   **(b)**
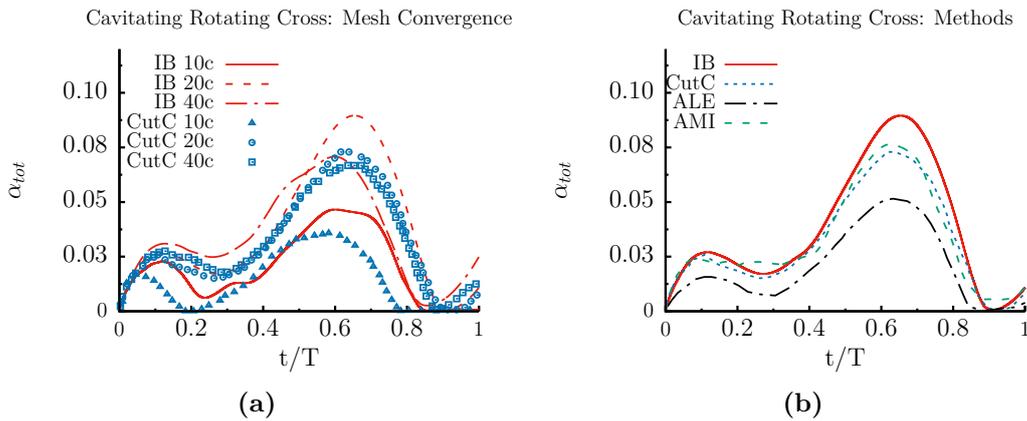
Figure 3.14: Integral vapour volume fraction's time evolution for rotating cross in water at rest. Mesh convergence comparison between current direct forcing IB method *(IB)* and cut-cell method *(CutC)* from [170], on the left. In addition, a comparison of different computational approaches is presented on the right, between the current IB method and the cut-cell calculations, conformal sliding mesh simulations performed using *AMI* approach and *ALE* results reported in [170].

58
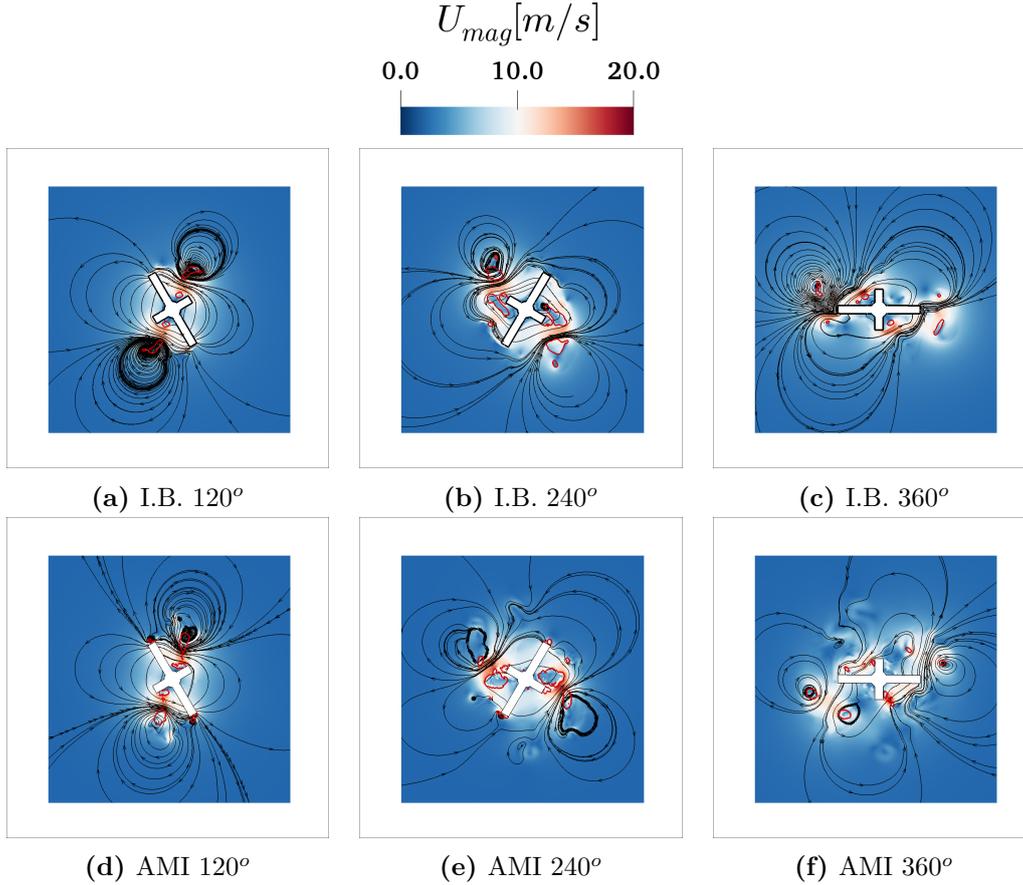
Figure 3.15: Velocity magnitude contours along with streamlines for I.B. (top) and AMI (bottom) simulations for rotating cross in water at rest, at three different rotation angles, for the medium mesh *(20 cells along w_{bar})*. Vapour volume fraction of 1% iso-line is plotted with red.

3.2.2 Cavitating Flow over a Stationary Hydrofoil in Channel

Another benchmark case of cavitating flow is the flow over the circular leading edge *(CLE)* symmetric hydrofoil, studied experimentally and numerically by Dular et al. [54]. The complexity of the unsteady cavitating flow poses an important challenge to the presented modelling approach and the available experimental data offer an excellent opportunity to validate the performance of the method.

In the experiment [54], a symmetric hydrofoil, $107.9mm$ long and $16mm$ thick, is placed in a $500mm$ long and $100mm$ high cavitation tunnel, at a 5° incidence angle. Both the hydrofoil and the tunnel are $50mm$ wide, but the simulations presented hereafter are two-dimensional for simplicity, as the numerical study of [54]. The computational domain and grid used in the current study can be seen in figure 3.16. A constant velocity U_{in} is imposed as boundary condition at the inlet on the left side of the domain and a constant pressure p_{out} is set as an outlet boundary condition on the right side. The value of pressure on the outlet is derived from the desired cavitation number of the flow $\sigma = (p_\infty - p_{vap})/(\frac{1}{2}\rho U_\infty^2)$. On the upper and lower side are considered no-slip walls.

The computational domain is discretised by a hexahedral orthogonal grid with additional refinement on the interface of the hydrofoil. On the side walls, the cell height reaches values

of $y^+ = 30$, whereas near the hydrofoil the cell size is equivalent of $y^+ = 20$. The final grid is composed by 100k hexahedral cells.

(a) Domain

(b) Mesh
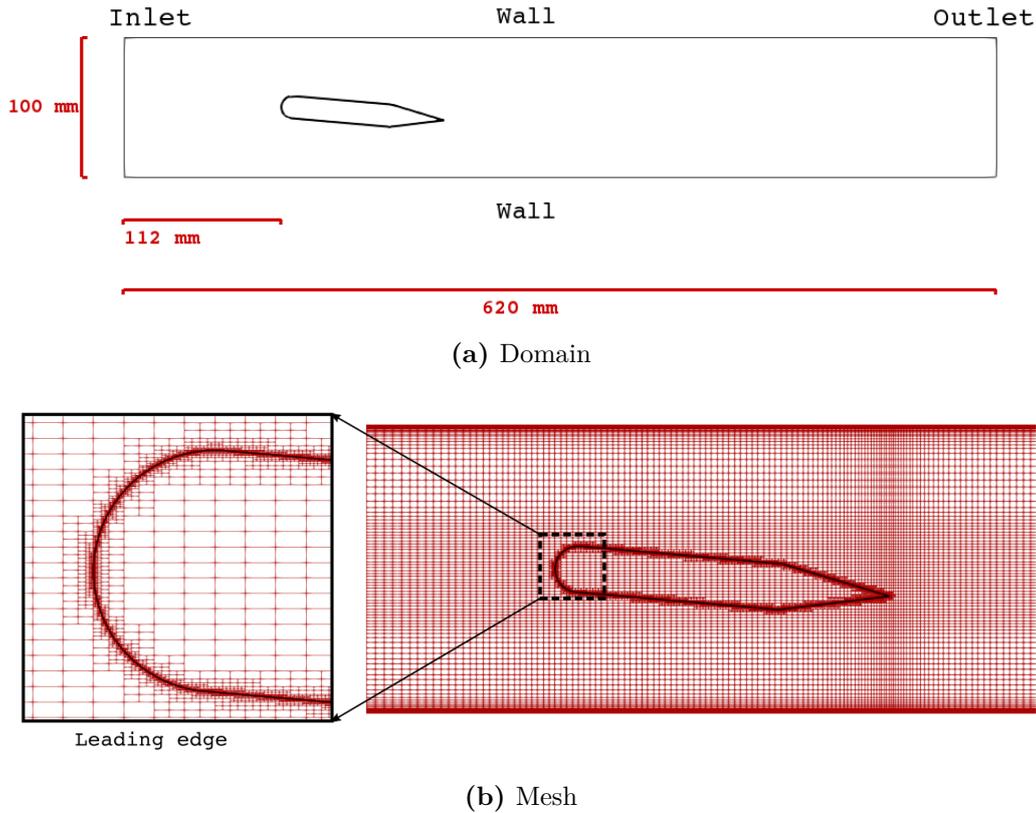
Figure 3.16: Computational domain (a) and mesh with telescopic refinement (b) for *CLE* hydrofoil in channel. A closer look on the leading-edge of the hydrofoil is shown at the left of frame (b).

The density and kinematic viscosity for water are set to $\rho_l = 998.16 \ kg/m^3$ and $\nu_l = 10^{-6} \ m^2/s$, and for the saturated vapour $\rho_v = 0.017312 \ kg/m^3$ and $\nu_v = 5.12 \cdot 10^{-4} \ m^2/s$. The saturation pressure is $p_{SAT} = 2339 \ Pa$.

From the test-cases presented in [54], the current study focuses on *Test 1*, with $U_{in} = 13m/s$ and $\sigma = 2$, for which experimental time-averaged velocity measurements are reported on different sections over the suction side of the hydrofoil, seen in figure 3.17. The resulting Reynolds number of the flow is $Re = 1.4 \cdot 10^6$.

In the current study, a modified $k - \omega \ SST$ turbulent model, employing the *Reboud correction* for the turbulent viscosity, is used. The simulations is run for few shedding cycles, with the time-step being limited by the *acoustic Courant Number* to be under 2. This yields time-steps of the order of $10^{-6}s$. The velocity is sampled on the same sections as the experiments every $0.5 \cdot 10^{-4}s$, and then time-averaged to produce velocity profiles to be compared with the experimental data of [54]. The comparison of the velocity profiles is presented in figure 3.18, for the in-line (3.18a) and cross direction (3.18b) components.

The comparison yields almost perfect match between the numerical and experimental profiles for the U_x velocity component, while for the U_y component a slight deviation is observed that weakens towards the upper wall. The measured U_y velocity at section $y = 0mm$ receives strictly negative values after $x = 50mm$ while the current computation predicts almost

60

(a)   **(b)**
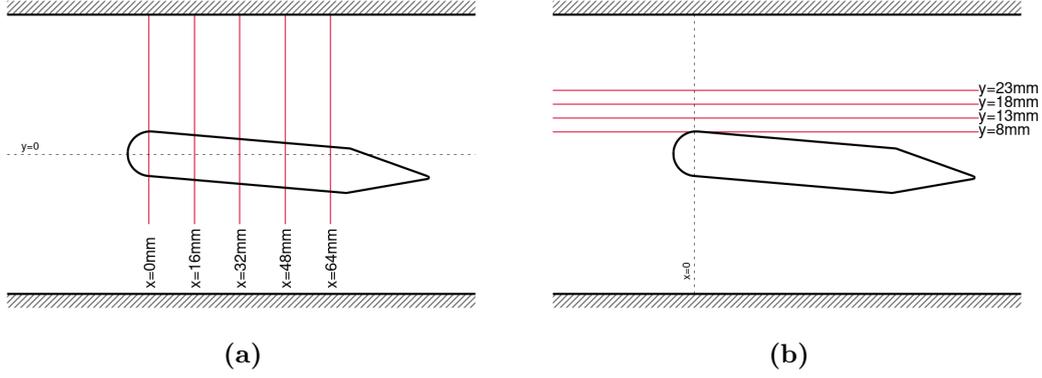
Figure 3.17: Sections where velocity is sampled for the flow over *CLE* hydrofoil according to [54].

(a)

(b)
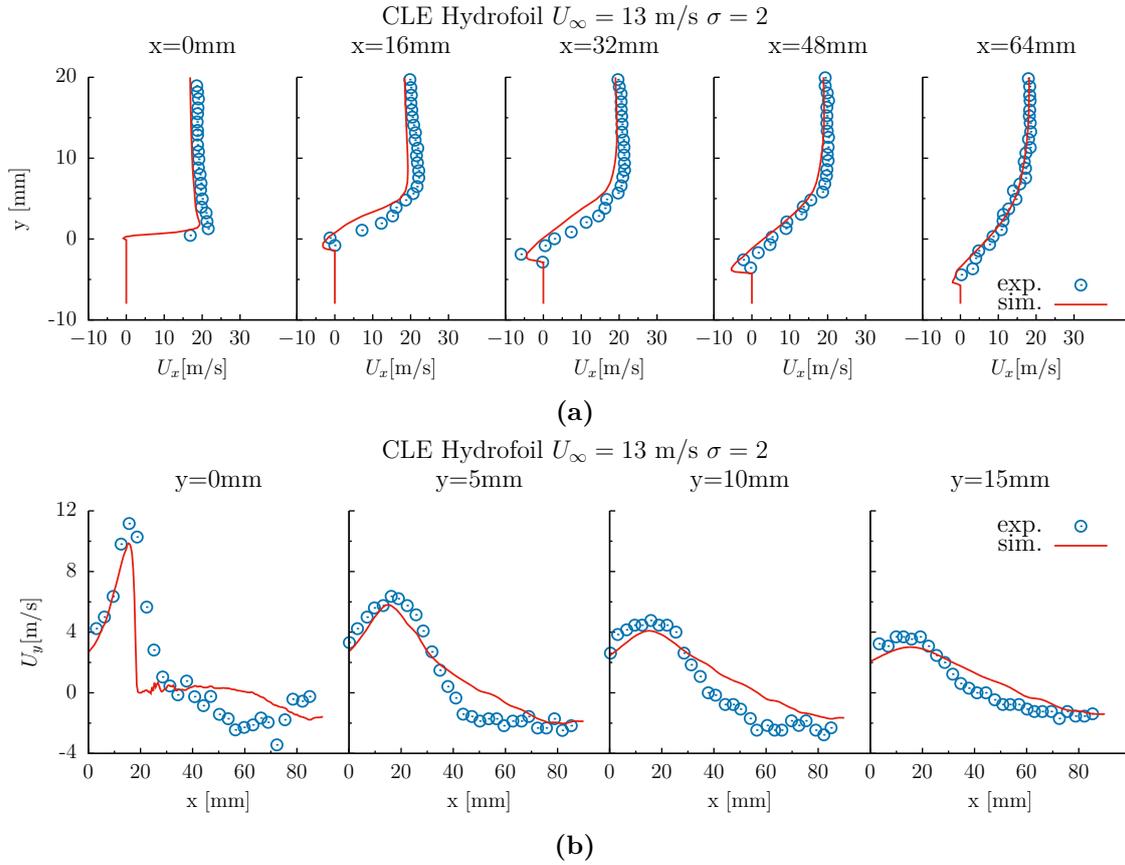
Figure 3.18: Time-averaged velocity profiles along stream and cross-stream directions for cavitating flow over *CLE* hydrofoil. Numerical results with the current IB method, plotted with continuous lines, are compared against experimental data from Dular et al. [54], presented with symbols.

$U_y = 0 m/s$ from $20mm$ to $60mm$ and start to decrease slowly. This small deviation on the cross-stream direction indicates that the proposed IB method produces a thicker boundary layer or longer cavity on average, as recirculation is pushed further towards the trailing edge.

     Overall the numerical results of the current numerical approach show good agreement with the experimental measurements. This demonstrates the ability of the method to deal with complicated turbulent cavitating flows.

3.2.3 Cavitating Flow over a Pitching Hydrofoil

An indicative case, demonstrating the ability of the proposed Immersed Boundary Method to deal with complex cavitating turbulent flows, is the flow over a pitching NACA0066 hydrofoil at $Re = 750000$ studied numerically and experimentally by Huang et al. [97].

In the aforementioned study, a NACA0066, with chord length $c = 0.15m$, is put in a hydraulic channel, where water flows at $U_\infty = 5m/s$ and set to rotate changing the angle-of-attack of the flow from $\alpha_{O,min} = 0^o$ to $\alpha_{O,max} = 15^o$ and back, for two different cavitating regimes (cavitating $\sigma = 3$, subcavitating $\sigma = 8$), at two different angular velocities $\dot{\alpha}^* = 0.18$ and $\dot{\alpha}^* = 1.89$, where the nondimensional rate is calculated as $\dot{\alpha}^* = \dot{\alpha} \cdot c/U_\infty$. The current study focuses only on the cavitating case with the fast pitching rate; the rotation angle is prescribed and follows the curve reported in [97], which is shown in figure 3.20 and passed to the code as tabulated data.
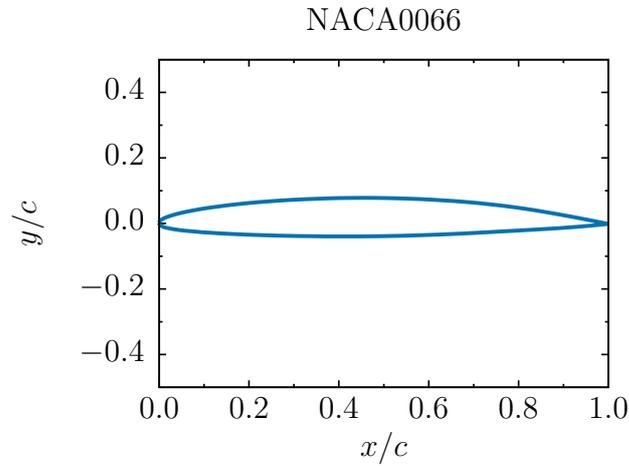
Figure 3.19: The *NACA0066mod* cambered hydrofoil's profile used in the study, extracted from [123]. Maximum thickness 12% of the chord.
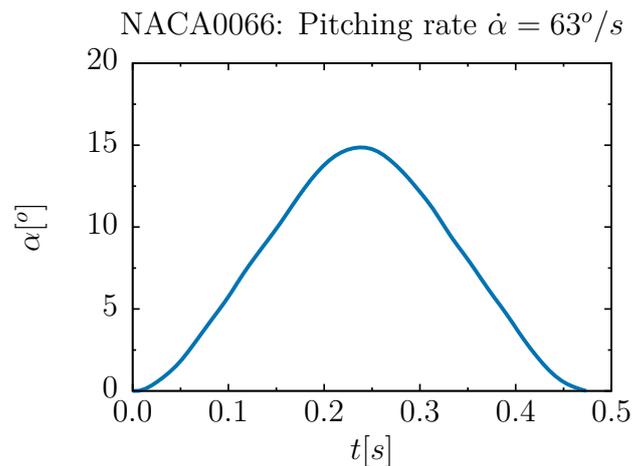
Figure 3.20: The prescribed rotation angle evolution through time as extracted from [97].

The computational domain is chosen $16c$ long and $1.28c$ high, in accordance with the

computations of Huang et al. [97]. As boundary conditions, the far-field velocity U_∞ is imposed at the inlet at the left of the domain, the value of pressure p_∞ is kept constant at the outlet in order to satisfy the condition of the cavitation number $\sigma = (p_\infty - p_{vap})/(\frac{1}{2}\rho U_\infty^2) = 3$. Moreover, following the reference study, at the top and bottom sides a *symmetry* boundary condition is set. The domain is discretised by an orthogonal hexahedral grid and telescopic refinement is used in order to increase the mesh density around the hydrofoil and its wake. Both the domain and mesh can be seen in figure 3.21.
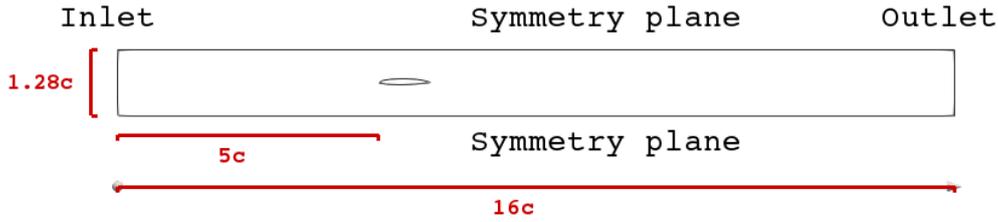

(a) Domain
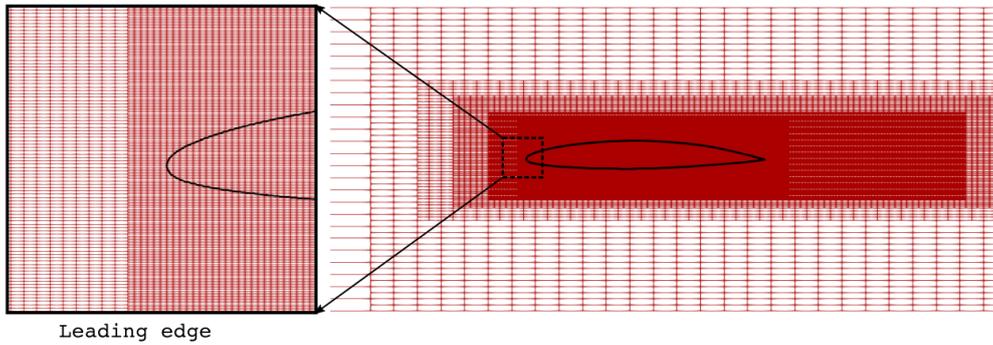
(b) Mesh

Figure 3.21: Computational domain (a) and mesh with telescopic refinement (b) for *NACA0066*. A closer look on the leading-edge of the hydrofoil is shown at the left of frame (b). The cells at the finest region, in the vicinity of the hydrofoil, have a height equivalent of $y^+ = 20$.

Using telescopic box refinement, the finest cell size reached, in an area around the NACA, is $0.47mm \times 0.12mm$, which, if the mesh was conforming to the hydrofoil's wall, would correspond to $y^+ = 20$. In order to always have a fine grid at the interface of the immersed body, while the hydrofoil is moving, the cell size has to be kept constant in a broad area covering the path of the immersed body motion. An alternative practice would be to use a technique of automatic mesh refinement at the interface or the area of the immersed boundary, but it is out of the scope of the current study.

When using an Immersed Boundary approach, it is not trivial to determine the height of the first cell over the (immersed) wall, as the grid does not conform to the solid wall and the normal to the boundary direction does not coincide with the cell edges. Therefore the y^+ servers rather as an indication of the grid resolution than an absolute characteristic measure of the turbulent modelling.

In their numerical computations, Huang et al [97], use a tetrahedral grid with additional

hexahedral layers over the hydrofoil's wall to capture the boundary layer. The layers ensure a mesh resolution of $y^+ = 1$ on the wall to accommodate the turbulent modelling. The computational domain is re-meshed in every time-step, to adapt to the new position of the hydrofoil. This approach of re-generation of the computational grid to deal with moving boundaries, may increase the computational cost, especially for complex geometries, and serves as a motivation for alternative techniques as the proposed Immersed Boundary.

Because of the severe transient nature of the flow, with the hydrofoil pitching past its stall-point, at an angle of $\alpha_{o,stall} = 13^o$, laminar to turbulent separation is expected to occur. For that reason, Huang et al. [97] make use of the $k - \omega \ SSTLM$ turbulence model, which is a combination of the transition model $\gamma - Re_\theta$ and the well-known low-Reynold $k - \omega \ SST$ model. They employ the *Reboud* correction for multiphase flows, which reduces the turbulent viscosity according to the local vapour volume fraction; they follow the modifications of Ducoin et al. [53] and set the value of the exponent n equal to 3 instead of 10 that was recommended by Coutier-Delgosha et al. [67]. When using the $\gamma - Re_\theta$ model in order to accurately capture the laminar to turbulent transition, the grid cell size should yield $y^+ \simeq 1$, while for $y^+ > 5$ the transition location would be erroneously determined and moved upstream, according to Menter et al. [140]. For this reason, in the computations of Huang et al. [97], the mesh resolution ensures $y^+ = 1$ over the hydrofoil wall.

In the present study however, achieving $y^+ = 1$ near the Immersed Boundary is computationally prohibiting because a wide are would require such a fine resolution, as explained in the previous paragraphs. Therefore, different turbulence models have been employed in an attempt to alleviate the uncertainties related to fully resolving the boundary layer over the immersed wall and capturing the laminar to turbulent transition. Apart from the $k - \omega \ SSTLM$ model, the one-equation Spalart Allmaras and the low-Reynolds $k - \omega \ SST$ models have been used. The first model solves two additional, compared to the $k - \omega \ SST$, equations for the intermittency γ and the transition momentum thickness Reynolds number Re_θ to estimate the position of the turbulent transition; it is used because it is chosen for the numerical study of Huang et al. [97]. The second model, Spalart Allmaras, is widely used in external aerodynamic flows over airfoils and solves for a single turbulent variable, the turbulent viscosity ν_t; it is chosen for its simplicity. Finally, the $k - \omega \ SST$ is also used, because it is one of the most widely applied model on problems of engineering interest. All the models incorporate the *Reboud* correction, to account for mixture effects on the turbulent viscosity.

Figure 3.22 presents the off-plane vorticity field for the three different turbulence models, at various indicative angles along the pitching cycle. The differences between the predicted vorticity is evident. The 50% vapour volume fraction iso-line is also plotted to indicate the cavitation regions. The close relation between vorticity and cavitation is visible. Cavities are initiated, grown and carried away by vortical structures generated on the leading and trailing edges of the hydrofoil. The interaction between leading edge cavities and trailing edge vortices, highlighted in [97], is captured by all the models. The vortical structures initiated at the trailing edge, grow until they interact with vapour structures shed over the hydrofoil from the leading edge and then they are separated from the hydrofoil and carried away in the wake. This interaction also brakes down the leading edge cavities.

(a) $9^{o(+)}$ **(b)** $9^{o(+)}$ **(c)** $9^{o(+)}$

(d) $12^{o(+)}$ **(e)** $12^{o(+)}$ **(f)** $12^{o(+)}$

(g) 15° **(h)** 15° **(i)** 15°

(j) $14^{o(-)}$ **(k)** $14^{o(-)}$ **(l)** $14^{o(-)}$

(m) $13^{o(-)}$ **(n)** $13^{o(-)}$ **(o)** $13^{o(-)}$

(p) $12^{o(-)}$ **(q)** $12^{o(-)}$ **(r)** $12^{o(-)}$
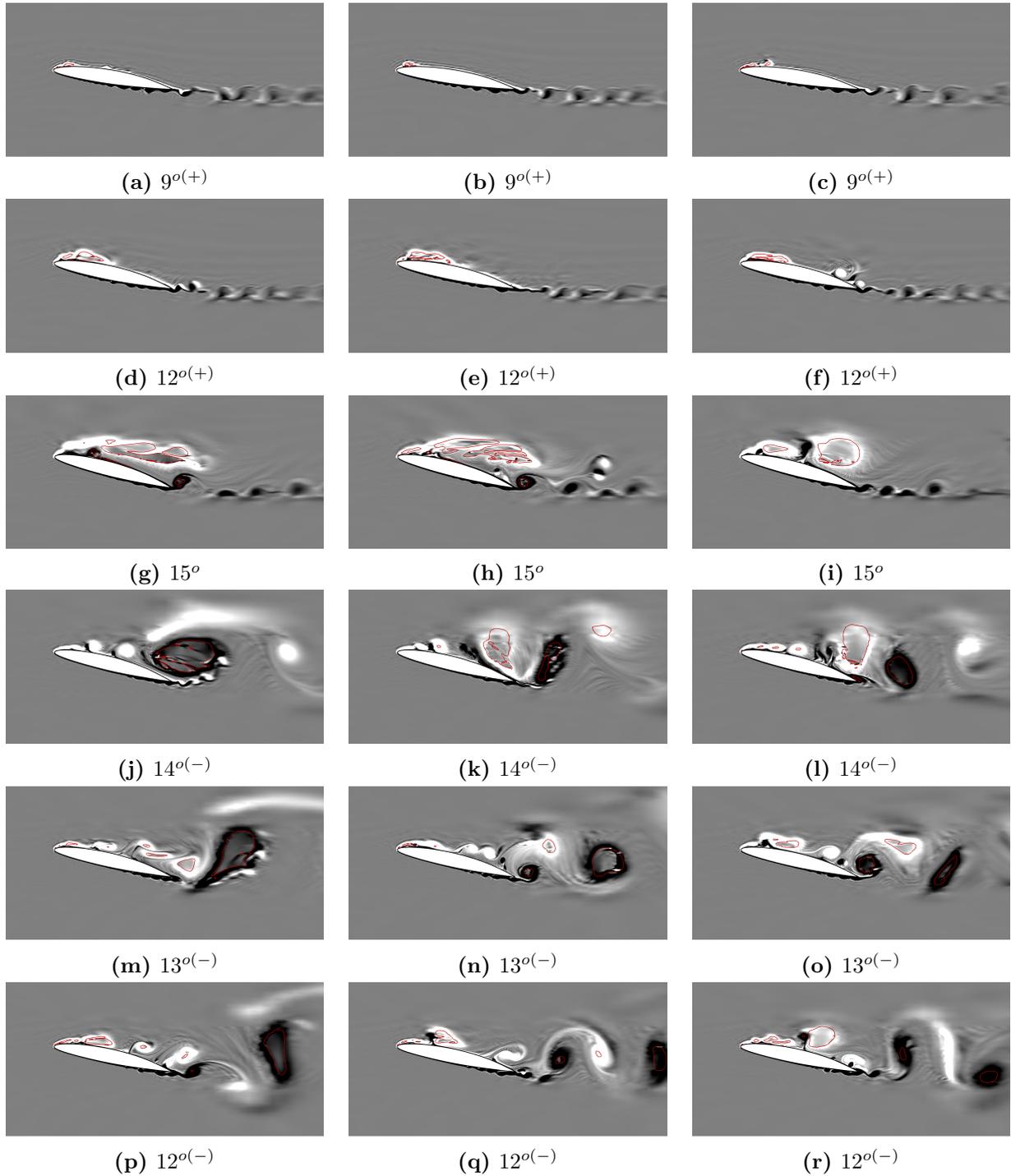
Figure 3.22: Vorticity field for pitching NACA0066, on different angles of attack along the motion, for the three different turbulence models. Spalart-Allmaras on the *left*, $k - \omega SST$ on the *middle*, $k - \omega SSTLM$ on the *right*. The red line in the figures represents the 50% vapour volume fraction iso-contour.

Cavitation formation initiates around $8^{o} - 9^{o}$ during ascending phase on the leading edge. After reaching peak angle at 15° and the descending commences, a trailing edge vortex is formed that grows significant, enclosing large amounts of vapour, which then interacts with

cavities and counter-rotating vortices from the leading edge and is shed on the wake. A striking difference between the models is that for the Spalart Allmaras this structure grows larger than for the other models, and its longer retained near the hydrofoil wall. On the other hand, for the other two models, this cycle is repeated more frequently and at a weaker intensity than for the Spalart Allmaras. Therefore, depending on the model, different cavity creation, growth and shedding cycle can be identified.

The influence of the model on the vapour creation cycle is also illustrated quantitatively by figure 3.23, which presents the integral vapour volume fraction evolution along the pitching motion, for the three models. The different shedding cycles for the models can be distinguished. Although all models seem to agree for the first cycle, between 9° ascending and 10° descending, they subsequently deviate, with Spalart Allmaras predicting a strong and slow second cycle, while the other two models demonstrate a faster cycle with over 50% reduced intensity from the first cycle. The greater reduction of vapour volume per cycle is observed for the $k - \omega\ SST$ model. Overall, the Spalart Allmaras model captures four vapour creation cycles along the pitching motion, the $k - \omega\ SSTLM$ five and the $k - \omega\ SST$ six.
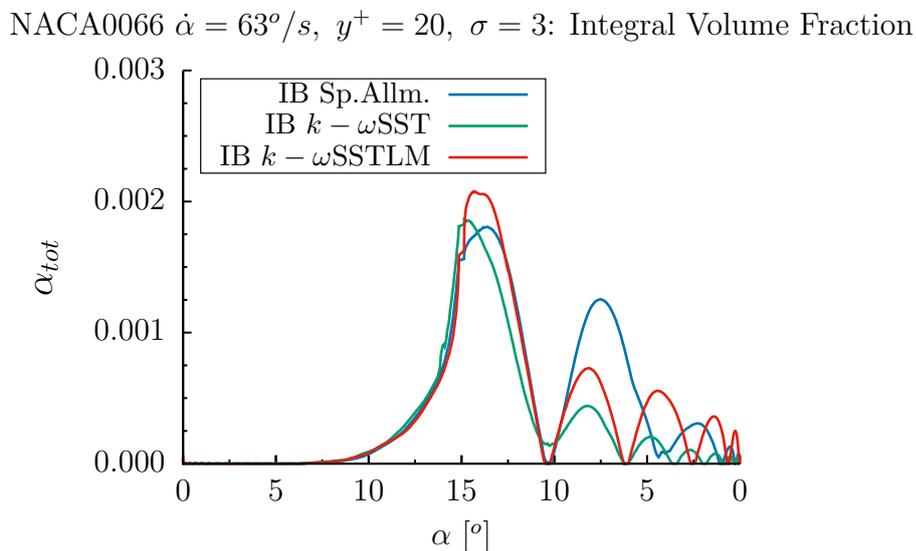
Figure 3.23: Integral vapour volume fraction for pitching NACA0066; comparison of simulation results with different turbulence models.

A straightforward quantitative measure of the performance of the herein proposed computational approach, would be the force coefficients' evolution throughout the rotation cycle. In figure 3.24, the lift, C_L, and drag, C_D, coefficients are presented for all three turbulent models used. The curves exhibit severe oscillations along the cycle and frequent high amplitude spikes around the peak angle and during descending phase, especially for the lift. In order to facilitate the assessment of the results, the Centered Moving Average *(CMA)* trend-line is estimated; it works as a filter that removes the high amplitude and high frequency noise and exposes the trend of the curves, as seen in figure 3.25. In addition, the plots compare the current simulations' results to numerical results using conformal grid reported by Huang et al. [97], employing $k - \omega\ SSTLM$; experimental values of the lift, measured for the subcavitating flow over a static hydrofoil on indicative angles of attack are shown as well. It is apparent that, while ascending,

the curves for all IB computations agree well with the referenced computations; some noise is present in both drag and lift coefficients. On the other hand, during the descending phase, although the IB results are extremely oscillatory, the averaged curves follow the conformal grid results but indicate noticeable discrepancies. Capturing the correct dynamics during the angle decrease is very challenging, due to the complex nature of the flow, the stall and the transition to turbulence near the wall, which is sensitive to the numerics and is hard to accommodate with the IB computations.

(a)

(b)
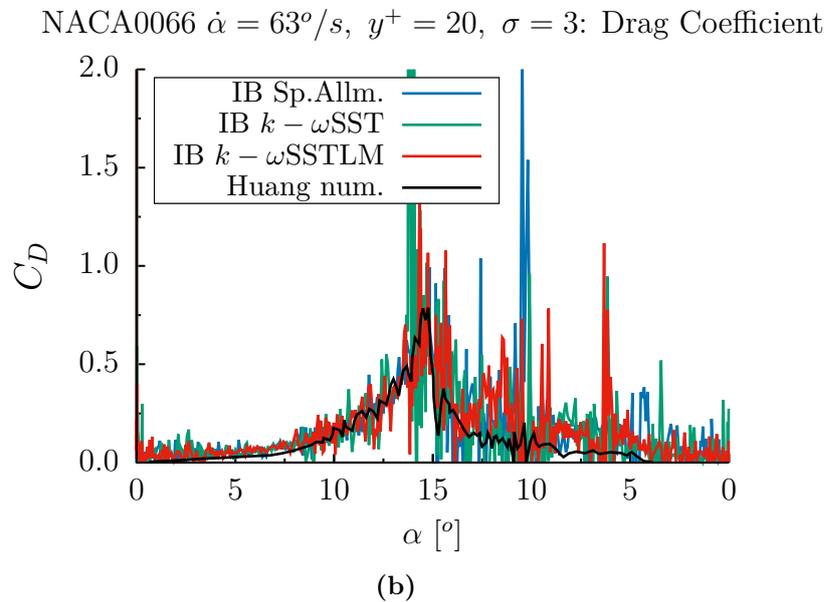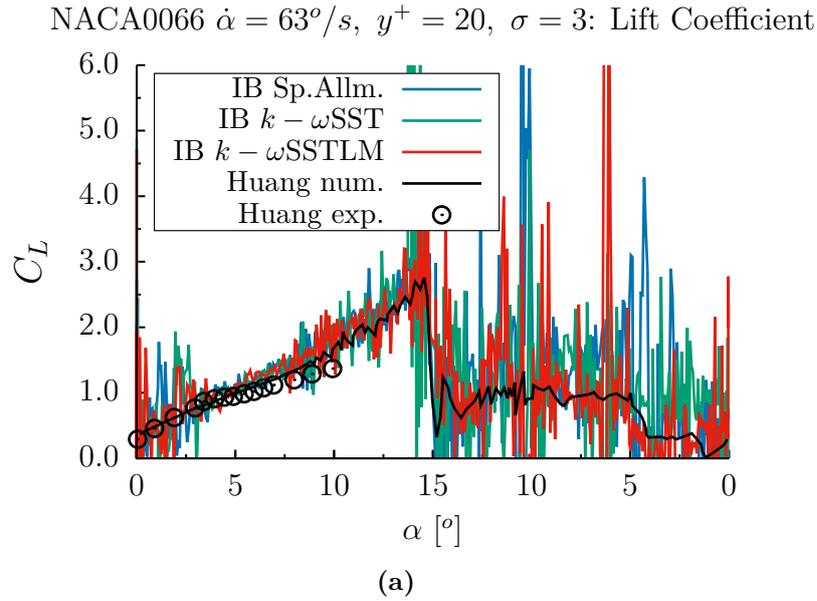
Figure 3.24: Force coefficients for pitching NACA0066; comparison of simulation results with different turbulence models. Numerical and experimental results of Huang et al. [97] are also presented; continuous black line refers to transient computations of cavitating pitching hydrofoil, while the black symbols are static lift measurements for fixed subcavitating hydrofoil.

NACA0066 $\dot{\alpha} = 63^o/s$, $y^+ = 20$, $\sigma = 3$: Lift Coefficient

(a)
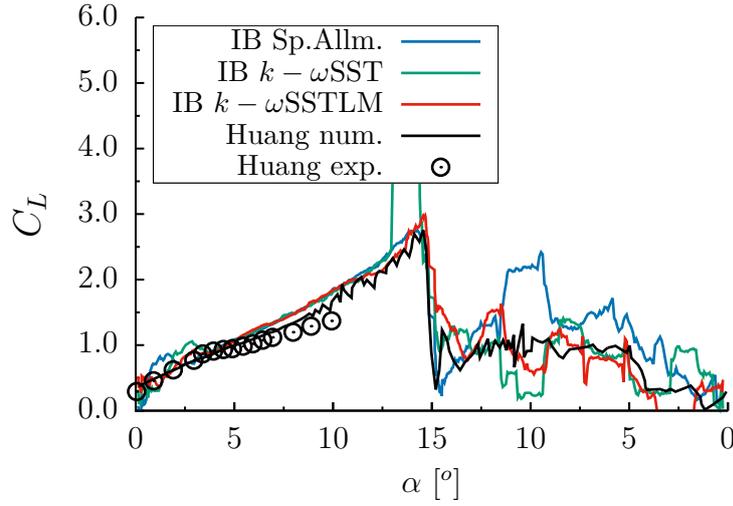
NACA0066 $\dot{\alpha} = 63^o/s$, $y^+ = 20$, $\sigma = 3$: Drag Coefficient
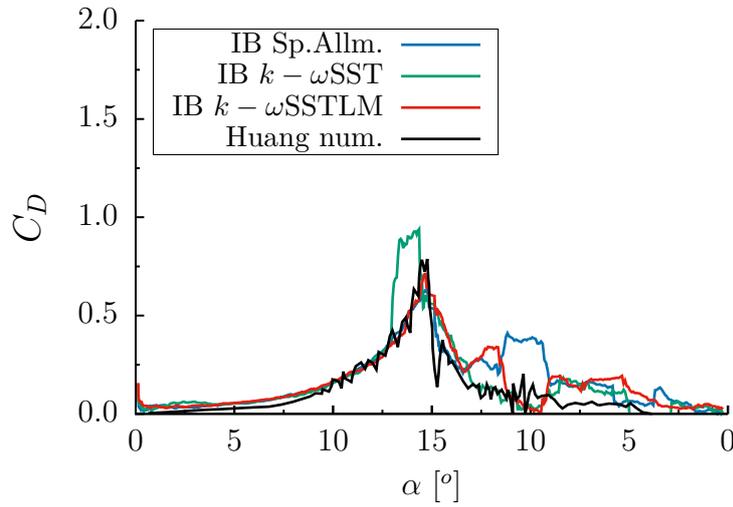
(b)

Figure 3.25: Centered Moving Average *(CMA)* trend-lines of force coefficients for pitching NACA0066; comparison of simulation results with different turbulence models. Numerical and experimental results of Huang et al. [97] are also presented; continuous black line refers to transient computations of cavitating pitching hydrofoil, while the black symbols are static lift measurements for fixed subcavitating hydrofoil.

It can be stated that, overall, the results of the IB and the conformal grid computations are close, despite the oscillations of the former. At the initial part of the motion, lift exhibits some oscillations, which are more likely caused by the abrupt acceleration from rest or the initialization of the simulations. It is hard to conclude which turbulent model performs better, as all three give similar results, with equivalent deviations from the referenced data at different instances, which do not favour any of the models. High amplitude spurious spikes are present in all curves at different time instances, however it can be safely argued that the $k - \omega SST$

exhibits the most high frequency noise, as seen in 3.24, and also the averaged curve captures a strong increase of the loading of the hydrofoil close to peak angle, as seen in 3.25 (the shift in time is relevant to the averaging window used). The CMA of the force coefficients reveal that the larger deviations occur around 10° during descending phase, After that point, and up until 4°, the $k - \omega\ SSTLM$ simulation seems to be closer to the referenced data for C_L and exhibits similar curvature for C_D, while the Spalart Allmaras constantly overestimates the coefficients. On the over hand, it has to be noted that the loss of lift and drag, at the beginning of the descending phase is better captured by the Spalart Allmaras model, with regards to the referenced data.

A qualitative assessment of the current computations is performed in figure 3.26, which presents experimental photographs and numerical vapour and vorticity fields provided by [97], along with the vorticity field and vapour iso-lines of the current numerical simulation with $k - \omega\ SSTLM$ model. The referenced photographs indicate the vapour cavities over the hydrofoil; good agreement among the computational and experimental results is found for the ascending phase. At 14.8^o descending, the referenced computational vapour field features two intense large well organised cavities over the hydrofoil towards and adjacent to the trailing edge, visible in frame 3.26g; these cavities are in the same position as two large counter-rotating vortices, one originated from the leading edge and one generated on the trailing edge *(Trailing Edge Vortex - TEV)*. On the contrary, the current computations predict different vorticity field and therefore smaller cavities, as seen in frame 3.26h; although the TEV is captured, it is not grown as in the referenced figures and the vortical field over the hydrofoil is shattered and features small elongated structures, separated from the solid wall and filled with vapour. These discrepancies could be attributed to the coarser grid used in the current IB calculations. Finally, on later stages of the descending phase, the referenced flow field is smoother than the result of the current simulations.

(a) $5.5^{o(+)}$ Huang   **(b)** $5.5^{o(+)}$ IB

(c) $9^{o(+)}$ Huang   **(d)** $9^{o(+)}$ IB

(e) $14.6^{o(+)}$ Huang   **(f)** $14.6^{o(+)}$ IB

(g) $14.8^{o(-)}$ Huang   **(h)** $14.8^{o(-)}$ IB

(i) $5^{o(-)}$ Huang   **(j)** $5^{o(-)}$ IB
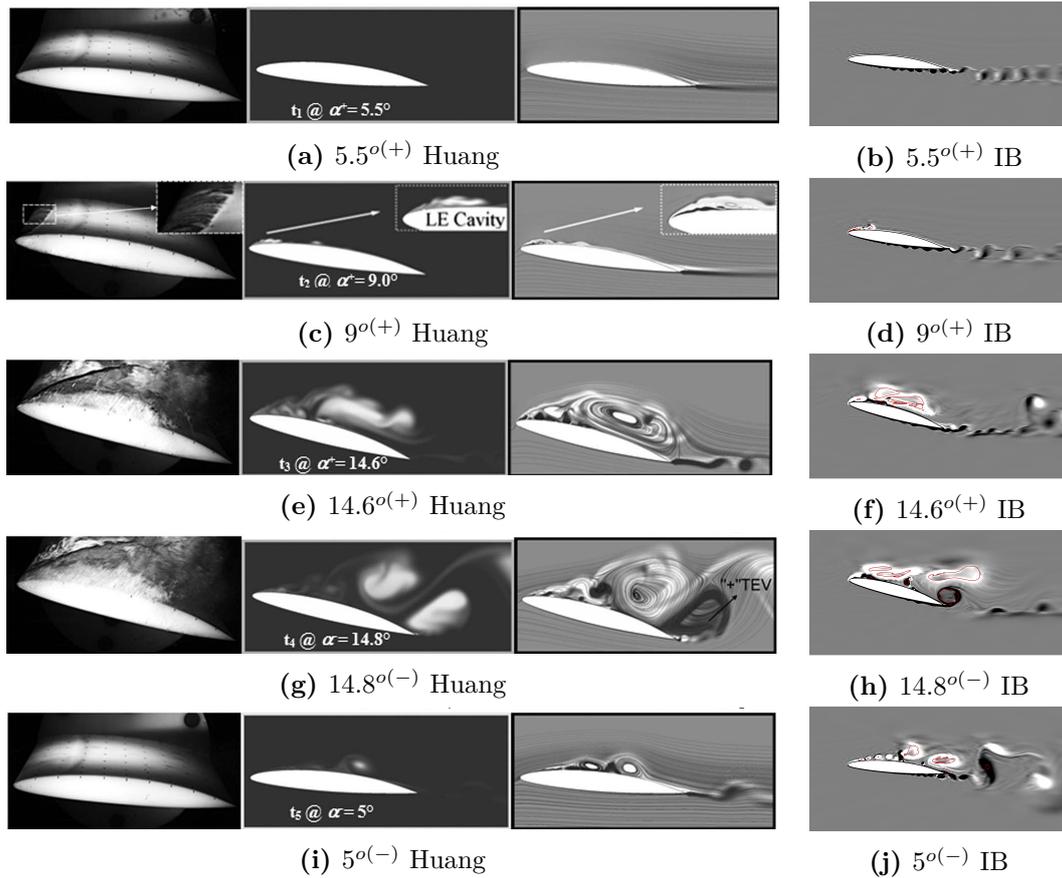
Figure 3.26: Vorticity field and vapour volume fraction for pitching NACA0066 calculated by the current IB methodology (right), compared against computational plots and experimental photographs of Huang et al. [97] (left). For the referenced figures of [97], experimental photographs, vapour volume fraction and vorticity field are presented from left to right respectively. On the numerical results of IB simulations (right column), the vapour volume fraction is represented by means of 50% iso-contour by the red line. On the referenced figure, the vapour volume fraction is presented on gray scale, with values ranging from 0 (black) to 0.8 (white), while vorticity is presented on reverse gray scale, from -500 (white) to $+500$ (black).

3.3   Concluding Remarks

A thorough validation of the herein proposed Immersed Boundary Method is presented, for a wide range of benchmark or well documented test cases extracted from the literature. The reason for this meticulous assessment of the tool over different flow regimes, is that each case tests a different aspect of the method.

The method is designed to address problems of caviting flows, with moving boundaries, for applications of micro and engineering scales. The complexity of the test cases increases from incompressible laminar flows, to incompressible turbulent and finally to highly compressible cavitating flows.

For the incompressible cases, excellent agreement is found between the current computations and the literature; first the flow over a stationary cylinder is simulated, then oscillating cylinders are considered, initially in stationary fluid and then in free stream. Then the incompressible

turbulent flow over a back-facing step, modelled as immersed boundary, is solved; the simple configuration of this case, which does not include moving solids, makes it easy to carry out conformal grid simulations as well. Thus, the IB results are compared against conformal grid as well as experimental data from literature and found in good agreement.

Finally, cavitating cases are tackled. Initially the cavitation induction for a moving cross in stationary water is computed. The results of the current method are compared to results of simulations with conformal grid employing sliding interfaces to accommodate the rotation, as well as cut-cell IB simulations from literature; the performance of the method is judged satisfactory. Then, the highly tubrulent cavitating flow over a stationary hydrofoil is addressed and time-averaged sampled velocity profiles are compared to experimental measurement from the literature and found in good agreement.

At the end, the complicated turbulent cavitating flow over a pitching hydrofoil is solved. The complexity of this case arises from the high Reynolds number and the pitching motion, which leads to laminar to tubrulent transition over the hydrofoil at a certain point during the computation. The results are compared against partial experimental and thorough conformal-grid computational results from literature; the physics of the problem is captured, however some limitations of the method are highlighted. The current simulations were unable to reach the level of spatial discretisation of the conformal-grid simulations, thus let the turbulence models accurately capture the boundary layer dynamics. Moreover, force coefficients exhibit strong oscillations, although they follow closely the referenced data. Better spatial resolution could improve the results. Achieving resolution of $y^+ = 1$ over a moving immersed boundary is computationally inefficient with homogeneous Cartesian grids, as very small cells should cover a wide area. To alleviate this drawback automatic mesh refinement could be used over the moving IB interface, which is not considered herein. The implicit treatment of the source term would be also beneficial. It is worth mentioning that the referenced computations employ automatic remeshing of the complete computational domain in each time-step; the IB methodology proposed herein tries to become an alternative to such computationally expensive strategies.

Chapter 4

Computational Study of Three-Phase Flow: Projectile Impact on Water Jet

Contents

Following the validation of the method presented in the previous chapter, the proposed Immersed Boundary method is applied on a challenging multiphase flow computation. The IB method is coupled with a two-phase flow compressible flow to study the high-velocity impact of a solid projectile on a flowing water column and investigate the shock-wave formation, structures and the cavitation induction. This case has been recently studied only experimentally by Field et al. [65]. The numerical simulation of this impact case poses significant challenges regarding the motion of the solid body, as well as the complex interface phenomena. Conventional deformable grid techniques could not accommodate the large displacement of the immersed solid boundary and re-meshing strategies seem not suitable for the high-velocity motion as they would be computationally very expensive. The use of IB method tackles this issue and makes it possible to model the moving body on a relatively simple stationary grid and study computationally the dynamics of this high-velocity solid-to-liquid impact.

The work presented on this chapter has resulted in a publication of Stavropoulos- Vasilakis E. et al. [231].

4.1 Scope of the Study

Wave interaction with material interfaces may regard physical problems of wave reflection on solid or liquid-gas interfaces, as well as shock dynamics resulting from liquid-to-solid or liquid-to-liquid impacts.

Such interactions have a wide range of applications of industrial [2, 58, 65, 91, 110, 115, 122] and medical or bioengineering [94, 96, 121, 143, 161, 162, 241] interest; they may refer to underwater explosions, laser-generated bubbles' dynamics, cavitation erosion of mechanical structures or machines and non-invasive medical procedures such as HIFU or injuries and head concussion accidents.

The solid understanding of the interaction of shock-waves with liquid-gas interfaces in fast-slow configurations (i.e. shock initially travelling in a liquid), has been established through computational studies, assisted by experiments such as those reported by Grove et Menikoff [84] and Nourgaliev et al. [160]. These studies demonstrate that compression waves are always reflected as expansion waves upon impacting the interface [160], which may lead to cavitation formation. The link between the reflected wave type and the acoustic impedance ratio is clearly illustrated by Davison [48], in the form of two asymptotic scenarios. According to this study, the first scenario involves a wave travelling in a material and interacting with a perfectly rigid wall (infinite acoustic impedance); in that case the wave is reflected back at the same amplitude. The second case involves interaction of the wave with perfect vacuum (acoustic impedance of zero); in that case the wave is reflected back with opposite amplitude.

In addition, many experimental works have extensively studied the mechanisms and the dynamics of liquid-to-liquids impacts [23, 163] or liquid-to-solid impacts [8, 24, 25, 30, 64, 66], have unveiled the phenomena taking place and highlighted cavitation induction, growth and collapse due to pressure waves, which in turn leads to erosion development. A comprehensive summary of the experimental findings on liquid to liquid or solid impacts can been found in the work of Field et al. [65]; the study, highlights the complicated wave structures interacting with free-surfaces and the potential of cavitation erosion development.

The theoretical study of LeVeque [125], has analytically examined the liquid drop impacts on solid surfaces, while the experiments reported of Field et al. [65] for liquid droplets impacting on a solid surface, reveal the strong effects of compressibility that occur locally in the liquid bulk near the impact region. A peak in pressure can be observed and a complicated shock wave structure develops, while high-speed jetting may occur at the impact location; at the same time, rarefaction waves form that may create enough tensile stress to induce cavitation within the liquid. The high-speed jetting characteristics have been investigated experimentally by Thoroddsen et al. [222] using free-falling spheres that impact on a liquid pool; the authors tried to link the Reynolds number with the jets' velocity and the shape of the lamella formed during splashing. Fractures of solid surfaces by liquid or solid impacts and shock-waves have been studied by Bowden et al [25].

On the modelling side, droplet impact on solid surfaces has been investigated numerically by many researchers using various numerical algorithms to account for the different phases, such as marker-and-cell (MAC) finite differences [87], front tracking approach [86], Volume of Fluid [89], multicomponent Euler solver [193] or two-fluid model for Euler equations [159], to name a few. Sanada et al. [193] studied the impact of a liquid droplet on a solid surface, the shock-wave structures, interfaces dynamics and jetting as well as solid surface compliance. Harvie et al [89] modelled the drop impact on hot solid surfaces, focusing both on dynamics of

the impact as well as the heat transfer. Haller et al. [86] presented a detailed numerical work on shock-wave formation upon the impact of a droplet on rigid wall, where the complex shock structure of the multiple overlapping waves that interact with the free surface and the moving contact line between the wall and the droplet have been unveiled. Moreover, the investigation of Obreschkow et al. [164] has focused on the shock confinement inside isolated liquid volumes and proposed a new model for erosion based on cavitation caused by trapped shocks. However, cavitation is not modelled in the aforementioned works, although the potential vapour regions may be identified as in the work of Niu et Wang [159] Cavitation induction during droplet impact on wall is studied by the author's research group in the work of Kyriazis et al. [157], where numerical results are compared to experimental findings from literature and found in good agreement.

Despite the importance of the underlying physical phenomena, from the above literature is concluded that limited information exists on quantifying the phenomena following liquid-to-solid impact that lead to cavitation, while there are no studies so far that simulate the combined motion of impinging solid objects onto liquids together with the induced cavitation.

The herein presented study aims to fill this gap in the existing literature. More specifically, it focuses on the simulation of a high-velocity impact of a solid projectile on a water-jet and investigates the shock-wave formation, structures and the cavitation induction. The experiment under consideration refers to an impact where the water target is wider than the solid surface. This comes to a contrast with the usual liquid-to-solid impact configuration, which is comprised by a small water droplet and a very wide solid wall, studied by numerous researchers [64, 65, 193, 257]. This difference in the blockage of the flow is expected to affect greatly the physics of the impact, as the water target being wider than the projectile, lets more room to the liquid to expand. Thoroddsen et al. [222] studied experimentally impacts with low-blockage ratio, where a solid sphere drops into a liquid pool, focused on the relationship of the impact jetting with Reynolds number and observed differences with high-blockage cases of drop impacts on wall [64,125]. Field, Lesser et Dear [64] and Lesser [125] studied impacts at lower velocities and did not investigated cavitation initiation or shock structures. The current study tries to shed light in low-blockage impact phenomena at high velocities and assess similarities to the high-blockage impacts regarding shock, vapour and jetting structures. Moreover, the case examined herein has been studied only experimentally [65] until now and the relevant simulations are presented herein for the first time.

A three-dimensional computational study is performed and numerical data are extracted that are qualitatively compared to the experimental observations, but also provide a more detailed insight on the vapour generation, growth and collapse upon the impact. In addition, a series of two-dimensional simulations is performed to investigate the shock and rarefaction waves structures, along with the high-speed jetting, in more detail, as well as to assess the influence of the flow blockage.

4.2   Test case description

4.2.1   3-D configuration

Both 3-D and 2-D cases have been simulated. The 3-D test case simulated can be seen in Figure 4.1. A projectile, with a diameter of 9 mm is traveling at a speed of 210m/s towards

the still water-jet target of 25 mm diameter; the water falls vertically down under the influence of gravity, at a velocity of approximately 1m/s. The computational domain is chosen to be a cylinder with $4 \times D_{jet}$ diameter and $3.6 \times D_{jet}$ height, where D_{jet} the diameter of the water-jet (figure 4.1a). The domain is discretised with 128 equally spaced cells along the jet diameter (figure 4.1b). The same cell width is maintained in the vicinity of the water-jet and then a cell expansion ratio of 1.2 is applied towards the cylindrical far-field. This discretisation results in 2.9 million cells and ensures approximately equal sized cells in the water region, where all the phenomena of interest occur.

(a)   **(b)**
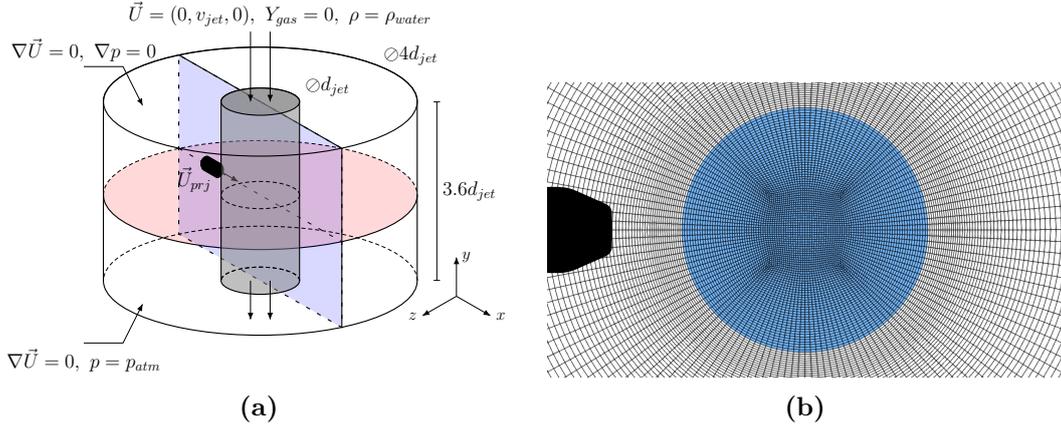
Figure 4.1: The three-dimensional computational domain (a) and the cylindrical mesh on the horizontal section (b), used in the three-dimensional simulation of projectile impact on vertical water-jet. Constant atmospheric pressure boundary condition is assigned on the periphery of the cylindrical domain and Neumann boundary conditions for both pressure and velocity are imposed on the top and bottom patches. Constant velocity, gas mass fraction and density values are placed on the water-jet inlet. The horizontal (red) and vertical (blue) mid-planes, where the results are presented on the following sections, are also shown.

The flowing water-jet is placed in the middle of the domain. The projectile commences to move instantaneously and impacts the jet after approximately 34 μs. A non-dimensional time scale is introduced, using the diameter of the jet $D_{jet} = 25\ mm$ and the speed of sound in the liquid $C_{water} = 1482.35\ m/s$, with respect to the time of impact: $\bar{\tau} = (t - t_{impact}) \cdot C_{water}/D_{jet}$.

The ambient air is initially stationary. The pressure of the domain is considered equal to 1 bar and the reference temperature set to 300 K. The Mach number with respect to the surrounding air is 0.6 and with respect to the impacted water 0.14.

4.2.2 2-D configurations

Since the resolution required for a full 3-D simulation limits the model predictions to scales that do not allow high resolution of the liquid-gas interface in affordable CPU times, two-dimensional simulations have been also performed. In these cases, the projectile is impacting a static water planar section of the jet. This set-up corresponds to the horizontal symmetry plane of the projectile of the three-dimensional set-up. A rectangular area $6.4D_{jet} \times 3.6D_{jet}$ is chosen as the computational domain, where D_{jet} is the jet diameter.

A grid dependence study has been performed to assess the dependence of the simulation on the spatial discretisation. The domain is initially discretised by 160×90 cells, resulting in

a constant complete hexahedral grid with 1 *mm* cell edge size.

Four grids are created, using telescopic box refinement in a region around the jet. First, a mesh with 2 levels of refinement *(2lvl)* is used, resulting in a canonical mesh with cells of 0.25 *mm* edge size near the jet, corresponding to 100 cells on the jet diameter and 36 on the projectile diameter. This mesh has a resolution equivalent to the mesh used in the three-dimensioned set-up. Then, three finer grids are developed, one with 3 levels of refinement *(3lvl)*, yielding 200 cells on jet diameter, one with 4 levels of refinement *(4lvl)*, yielding 400 cells on jet diameter and finally one with 5 levels of refinement *(5lvl)*, yielding 800 cells on jet diameter and a cell edge of 0.03125 *mm*.

The jet is placed in the center of the domain. The water-jet and the surrounding air are initially at rest and the pressure is 1 *bar*. At the beginning of simulation, the bullet starts instantaneously to travel from left to right, at 210 *m/s*, and hits the jet after approximately 34 *μs*.

4.2.3   Numerical Tool

The herein proposed forcing IB method is coupled with an explicit density-based in-house compressible multiphase solver developed in the author's research group by Kyriazis et al. [157].

The solver accounts for a gaseous phase and a liquid-vapour mixture, where the gas is considered as non-condensable and immiscible media, whereas phase-change is considered between the liquid and vapour phases by utilising a barotropic model. It follows a density-based approach, since cavitating flows have a large variation over the speed of sound, with a Mach number ranging from 1 up to 100 (in the liquid/vapour mixture region) [26, 69].

Whereas more common pressure-based solvers can handle such flows, the large variability in the speed of sound in the transition from liquid to liquid/vapour mixture make convergence difficult, since the speed of sound is used for the density correction corresponding to the pressure correction. Thus, the proposed density-based methodology offers robustness and fast, explicit time marching. Moreover, a hybrid numerical flux is proposed that makes the solver suitable for a wide range of Mach numbers, even low-Mach flows where usually the density-based yield issues. It is highlighted that such solvers are not available in the open literature, since multiphase flows are commonly treated with pressure-based methodologies.

The solver is aimed to be used on problems where surface tension does not play an important role compared to inertial or compressibility phenomena, such as high-speed solid-to-liquid impacts studied here. Therefore, surface tension is neglected.

4.3   Numerical Results

In this section, the numerical results obtained are presented. These are divided into two groups. Initially, 3-D results are presented, followed by high resolution 2-D simulations allowing to capture scales that cannot be resolved in 3-D.

4.3.1   3-D Simulations

In figure 4.2 pressure and vapour structures evolution upon the impact are presented for the 3-D simulation, and then in figure 4.3 the numerical Schlieren [200] is compared against the

experimental shadowgraphy images in different time-steps and is accompanied by the respective velocity and pressure fields. The numerical results are plotted on the vertical and horizontal middle-planes, annotated in figure 4.1.

When the projectile impacts the water-jet, a shock-wave is released that starts to travel inside the water volume and to expand radially away from the impact point. When the shock reaches and interacts with the deforming interface, it gets reflected as a rarefaction (4.2a), which is in accordance with the observations of numerous studies [84, 96, 160, 164]. This rarefaction interacts with the shock front, weakens it near the interface and finally splits the high-pressure envelope in two parts (4.2b), one attached on the solid front and another that propagates towards the opposite free-surface. This shock reflection pattern appears to be similar to the *anomalous reflection* [84, 96, 160].

While the initial shock travels along the convex interface, the incidence angle between the shock front and the interface changes continuously and after a specific point, the reflected rarefactions become more intense and pressure values fall under the saturation threshold and vapour is formed on the periphery of the jet (4.2b). As the expansion waves cover the region next to the opposite to the entry point free-surface, the cavity expands mainly vertically (4.2c) and then collapses, emitting pressure waves that travel in the water volume and get reflected on the front free-surface of the jet, again as expansion waves that produce new small vapour cavities (4.2d).

In figure 4.3n it can be seen that the two initially symmetrical vapour cavities, visible in figure 4.2b, expand mainly on the periphery of the water-jet, following the rarefaction waves, and concentrate in the *catacaustic* region [164] into one main cavity. The main cavity expands vertically and shrinks horizontally (4.3o) and finally breaks up into two cavities (4.3p), which then collapse and vanish.

These results are in qualitative agreement with the experimental data of Field et al. [65], where the reflection of the initial impact shock-wave on the free-surface of the jet, creates multiple vapour cavities that act as reflective surfaces for upcoming waves. Comparison between the side view experimental shadowgraphy images and the magnitude of the density's gradient from the simulation, plotted on the vertical and horizontal middle plane (figure 4.3), indicates that the shock and the cavitation regions (dark regions in experiments and blue iso-surface on simulations) are predicted correctly, as well as the bulk dynamics of the deformation of the free-surface.

In the work of Obreschkow et al. [164] on cavitation induction by confined shocks in spherical droplets, the region of higher cavitation bubble density was identified as the *catacaustic* region of shock reflection concentration, near the opposite free-surface. The current numerical results agree with this observation (4.3n); however, cavitation appears near the opposite free-surface as a later stage of the vapour growth, which is initiated symmetrically on the periphery of the jet (4.2b). In addition, the vapour cavities do not form or collapse in great proximity to the solid surface, as reported in the experimental data of Field et al. [65] or suggested for impacts of velocities higher than $100 \ m/s$ by Obreschkow et al. [164].

The main characteristics of liquid-to-solid impacts, have been identified by numerous studies [64, 65, 86, 125, 193], and include high-speed jetting, strong shock-waves, with pressures exceeding *water-hammer* value, generation and reflection upon interaction with free-surfaces, rarefactions and potential cavitation induction. Most of these studies regard either spherical or planar droplet impact on solid wall.

(a) $\bar{\tau} = 0.77$ **(b)** $\bar{\tau} = 1.01$ **(c)** $\bar{\tau} = 2.43$ **(d)** $\bar{\tau} = 5.81$
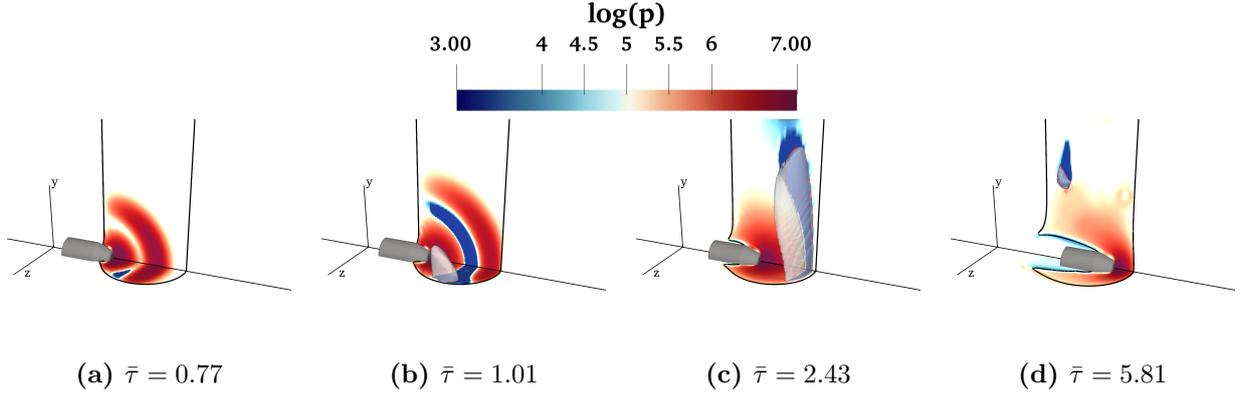
Figure 4.2: Pressure contours in logarithmic scale, *(common logarithm $log_{10}(\cdot)$)*, and vapour volume fraction iso-surface of 0.1% in different time steps are presented for projectile impact on water-jet, at $U_{prj} = 210\ m/s$. 50% iso-line for liquid volume fraction is plotted with black on the vertical and horizontal middle-plane, along with the 0.1% vapour volume fraction with red.

The experiment of Field et al. [65] with the projectile impact on the water-jet tries to expand the knowledge basis of liquid-to-solid impacts on cases of higher velocities. However, the qualitative differences are apparent, as in this case, a projectile of 9 *mm* diameter is impacting a water-jet of 25 *mm* diameter and can be fully immersed in to the water volume. Because the solid can be completely immersed in to the water the shock-wave would propagate radially from the solid front, while in the case of a droplet hitting an *infinite wall*, a broader wave front would be generated. Moreover, the contact-edge dynamics would be different as the liquid would have less room to expand in the latter case.

4.3.2   2-D Simulations

Although the numerical results presented in the previous section are in agreement with the experimental findings and provide a qualitative insight, the mesh used was not dense enough to capture the detailed jetting phenomena and to provide sharp description of the shocks. Two-dimensional computations were carried out and are presented in this section; this gives the opportunity to achieve high spatial resolution that is computationally impossible to reach with three-dimensional simulations. Moreover, the projectile impact simulation is compared to a case where an infinite flat wall impacts on the water-jet, in order to assess the influence of the corresponding flow blockage which in turn affects the shock-wave emission.

Figure 4.4 presents the velocity, pressure and density gradient contours, for the four different 2-D grids, at $\bar{\tau} = 1.60$, along with the 50% iso-lines of gas mass and volume fraction, indicating the interface between the water-jet and the ambient air, and the 0.1% isoline of vapour volume fraction, indicating the cavitation region. These results can be compared against results on the vertical mid-plane of the 3-D simulation, as seen in figure 4.2 and 4.3i-4.3p.

The results obtained for the 2-D cases show similar pressure and vapour structures to the three-dimensional configuration. Following the impact, a high-pressure envelope is detached from the contact region and moves towards the opposite free surface. Two low-pressure regions form near the interface of the jet, due to shock reflection as rarefaction, vapour cavities are induced that expand mainly along the periphery of the jet following the reflections and concentrate in the *catacaustic* region [164].
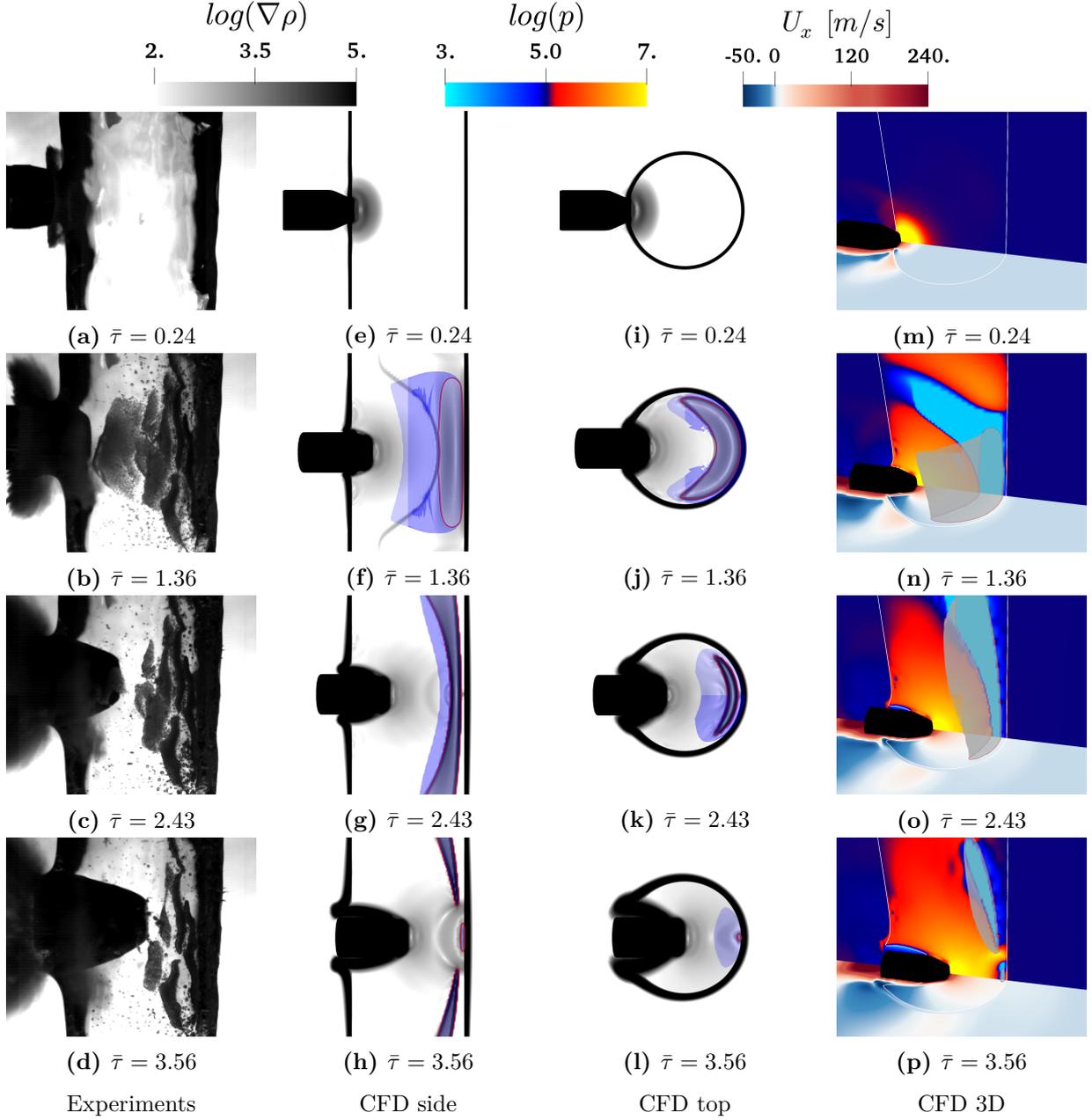
Figure 4.3: Experimental data (a-d) and numerical results (e-p) for the impact of projectile on water-jet, with $U_{prj} = 210 \, m/s$. For the CFD results, the numerical Schlieren [200], computed as the logarithm of the gradient of density, is plotted on the side (e-h) and top (i-l) middle-plane on grey-scale and pressure (vertical plane) and longitudinal velocity component (horizontal plane) contours on the same middle planes (m-p). The vapour is represented by the 0.1% of volume fraction contours, with the blue iso-surface and red iso-lines on the planes on frames (e-l), and the grey iso-surface on frames (m-p). The common logarithm $log_{10}(\cdot)$ is used in for the density and pressure fields.

However, in these cases, due to the higher grid density, high-speed jets are easily captured along the solid surface at the entry point. The water, following the violent compression upon the impact, jets out parallel to the solid surface with velocities even 16 times greater than

the impact velocity (for the finest grid used), reaching Mach 2.2 with regards to the sonic velocity of the liquid. This is closer to what is observed in experiments on similar impacts [64] and although jetting has been reported in the experiment [65], it was not captured by the three-dimensional simulation.

Comparison of the velocity, pressure and density gradient contours for the four different grids, in figure 4.4, shows clearly that higher spatial resolution enhances jetting capturing, as well as sharpens the shocks. Moreover, from figure 4.5, where the instantaneous maximum values of pressure and velocity magnitude, as well as the vapour volume evolution are plotted, it is evident that pressure values converge with mesh refinement, in contrast with velocity and vapour volume. The higher spacial resolution, finer details of the flow are captured and that is depicted on the diagrams of velocity and vapour.

Refining the computational grid enables to capture finer details of the flow that have strong transient nature, such as the high-speed jetting initiation upon the impact. The coarser grid do not capture the jetting at all, as seen in frame 4.4a, whereas with additional refinement the jetting becomes first visible (4.4b), and then less diffused and stronger, as seen in frames 4.4c and 4.4d. Moreover, figure 4.5b, where the maximum velocity magnitude time evolution is plotted for the four grids, shows that for the two finer grids *(4lvl, 5lvl)* supersonic velocities with respect to the liquid are captured, which correspond to the high-speed jets.

Moreover, although mesh density affects the vapour formation intensity, as seen in 4.5c, similar structure is captured by all grids, with the vapour cavity to be initiated on the periphery and finally concentrate on the *catacaustic* region [164]. In contrast, although pressure maxima seem uninfluenced by the mesh refinement, a sharper and more detailed description of the shocks is provided by the denser meshes (*4lvl* in 4.4c, *5lvl* in 4.4d), including pressure waves related to the jets that where absent in the coarsest grid simulation (*2lvl*, 4.4a).

4.3.3 Richtmyer-Meshkov Instability

In addition to the induced shock structures, flow patterns and vapour formation, in the results of the finest mesh *(5lvl)*, some perturbations are observed on the liquid-gas interface, that may be related to Richtmyer-Meshkov instability [27].

Richtmyer-Meshkov instability *(RMI)* arises when a shock-wave accelerates impulsively a density interface. It manifests itself with the formation of wave structures that grow over time, forming mushroom-like protrusions at the interface [27,92]. It mainly concerns a shock-wave impacting on the interface between gases with different densities [39,92,135], but is also observed on liquid-gas interfaces in numerical works [135,192,217] and experiments [197]. The main mechanism of this instability is the misalignment of the density and pressure gradient, as the shock reflects on the interface, that produces baroclinic torque.

The RMI finds various applications in combustion systems and mixing [27], scramjet engines [247], Magnetized Target Fusion [192], as well as dissemination of chemical agents [39].

In figure 4.6, the gradient of the density, along with the vorticity, the baroclinic torque and an estimation of the viscous stresses are presented. This baroclinic torque causes high velocity jetting (figure 4.4d), first near the entry point (figure 4.6a), that then spreads on the entire periphery of the liquid (figure 4.6e) and results in a wavy interface. The dominance of the baroclinic torque in the generation of vorticity and creation of RMI, over the viscous stresses, becomes more clear in frames 4.6c,4.6d,4.6g,4.6h, where it can be seen that these two sources
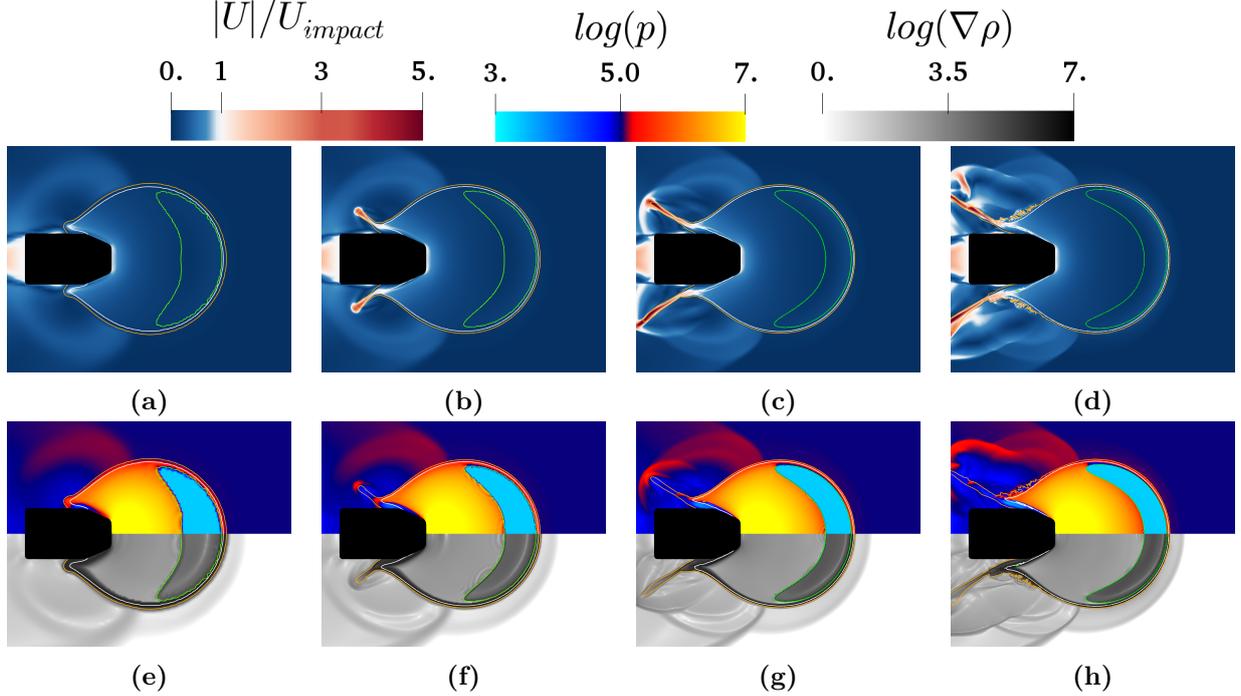
Figure 4.4: Comparison of velocity magnitude (a-d), normalized with the impact velocity $U_{impact} = 210\ m/s$, at $\bar{\tau} = 1.60$, pressure (upper half) and the numerical Schlieren [200] (lower half) contours in logarithmic scale (e-h) *(common logarithm $log_{10}(\cdot)$)*, for solid projectile impact on two-dimensional planar water-jet, for the four different meshes: (a,e) *2lvl - 100 cells/D_{jet}*, (b,f) *3lvl - 200 cells/D_{jet}*, (c,g) *4lvl - 400 cells/D_{jet}*, (d,h) *5lvl - 800 cells/D_{jet}*. The isolines of 50% gas mass fraction is plotted with orange color and 50% gas volume fraction contour with white to represent the interface between ambient air and water-jet. The 0.1% iso-line of vapour volume fraction is visible with green.

of vorticity differ by two orders of magnitude. This fact justifies the option to neglect viscosity in the current simulations as well.

Interface roughness plays a role in RMI initiation, where small perturbations of the interface will cause pressure-density gradient misalignment as the shock passes over and will get amplified leading to mashroom shaped spikes. However, as it has been demonstrated by Saurel et al. [197], RMI can be initiated by a shock passing over a simple curved sharp interface, without perturbations. Similar conclusion can be extracted by the current study, where surface roughness on the water-jet interface, present in the experiment, are not considered and RMI occurs on a sharp circular interface.

4.3.4 Influence of Flow Blockage

In order to assess the influence of flow *blockage* on the pressure peaks and high-speed jetting during the solid to jet impact, a two-dimensional planar simulation of a wall impacting a jet is performed and compared to the projectile impact on the jet. This configuration is closer to the geometries reported relevant studies [64, 65, 193, 257].

Comparing the two two-dimensional planar simulations in figure 4.7, it is apparent that although shock reflection and vapour structures follow similar patterns and jetting is captured in both cases, for the case of the wall, a more homogeneous distribution of higher pressure
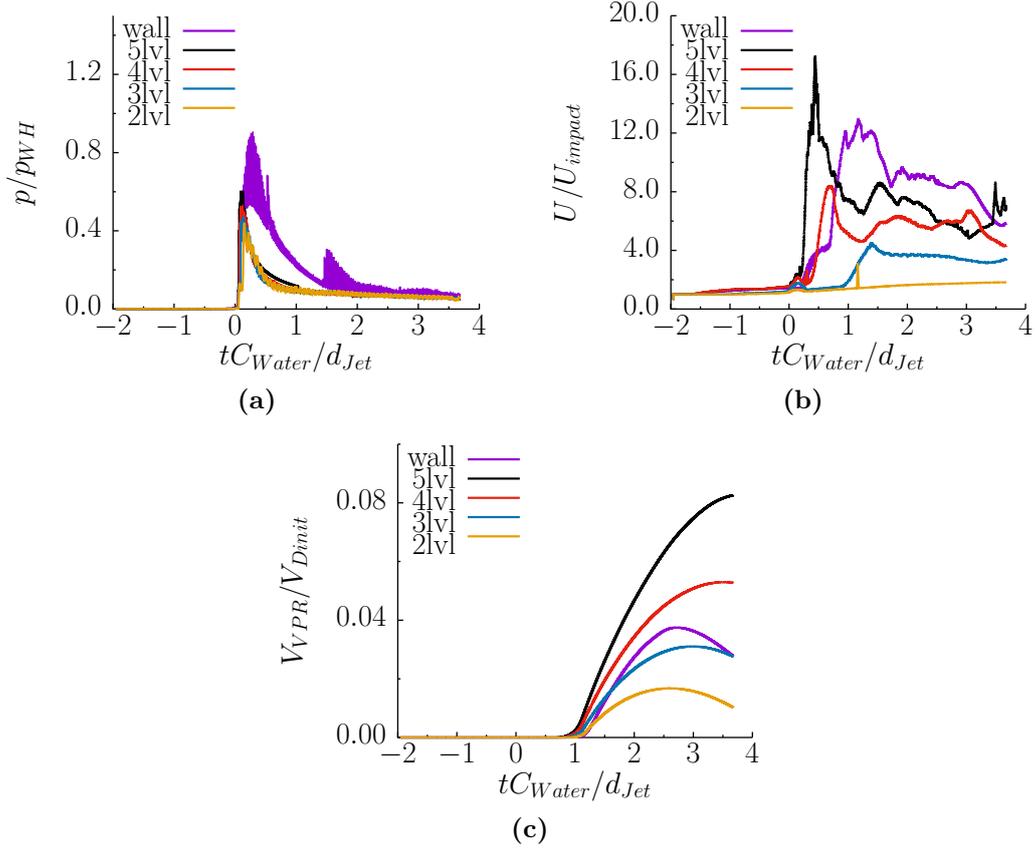
Figure 4.5: Comparison of different 2D meshes for projectile impact on jet: (a) Maximum pressure normalized with water hammer pressure ($P_{WH} = 398.7\ MPa$) (b) Maximum Velocity magnitude normalized with impact velocity $U_{imp} = 210\ m/s$, (c) Vapour Volume (V_{VPR}) normalized with the initial volume of the water-jet (V_{Dinit}). The equivalent results from the wall impact on the jet (using the *4lvl* mesh) are also plotted (purple line) for demonstration of the influence of the *blockage*.

values is reported, and vapour cavities are initiated further from the solid surface. From the diagram 4.5a, it can be seen that instantaneous maximum pressure values are higher for the impacting wall rather than the projectile. The high-speed jetting is initially more intense in the case of the projectile, as it can be seen in 4.7a, 4.7b, 4.7c, but the instantaneous maximum velocity reaches higher values for the case of the wall as seen in graph 4.5b. Finally the vapour production is lower for the impacting wall (4.5c). These observations confirm that higher *blockage*, or wider solid surface, compresses more the liquid and yields higher pressure values and lower *blockage* intensifies the liquid expansion.
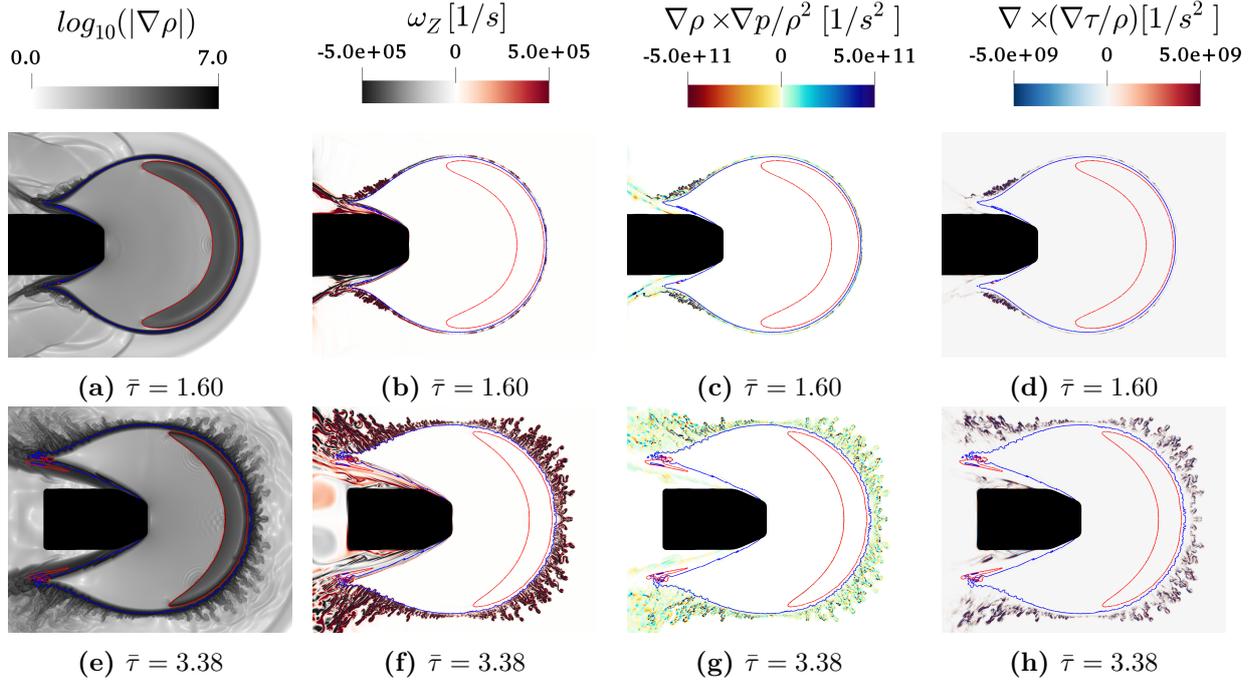
Figure 4.6: Evidence of Richtmyer-Meshkov instability [27] for solid projectile impact on two-dimensional planar water-jet. From left to right: numerical Schlieren [200] contours in logarithmic scale *(common logarithm $log_{10}(\cdot)$)*, vorticity contours (ω_z [1/s]), baroclinic torque ($\nabla\rho\times\nabla p/\rho^2$ [1/s²]), viscous shear stresses ($\nabla\times(\nabla\tau/\rho)$ [1/s²]). For the estimation of viscous stresses, which are neglected in the simulation, dynamic viscosity is given by $\mu = (1 - \alpha_{gas}) \cdot \mu_{liquid} + \alpha_{gas} \cdot \mu_{gas}$, based on gas volume fraction, with $\mu_{liquid} = (1 - \alpha_{vapour}) \cdot \mu_{water} + \alpha_{vapour} \cdot \mu_{vapour}$ and $\mu_{water} = 9.99 \times 10^{-4}$ Ns/m^2, $\mu_{vapour} = 9.99 \times 10^{-6}$ Ns/m^2, $\mu_{gas} = 1.84 \times 10^{-5}$ Ns/m^2. Results of the simulation using the *5lvl* mesh *(800 cells/D_{jet})*. The isolines of 50% gas volume fraction contour, which represents the interface between ambient air and water-jet, is plotted with blue and of 0.1% vapour volume fraction with red.
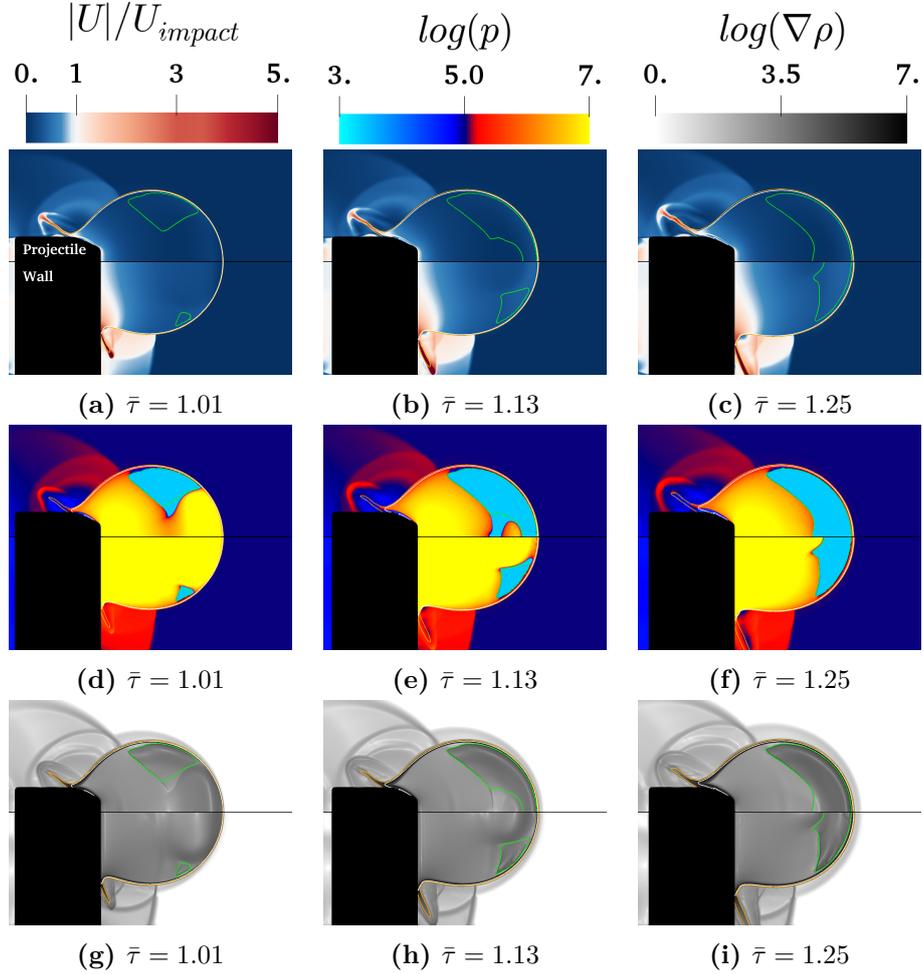
Figure 4.7: Contours of velocity magnitude normalized with the impact velocity $U_{impact} = 210 \, m/s$ (a-c), pressure in logarithmic scale (d-f) and the numerical Schlieren [200] in logarithmic scale (g-i) for solid projectile (upper half) and solid wall (lower half) impact on two-dimensional planar water-jet. The IB body (black region of left) moves from left to right. 50% gas mass fraction is plotted with orange color and 50% gas volume fraction contour with white to represent the interface between ambient air and water-jet. The 0.1% isoline of vapour volume fraction is visible with green. The *4lvl* mesh is used in both cases. The common logarithm $log_{10}(\cdot)$ is used in for the density and pressure fields.

4.4 Concluding Remarks

The herein proposed Immersed Boundary method, enables us to study the high-velocity impact of solid projectile on a flowing water column, so far only qualitatively studied by the experiments of Field et al. [65].

The underlying physical processes of the simulated case was found to be in qualitative agreement with the relevant experimental observations of [65]. Pressure shock-waves, rarefaction waves and cavitation formation, development and subsequent collapse, that follow the impact are numerically captured. A detailed description of the vapour cavity was provided that was in accordance with the analysis of the experimental data. High-speed jetting was also observed in the simulations, although was found highly dependent on the grid resolution of the jet interface, near the impact region, and therefore was captured on the two-dimensional simulations, where the use of denser meshes was less CPU time demanding.

The influence of flow blockage on the dynamics of the impact was assessed by comparing the case of the projectile to the case of a wall hitting the water target. The study showed that in the case of the projectile, where the liquid is free to expand in the direction of the projectile motion, the pressure and velocity peaks during the initial stage of the impact reach lower values than in the case of the wall; in this case, the flow was found to decelerate faster, whereas the vapour production was higher for the projectile case.

Finally, the importance of the use of the IB method is illustrated by the fact that the numerical simulation of this case with conventional (deformable or adaptive) boundary-conformal mesh techniques would be extremely complex and computationally expensive. This is apparent from the level of detail unveiled in the two-dimensional simulations in comparison with the three-dimensional one. Such fine spatial resolution, in conjunction with re-generation or deformation of the mesh in every time-step, would be almost impossible to achieve because the computational cost would be prohibiting.

Chapter 5

Computational Studies of Biological Flows

Contents

This chapter is dedicated to flows of bio-engineering interest. More precisely, the pulsatile incompressible flow through a model aorta with a 180° bend and arterial branches on the apex is studied, with special focus on the developed wall shear stresses. A preliminary investigation of the flow through a configuration without the Valsalva sinuses and without the a heart valve is first carried out, to collect detailed information on the flow patterns and the on shear stresses developed by the pulsatile flow. This preliminary study is supported by experimental findings, provided by Mrs. Li and Prof. Bruecker of CITY, University of London. Then the developed Immersed Boundary method is employed to simulate the flow through a bi-leaflet Mechanical Heart Valve, in a configuration with the Valsalva sinuses.

Part of the work presented in the first section of this chapter, has been prepared for publication as a joint work of numerical computations and experimental campaign of Li Q., Stavropoulos- Vasilakis E. et al. (see Appendix F).

5.1 Scope of the Study

The field of CFD which specialises on blood flows, can be referred to as Computational Hemo-dynamics *(CHD)* [226]. Studies of blood flows may prove challenging, as they are of *pulstatile* nature, due to the cardiac pulses, are characterised by moderate Reynolds numbers, and involve complex domains with non-smooth, and usually elastic, boundaries. CHD may be used to research blood vessel diseases or investigate the influence of prosthetic medical devices and aid in design or surgery.

Numerous studies have examined the flow through Mechanical Heart Valves *(MHV)*, utilising IB approach [17–19, 21, 45, 47, 49, 71, 72, 228, 245]. Dasi et al. [47] analysed the vorticity structures of the flow through a bi-leaflet MHV and Ge et al. [71] evaluated the importance of Reynolds and Viscous forces in this flow; the numerical studies were assisted by experiments. Yang et Balaras [245] performed LES computations on the bi-leaflet MHV flow, whereas Borazjani et al. [19] and De Tullio et al. [228] studied the same flow in the context of FSI. Borazjani et al. [20] assessed the validity of using idealised model aortas in simulations, by examining the different patterns developed from the flow through a bi-leaflet MHV placed in an idealised straight aorta and in an anatomic aorta model. The influence of the computational domain was pronounced. A similar investigation was carried out by De Tullio et al. [49], with regards to the root geometry; such a study, apart from the academic interest, is relevant to a surgical operation called *Bentall procedure*, which replaces not only the valve, but also the *Valsalva sinuses* of the root and the ascending part of the aorta. In addition, Borazjani et al. [17] compared the flow generated by a bi-leaflet MHV against that of a bio-prosthetic heart valve *(BHV)*. Because the geometry of the BHV is by design closer to the natural valve, the flow results in more physiological structures.

Apart from MHV studies, numerical simulations aid in the investigation of the flow through a stenosed blood vessels [7, 146, 173, 245]. Mitall et al. [146] assessed the use of LES or DNS approach for turbulence modelling of the pulsitile blood flow. Papadopoulos et al. [173] performed simulations of flow throw stenosed coronary arteries to asses the risk of development of Coronary Artery Disease *(CAD)* or Acute Coronary Syndromes *(ACS)*; it was demonstrated that computational results can be a valuable input to mathematical models for thrombin generation [172]. It has to be noted that while the blood flow in the circulatory system is driven by pressure pulses, the accurate imposition of boundary conditions in the computational studies is anything but trivial; Grinberg et Karniadakis [83] have developed a method to impose *patient-specific* pressure boundary conditions, based on the impedance of the flow, relying on flow rate and pressure measurements on multiple vessels, which is applicable to full-scale arterial trees.

In the aforementioned studies, the working fluid (blood) was often treated as incompressible Newtonian (viscous) fluid. Normally, blood is a non-Newtonian fluid, therefore its mechanical properties (viscosity) does not depend only on the temperature but is a function of the applied strain as well. However, when the flow through the larger blood vessels is considered, it can be safely assumed to behave as a Newtonian fluid with constant viscosity [227]. This practice is followed in both computational, as well as experimental [28, 128] studies. In particular, when conducting experiments in models mimicking blood vessels and parts of the cardiovascular system, water solutions are used as working fluid, with calibrated properties to match the density and viscosity of blood.

The developed pulsatile flow is characterised by the non-dimensional Womersley number [239], which is calculated as the ratio of inertial and viscous forces, as in relation 5.1, and

expresses the lag between the pressure pulse that generates the flow and the velocity profile. During a pulse generated flow through a pipe, the velocity profile may deviate significantly from the well-known parabolic profile of the *Poiseuille* flow [250]. The flow near the wall and in the centre of the tube are in phase lag depending on the inertia of the fluid. For low Womersley numbers, viscous forces dominate the flow and a parabolic velocity profile develops. For higher values, the inertial forces dominate and the influence of viscosity is limited near the rigid walls; therefore the parabolic velocity profile gets disturbed and flattens towards the core of the pipe.

$$Wn = R \cdot \sqrt{\frac{\omega \rho}{\mu}} = \sqrt{\frac{2\pi f R^2}{\nu}} \tag{5.1}$$

where:

R : a characteristic length for the flow, usually the radius or diameter of the tube

$\omega = 2\pi f$: the angular frequency of the driving pressure pulse

$\nu = \mu/\rho$: the kinematic viscosity of the fluid

The transient nature of the pulsatile flow under consideration, along with the moderate Reynolds, suggests that turbulence is not fully developed throughout the systolic cycle. Rather, turbulence is expected to play an increasingly important role on the second part of the systolic cycle, during the deceleration phase where backward flow develops. The transition to turbulence depends on the driving pulse and it is reported that for Womersley numbers greater than 10, the flow becomes turbulent past the peak systole [214, 225, 244].

For pulsatile arterial flows, which usually reach Reynolds numbers ranging from 600 to 5000, and where the turbulent flow is not fully developed, conventional RANS modelling seems not suitable [146]. Researchers tend to prefer either the laminar approach [226] or the more accurate, yet more computationally demanding, LES [7, 146, 245] or DNS [17–19, 21, 47, 71, 72, 228] approach.

To assess the resolution of spatial and temporal discretisation, with regards to the accurate capturing of the turbulence structures, the *Kolmogorov scales* should be considered. The spatial and temporal Kolmogorov scales are estimated as $\eta_k = (\nu^3/\varepsilon)^{1/4}$ and $\tau_k = \sqrt{\nu/\varepsilon}$ respectively, assuming the dissipation rate is estimated with regards to the peak velocity of the pulsatile flow under examination, $\varepsilon = U_p^3/D_A$.

Different meshing approaches are being used in *CHD*, including hexahedral, tetrahedral or polyhedral grids [226]. The mesh strategy depends mainly on the geometry of the domain, whether it is a physiological artery model, obtained by means of Magnetic Resonance Imaging *(MRI)* or Computerized Tomography *(CT)*, or an idealised cylindrical pipe, and whether it is comprised by a single branch or has bifurcations.

In numerical studies of pulsatile flows through Mechanical Heart Valves (MHV), in idealised straight cylindrical aortas [19, 47, 71, 228] or accurate anatomic domains [17, 20], structured hexahedral curvilinear grids, with mostly equally spaced cells on the azimuthal direction, are used for DNS calculations. This practice results in large homogeneous grids, with few highly skewed cells near the wall [226]. For these grids the cell sizes are close to $3 \sim 4\eta_k$. The numerical data of [47] are directly compared to instantaneous and time-averaged experimental fields and are found in good agreement.

Herein, numerical simulations are carried out, in order to provide a detailed description of the flow inside a model aortic arch, with 180° bend, which includes the triple Valsalva sinuses on the root and three aortic branches on the apex of the turn.

The computational study is assisted by experiments performed by Prof. Bruecker and Mrs. Li, of CITY, University of London. Their experimental campaigns focus on the influence of the flow through MHV on the wall shear stress distributions on the aorta wall. In their recent publication [128], they implemented specialised wall shear stress sensors, comprised by flexible micro-pillars of $1mm$ length mounted on the aorta wall, and compared the stress distributions of a bi-leaflet and a novel tri-leaflet MHV. These micro-pillars bend along the flow, and following beam theory the load can be extracted from their deflection; thus the velocity and its gradient can be estimated, which would eventually provide the shear rate.

In the current study, laminar flow simulations have been performed using the incompressible Navier-Stokes equations 2.7, where the stress term $\tilde{\tau}$ 2.8 is calculated and not modelled. This approach is chosen considering the computational cost of the simulations and the discretisation approach followed by aforementioned equivalent numerical works.

First, a preliminary study is performed, where the MHV is not mounted on the aorta arch and the sinus region is covered by a convergent nozzle, to assess various characteristics of the flow and compare numerical wall shear rate estimations to experimental measurements. Then, a simulation with the MHV is performed, where the leaflets and the casing of the valve are modelled with the Immersed Boundary Method proposed herein, in the complete model, that include the sinuses.

Bi-leaflet Mechanical Heart Valve

The flow through bi-leaflet Mechanical Heart Valves (MHV), has been thoroughly investigated by the works of Ge, Dasi, Borazjani et al. [17–20, 22, 47, 71, 72]. An indicative model can be seen in the photograph of frame 5.1a.

Dasi and Ge et al. [47, 71] conducted experiments on the pulsatile flow through a bi-leaflet MHV mounted on a straight aorta, performed supplementary numerical simulations and analysed the induced vortical structures and shear stress distributions. While these computations employed prescribed motion of the leaflet, Borazjani et al. [19] repeated them within the framework of FSI, so that the motion is induced by the pulsatile flow.

Borazjani later extended the work in [19] which referred to bi-leaflet valve mounted on a straight axisymmetric aorta, to investigate the same flow in an *anatomic* aorta-model [20], which includes the Valsalva sinuses and is not axisymmetric, and furthermore to study the influence of the orientation of the valve [22] inside the anatomic model. Finally, they compared a bio-prosthetic heart valve *(BHV)*, composed by three thin, membrane-like, semi-circle shaped leaflets, to the bi-leaflet valve [17]; the study was carried out on the straight aorta of [19], under the same conditions.

All these studies were focused on the shear stresses excessed on the blood; the flow developed through a bi-leaflet valve exhibits non-physiological structures and vorticity patterns unalike those generated by a natural valve. The two leaflets of the MHV open in the center of the flow field, forming three orifices upstream the sinus region, which accelerate the flow, as qualitatively depicted in frame 5.1b. On the contrary, the tri-leaflet bio-prosthetic valve, which resembles more to the geometry of the actual heart valve illustrated in figure 5.1c, results in a flow closer to the physiological, as the leaflets open towards the aorta walls, inside the sinus region,
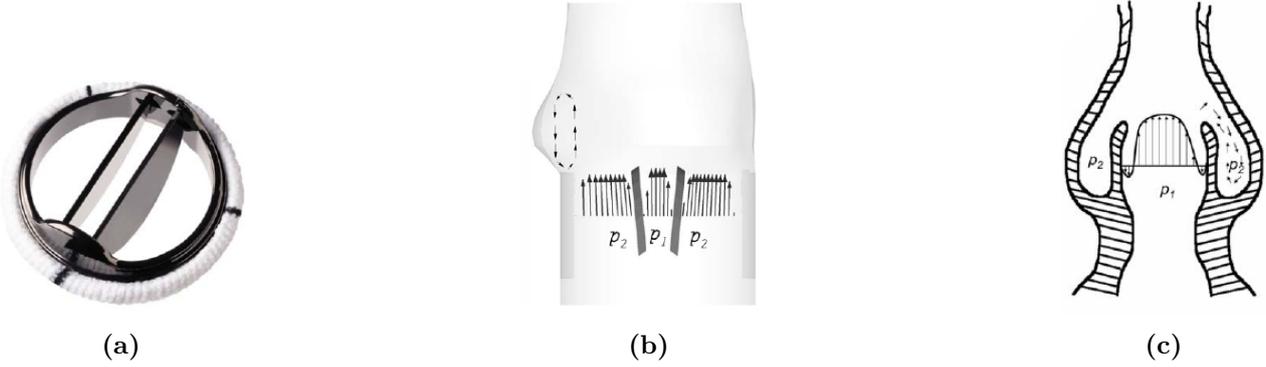
Figure 5.1: Bi-leaflet Mechanical Heart Valve and subsequent induced flow. A photo of a *St. Jude Regent 23mm* bi-leaflet valve is presented on the left and a qualitative representation of the developed velocity profiles through a similar MHV in the middle and a natural on the right. All frames are reproduced from the work of Borazjani et al. [20].

creating a single orifice of similar to the aorta diameter.

As it can be seen in [17], during the opening phase the sinus region is isolated, the vortical structures develop mainly downstream the sinuses and are washed away faster when the BHV fully opens, while for the MHV, the organised large-scale vortical structures, which initiated over the leaflets and the aorta wall into the sinuses, break down into chaotic small structures that may remain in the flow field until the next cycle.

In addition, in [20] it is shown that the cylindrical symmetry of the computational domain is a rather harsh simplification that deviates a lot from the actual physiological case; the anatomic aorta is curved and features an offset from the vertical plane, that highly impact the flow and make it three-dimensional. In the case of the anatomic aorta, the leaflets undergo significant asymmetric motion, rebound when reaching both fully open and fully closed positions, as well as open faster but close slower, after the reversal of the flow, than in the case of the axisymmetric straight aorta. The delayed closure of the valve may have important negative consequences, because if the leaflets are open during reversal of the flow, blood would flow back in to the heart *(regurgitation)*.

However, the late closure of the valve is not related only to the geometry of the aorta model, but is an inherent attribute of the bi-leaflet MHV. Because of the formation of three orifices upstream of the sinus region, visible in frame 5.1b, the pressure difference on the two sides of each leaflets is not high enough to accelerate it away from the equilibrium and close it; rather, is the reversal of the flow that drives the closing motion of the leaflets. This is dissimilar to the operation of the natural valve, which opens inside the sinus region and creates a recirculation area towards the sinus wall, on one side of the valve, while the blood flows through the single large orifice, as seen in frame 5.1c. As a result, the pressure difference on the two sides of the valve during deceleration phase is high enough to close it. Similar dynamics may be developed from the flow through a BHV [17], which opens far inside the Valsalva region and forms a single orifice, while novel designs of tri-leaflet MHV, also featuring a single orifice, close after reversal of the flow [128] as they are not affected by recirculation inside the sinuses.

5.2 Preliminary Investigation of Pulsatile Flow in a Model Aorta

The simulations are performed on an aorta model with identical geometry with the one used in the experiments, during the calibration of the measurement apparatus, which is presented in figure 5.2. There is a difference in the orientation of the computational domain and the experimental test-rig; the coordinate system O_{xyz} of the computational domain correspond to the mirrored coordinate system O_{-xy-z} of the experimental set-up.

The diameter of the aorta is $D_A = 25mm$. A converging inlet nozzle, with initial diameter $D_N = 40mm$, has been placed before the aortic arch, with total length of $L = 6D_N$ and $L_{up} = 4D_N$ before the converging part. Two cylindrical volumes where added at the outlets of the aorta and the arterial branches to facilitate more accurate boundary condition assignment.

The working fluid has the same properties as the glycerine-water solution (58/42% by mass) used in the experiments, with density $\rho = 1140kg/m^3$ and kinematic viscosity $\nu = 4.386 \cdot 10^{-6} m^2/s$. The Reynolds number as estimated using the peak velocity, $U_{peak} = 0.95m/s$, observed during the experiments just after the inlet nozzle, is $Re = U_{peak}D_A/\nu = 5340$. As the flow under consideration is pulsatile, this corresponds to the maximum Reynolds number during the systolic cycle, and the flow considered to be on a transitional turbulent regime.

The spatial and temporal Kolmogorov scales that characterize the pulsatile flow under examination, yield $\eta_k = (\nu^3/\varepsilon)^{1/4} = 39.6\mu m$ and $\tau_k = \sqrt{\nu/\varepsilon} = 0.358ms$ respectively, assuming the dissipation rate is estimated with regards to the peak velocity as $\varepsilon = U_p^3/D_A = 34.295m^2/s^3$. These scales are considered for the spatial and temporal discretisation of the governing equations.

(a)　　　　　　　　(b)
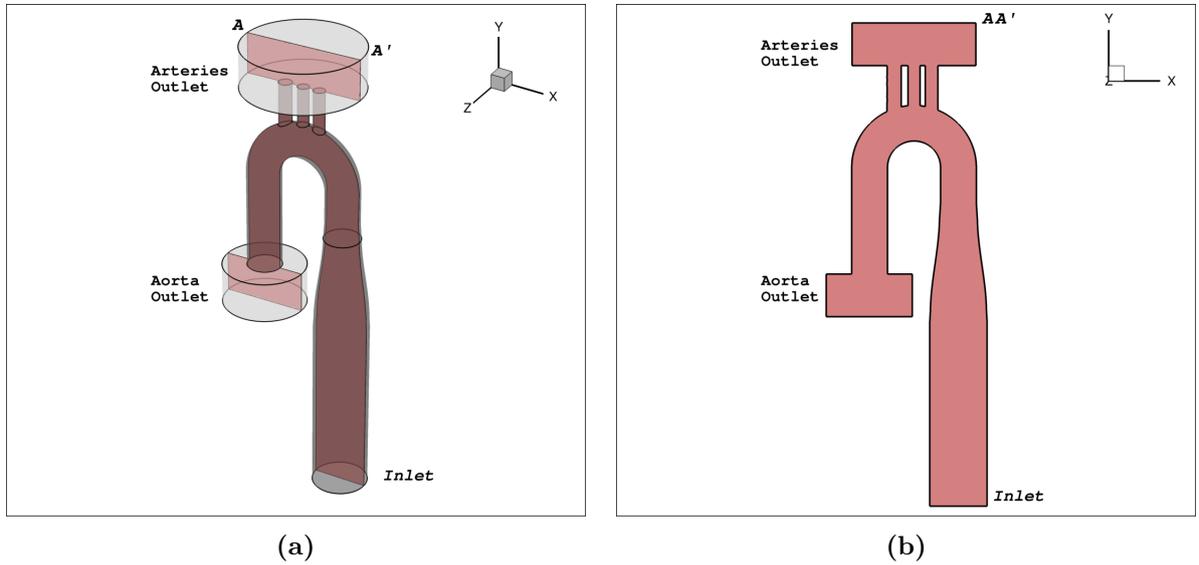
Figure 5.2: The computational domain of the aorta model. The inlet has a total length of $6D_N$ ($4D_N$ before the convergent part) to ensure the flow is fully developed before the aorta bend. Two volumes have been put at the outlet of the aorta and the outlet of the arterial branches. The plane AA' corresponds to the side centre plane. The nozzle has a diameter of $D_N = 40mm$ and the aorta $D_A = 25mm$. It has to be noted that the orientation of the computational domain is the opposite than the experiments.

Shear stress measurements are provided by the micro-pillar sensors on the outer wall of the aorta. Twelve micro-pillars are clammed on the wall, laying on the side centre plane *AA'*, on the bend of the aorta, equally spaced between an angle of 10.5^o and 49°.

5.2.1 Numerical Set-up

At the inlet, the time dependent volumetric flow rate, measured during experiments, visible in figure 5.3, was assigned as boundary condition. The Womersley number of the flow and the amplitude of the pulse are estimated as $Wn = 16$ and $A_p = U_p/U_m = 5$ respectively. These numbers characterise the phase lag between the pulse and the oscillation of the velocity profile, as well as the transition to turbulence, for the pulsatile flow. Studies [214, 225, 244] suggest that transition to turbulence is delayed towards the deceleration phase for $Wn > 10$. Also, analytic expressions of the velocity profile as function of the flow characteristics, expressed by the Womersley number, have been derived by Sexl, Womersley, Uchida, McDonald and Milnor [250].

However, in the present numerical study, the inlet velocity profile has been assigned as uniform block profile along the diameter and the inlet nozzle was given such a length that the flow would be developed before the converging part. By numerical test of the same pulsatile flow on a long straight tube it has been found that after 4 diameters the flow can be safely considered developed.
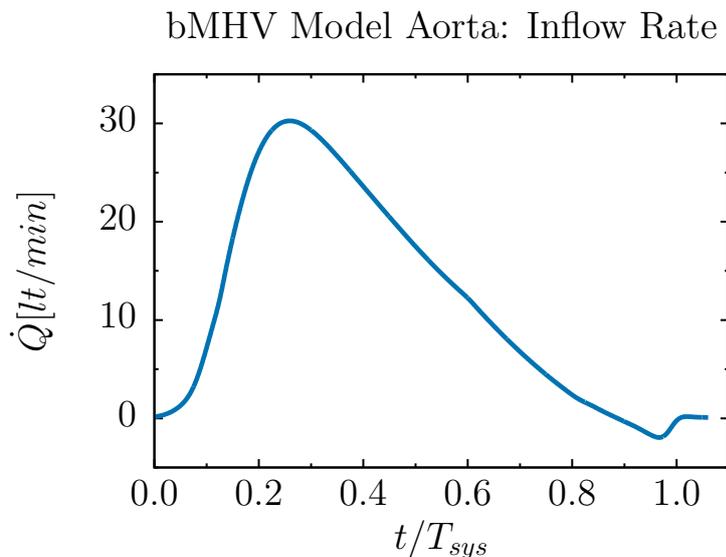
Figure 5.3: The imposed pulsatile inlet flow rate condition, measured during experiments.

On the outlet volumes, zero-gradient velocity and fixed total pressure boundary conditions have been assigned because the precise pressure value is not known at the outlet of the aorta or of the arteries and assigning the ambient pressure on the outlets would constrain the computation algorithm and would not correspond to the actual physics.

Because the domain consists of the aorta, as well as three arterial branches, an unstructured tetrahedral mesh is used, with additional prismatic cells on the wall to better capture the boundary layer.

In order to assess the influence of spatial resolution on the numerical calculations of the pulsatile flow under consideration and on the estimation of the wall shear stress, a mesh independence study has been performed. Three different unstructured tetrahedral meshes, visible in figure 5.4, have been used with total cell count of 2M (coarse), 8.6M (medium) and 11M (fine) cells. Table 5.1 presents the details of the three different meshes.

All meshes have additional prism layers near the wall covering the pillars, which controls better the cell height growth away from the wall and assists in better capturing the boundary layer. For the coarse and medium meshes, 10 layers with first cell height $y_1 = 39\mu m$ and growth factor $\gamma = 1.2$ are used, whereas for the fine mesh 15 layers with $y_1 = 20\mu m$ are used.

An implicit Crank-Nicolson scheme is chosen for the time integration, to ensure the robustness of the computation, and a linear scheme for the spatial interpolation, which is second order accurate central differencing scheme. The time step is automatically adjusted for the maximum calculated Courant number to always respect Courant-Friedrichs-Lewy (CFL) condition $Co_{max} = \Delta t \Sigma_{faces} |\phi_i|/2V \leq 1$, with regards to the magnitude of the fluxes ϕ_i on the faces of the computational cells. Additionally, the maximum time-step is restricted to $0.1ms$ which corresponds approximately to $\tau_k/3$, in order to ensure that all the structures of the flow are resolved.

(a) Coarse   **(b)** Medium   **(c)** Fine

(d) Medium Apex
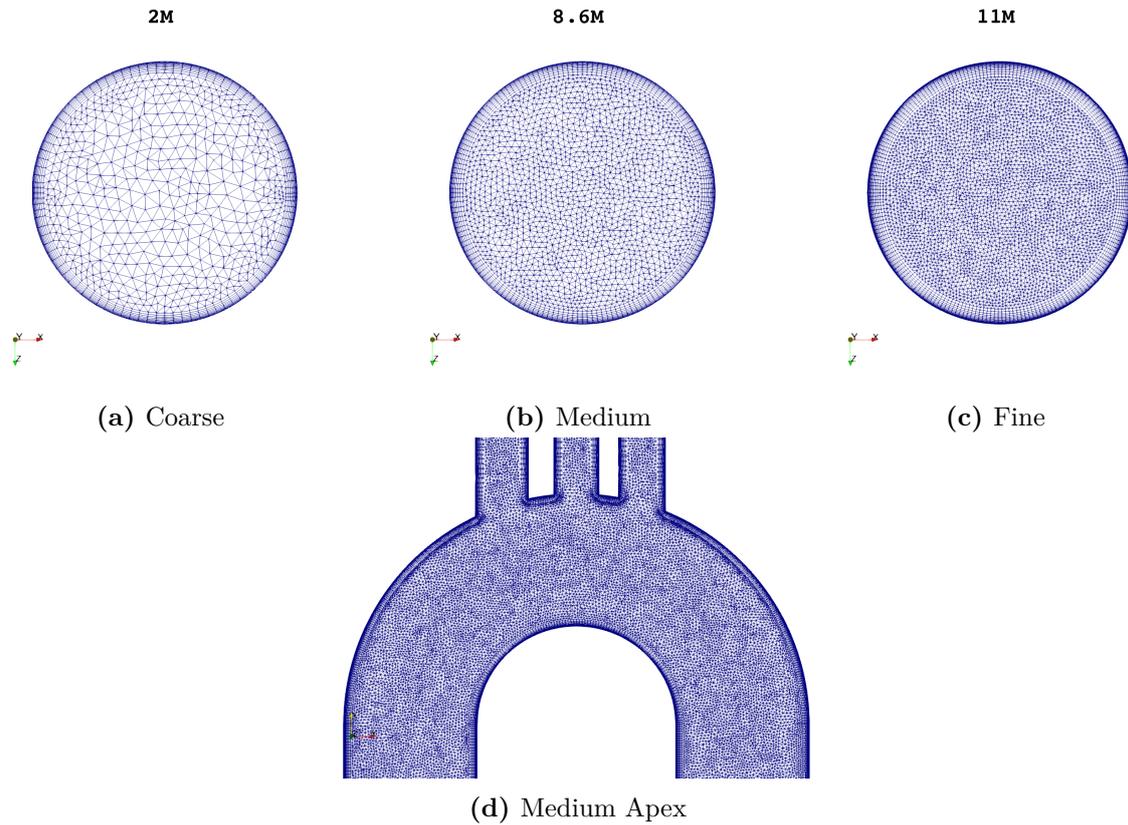
Figure 5.4: A cross-section slice of the mesh on the beginning of the aorta bend ($\theta = 0$), on top, and a detail of the mesh at the apex of the arc on the AA' plane. The three different grids shown are used in the spatial resolution study. All three are unstructured tetrahedral grids, with additional structured hexahedral layers in the near-wall region to better capture the boundary layer of the flow. The coarse grid is composed by 2 million cells, the medium by 9 million cells and the fine by 11 million cells.

Mesh	N_{tot}	dl_s	dl_n	y_1	N_p	dl_t
Coarse	2M	$15\eta_k$	$10\eta_k$	$1\eta_k$	180	$30\eta_k$
Medium	9M	$11\eta_k$	$6.5\eta_k$	$1\eta_k$	248	$14.25\eta_k$
Fine	11M	$8.25\eta_k$	$5.25\eta_k$	$0.5\eta_k$	324	$10\eta_k$

Table 5.1: Characteristics of the three meshes used for the mesh independence study of pulsatile flow through model aorta. Along with the total number of cells (N_{tot}), the table shows the cell length along the streamwise direction (dl_s), the cell size normal to the wall above the layers (dl_n) and the first cell height (y_1), as well as the number of nodes on the perimeter of the aortic tube (N_p) and the resulting width of the cell along the wall (dl_t). The lengths are reported with respect to the Kolmogorov length scale estimated as $\eta_k = 39.6\mu m$.

5.2.2 Numerical Results

During the simulation, velocity data are sampled along the diameter of the aorta on the locations of the pillars, as well as wall shear stress is calculated on the wall of the whole model. Except if otherwise stated, the results reported in the following paragraphs correspond to the side view middle plane AA', annotated in 5.2b, where the pillars also lay. Moreover, experimental data from micro-pillar 4, located at 21° are referenced.

Grid Independence

A visualisation of the flow field for the three different computational grids, on peak systole ($t = 105ms$) and indicative later time instance during deceleration phase ($t = 210ms$), is shown in figure 5.5. Although the figure can mainly serve for the qualitative comparison of the grid resolutions, it is evident that at peak systole the flow fields are almost identical, with the exception of the branches near the outlet, where the mesh is of lower quality. All grids converge on the prediction of the main recirculation area, on the apex of the bend and seem to agree on the flow field in both the acceding and the descending part. In contrast, during deceleration, significant differences are observed in the description of the recirculation area after the apex and in the descending part; even between the fine and the medium mesh, discrepancies are spotted.

However, assessment of the influence of the spatial resolution is performed by comparing the simulations on the three different grids in terms of velocity profiles and wall shear rate values. Streamwise velocity profiles along the aorta diameter are presented on figure 5.6, for different time instances, and wall shear rate evolution over the systolic cycle is visible on figure 5.7. Both figures refer to the position of pillar 4. In addition, the shear stress distribution along the inner and outer wall of the aorta, is plotted in figure 5.11, for the three different grids on peak systole.

It can be seen in figure 5.6 that the velocity profiles converge for all three meshes. Weak noise present on the profile of the coarse grid, diminishes for the medium grid and vanishes completely at the fine grid. Moreover, the three simulations calculate the same shear rate along the cycle, seen in figure 5.7, with perfect match during the acceleration phase, and slight divergence near the half of the cycle, when the coarse mesh gives lower values. During peak systole, the shear stress distribution for the three meshes is identical along the entire aortic bend, not only in the area of the pillars as it is shown in figure 5.11.

It can be safely argued that the medium mesh resolution (8.6M), with a resolution in the normal to the wall direction of $1\eta_k$ next to the wall and $6.5\eta_k$ in the core, along with a resolution of $11\eta_k$ in the streamwise direction was found adequate to capture the flow structures.

(a)

(b)
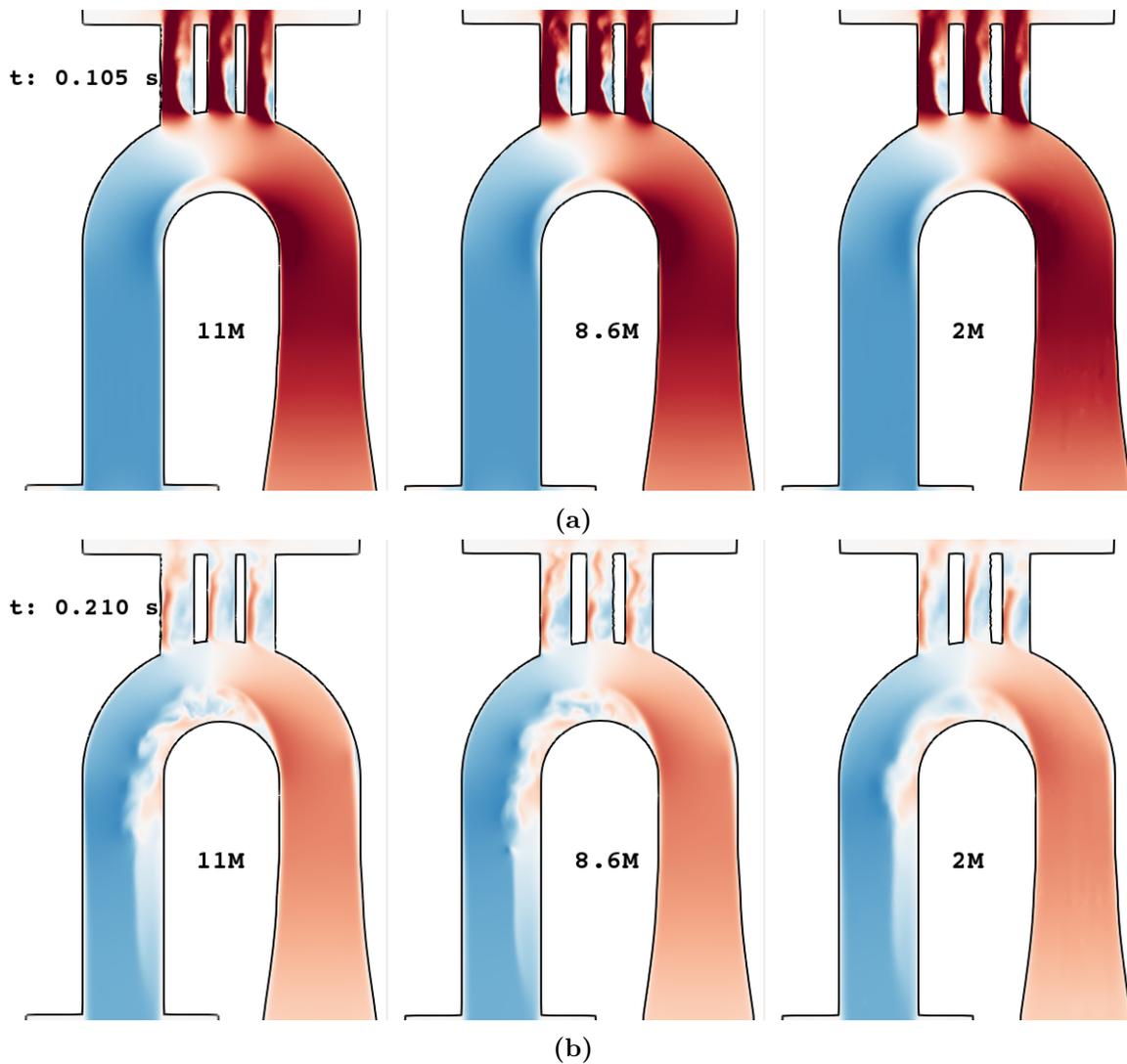
Figure 5.5: Comparison of vertical component of the velocity, for the three different meshes. The contours are plotted on the AA' plane. The coarse mesh (2M) is shown on the right, the medium (8.6M) in the middle and the fine (11M) on the left.
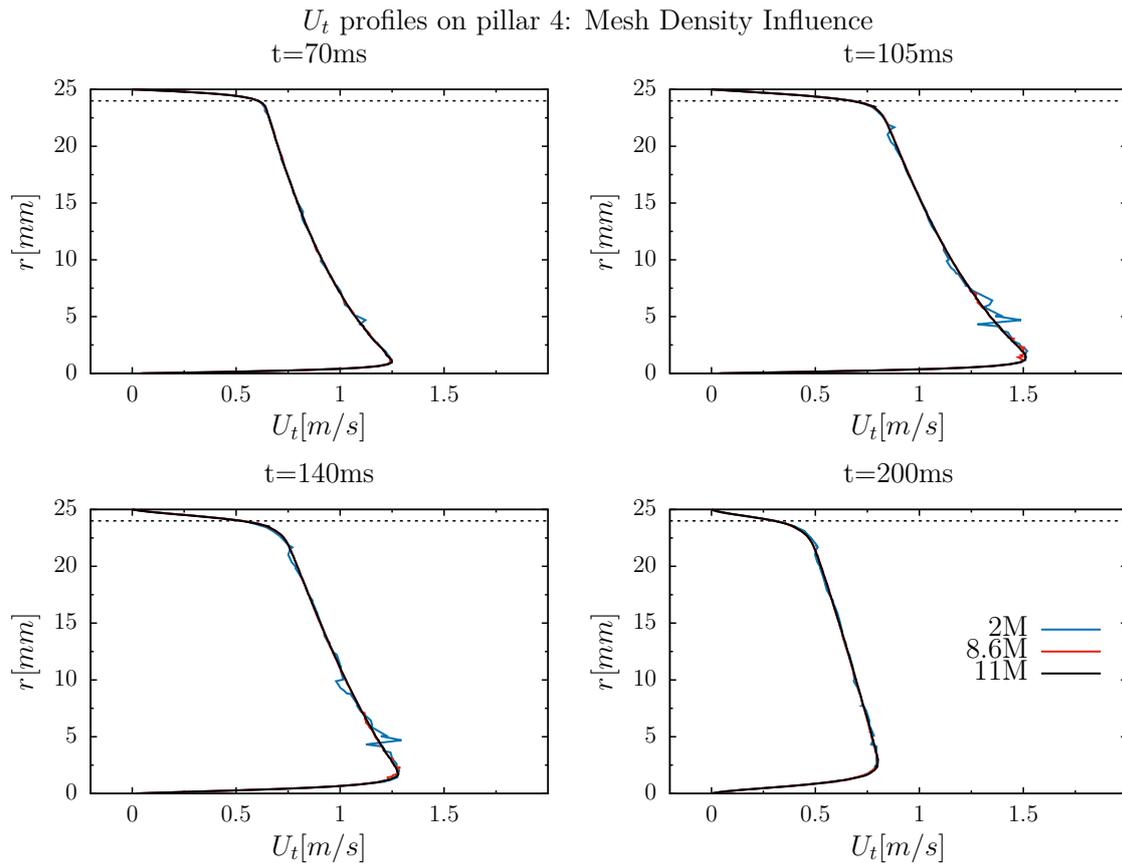
Figure 5.6: Profiles of the tangential velocity $u_\theta(r)$ in the bend at the center plane AA', at angle $\theta = 21^o$, corresponding to the position of pillar 4. Results for the three different grids are shown, where T is the period of the systolic cycle. The dotted line, at $r = 24mm$, indicates the location of the tip of the pillar sensor.
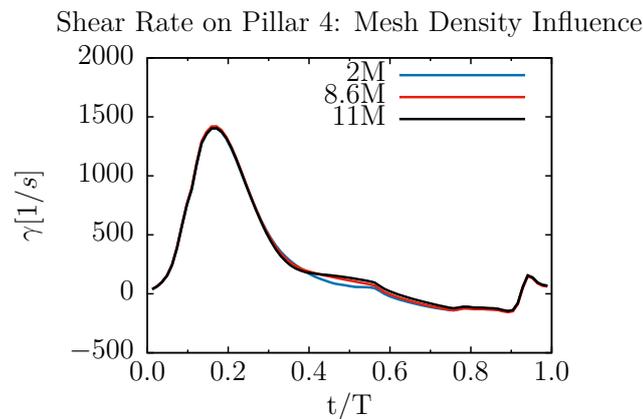
Figure 5.7: Evolution of wall shear rate over the systolic cycle on the outer wall at angle $\theta = 21^o$, corresponding to the position of pillar 4, shown for the three different grids.
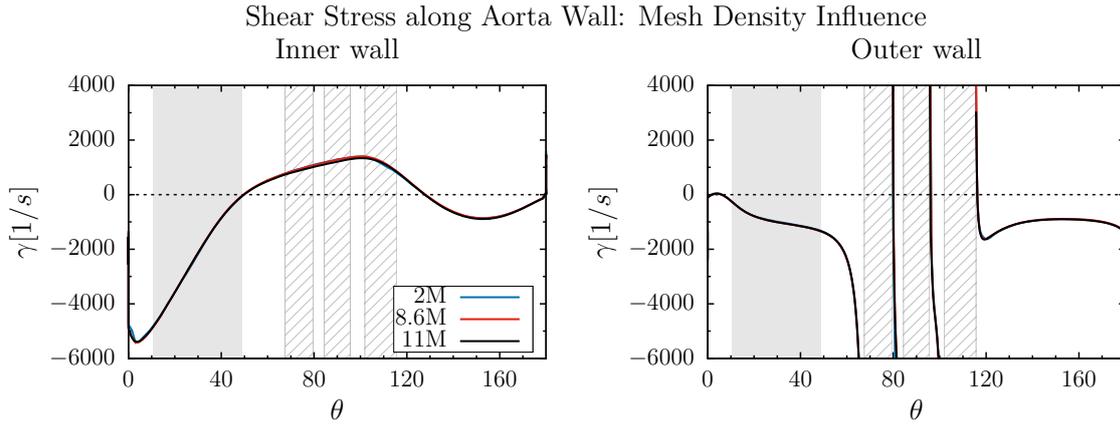
Figure 5.8: Wall shear rate along the aorta bend at peak systole, $t = 105ms$, along the inner (left) and outer (right) wall, on the center plane AA'. The numerical results are presented for the three different grids. The gray shaded area corresponds to the angles of the sensor array, positioned on the outer wall, and the hatched areas indicate the position of the three branches.

Discussion and comparison with experimental data

Figures 5.9 and 5.10 depict the velocity and vorticity contours, throughout the systolic cycle, for the simulation on the medium mesh (8.6M). It can be seen that flow separation initiates on the inner wall early during the systolic cycle, at a location right downstream of the apex, which then develops and extends further downstream. On the other hand, the flow seems laminar and no separation is detected on the outer wall, until later times, where a slender recirculation area can be observed on the beginning of the bend. Most importantly, on the area where the sensors are located, between 10.5^o and 49° on the outer wall, no separation is detected for the largest part of the simulation. This can be concluded from figure 5.6 as well, where the tangential to the wall velocity profiles are plotted over the position of pillar 4, for different time instances.

By plotting the shear rate along the aorta walls on different time instances, during acceleration, on peak systole and during deceleration, in figure 5.11, the exact positions of recirculation can be identified by the change in sign. As expected, no reverse flow is detected during the acceleration phase. On the inner wall, recirculation extends between 50 and 120 degrees at peak systole and during deceleration the flow near the wall becomes chaotic. On the outer wall, on the other hand, no recirculation is observed on these time instances, apart from an interval of 20 degrees in the beginning of the bend during deceleration phase. This corresponds to the are identified by the velocity and vorticity contours. However this plot suggests that the measurement positions are within the recirculation bubble on the later stages of the systolic cycle.

In order to provide a quantitative comparison between the simulations and the experiments, the wall shear rate measurement on pillar 4 are considered. The velocity samples near the wall are fitted by polynomials of first order, following the technique used for the experimental PIV data. Only 10 points are used, which correspond to a total height of approximately $1mm$, covering the pillars. The shear rate is then calculated as the tangent of the fitted polynomials at the wall ($y = 0$). The results for the medium mesh (8.6M) are plotted on figure 5.12, along with the exact shear rate on the wall, extracted during the simulation, and the experimental data.
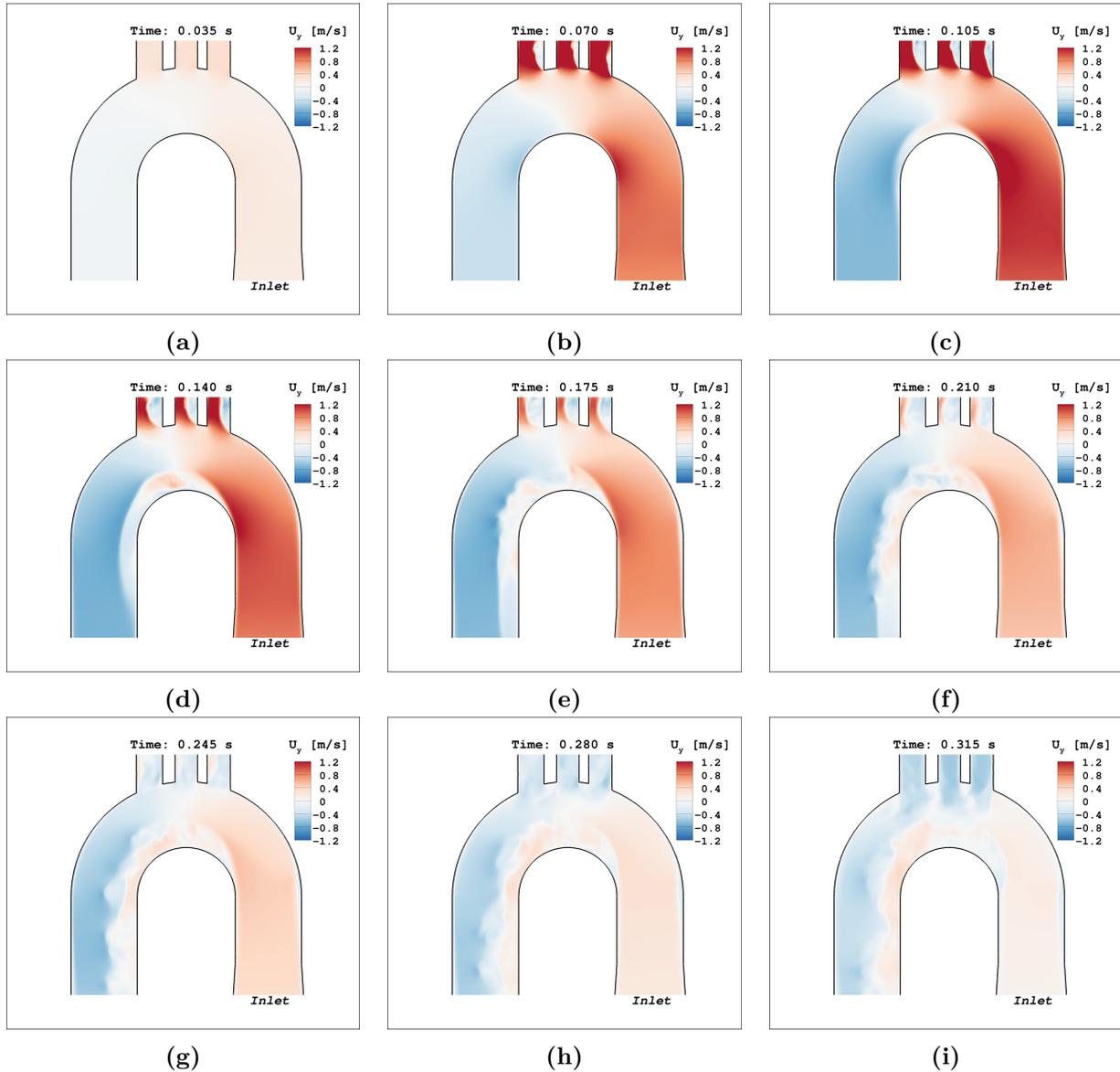
Figure 5.9: Vertical velocity component contours for the pulsatile flow through the model-aorta arc. The results are presented on plane *AA'* for the medium mesh (8M cells).

It can be seen that the shear rate calculated on the wall by the simulation exhibits peak value two times higher than the experimental or the linear fit, as well a steeper descent and slight negative values during the deceleration phase. However, the linear fit produces results that match the measurements for pillar 4. The comparison between numerical and experimental shear rate values suggests that the sensors exhibit 1st order accuracy. In addition, by using 3 sampling points, and considering the linear fit up to $0.3mm$, the estimated shear rate values increase towards the "real" values extracted by the CFD on the wall.

A qualitative comparison between the numerical and experimental results is presented in figure 5.13, for three indicative time instances from the peak systole and on. The path-lines of the PIV particles, integrated over images recorded during experiments are compared with the streamlines extracted from the simulation. Although a proper quantitative comparison can not
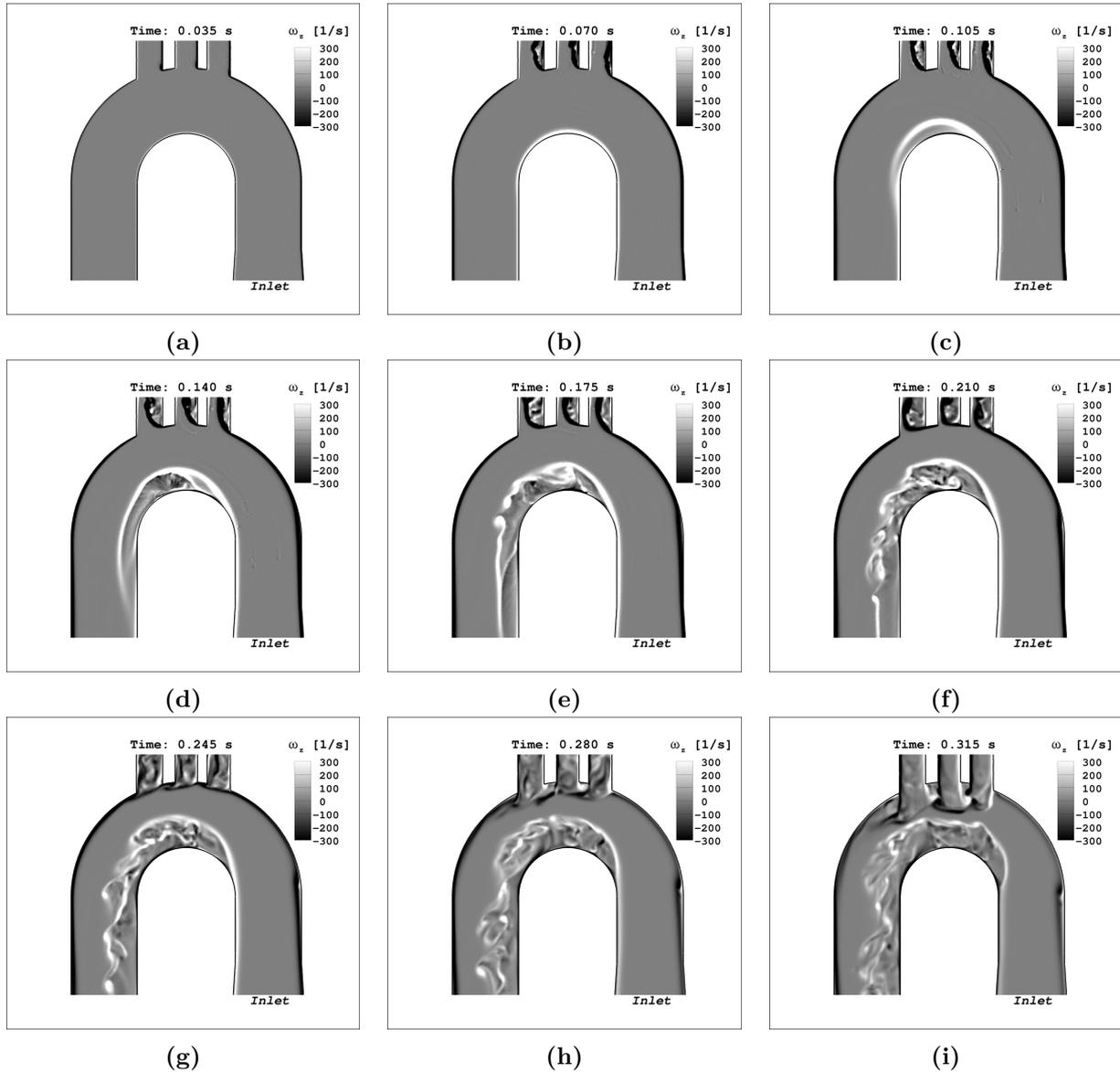
Figure 5.10: Off-plane vorticity contours for the pulsatile flow through the model-aorta arc. The results are presented on plane *AA'* for the medium mesh (8M cells).

be performed, the figure could provide valuable information regarding the recirculation areas. It can be seen that the flow is mostly smooth and can be regarded as laminar during peak systole. However, during deceleration, the hight of the recirculation area on the apex is shown larger in the experiments and during the latest time, a second recirculation area is formed on the outer wall near the beginning of the bend. This secondary recirculation, although predicted by the simulations is much wider in the experiments.

100
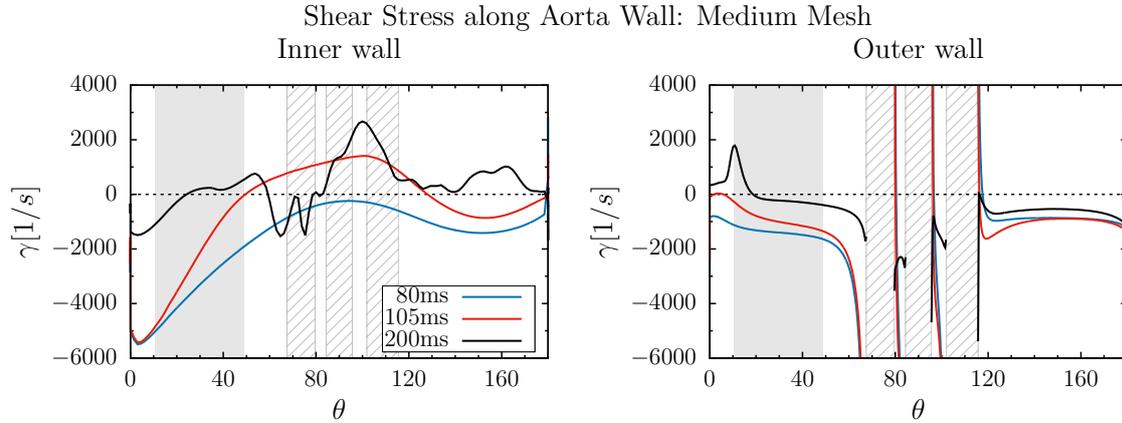
Figure 5.11: Wall shear rate along the aorta bend, along the inner (left) and outer (right) wall, on the center plane AA'. The numerical results are presented for the medium mesh (8.6M) for three different time instances. The gray shaded area corresponds to the angles of the sensor array, positioned on the outer wall, and the hatched areas indicate the position of the three branches.
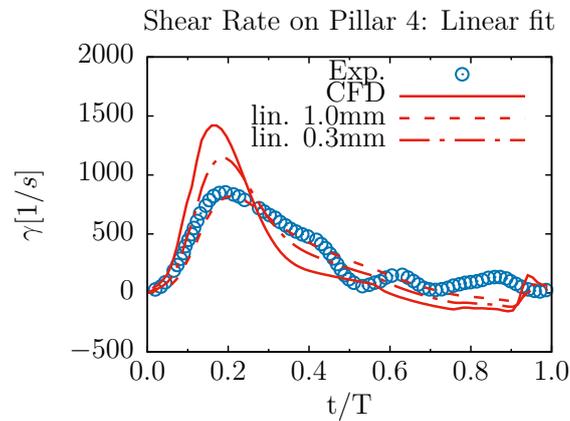
Figure 5.12: Evolution of wall-shear over the systolic cycle on the outer wall at angle $\theta = 21^o$, corresponding to the position of pillar 4. Comparison of numerical results (on medium mesh with 8.6M cells), with experimental data provided by Mrs. Li and Prof. Bruecker. The numerical values of shear rate presented are extracted directly on the wall or by linear reconstruction of the velocity profile near the wall.
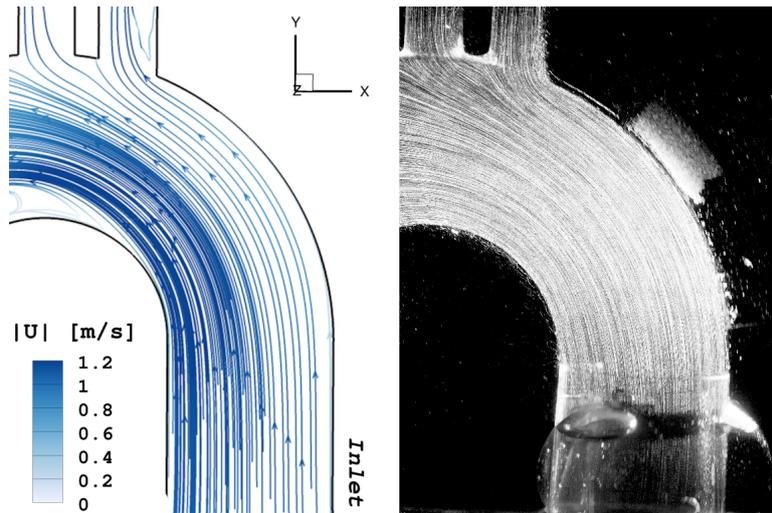
(a) $t = 105ms$
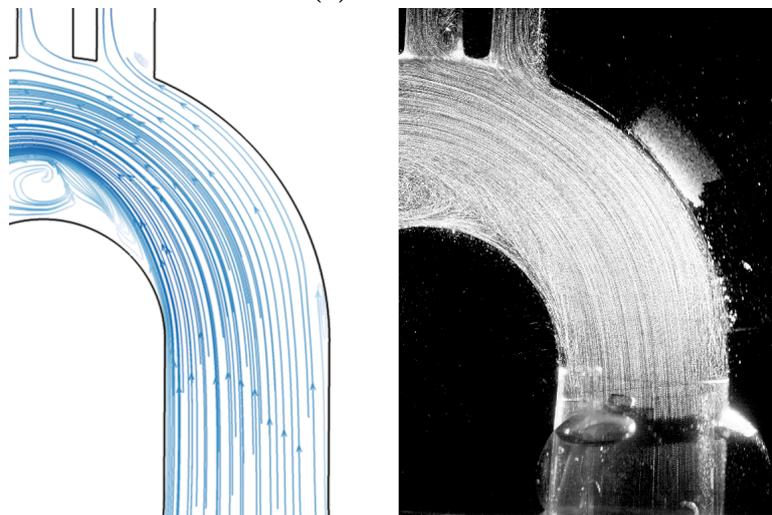
(b) $t = 175ms$
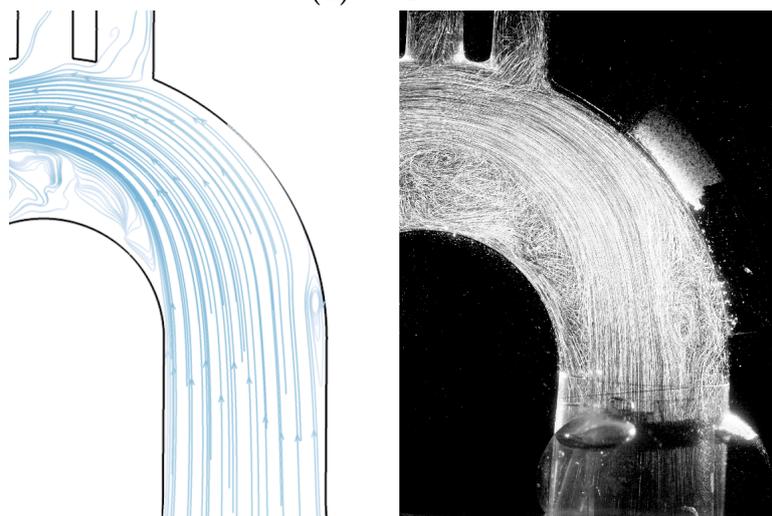
(c) $t = 245ms$

Figure 5.13: Experimental flow field (right), provided by Mrs. Li and Prof. Bruecker, represented by *pathlines*, compared to numerical flow field (left), represented by *streamlines*, for the pulsatile flow through the model aorta arc. The numerical streamlines are plotted on the plane AA' for the medium mesh (8M cells).

5.3 Investigation of Pulsatile Flow through a bi-leaflet Mechanical Valve

Following the study of the pulsative flow through the model aorta, presented in the previous section, the computational work is extended to study the flow through a model bi-leaflet Mechanical Heart Valve.

A *(approximate and not precise)* model of *St-Jude* bi-leaflet MHV 5.14a, is used. It is composed by a simplified version of the casing and the $1mm$ width leaflets. The geometric simplifications are a result of limited information on the fine details of the valve design as well as of a failed attempt to create an accurate 3D scan with the equipment of the Machining Laboratory of the University, due to the reflective metal surface of the valve which would scatter light and prohibit the scanner from mapping the object. In addition, the $1mm$ diameter hinges are neglected, both from the leaflets and the casing, because the flow there would require a very fine computational grid to be accurately resolved which would increase significantly the computational cost.

A similar valve, but with different full-open angle, has been used by Li et Bruecker [128] in the experimental study of wall shear stress measurements, where the performance of the bi-leaflet vale is compared against the one of a novel tri-leaflet valve; the latter valve has the advantage of generating more physiological flow patterns. An important characteristic of the bi-leaflet valve, is that when fully open, it forms three orifices between the two leaflets and the walls of the aorta, visible in figure 5.14b and 5.14c, where the blood flow is accelerated. This configuration deviates a lot from the opening of the real valve and thus non-physiological flow develops. Non-physiological levels of shear stress may be generated which could be related to blood-cell damage and fatigue or tear of the blood-vessel walls. Moreover, the abrupt and intense acceleration of the flow through the orifices or in the small gaps between the leaflets and the casing, or the hinges, may cause high-speed jetting or leakage, which have been identified by researchers as potential cavitation initiators.

The same model aorta is used as in the preliminary study, including the Valsalva Sinuses, seen in figure 5.15, in accordance to the experiments reported in [128]. Under identical flow conditions, regarding fluid properties, inflow rate and boundary conditions, the MHV is placed at the end of the inlet nozzle, just before the entry to the sinus region, visible in subfigure 5.15c. The casing has a smaller diameter than the diameter of the aorta, $D_A = 25mm$, and therefore is partially submerged in the fluid domain as well. The two leaflets, as well as the casing, are represented by a triangulated surface mesh, in a stereolithography file format (STL), and are modelled as immersed boundaries, employing the method proposed herein. The motion of the leaflet is induced by the hemodynamic forces exerted on them by the flow.

Motion of the Leaflets

The motion of the leaflets is coupled with the flow through a FSI algorithm of *loose coupling*. The solid leaflets are considered undeformable; their rotation around the hinges' axes is governed by the equation 2.27b, which is repeated here for sake of completeness:

$$\tilde{\mathbf{I}}_R \cdot \frac{\partial^2 \theta}{\partial t^2} = \mathbf{M}_{ext} \tag{5.2}$$

The moment of inertia tensor is calculated with regards to the center C_H of the rotation
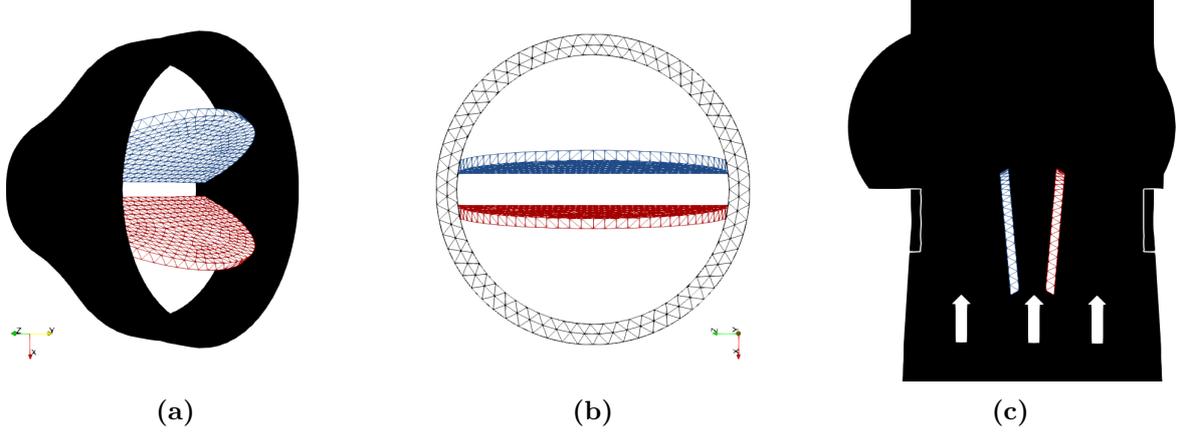
Figure 5.14: The model of the bi-leaflet Mechanical Heart Valve with the casing. A perspective view with open leaflets at 40° (a), a top view with the leaflets in fully-open position of 53° (b) and a side view of the valve placed before the sinus region of the model aorta (c). The casing restrains the diameter of the aorta, as seen by the white-colored edges near the aorta walls in (c). In fully open position of the leaflets, three orifices are formed (c). The casing and the leaflets are represented by a triangulated surface mesh.

(hinge's) axis for each leaflet, which is parallel to the Oz axis of the coordinate system:

$$\tilde{\mathbf{I}}_R = [I_{ij}] \Rightarrow I_{ij} = \sum_{k=1}^{N} dm_k \left(|\mathbf{r}_k|^2 \cdot \delta_{ij} - x_i x_j \right), \quad i, j = x, y, z$$

where dm_k is the elementary mass of each element k of the solid leaflet, $\mathbf{r}_k$ the distance vector of each elementary mass from the center of rotation C_H and δ_{ij} the Kronecker delta:

$$\delta_{ij} = \begin{cases} 1, & i = j \\ 0, & i \neq j \end{cases}$$

The MHV is considered to be composed by a Polycabronate material, similar to [19] where an equivalent valve is used, with density $1750 kg/m^3$ and the mass is uniformly distributed on the solid IB surface.

The rotation angle θ_z is limited between $\theta_{min} = 25°$ and $\theta_{max} = 78°$. All other rotations and translations are constrained. Gravity is neglected, therefore the moment vector $\mathbf{M}_{ext}$ is composed only by the moments of the hemodynamic forces.

An assessment of the FSI algorithm for the proposed IB method is presented in Appendix B, where the applicability of the method on Vortex Induced Vibrations is addressed. Furthermore, in Appendix C, where the method is applied onto the simulation of pulsatile flow through a bi-leaflet MHV in an axisymmetric straight aorta; the results are validated against computational and experimental data from the literature and found in good agreement. The performance of the methodology for such complicated flows is found satisfactory and thus, it is employed for the herein presented study.
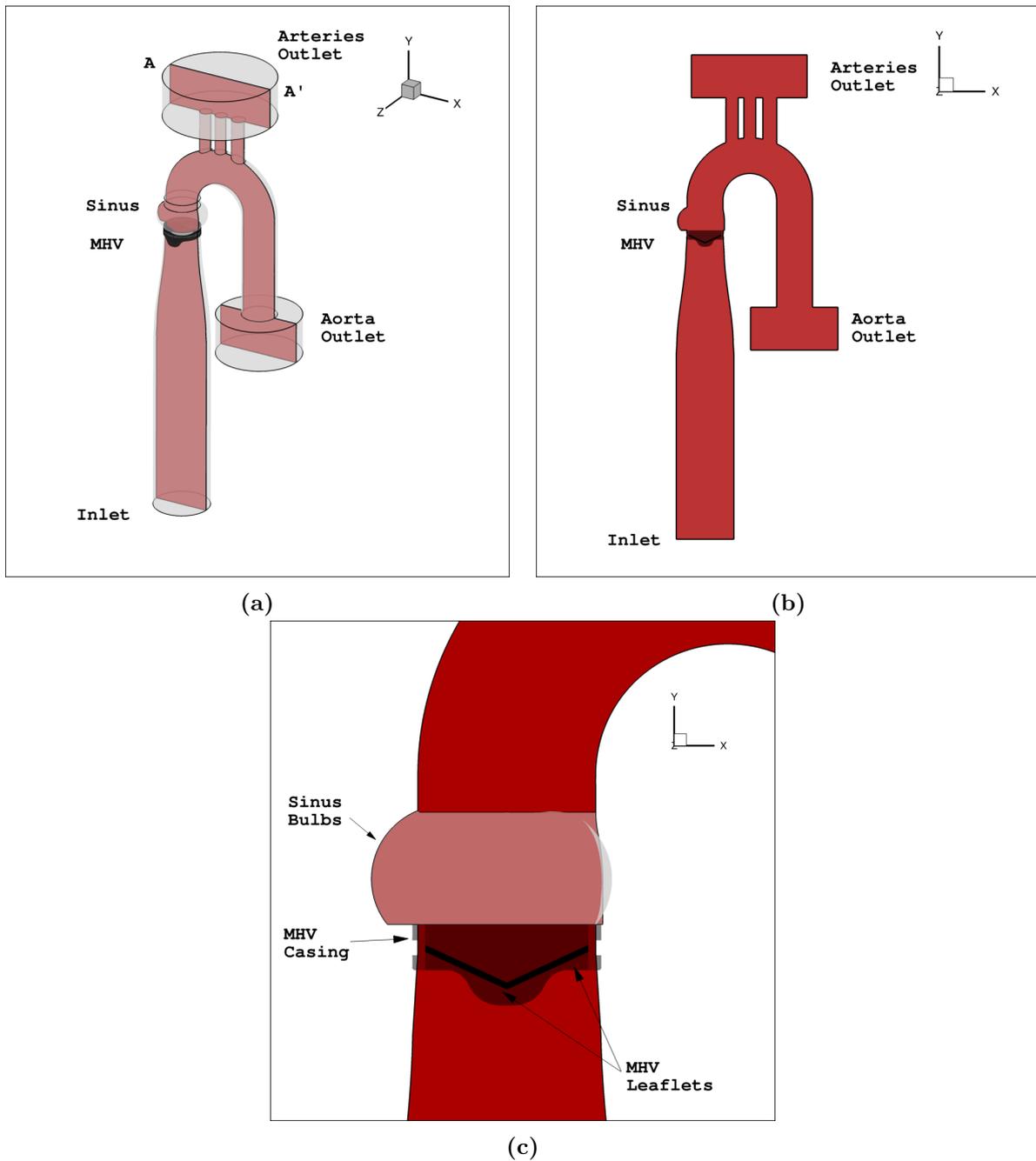
Figure 5.15: The computational domain of the aorta model with the bi-leaflet Mechanical Heart Valve. The inlet has a total length of $6D_N$ ($4D_N$ before the convergent part) to ensure the flow is fully developed before the aorta bend. Two volumes have been put at the outlet of the aorta and the outlet of the arterial branches. The plane AA' corresponds to the side centre plane. The nozzle has a diameter of $D_N = 40mm$ and the aorta $D_A = 25mm$. It has to be noted that the domain follows the orientation of the experiments (as reported in [128]), and differs from the simulations of section 5.2.

5.3.1 Numerical Set-up

A mesh of 2.3 million (2.3M) tetrahedral cells is used to discretise the computational domain. The choice has been made after taking into consideration the findings of the preliminary study

presented in the previous section regarding the grid independence of the numerical results and the computational cost of the simulations. Indicative view of the mesh are presented in figure 5.16.

The focus is placed primarily on the flow development immediately after the MHV and inside the region of the Valsalva Sinuses, as seen in sub-figure 5.16c, where the accelerated through the orifices flow is expected to be transitioning to turbulence and chaotic vortical structures to be forming. On the other hand, for the recirculation area beyond the apex, which during the deacceleration phase moves upstream, as observed previously, will probably affect the area of interest.

Layers of 6 canonical hexahedral cells cover a region of $1.9mm$ over the walls of the aorta, with an expanding ratio $\gamma = 1.2$ and a first cell height $y_1 = 0.2mm = 5\eta_k < 5y^+$, in order not to violate the spatial resolution constraints for the boundary layer development. The maximum cell size along the aortic arch is set to $0.8mm$, which expands towards the outlet volumes. Special care is taken for the resolution of inside the Valsalva Sinuses and at the end of the inlet nozzle, where the MHV is positioned; the maximum cell size is $0.3mm = 7.5\eta_k$ and $0.3 - 0.8mm = 8 - 20\eta_k$ respectively.

The time-step size is governed by the CFL condition $Co_{max} \leq 0.5$, and in addition it is further constrained under one millisecond, so that it always remains smaller than the Kolmogorov temporal scale, $dt \leq 10^{-4}s \ll \tau_k$.

| (a) | (b) | (c) |
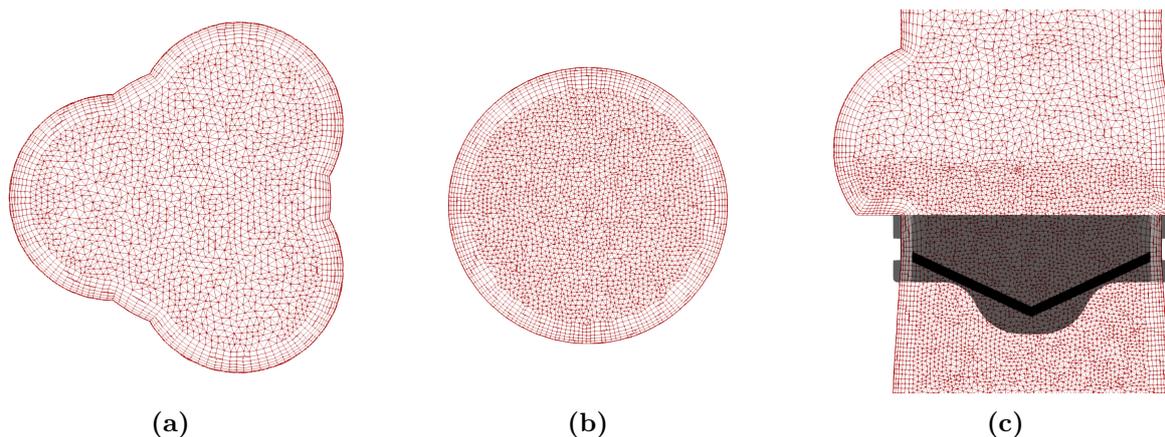
Figure 5.16: The computational mesh of the aorta model with the bi-leaflet Mechanical Heart Valve. Two horizontal slices, perpendicular to the flow direction, at the sinus region *(a)* and the position of the valve *(b)*, as well as a view of the valve and sinus region on the vertical middle-plane *AA' (c)*, are shown. A tetrahedral grid is used, refined near the valve's casing and inside the sinus bulbs. In addition, hexahedral cell layers have been added on the aorta wall, ensuring $y^+ < 5$ on the wall.

5.3.2   Results

The evolution of the flow field along the systolic cycle, is presented in figure 5.17, in terms of off-plane vorticity contours plotted on the side view middle plane *AA'*. The main characteristics of the flow can be identified as the vortex shedding over the leaflets and over the aorta wall in the Valsala sinuses, as well as the recirculation are formed at the apex of the turn.

Leading edge vortices start shedding from the lower side of each leaflet (the *upstream* or *wall-facing* side) as the valve is opening and continue throughout the cycle. In addition, in

the early opening stage of the valve, vortex rings are generated over the casing and after the end of the sinus region into the root of the downstream part of the aorta, seen in frames 5.17a and 5.17b. The vortex ring of the casing rolls up and grows into the bulbs of the sinus region (frames 5.17b and 5.17c), forming constant, yet highly unsteady, recirculation areas (frames 5.17d-5.17l).

Near peak-systole, the leading edge vortices start to interact with the flow features induced by the 180° turn of the aorta, visible on frame 5.17c; the shear layer on the outer wall at the middle of the turn, where separation initiates, and the recirculation area on the inner wall of the apex, which has thicken significantly. This interaction breaks the large vortical structures into smaller and un-organised structures, as shown in frames 5.17d-5.17f. During later stages of deceleration phase, visualised through frames 5.17g-5.17i, these vortical structures breakdown even more and become chaotic along the entire aortic arch, however during back-flow they do not get destroyed nor does the reverse flow from the branches wash them away, as shown in frames 5.17j-5.17l.

A quantitative comparison of the numerical results against experimental data from Li et Bruecker [128], can be performed regarding leaflet kinematics. The valve model used in the current computational study differs from the model used in the experiments, in terms of final opening angle and position of the hinges. These discrepancies between the geometries alter the width of the orifices and the angle of attack of the leaflets. As a result, the velocity profiles developed in the orifices would be different, especially with respect to the maximum velocity value. The pressure field developed in the middle orifice can be different for the two models, and therefore the hydrodynamic loading of the leaflets as well, which would lead to different kinematics. In addition, in computations gravity is neglected, which could influence the motion of the bodies.

As it can be seen in figure 5.18, in the numerical simulations the valve opens more rapidly than the valve in the experiments, however the non-symmetrical closure of the leaflets is captured in both cases. More precisely, the left side leaflets, which is facing one of the thee sinus bulbs, is closing faster than the right one, which faces the wall between the two other bulbs. The closure of the right leaflet is the same for both simulation and experiment, while the left leaflet starts to close earlier during experiments. Finally, a significant rebound is observed after the closure of the valve in the numerical results.

in addition to predicting a more rapid opening, the CFD results exhibit a higher and constant slope during opening, which indicates more abrupt motion and linear acceleration, while during experiments the leaflets decelerate after reaching 80% of the final angle. During closing phase, the motion of the right leaflet is very well captured by CFD, both in terms of trajectory and slope, while the left leaflet closes later in CFD than the experiments, yet earlier than the right leaflet, demonstrating a gradual increase of the rate of change, which is also observed in the experiments, in a more pronounced manner though.

Leaflet rebound has been found in simulations of a similar bi-leaflet valve mounted on a anatomic aorta model [20], which exhibits a high-angle turn downstream of the sinus region. This instability of the closure of the valve may be related to the geometry of the aorta, since in simulations and experiments with valves placed in a straight aortas is absent [19]; these findings have been reproduced by the herein proposed method as well, as it can be seen in Appendix C.
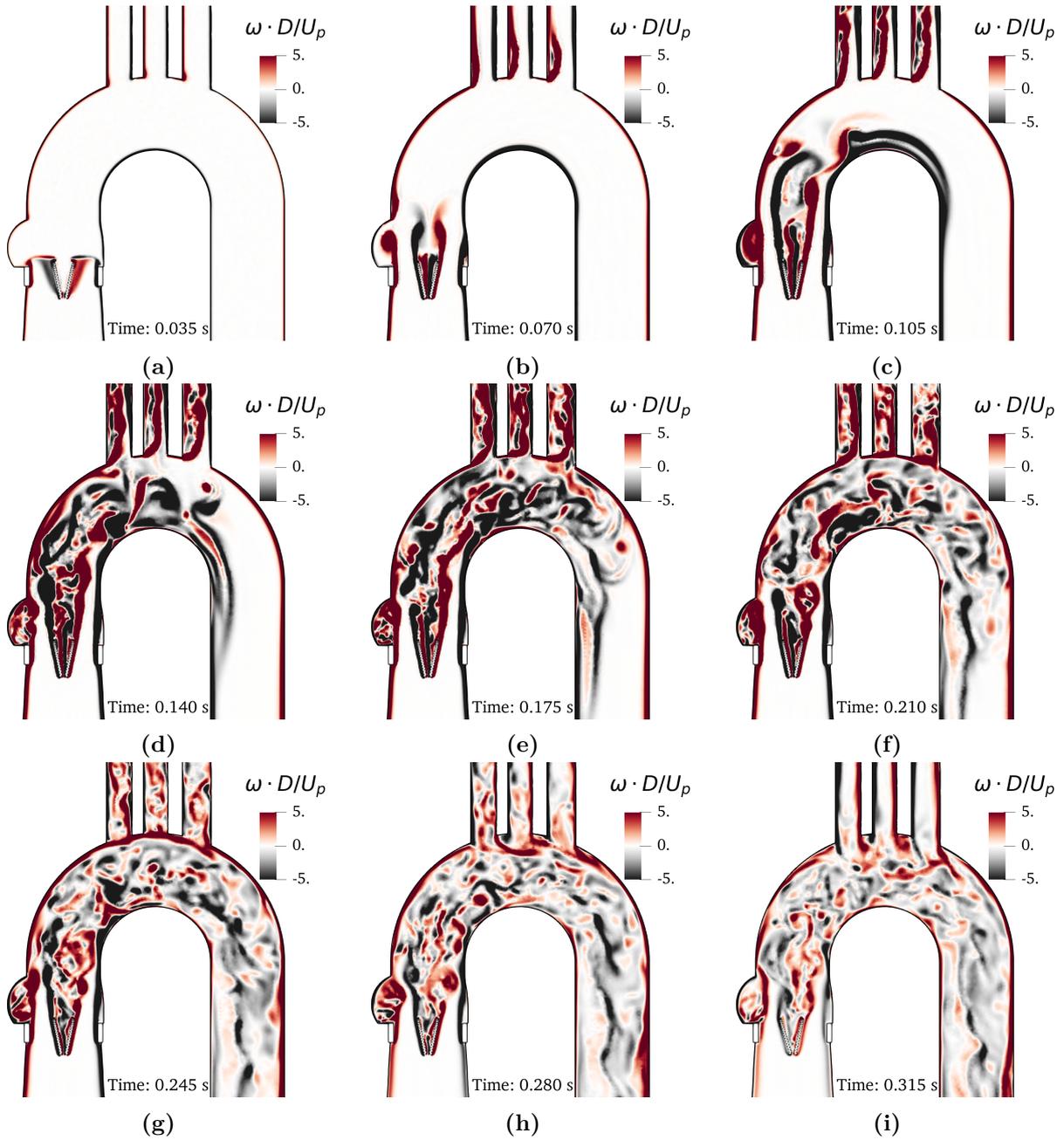
Figure 5.17: Simulation of the pulsatile flow through the a bi-leaflet MHV mounted on a model-aorta. Off-plane vorticity contours, presented on plane AA'. The non-dimensional values are presented, estimated as $\omega' = \omega \cdot D_o/U_p$, using the diameter D_o on the inlet nozzle and the peak inlet velocity U_p.
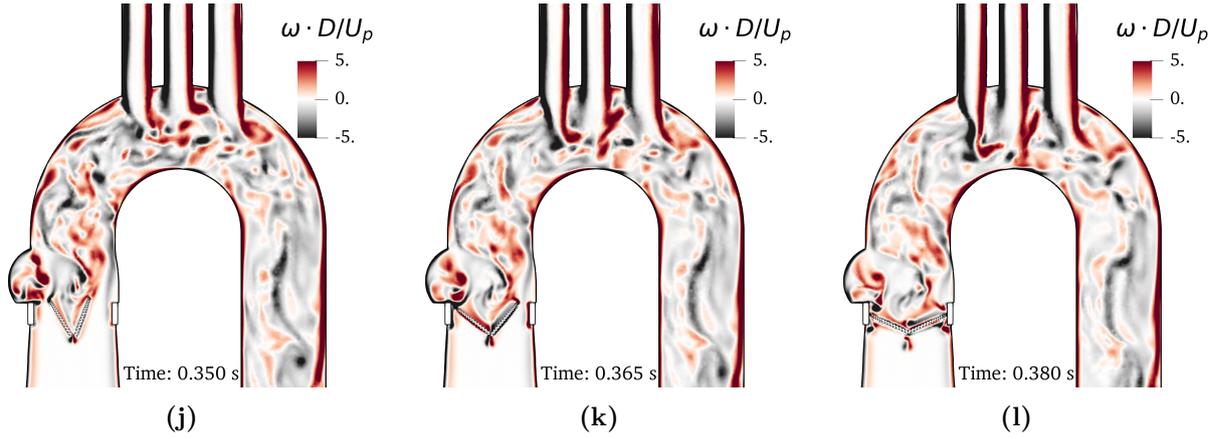
Figure 5.17: *Continued*: Simulation of the pulsatile flow through the a bi-leaflet MHV mounted on a model-aorta.
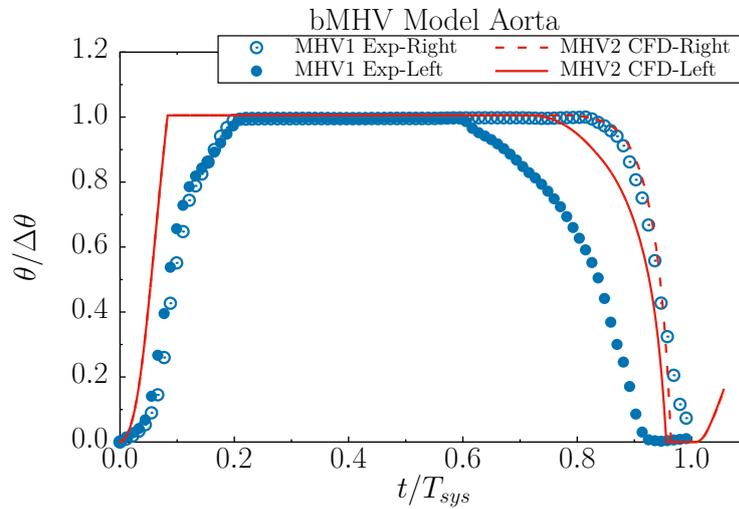
Figure 5.18: Simulation of the pulsatile flow through the a bi-leaflet MHV mounted on a model-aorta. Leaflet kinematics. The results of the simulations are compared to the experimental measurements of the angular position of the leaflets of the similar flow from Li et Bruecker [128]. CFD and Exp. results refer to valves with different final position. The non-dimensional angle is plotted, with regards to the difference between fully open and fully closed position $\Delta\theta = \theta_{open} - \theta_{closed}$.

5.3.3 Discussion

Regarding the developed flow through the bi-leaflet MHV, the focus is shed on the the resulting shear stresses. Following the rationale of the previous section, the wall shear stress is extracted from the velocity profile over the outer wall of the aorta, on the location of the measuring pillars, via means of linear fit. Figure 5.19 presents the wall shear rate evolution along the systolic cycle for the current computation and compares it with the case without the valve (and without the Valsalva sinuses) of the previous section. The computational results are compared with experimental data available in [128]. The influence of the valve, in the resulting shear stresses on the aorta wall is evident; higher shear stresses loading of the walls is observed during deceleration phase, when the valve is used.

109

However, although in the case without the valve, the numerical results matched the experimental measurements, in the case with the valve the simulations capture a quite different behaviour. The CFD predict lower levels of shear rate, however the results exhibit much more violent oscillations of larger amplitude. A significant difference is an abrupt decrease of shear rate right after peak systole (0.2 t/T) captured by the CFD; the experiments do not record such a drop. This could be a result of the interaction of the vortex rings initiated from the sinus region and the vortex street developed on the wake of the leaflets, visible in frame 5.17c. The large amplitude of the oscillations, as well as the differences in maximum shear values, prevent us from drawing safe conclusions.

Moreover, the differences between the curves with and without the valve, indicate the influence of the MHV on the flow field, and in conjunction with the visualisation of the vorticity field, seen in figure 5.17, the resulting chaotic flow structure. Although, the spatial resolution influence is not studied here, is seems to affect the results. It has to be taken into account, that the wall shear estimates of figure 5.19, demonstrate accuracy of first order. This would be sufficient for the relatively simple flow studied in the previous section, which is mainly characterised by the recirculation over the inner wall on the apex. For the case of the flow through the bi-leaflet valve though, it could indicate that the spatial resolution is inadequate. An question then arises, regarding whether the Reynolds number, which determines the spatial resolution, is correctly estimated using the aorta diameter as a characteristic length scale or should be the orifice width considered instead. In any case, the use of advanced simulation strategies for the more accurate resolution of turbulence, such as LES computations, may drastically improve the results.
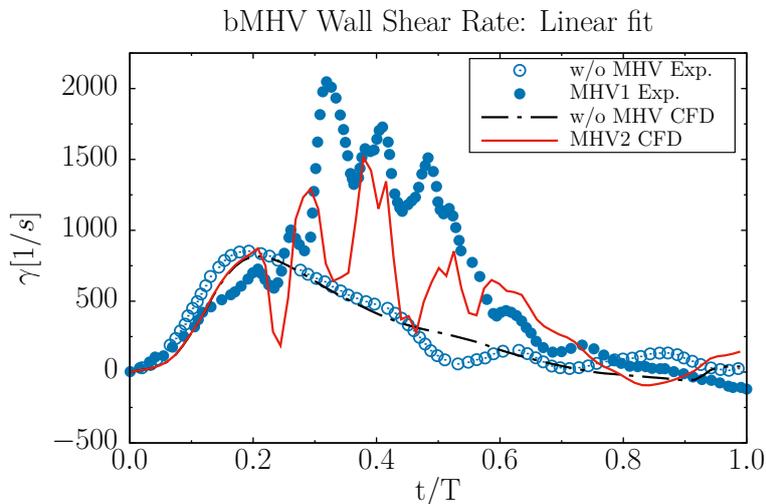
Figure 5.19: Evolution of wall-shear over the systolic cycle on the outer wall at angle $\theta = 21^o$, corresponding to the position of pillar 4. Comparison of numerical results, for cases with and without MHV, against experimental data from Li et Bruecker [128]. The numerical values of shear rate presented are calculated by linear reconstruction of the velocity profile near the wall.

Regarding leaflet kinematics, the assessment of the numerical results is more complicated. Although the differences of the leaflets' motion curves between computations and experiments, visible in figure 5.18, could be attributed to the geometrical differences of the models used or the absence of gravity in the simulations, some comments should be made, especially in the

slope of the motion curves, from which qualitative observations could arise.

The flow during the acceleration, before peak systole, is mostly regarded as laminar and turbulence is not developed; therefore the numerical predictions of rapid and steady acceleration motion for the leaflets seems valid. The deceleration of the leaflets measured during experiments, which commences before the the deceleration of the inlet signal and well before peak systole, could indicate that apart from the hydrodynamic loading, additional forces act upon the leaflets. These forces could be a result of the hinge mechanism, such as friction, or a result of gravitational acceleration.

Firstly, since the hinge mechanism is not considered, nor friction between the leaflets and the casing or micro scale flow features in the structure's gaps are taken into account. However, this practice is followed in similar studies in the literature [17–22, 45, 47, 49, 71, 72, 228, 245] and it is found that the kinematics are not affected; the same assumption is made here as well, thus the differences in kinematics should not be attributed to that.

Secondly, because the density ratio between the valve's material (Polycabronate: $\rho_p = 1750 kg/m^3$) and the working fluid (water: $\rho = 1140 kg/m^3$) is not high, it is uncertain whether the gravitational force would lead to more gradual opening and faster closing of the leaflets or it would be counteracted by the hydrodynamic forces of the flow. It is known that such MHV simulations are inherently unstable because of the materials' density ratio and sensitive to the *added mass* effects [19, 20]. However, seems unlikely for the gravity to affect the leaflets' kinematics a lot, since the moment arm of the gravitational force should reduce as the leaflet rotates and tends to align with the direction of gravity; the gravity vector in the experimental configuration is vertical, corresponding to a leaflet angle of 90° while the fully open position corresponds to 85°.

In contrast, it seems more likely that the differences in the rate of change of the leaflets' motion occur from the differences in the effective angle of attack; lower angles of the leaflet with regards to the closed position corresponds to high angles of attack and vice versa for angles near the full open position. Since the final angle of the leaflets, in full open position, is larger in the experiments ($\theta_{MHV1,open} = 85^o$ in contrast to $\theta_{MHV2,open} = 78^o$ of the simulation), different hydrodynamic loading would develop towards the end of the opening phase. As the leaflets would approach the fully open position, the hydrodynamic lift would decrease, which could probably explain the deceleration visible in the motion curves of figure 5.18. In addition, differences in the width of the central orifice could lead to differences in the acceleration of the flow on the sides of each leaflet and the resulting pressure ratio, affecting the leaflet kinematics.

Finally, the numerical method is of great importance. The resolution of the flow field, as well as the strategy of the coupling algorithm, it is expected to influence the leaflet kinematics, as it was shown in the work of Borazjani et al. [19]. Most importantly, the aforementioned study reports that the *strong-coupling* of the flow and solid solvers, which dictates that the solid motion and flow field are solved iteratively in each time-step until convergence, is a necessity for the accurate computations. As it is demonstrated in Appendix C, the *loose-coupling* employed herein, was adequate to replicate the numerical and experimental results of [19] for an axisymetric aorta, in terms of leaflet kinematics. However, the influence of the flow solution was also clear from the parametric two-dimensional studies. As the flow becomes more complicated, because of the aortic bend, a strong-coupling algorithm may prove more appropriate or even essential for correct simulations.

Overall, taking into account the geometrical differences of the valves, the simplifications

applied on the model used in the simulations, as well as the absence of gravity, the computational results and the performance of the herein proposed methodology for fluid and solid motion coupling are found satisfactory, although room for improvement exists.

5.3.4 On the potential of cavitation induction

Although the focus of this chapter is shed primarily on the shear stress development on the aorta walls, few comments ought to be made on the cavitation induction potential during the operation of bi-leaflet MHV.

As it has already been mentioned in the introduction of the Thesis, *water hammer, squeeze flow, vortex* and *Venturi effects* have been pinpointed as possible causes of cavitation in the vicinity of MHV leaflets or casing during late closure phase [79, 109, 133]. From the results of the computational investigation presented herein, some quantitative observations can be made with regards these factors.

Firstly, the velocity of the leaflets is easily accessible as the output of the motion solver, in addition to their position; from figure 5.20a it can be seen that the maximum angular velocity of the leaflets can reach 100 rad/s. Although the comparison between numerical predictions of leaflet kinematics and experimental measurements, visible in figure 5.18, revealed more abrupt opening in the simulations and better agreement during closure, especially for the right leaflet, which is facing the aorta wall rather than a sinus bulb and its closure dynamics are perfectly captured. Therefore, although the velocities of the opening-phase may deviate from real values, the closing-phase values can be trusted, and more precisely the aforementioned maximum value captured for the right leaflet. This value of angular velocity corresponds to a ~ 1.11 m/s velocity on the tip of the trailing edge of the leaflet, which impacts the casing upon closure, and it is reached just before the impact. A conservative estimation of the water hammer pressure related to this impact, is $P_{wh} = u_{max} \cdot c_w \cdot \rho = 1.5$ MPa, calculated using the formula for solid-to-liquid impacts [65] and approximating the speed of sound in the glycerine-water solution with that of the the water. These values are far higher than the pressure levels observed in the computational domain and the area of the valve casing or the averaged pressure difference along the valve casing, presented in figure 5.20b, which reach values of $|\Delta p_d|_{max} = 6\rho = 6840$ Pa, $|\Delta p_c|_{max} = 4\rho = 4560$ Pa and $|\Delta \bar{p}_c| = 1.2\rho = 1368$ Pa respectively. Hence, the water hammer effect is not relevant to the current set-up and cannot contribute towards cavitation initiation.

On the other hand, squeezed flow and high-speed jets are captured mainly in the contact areas between the leaflets and the casing, during the later stages of closing-phase, as figure 5.21 shows. However, the sudden and short-lived acceleration of the flow in these areas, it is not severe enough to lead to velocities higher than 0.5 m/s, a fact that, although the fluid upstream the valve is almost stagnant with velocities ≤ 0.1 m/s, cannot create cavitation. It has to be mentioned though, that the velocities of the observed jets may be influenced by the spatial resolution and the frequency of the sampling. Similar but more intensive jetting, probable due to the use of finer grid, have been captured also in the simulations of a bi-leaflet MHV on an axisymmetric aorta presented in appendix C. These jets can roll up and form vortices just upstream the valve casing, where a backward facing step is formed, where it is possible to be considered as potential areas of pressure drop bellow saturation levels. However, as it is visible in frames 5.21e to 5.21h, the pressure drop across the valve is never higher than 1.2$\rho = 1368$ Pa.

Finally, all these comments are limited to the studied set-up. Different computational representation of the aortic arch, preferably closer to the anatomic geometry, would have an impact on the results [20], but more important would be the influence of the inflow-rate pulse. The pulse utilised in the current study corresponds to a heart-beat rate of approximately 70 *bpm* [128]; pulses of higher rate or irregular form, that may correspond to non-rest conditions or mimic common heart diseases, might provide conditions, qualitatively similar to but quantitatively more severe from the ones observed herein, favouring cavitation formation.
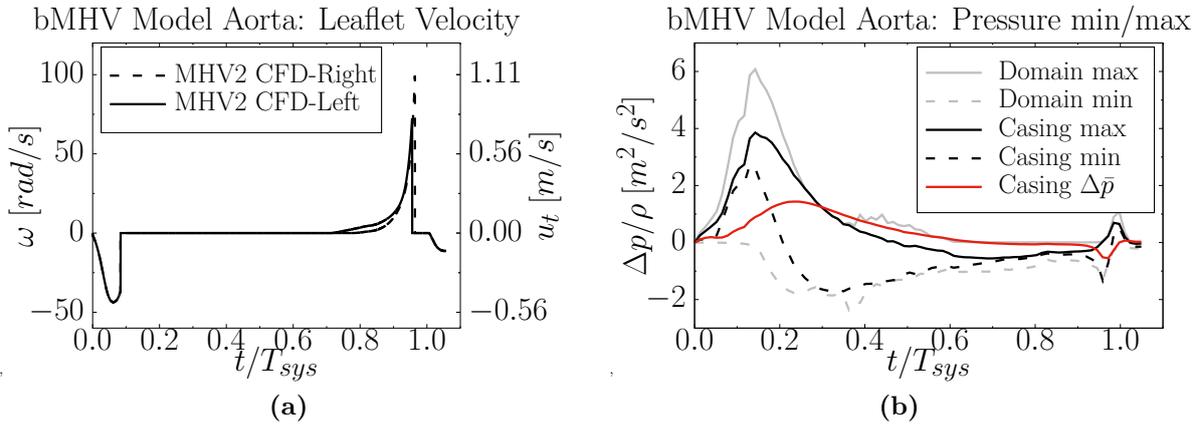
Figure 5.20: Simulation of the pulsatile flow through the a bi-leaflet MHV mounted on a model-aorta. Investigation of water-hammer effect by means of computed leaflet velocities *(a)* and captured pressure difference with respect to ambient conditions on the outlets *(b)*.
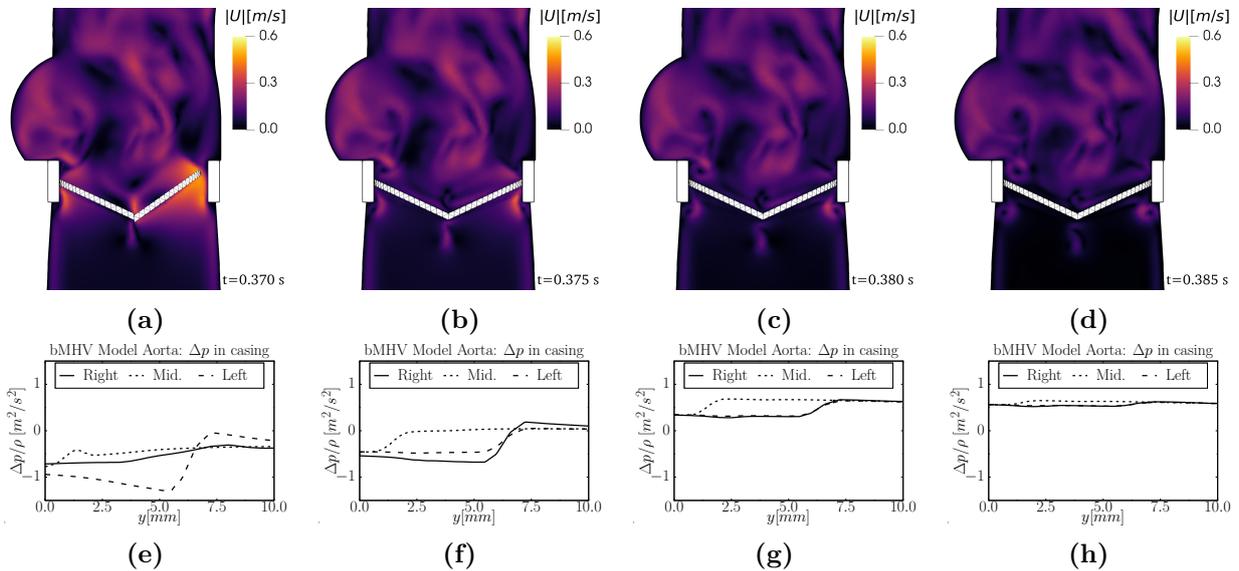
Figure 5.21: Simulation of the pulsatile flow through the a bi-leaflet MHV mounted on a model-aorta. Visualisation of captured squeezed flow and high-speed jetting between leaflets and casing, *on top*, and equivalent pressure difference along the casing, *on bottom*, next to the ring (Right, Left) and in the middle, upon valve closure.

113

5.4 Concluding Remarks

The pulsatile flow through models of the circulatory system is complicated nature, involving transitional turbulent regimes in larger arteries and non-Newtonian physics in smaller vessels. CFD tools can aid to unveil the flow dynamics and assist in-vitro experimental campaigns. Regarding diseases such as thrombosis or heart-valve failures, CFD can be used in understanding the underlying mechanisms or design solutions, even for patient specific tailoring.

The blood flow through MHV and the subsequent development of non-physiological vortical structures and shear stresses is of high importance. The herein IB method is employed to investigate the wall shear stress developed by the pulsatile flow through a bi-leaflet MHV mounted on a model aorta, featuring a 180° turn, as well as an approximation of the Valsalva sinuses and three arterial bifurcations.

First, a case without the valve and with a simplified inlet nozzle geometry is considered, where wall shear stress predictions are compared to experimental measurements using a specialised technique by Prof. Bruecker and Mrs. Li, of CITY, University of London, and have been used to asses the performance of a standard bi-leaflet MHV and of a novel tri-leaflet MHV [128]. The measurement technique employs flexible micro-pillars mounted on the aorta wall, which bend along the flow and provide estimates of the shear stress. The CFD computations confirmed the measurements and validated that the technique achieves first order of accuracy. It is also shown that smaller pillars would provide better results.

Then, a simulation of the flow through a bi-leaflet MHV mounted on the aorta model is carried out. The performance of the herein proposed methodology is assessed and found satisfactory. Detailed quantitative information about the developed flow field is provided. However, the wall shear stress estimates for this case deviate from the equivalent measurements of Li et Bruecker [128]. This demonstrates the complex nature of the flow under examination and the sensitivity of the induced flow and leaflet dynamics to the numerical methods used. The use of LES computations for the flow though MHV seems necessary to correctly predict the flow field evolution.

Chapter 6

Conclusions and Outlook

This thesis is concerned with the development of an Immersed Boundary Method, suitable for simulations of complex cavitating and biological flows. Regarding the former, a complex case of pronounced academic interest was investigated, while regarding the latter a thoroughly studied flow was re-examined from another point of view.

The main motivation lies on applications of cavitation with industrial or bio-engineering interest, involving complex topology or arbitrary moving boundaries. The use of Immersed Boundary method minimises the complexity and cost of grid generation and alleviates the difficulties arising from the use of conventional conformal grids, which demand continuous reconstruction and adaptation [11, 97, 112] or advanced complex techniques (over-set or sliding grids) [61, 139, 224]. The herein proposed method follows the *direct-forcing approach*, according to which the immersed body is modelled through addition of forcing source terms in the governing equations. The volumetric source terms are localised on the region covered by the Immersed Boundary, using a scalar field expressing the coverage of the computational cells by the solid. This formulation, which falls into the category of *indirect* boundary condition imposition Immersed Boundary methods, is preferred over *ghost-cell* or *cut-cell* approaches (*direct* boundary condition imposition), because it avoids the complexities and the computational burden of the latter. In addition, the forcing is applied not only on the cells intersected or in the immediate vicinity of the solid interface, but in the entire solid region. In this way, the sometimes cumbersome interpolation between Lagrangian and Eulerian frame of reference, employed by other *indirect* imposition methods, is also avoided.

The simplicity of the method makes it suitable for complex flow regimes, including phase change, strong shocks and compressibility effects, as well as Fluid Structure Interaction. A thorough assessment of the method is carried out for a wide range of flow regimes, with increasing complexity from laminar incompressible flows around stationary boundaries to highly turbulent cavitating flows past moving bodies. The performance of the method was satisfactory although some limitations of the method were identified, regarding spatial resolution and smoothness of the forcing term. These observations regard complex highly transient turbulent cavitating flows, are mainly driven by inadequate resolution for turbulent models to correctly treat the near wall region, and are not discouraging. Therefore, the method has been further applied on studies of complex cavitating and biological flows.

The high-speed impact of a solid projectile onto a flowing water jet was studied, so far only experimentally investigated [65]. Inviscid computations of the multiphase flow, involving liquid-vapour mixture and non-condensable gas were carried out; the phase interfaces were not

reconstructed, resulting in a diffused representation. Conventional boundary conformal grid simulations cannot accommodate the motion of the projectile, therefore it is the herein proposed method that enables us to unveil the rich dynamics and physical processes involved in this case. This study regards shock-wave interaction with material interfaces in a *fast-slow* configuration, where shocks are travelling from the liquid, with higher speed of sound, to the gas phase, with lower speed of sound, and the subsequent cavitation formation. The shocks released during impact, travel inside the liquid, interact with the convex liquid-gas interface, get reflected as rarefaction and generate cavitation. It is found that vapour cavities expand and collapse on the periphery of the jet and not in the vicinity of the solid projectile. High speed jetting, as a result of the impact, was also captured near the entry point. Finally, perturbations possibly related to Richtmyer-Meshkov instability were observed on the liquid-gas interface. The main mechanism of this instability is the miss-alignment of the density and pressure gradients during shock interaction with the interface, that produces baroclinic torque.

Moreover, the herein proposed methodology was applied on the thoroughly studied incompressible pulsatile flow through a bi-leaflet Mechanical Heart Valve, in a Fluid Structure Interaction framework, to provide additional information regarding shear stress development. The blood flow inside a model aorta, featuring a 180° bend, as well as Valsalva mimicking sinuses and three arterial bifurcations, which replicates the geometry of a natural aorta, was studied. This configuration has been used in laboratory experiments, under physiological conditions, to measure wall shear stress on the aorta along the systolic cycle, downstream of the valve, via a novel technique of flexible micro-pillars attached to the wall [128]. Because turbulence is not properly developed throughout the cycle, the flow was treated as laminar and no turbulence modelling was used and the blood was considered as Newtonian fluid, which are common practices for these flows. The simulations tried to provide detailed quantitative information for the flow and the shear stresses on the aorta walls. For the calibration of the measuring apparatus, experiments were run without the valve; the numerical and the experimental results were found in excellent agreement. It is confirmed that the micro-pillars act as first order filter of the near wall velocity gradient and their accuracy depends upon their length. However, when the bi-leaflet valve is mounted on the aorta, the developed flow quickly becomes chaotic; the vortex street generated on the wake of the leaflets interacts with the shear layer on the root of the bend and with the growing recirculation area on the apex of the bend, and the large well organised vortices are break-down into small scale structures. For this case, the computational shear stress estimates deviate from the experimental measurements. The delicate nature of the flow, with the transitional turbulent regime and the complex vortical structures of wide range of length scales, prevent us from drawing safe conclusions, however they indicate the need of more precise numerical investigation and thorough resolution of all turbulent scales, which can be achieved by means Large Eddy Simulations.

The method has been successfully applied to the aforementioned cases where conventional techniques are not easily or at all applicable, and provided useful insights on the flows under examination. However, cavitating and biological flows have been studied separately. A synthesis, where the proposed method is employed to investigate cavitation development in bio-engineering applications, is yet to be performed.

Future applications of the method, could be oriented to bio-engineering flows. Advanced computational techniques, like Large Eddy Simulations, should be employed to extend the numerical investigation of the pulasatile flow through Mechanical Heart Valve on model aor-

tas incorporating curvature and arterial bifurcations; novel tri-leaflet valves, additional to the standard bi-leaflet, could be examined. Moreover, potential cavitation initiation in biological flows should be addressed; the potential link of cavitation with *hemolysis* and *thrombosis* should be investigated. Finally, a rather sophisticated extension, yet of high potential, of the method towards Fluid Structure Interaction problems involving with structural deformation, could could enable the investigation of highly complex physical problems including cavitation interaction with vascular soft tissue or novel targeted drag delivery techniques.

Regarding the performance of the herein proposed method, although it has been successfully employed on complex numerical studies, room for improvement exists. The pressure gradient imposition across the fluid-solid interface via source terms, proposed for direct forcing methods for compressible flows by Riahi et al. [186], could be easily incorporated in the methodology and its influence on cases of cavitating flows could be investigated; with the current formulation forcing is added to the momentum equation and no-slip condition is only applied inside the solid region, while the flow is let to evolve naturally. In addition, the influence of the implicit treatment of the forcing source term, via linearisation [16, 152], could be examined; this could reduce the stiffness of the equations, alleviate force oscillations observed in highly transient turbulent flows accelerate convergence and eventually improve the method. Moreover, regarding Fluid Structure Interaction, the sensitivity of the Runge-Kutta time-integrator to solve solid body motion equations suggests consideration of more robust techniques, like *Lagrange-Hamilton* formulations [103] and Verlet (leap-frog) algorithms [55]. Finally, the coupling of the direct forcing Immersed Boundary method with an automatic mesh refinement algorithm would ensure an adequate mesh resolution near the immersed solid wall to enhance the performance of turbulent models and further improve the efficiency of the method.

The herein developed methodology and the current research work try to contribute to the ongoing struggle to thoroughly investigate and deeply understand Fluid Dynamics. This Thesis intends to provide the tools for more elaborate and complex numerical investigations.

Appendix A

Derivation of URANS equations

According to the *Reynolds-Averaged Navier-Stokes* equations approach, the governing Navier-Stokes equations are time-averaged, so as the flow at any given time-instant can be described by turbulent fluctuations over an average flow field. In other words, the flow quantities (velocity, pressure, energy) can be decomposed in to an average (mean) value (bar) and a fluctuation (prime):

$$\phi(\mathbf{x}, t) = \bar{\phi}(\mathbf{x}, t) + \phi'(\mathbf{x}, t)$$

The time-averaged value, over a temporal window T, is computed as:

$$\bar{\phi}(\mathbf{x}, t) = \frac{1}{T} \int\limits_{t}^{t+T} \phi(\mathbf{x}, t) \mathrm{d}t$$

For the sake of simplicity, the incompressible Unsteady RANS *(URANS)* are derived here, using the incompressible NS 2.7. First the flow variables are decomposed into mean and fluctuating parts, and then the equations are time averaged, which yield the form of A.1.

$$\overline{\nabla \cdot (\bar{\mathbf{u}} + \mathbf{u}')} = 0$$

$$\overline{\rho \frac{\partial(\bar{\mathbf{u}} + \mathbf{u}')}{\partial t} + \rho \nabla \left((\bar{\mathbf{u}} + \mathbf{u}')(\bar{\mathbf{u}} + \mathbf{u}')\right)} = \overline{-\nabla(\bar{p} + p') - \mu \nabla \cdot (\nabla(\bar{\mathbf{u}} + \mathbf{u}') + \nabla(\bar{\mathbf{u}} + \mathbf{u}')^T) + \mathbf{S}}$$

$$(A.1)$$

The process of averaging the equations, follows some rules:

$$\overline{\phi'(\mathbf{x}, t)} = 0 \qquad \overline{\bar{\phi}(\mathbf{x}, t)\psi(\mathbf{x}, t)} = \bar{\phi}(\mathbf{x}, t)\bar{\psi}(\mathbf{x}, t)$$

$$\overline{\bar{\phi}(\mathbf{x}, t)} = \bar{\phi}(\mathbf{x}, t) \qquad \overline{\phi(\mathbf{x}, t)\psi(\mathbf{x}, t)} = \bar{\phi}(\mathbf{x}, t)\bar{\psi}(\mathbf{x}, t) + \overline{\phi'(\mathbf{x}, t)\psi'(\mathbf{x}, t)}$$

$$\overline{\nabla\phi(\mathbf{x}, t)} = \nabla\bar{\phi}(\mathbf{x}, t) \qquad \overline{\bar{\phi}(\mathbf{x}, t)\psi'(\mathbf{x}, t)} = 0$$

$$\overline{\phi(\mathbf{x}, t) + \psi(\mathbf{x}, t)} = \bar{\phi}(\mathbf{x}, t) + \bar{\psi}(\mathbf{x}, t)$$

For the continuity equation, where only the decomposed velocity field appears, the derivation is straightforward:

$$\overline{\nabla \cdot (\bar{\mathbf{u}} + \mathbf{u}')} = 0 \Rightarrow \nabla(\bar{\bar{\mathbf{u}}} + \overline{\mathbf{u}'}) = 0 \Rightarrow \nabla\bar{\mathbf{u}} = 0$$

Similarly, for the momentum equation, it is:

$$\rho \frac{\overline{\partial (\bar{\mathbf{u}} + \mathbf{u}')}}{\partial t} + \rho \overline{\nabla \left((\bar{\mathbf{u}} + \mathbf{u}')(\bar{\mathbf{u}} + \mathbf{u}') \right)} = \overline{-\nabla(\bar{p} + p')} - \mu \overline{\nabla \cdot \left(\nabla(\bar{\mathbf{u}} + \mathbf{u}') + \nabla(\bar{\mathbf{u}} + \mathbf{u}')^T \right)} + \mathbf{S}$$

$$\Rightarrow \rho \frac{\partial \bar{\mathbf{u}}}{\partial t} + \rho \nabla \cdot \overline{(\bar{\mathbf{u}}\bar{\mathbf{u}} + \bar{\mathbf{u}}\mathbf{u}' + \mathbf{u}'\bar{\mathbf{u}} + \mathbf{u}'\mathbf{u}')} = -\nabla \bar{p} - \mu \nabla \cdot \left(\nabla \bar{\mathbf{u}} + \nabla \bar{\mathbf{u}}^T \right) + \mathbf{S}$$

$$\Rightarrow \rho \frac{\partial \bar{\mathbf{u}}}{\partial t} + \rho \nabla \cdot \left(\overline{\bar{\mathbf{u}}\bar{\mathbf{u}}} + \overline{\mathbf{u}'\mathbf{u}'} \right) = -\nabla \bar{p} - \mu \nabla \cdot \left(\nabla \bar{\mathbf{u}} + \nabla \bar{\mathbf{u}}^T \right) + \mathbf{S}$$

$$\Rightarrow \rho \frac{\partial \bar{\mathbf{u}}}{\partial t} + \rho \nabla \cdot (\bar{\mathbf{u}}\bar{\mathbf{u}}) = -\nabla \bar{p} - \underbrace{\mu \nabla \cdot \left(\nabla \bar{\mathbf{u}} + \nabla \bar{\mathbf{u}}^T \right)}_{\nabla \cdot \tilde{\tau}_{ico}} - \underbrace{\rho \nabla \cdot (\overline{\mathbf{u}'\mathbf{u}'})}_{\nabla \cdot \tilde{\tau}_R} + \mathbf{S}$$

Eventually, the final form of incompressible URANS is given by A.2. The Reynolds stresses tensor $\tilde{\tau}_R$, introduces six new unknowns, which are not solved for but rather handled by turbulence models. For the case of compressible flow, the derivation is performed in an analogous manner.

$$\nabla \cdot \bar{\mathbf{u}} = 0 \tag{A.2a}$$

$$\rho \frac{\partial \bar{\mathbf{u}}}{\partial t} + \rho \nabla \cdot (\bar{\mathbf{u}}\bar{\mathbf{u}}) = -\nabla \bar{p} - \nabla \cdot \left(\bar{\tilde{\tau}}_{ico} + \tilde{\tau}_R \right) + \mathbf{S} \tag{A.2b}$$

Appendix B

Vortex Induced Vibrations

Immersed boundary methods prove useful for Fluid Structure Interaction (*FSI*) problems, because the complexities of transforming body conformal meshes are diminished. Sotiropoulos and Yang [209] report various FSI applications of IB methods, raging from mechanical structures, such as wind turbines, to biological flows, such as insect flight. The solid body may be considered completely rigid, as in the work of Zhong et al. [255] on vibrating rigid bodies due to vortex shedding or the study of flow through bi-leaflet Mechanical Heart Valve by Borazjani [17], or fully deformable as in the work of Pasquariello et al. [175], where a cut-cell finite-volume immersed boundary method is coupled with finite element solid solver.

Vortex induced vibrations *(VIV)* of structures submerged into a free-stream, is a benchmark FSI problem [209, 238]. VIV is the result of low Reynolds incompressible flow over an elastically mounted rigid cylinder, which is let free to oscillate under the influence of the aerodynamic or hydrodynamic forces. The oscillation of the cylinder, in its turn, influences the flow field. This flow regime yields rich and complicated flow patterns with important characteristics, relevant to many engineering applications.

The main characteristics of VIV, are the amplitude and the frequency of the structure's oscillation, as well as the mode and the frequency of the vortex shedding. A situation of high importance is the *lock-in* or *synchronization* of the shedding with the vibrations. This state is achieved when the shedding and the vibration frequencies match [206] or reach the natural frequency of the dynamic system of the structure [238]. In the state of *synchronization*, the maximum of the amplitude of the vibrations is observed.

The flow-structure system is very sensitive and small changes in the parameters may result in completely different flow regimes. Hysteresis phenomena between the shedding and the vibration may be observed close to the *lock-in* region. In the case of varying free-stream velocity, hysteresis may be even observed in different conditions, depending whether the velocity is increasing or decreasing. Moreover, depending on the flow regime, different vortex shedding modes are observed. When two *single* vortices are shed on the wake of the cylinder per cycle, the mode is dubbed *2S*. When two *pair* of counter-rotating vortices are released per cycle, the mode is dubbed *2P*. A *P+S* pattern (one single and one pair of vortices per cycle) is also reported, especially on controlled vibrations studies [238].

A comprehensive review study on the advances and the findings of the research on VIV, can be found in the work of Williamson and Govardhan [238].

Hereafter, an indicative parametric study is presented, which aims to assess the performance of the developed immersed boundary method in FSI problems.

B.1   Numerical Set-up

The equations of motion for the center of gravity of the immersed solid body, in the case of two-dimensional motion with two degrees of freedom (d.o.f.) ($\mathbf{q} = (x, y)$), define *M-C-K* (mass, damper and spring) dynamic system of B.1. Figure B.1 illustrates the two-dimensional dynamic system for a cylinder immersed in a free stream.

$$\ddot{\mathbf{q}} + \frac{c}{m}\dot{\mathbf{q}} + \frac{k}{m}\mathbf{q} = \frac{\mathbf{F}}{m} \tag{B.1}$$

with $\zeta = c/m$ the structural damping ratio, k the spring coefficient. The dynamic system is highly characterised by its natural frequency $f_n = \omega_n/2\pi = \sqrt{k/m}/2\pi$. If a time evolving external load $\mathbf{F}(t)$ is applied to the system with an oscillating frequency matching or approximating the system's natural frequency, the displacement is *synchronised* with the loading and may receive very large values. The *damping* can control the excitation of the system and diminish the impact of *synchronisation*.
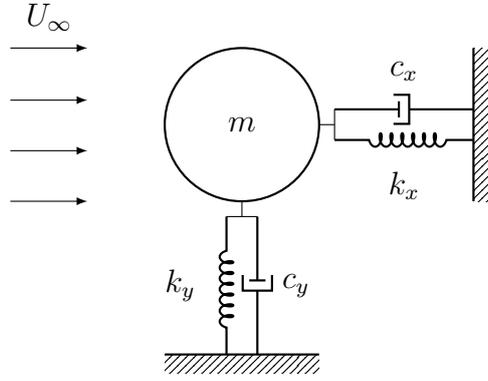
Figure B.1: A two-dimensional *M-C-K* dynamic system, comprising from a mass m (cylinder), a damper of coefficient c and a spring of elastic modulus k on each axis.

A common practice in *FSI* problems is to normalise the acceleration, velocity and displacement ($\ddot{\mathbf{q}}, \dot{\mathbf{q}}, \mathbf{q}$), using the characteristic velocity and length of the flow, in order to highlight the coupling. In this way, the coupling between the solid and the fluid is better illustrated, as quantities that characterise the physical problem appear in the place of the coefficients or the solving variables. Following Prasanth [183], using the upstream velocity U_∞ and the diameter D of the cylinder, we can define the normalised variables $\mathbf{Q}_n = (X_n, Y_n)$ as:

$$\begin{cases} \mathbf{Q}_n = \mathbf{q}/D \\ \dot{\mathbf{Q}}_n = \dot{\mathbf{q}}/U_\infty \\ \ddot{\mathbf{Q}}_n = (\ddot{\mathbf{q}} \cdot D)/U_\infty^2 \end{cases}$$

and derive from B.1 the following form for the motion equation:

$$\begin{cases} \ddot{X}_n + 4\pi F_n \dot{X}_n + (2\pi F_n)^2 X_n = 2C_D/\pi m^* \\ \ddot{Y}_n + 4\pi F_n \dot{Y}_n + (2\pi F_n)^2 Y_n = 2C_L/\pi m^* \end{cases} \tag{B.2}$$

with $F_n = f_n D/U_\infty$ the reduced natural frequency, C_D and C_L the drug and lift coefficients, $m^* = 4m/\pi\rho_\infty D^2$ the dimensionless mass of the cylinder, and finally $U^* = U_\infty/f_n D = 1/F_n$ the reduced velocity.

These newly introduced coefficients, better illuminate the coupling between the fluid and the solid. The dimensionless mass expresses the mass ratio between the solid and the fluid (occupying the same volume) and the reduced frequency can be seen as the relative velocity between the two mediums. Although in the following analysis the aforementioned form of B.2 is not adopted, the reduced velocity will be used as a basis for the comparison of the computational results.

Within the framework of forcing Immersed Boundary approach, the force applied on the cylinder is calculated as the integral of the source term over the volume of the domain:

$$\mathbf{F} = -\int_V \rho \cdot \mathbf{F}_{IB} dV \tag{B.3}$$

Herein, the system of differential equations B.1 is solved, using an Runge-Kutta time advancing algorithm. An adaptive time-step technique is used to ensure the solution does not diverge, by slowly advancing with multiple sub-steps, from the old to the new time-step. The incompressible NS 2.7 are solved for the fluid, using an explicit *Euler* time-stepping and an *upwind* interpolation scheme for the fluxes.

In order to numerically solve the motion equations B.1 for the position vector $\mathbf{q}$, a common practise is for the second order differential equation to be split into a first order differential system of two equations. By taking into account the relation between position, velocity and acceleration, $u_i = \dot{q}_i$ and $\ddot{q}_i = \dot{u}_i$, for the ith d.o.f., the 2nd derivative of the position can be replaced by the 1st derivative of the velocity in B.1, so that we get the system B.4.

$$\dot{u}_i = -\frac{c}{m}u_i - \frac{k}{m}q_i + \frac{F_i}{m} \tag{B.4a}$$

$$\dot{q}_i = u_i \tag{B.4b}$$

If the state vector $\mathbf{w}_i = [u_i, q_i]^T$ is introduced, the system can take the compact form of B.5, for each d.o.f. i, resulting into four first order differential equations that fully determine the dynamic response of the solid into the excitation from the aerodynamic or hydrodynamic forces.

$$\begin{bmatrix} 1 & 0 \\ 0 & 1 \end{bmatrix} \begin{bmatrix} \dot{u}_i \\ \dot{q}_i \end{bmatrix} + \begin{bmatrix} c/m & k/m \\ -1 & 0 \end{bmatrix} \begin{bmatrix} u_i \\ q_i \end{bmatrix} = \begin{bmatrix} F_i/m \\ 0 \end{bmatrix} \tag{B.5a}$$

$$\Rightarrow \mathbf{A} \cdot \dot{\mathbf{w}}_i + \mathbf{B} \cdot \mathbf{w}_i = \mathbf{S}_i \tag{B.5b}$$

The same set-up as for the incompressible flow past static cylinder, presented in chapter 3, is used. Moreover, the aforementioned case used as initialisation, as it is preferable to have a fully developed flow and vortex street before letting the cylinder free to oscillate.

B.2 Results and Discussion

In the following, a parametric study is performed with varying the reduced velocity U^*. The dynamic parameters $m* = 10$, $\zeta = 0$ are chosen in order to observe oscillations of larger amplitude. These, as well as the free-stream velocity, are kept constant, so that the spring coefficient k of the system is determined solely by the value of U^* and the Reynolds number is fixed at $Re = 100$. However, usually in VIV studies both the reduced velocity (and therefore frequency) and the Reynolds number vary. This is followed primarily in experiments as it is far more practical to calibrate the inflow velocity than change the spring constant, but extends to computational works which often take the experimental works as reference.

The results hereafter are assessed against the findings reported in the studies of Zhong et al. [255], Chern et al. [40], Singh et al. [206]. However, the comparison is not always consistent as not all type of parameters presented here are reported in all of the aforementioned works.

Zhong et al. [255] reports a lock-in region for $4.4 < U^* < 7.7$, whereas Prasanth [183] reports the lock-in range at $4.6 < U^* < 8.4$. The present study, identifies a slightly wider lock-in region, with the lower edge closed to the aforementioned works but the higher edge moved to higher values than Prasanth; synchronisation occurs for values of the reduced velocity in the interval $[4.6, 9.0]$. As seen in figure B.2, although good agreement is observed in the lower edge of the lock-in region for the current and the reported numerical results of Singh et al. [206] and Zhong [255], a definite deviation exists in the upper edge of the region.
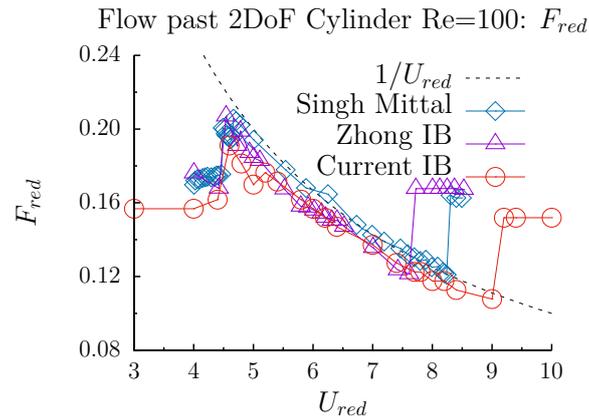
Figure B.2: Reduced frequency dependence on reduced velocity, for flow over Cylinder, with 2 degrees of freedom (d.o.f.), at $Re = 100$.

In figures B.3 and B.4 the aerodynamic load coefficients and the characteristic quantities of the 2 d.o.f oscillations are presented. The results of the current computations are compared to results from different sources of the literature and small deviations are easily spotted. Although the overall trends are accurately captured by the current method, small hysteresis or complete slight shift to larger values of reduced velocities are clear. In addition some maxima and minima, with regards to R.M.S. value of the horizontal (in-line) oscillation's amplitude A_x, are not captured; these correspond to instabilities arising towards the end of the lock-in region. The discrepancies amongst the reported data of Chern et al. [40] and Singh et al. [206], in terms of lift coefficient and vertical oscillation amplitude A_y have to be noted as well.

To illustrate the influence of the reduced frequency U^*, and essentially of the spring coefficient k, over the induced vibrations of the cylinder, the oscillation of the body on the horizontal
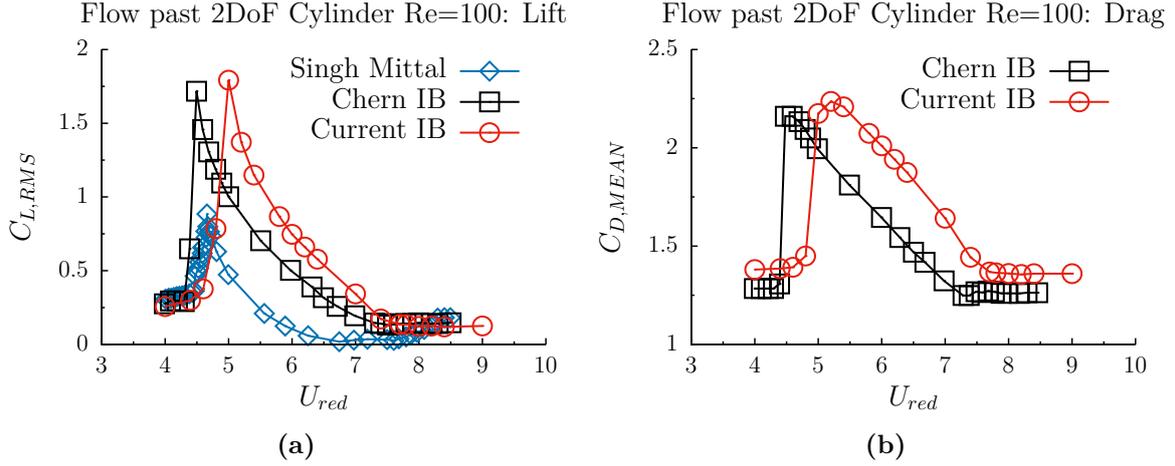
Figure B.3: Force coefficients dependence on reduced velocity for flow over Cylinder, with 2 degrees of freedom (d.o.f.), at $Re = 100$.
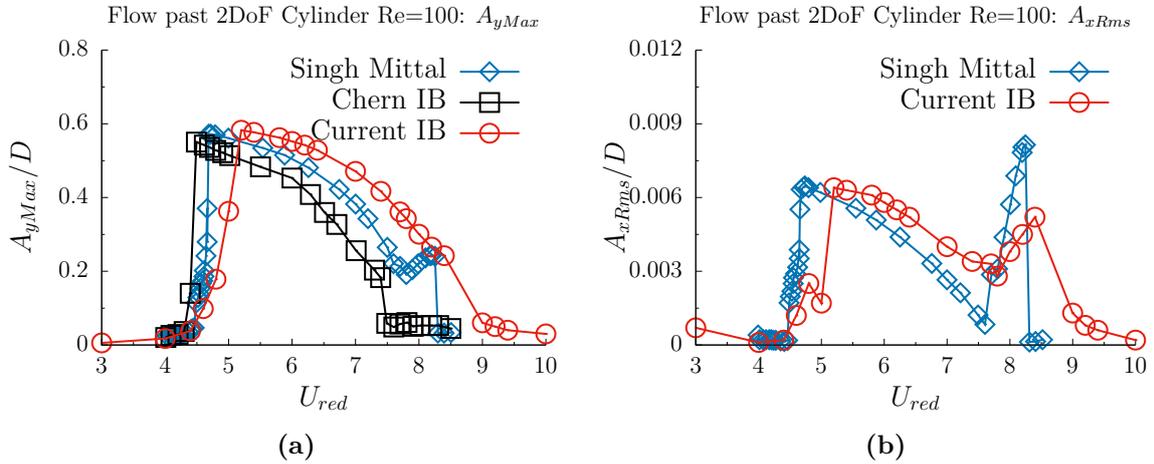
Figure B.4: Displacement characteristic estimates for flow over Cylinder, with 2 degrees of freedom (d.o.f.), at $Re = 100$.

and vertical axes, for four indicative regimes ($U^* = 4.8, 5, 6.2, 8$), are presented in figure B.5. It is visible that apart from the case of $U^* = 6.2$, a secondary oscillation is observed; for the horizontal oscillation the equilibrium position is periodically displaced and for the vertical the oscillating amplitude periodically changes. For $U^* = 4.8$ these secondary oscillations are in sync and yield a period of approximately 60 dimensionless time units, whereas for $U^* = 5$ the period exceeds 200. For the case of $U^* = 8$ though, the response of oscillating cylinder changes after $t^* = 180$ and the equilibrium position for the horizontal vibrations on one hand, and the amplitude of the vertical oscillations on the other, show a tendency to increase. The total simulated time, of $t_{total}^* = 360$, seem not enough to capture the full dynamics for the latter case. Maybe if the computations have not been halted, the maximum A_y and mean A_x would be different and plot in figure B.4 would compare better with the literature.

To illustrate the influence of the reduced frequency U^* on the shedding patterns, the vorticity contours for the for four aforementioned regimes are presented in figure B.6. Vortex
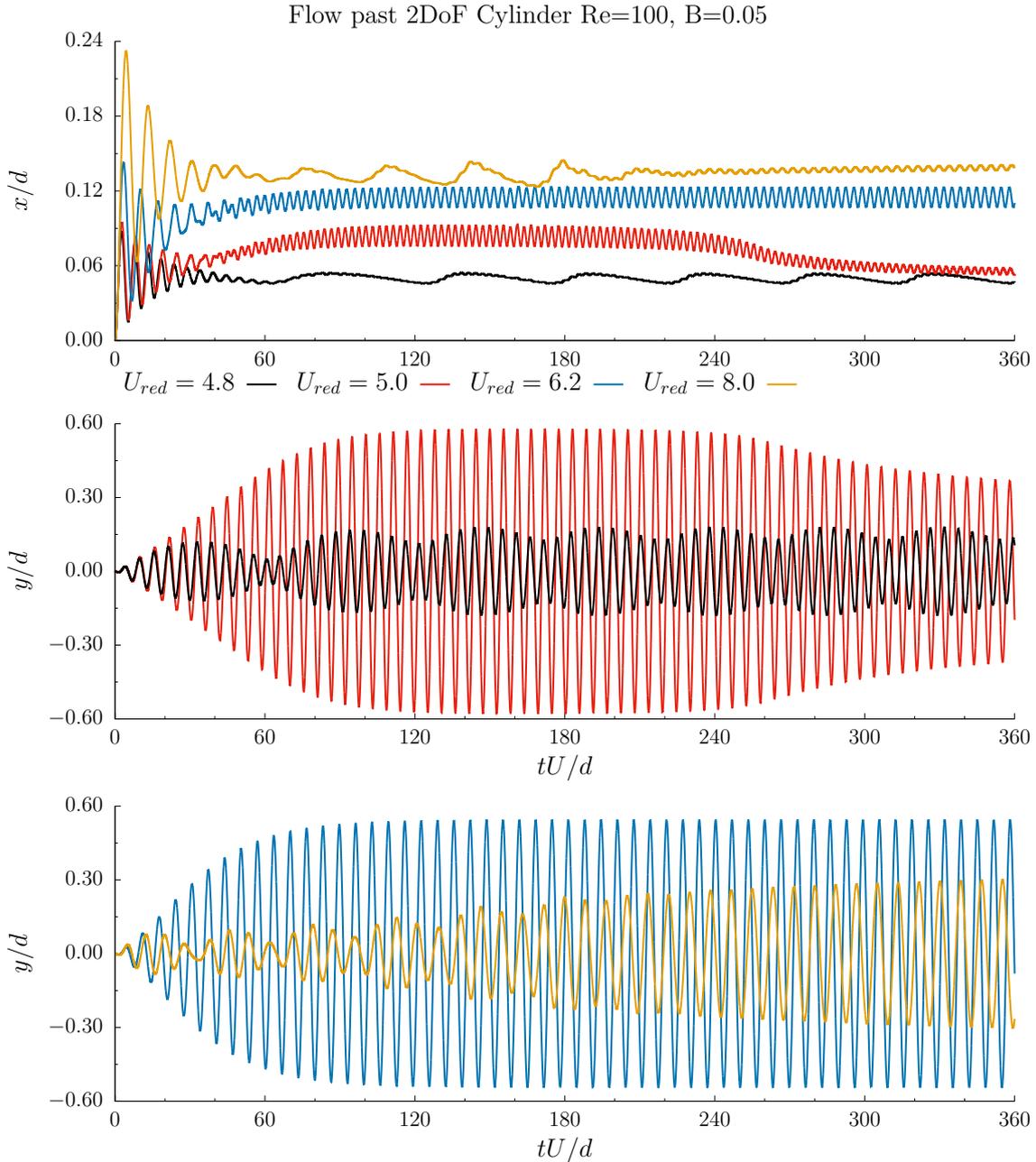
Figure B.5: In-line (top) and cross-directional oscillation evolution through time, for four different reduced velocities, for flow over Cylinder, with 2 degrees of freedom (d.o.f.), at $Re = 100$. (The cross-directional oscillation is presented in two plots, each presenting only two of the four cases, for sake of clarity.)

shedding of mode *2S* can be observed for most cases of low or high U^*, with varying shedding frequency, but for $U^* = 5$, which is close to beginning of the lock-in region, vortex shedding switches to type *2P*. The difference in shedding frequency is nicely illustrated from the height of the vortex street and the distance between the shed vortices.

The discrepancies between the results of the current simulations and those reported in the aforementioned literature, [40, 206, 255], regarding either the prediction of wider lock-in region
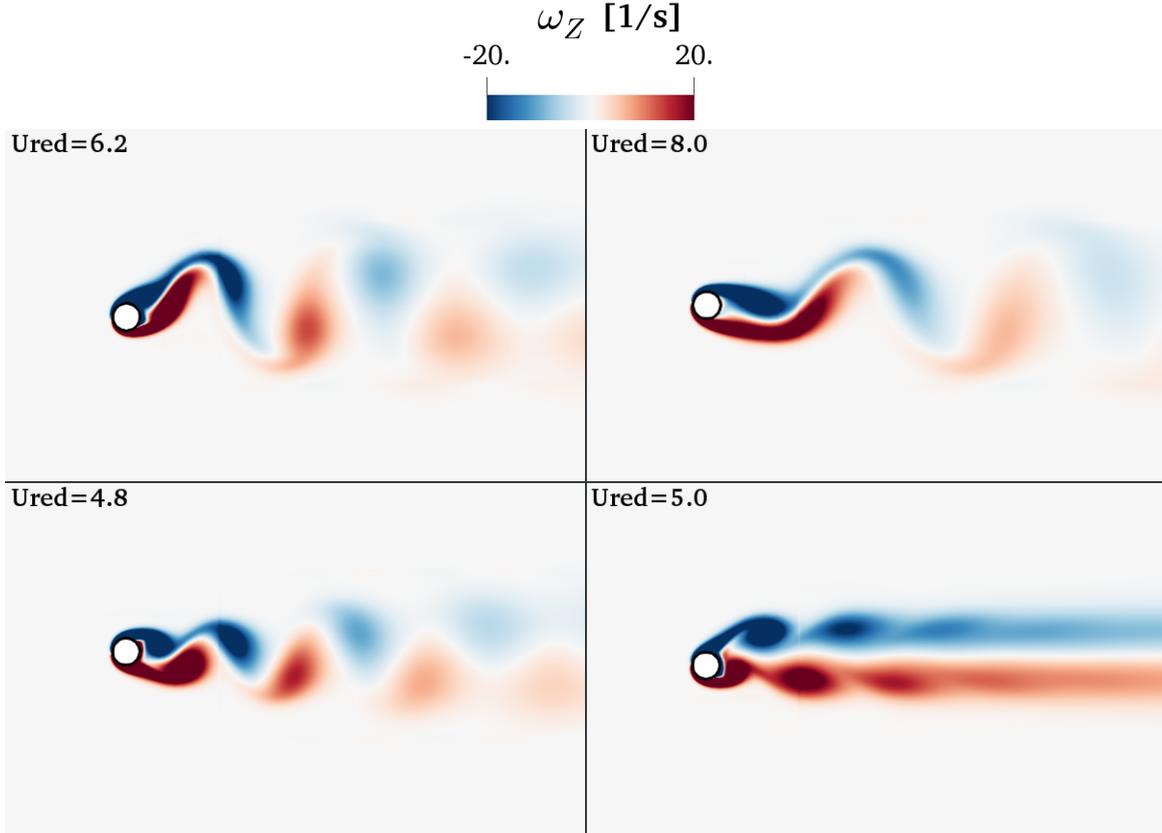
Figure B.6: Off-plane vorticity contours, for four different reduced velocities for flow over Cylinder, with 2 degrees of freedom (d.o.f.), at $Re = 100$.

or deviations in vibration amplitudes, might be caused by the *loose coupling* of the solid and fluid solvers or the explicit evaluation of the IB forcing. Moreover, regarding the flow field, higher-order time-advancing and interpolation schemes would definitely improve the solution of the fluid which would enhance in turn the dynamics of the solid motion.

In addition, the use of the Runge-Kutta time-integrator to solve B.1 might be a source of inaccuracies. It is a common practise to solve the motion equations in a *Lagrange-Hamilton* form [103] and employ alternative time-integrator, such as a Verlet (leap-frog) algorithm which promise more accurate and more robust results [55].

Finally, the convergence of the system in a "stable" oscillatory regime is not trivial. Reaching convergence might be a slow procedure of high computational cost; Chern et al. [40] report their longest simulation, in order to reach $t^* = 1000$, to last 20 days. In the present study the total simulated time might have not been adequate to capture the full dynamics and reach converged response for some flow regimes.

Taking into account these discrepancies, the possible causes as well as the complexity of the problem, it can be concluded that the overall performance of the herein proposed IB method, in the application on FSI problems, is found satisfactory.

127

Appendix C

Flow through bi-leaflet Mechanical Heart Valve in Axisymmetric Aorta

A preliminary study of the pulsatile flow through an idealised bi-leaflet Mechanical Heart Valve (MHV) is presented herein. The leaflets of the valve are represented by a triangulated surface mesh and are modelled as immersed boundaries, utilising the proposed method, whereas the casing is considered as a conventional wall boundary. The leaflets are show in figure C.1 in fully closed and fully open position, inside the valve casing represented by its inner wall. The rotation of the leaflets is induced by the flow.

The case configuration and the geometries of both the computational domain and the valve itself, are in accordance to the experimental work of Dasi et al. [47] and the computational studies of Borazjani et al. [19]. Initially the flow was studied experimentally [47], providing detailed information on the velocity profiles and off-plane vorticity structures through PIV measurements, as well as leaflet kinematics. In addition, the experiments are supported by numerical simulations employing a ghost-cell Immersed Boundary method, where the leaflet rotation is prescribed by measured kinematics from the experiment. Later, the aforementioned ghost-cell IB method was extended to accommodate Fluid-Structure Interaction computations and the flow was studied in a FSI context [19]. Both the leaflet solid body kinematics and the vorticity dynamics where validated against to the experimental findings and found in good agreement.

The studies [19, 47] refer to a *St. Jude Regent 23 mm* valve. Its geometry is drastically simplified in the numerical simulations, so that the casing and the hinge mechanism are neglected and the leaflets are represented by semicircle disks. The model used herein, presented in figure C.1, is reproduced following the same philosophy, with geometric details extracted from [19]. However, the model used herein, may differ from the actual geometry or the one used in the referenced works [19, 47].

The aim of this study is to validate the proposed IB method and assess its performance on complicated flows of bio-engineering interest, including fluid-structure interaction, pulsatile inflow conditions and transition to turbulence, as well as to investigate the influence of the temporal and spatial discretisation and schemes on the numerical solution. Validation is performed against experimental and computational data referenced in [19].

(a) Fully Closed   **(b)** Fully Open
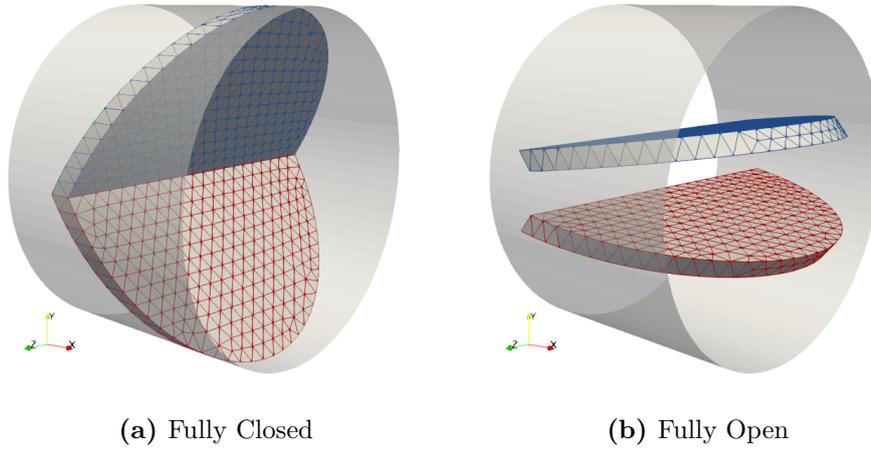
Figure C.1: The idealised model of the bi-leaflet Mechanical Heart Valve, enclosed by the casing inner surface. The two leaflets are represented by triangulated surfaces and are shown in fully closed (a) and fully closed (b) position, at $\theta = 20^o$ and $\theta = 73^o$, relative to the vertical plane Oyz, respectively.

Pulsatile In-Flow

The flow is driven by the unsteady flow rate show in figure C.2, assigned as an inlet boundary condition. The total duration of the cardiac cycle is $T_c = 860\ ms$, while the systolic (acceleration and deceleration) phase lasts for $T_{sys} \approx 450\ ms$.
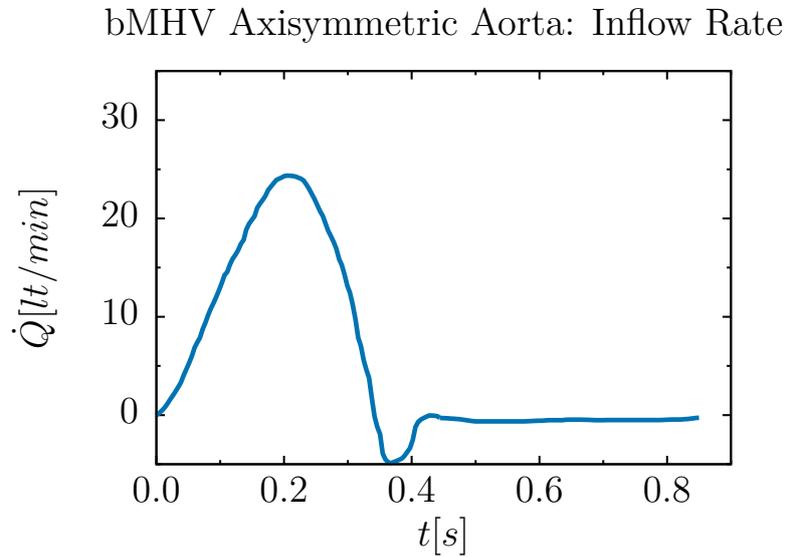
Figure C.2: Axisymmetric bMHV simulation: The flow rate, extracted by [19], used in the simulations. The cycle lasts $T_c = 860\ ms$ and the systolic phase $T_{sys} \approx 450\ ms$.

The developed pulsatile flow is characterised by the nondimensional Womersley number [239], which is calculated as the ratio of inertial and viscous forces, as in relation 5.1, and expresses the lag between the pressure pulse that generates the flow and the velocity profile. During a pulse generated flow through a pipe, the velocity profile may deviate significantly

from the well-known parabolic profile of the *Poiseuille* flow [250]. For low Womersley numbers, viscous forces dominate the flow and a parabolic velocity profile develops. For higher values, the inertial forces dominate and the influence of viscosity is limited near the rigid walls; therefore the parabolic velocity profile gets disturbed and flattens towards the core of the pipe.

Although analytic expressions of the velocity profile as function of the flow Womersley number have been derived by Sexl, Womersley, Uchida, McDonald and Milnor [250], in the present studies a uniform velocity profile is assigned at the inlet; similar approach is followed in the referenced studies [19, 47].

Motion of the Leaflets

The rigid solid leaflets are modelled as immersed boundaries and their motion is coupled with the flow through a FSI approach of *loose coupling* for undeformable bodies. An assessment of the FSI algorithm for the proposed IB method is presented in Appendix B, where the applicability of the method on Vortex Induced Vibrations is addressed.

The rotation of the leaflets around the hinges' axes is governed by the equation 2.27b, which is repeated here for sake of completeness:

$$\tilde{\mathbf{I}}_R \cdot \frac{\partial^2 \theta}{\partial t^2} = \mathbf{M}_{ext} \tag{C.1}$$

The moment of inertia tensor is calculated with regards to the center C_H of the rotation (hinge's) axis for each leaflet, which is parallel to the Oz axis of the coordinate system:

$$\tilde{\mathbf{I}}_R = [I_{ij}] \Rightarrow I_{ij} = \sum_{k=1}^{N} dm_k \left(|\mathbf{r}_k|^2 \cdot \delta_{ij} - x_i x_j \right), \quad i, j = x, y, z$$

where dm_k is the elementary mass of each element k of the solid leaflet, $\mathbf{r}_k$ the distance vector of each elementary mass from the center of rotation C_H and δ_{ij} the Kronecker delta:

$$\delta_{ij} = \begin{cases} 1, & i = j \\ 0, & i \neq j \end{cases}$$

The MHV is composed by a polycabronate material [19] with density $1750 kg/m^3$ and the mass is uniformly distributed on the solid IB surface.

The rotation angle θ_z is limited between $\theta_{min} = 0^o$ and $\theta_{max} = 53^o$ [19, 47]. All other rotations and translations are constrained, therefore the system possesses a single degree of freedom. Gravity is neglected, as in [19], therefore the moment vector $\mathbf{M}_{ext}$ is composed by the moments of the hemodynamic forces only.

C.1   Numerical Set-up

The working fluid is assumed Newtonian, with density $\rho = 1000 \ kg/s$ and kinematic viscosity $\nu = 3.5e - 5 \ m^2/s$, as referenced in [19, 47]. This assumption is valid because although the blood is not a Newtonian fluid, it can be safely regarded that it behaves as such in larger vessels [226]. Based on the upstream pipe diameter and the peak bulk velocity, the Reynolds

number is estimated around 5960 in the experiments [47], while in the FSI computations is rounded up to 6000 [19]. Therefore the peak bulk velocity in the upstream pipe can be calculated about $U_p = 0.8\ m/s$. The Womersley number is estimated using the period of the systolic phase, $f = 1/T_{sys}$, at $Wn = 9.8$, a value that differs from the one reported in the experiments [47]; the values of the variables used in the formula in [47] are not clearly stated and a typographic error also exists. Finally, the experiments of [47], which act as a reference, are reported in atmospheric ambient conditions.

The computational set-up is extracted from the literature [19, 47]. The computational domain consists of a straight, axisymmetric model of an aorta, visible in figure C.3, which includes a sinus region adjacent to the valve, to mimic the Valsalva Sinuses. The casing of the valve is included in the computational domain, and thus it is taken into account by the background conformal mesh.

The domain extends $4D_o$ upstream the casing and $\sim 9D_o$ downstream of the sinus region, as seen in C.3a, where D_o represents the diameter of the inlet and outlet pipes. The casing constrains the flow domain because it has an internal diameter D_c, smaller than the inlet pipe, therefore a forward facing step forms upstream of the valve leaflets. On the other hand, as the valve is placed just upstream to the sinus region, which has a larger diameter D_s than both the casing and the pipes, a backward facing step is formed on the exit of the casing as the domain expands. The sinus diameter then transitions smoothly to the outlet pipe diameter D_o. The area of interest, including the valve casing and the sinus region, is shown in figure C.3b, where the aforementioned diameters are annotated; they are $D_o = 25.4\ mm$, $D_c = 21.3\ mm$ and $D_s = 31.75\ mm$. A three-dimensional view of the area of interest, where the valve is mounted is shown in figure C.4.

The domain is discretised by a non-uniform hexahedral mesh of 1.3M cells; a view of the computational mesh on slices *AA'* and *BB'*, parallel and perpendicular to the axis of the pipe respectively, is presented in figure C.5. The grid cells are clustering from the inlet and outlet towards the area of interest (MHV and Sinus bulbs), and near the rigid boundary walls to capture the interaction of the mean flow with the boundary layers, yielding $y^+ < 5$. In the casing, the cells exhibit edge ratio near to unity. Additional telescopic refinement is applied in an area enclosing the complete path of the valve leaflets, to secure the precise representation of the IB bodies and better capture the initiation of vortex shedding over the leaflets.

Parametric Studies

To assess the influence of the different numerical parameters on the computational results, a two-dimensional configuration is considered, the geometry of which corresponds to the mid-plane slice *AA'* of the three-dimensional domain. Although such a 2D configuration corresponds a 3D planar channel flow and not to a 3D pipe flow, it facilitates the quicker and computationally inexpensive test of numerical strategies.

Three different 2D hexahedral computational grids are used, shown in figure C.6. The coarse mesh consists of 31k cells, the medium of 76k and the fine of 220k cells. They are generated based on a reference hexahedral grid, with non-uniform distribution of the cells, using one, two and three levels of telescopic refinement respectively. The reference grid created using a *blocking* technique and has 81 cells along the diameter in the sinus region and the upstream and downstream pipe and 45 in the casing. Along the axis of symmetry the cell length increases from the area of interest towards the outlets. In addition, layering is employed
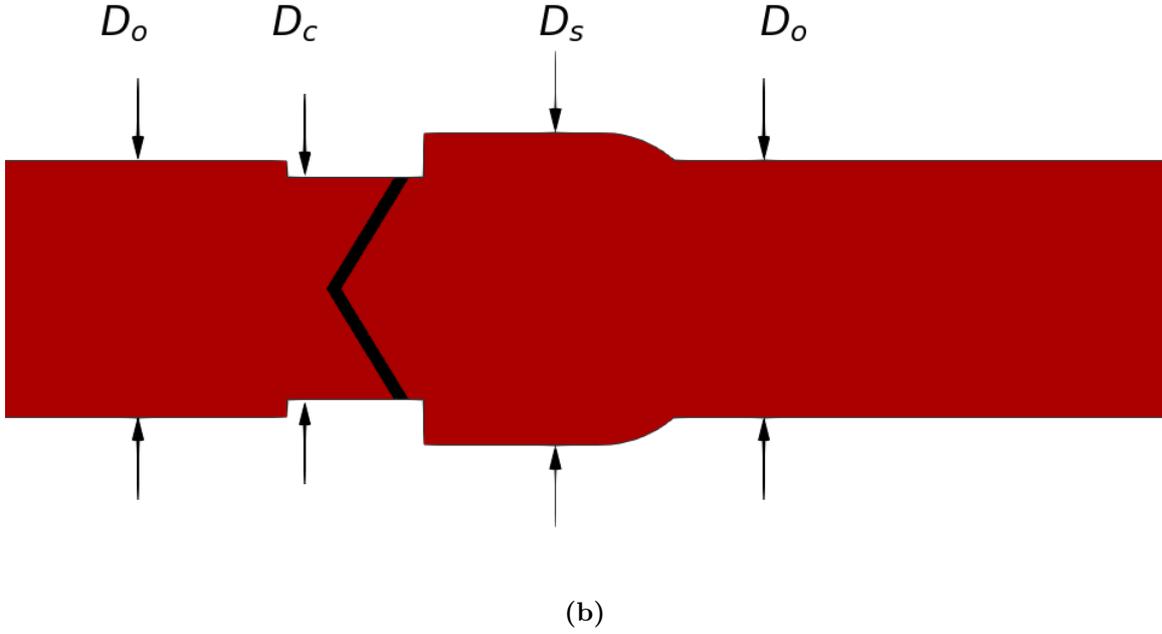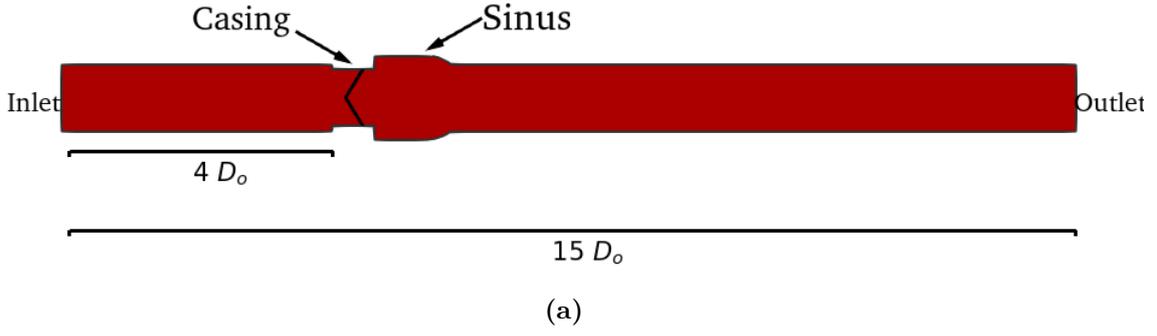
Figure C.3: Axisymmetric bMHV simulation: The computational domain. The basic lengths are presented. The entire domain is visible on the top, along with the position of the area of interest (MHV casing and Sinus region) relative to the inlet and outlet of the domain. A close up view of the area of interest, along with the characteristic diameters are shown on the bottom.

near the wall of the aorta, apart from inside the casing, to ensure again $y^+ < 5$ and, therefore, resolution of the boundary layers. During the telescopic refinement, each level divides the cells into two new cells in each direction.

Regarding the temporal and spatial discretisation, different schemes have been considered. For the advancement in time, either the first order *Euler* or the second order accurate *Crank-Nicolson* have been used. In a similar way, the fluxes, which for the incompressible flow it is expressed by the divergence of the velocity vector ($\nabla \mathbf{U}$), are discretised with an *Upwind* or *Linear- Upwind* schemes, achieving first or second order accuracy respectively.

To assess the influence of the different numerical parameters on the computational results, two parametric studies are carried out on the two-dimensional configuration, one for the spatial resolution and one for the numerical schemes. Combining different meshes, schemes and time-step size, six different cases are run for the 2D configuration; table C.1 groups all the
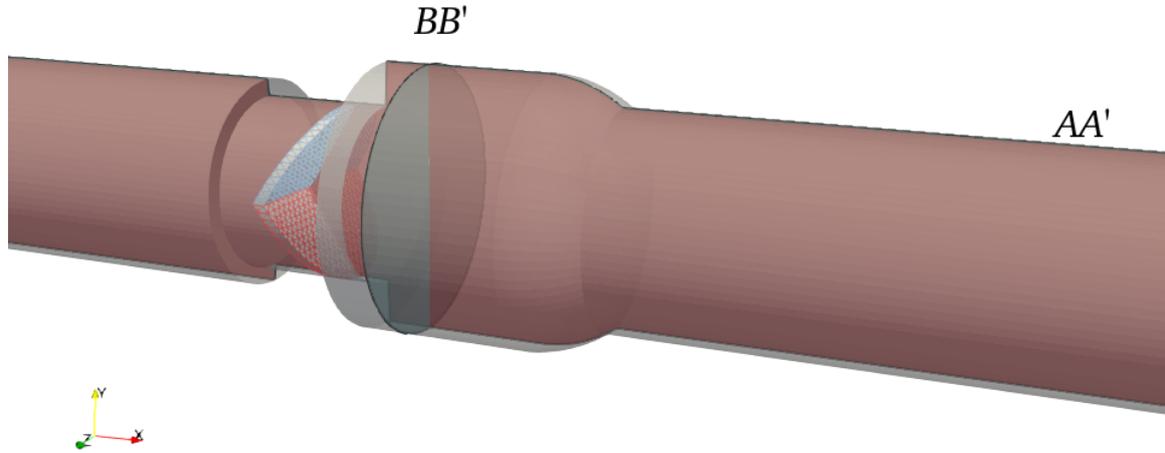
Figure C.4: Axisymmetric bMHV simulation: A close-up view of the area of interest, on three-dimensional computational domain with the two leaflets positioned in the casing. The vertical mid-plane *AA'*, along the axis of symmetry *Ox*, is used to present the results; it corresponds to the two-dimensional domain as well.

(a) AA' **(b)** BB'
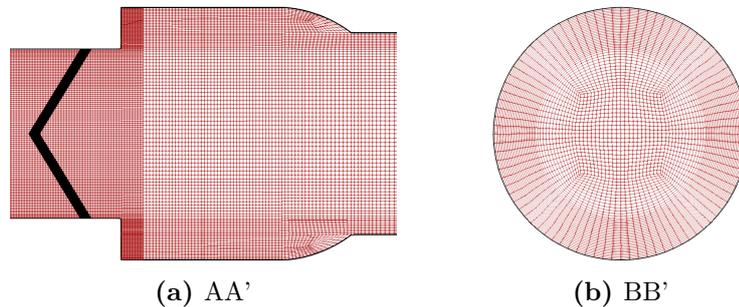
Figure C.5: Axisymmetric bMHV simulation: The three-dimensional grid, presented on vertical slices *AA'* and *BB'*, visible in figure C.4.

computational configurations.

A mesh independence study is performed using the three different grids, *Euler* time advancement and *Upwind* discretisation for the fluxes; the time step is limited by the Courant-Friedrichs-Lewy (CFL) condition $Co_{max} = \Delta t \Sigma_{faces} |\phi_i|/2V \leq 0.5$. This study refers to the configurations *CEU0.5, MEU0.5, FEU0.5* of table C.1. On the other hand, the different time and spatial schemes are evaluated by multiple simulations over the Medium mesh (76k); namely, with regards the table C.1, *MEU1.2* or *MEU0.5* for Euler and Upwind schemes, with fixed time-step $dt = 0.33\ ms$, or fixed $Co_{max} \leq 0.5$ and *MCL1.2* or *MCL0.5* for Crank-Nicolson and Linear-Upwind schemes, similarly with fixed time-step or Courant number. It has to be noted that the value of the fixed time-step is chosen to be the same used in the computations reported in the references [19, 47].

(a) Coarse **(b)** Medium **(c)** Fine
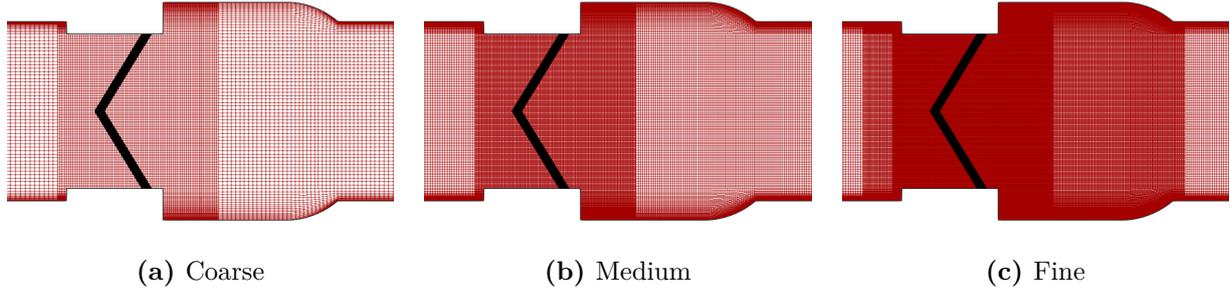
Figure C.6: Axisymmetric bMHV simulation: The three different meshes for the two-dimensional configuration: Coarse mesh with 31k cells (a), Medium mesh with 76k (b) and Fine mesh with 220k (c). The different grids are created by successive telescopic refinement passes.

Finally, the simulation on the 3D configuration aims to higher accuracy and thus employs second order accurate schemes (Crank-Nicolson, Linear-Upwind) and strict constraints of the time-step ($Co_{max} \leq 0.5$).

Turbulent scales

During a cardiac cycle, the flow through the blood vessels ranges from low up to moderate Reynolds numbers and therefore the transition to turbulence is not well established nor lasting. Especially, the flow downstream the heart valve and inside the sinus bulbs, exhibits chaotic behaviour. Turbulence modelling through RANS, with models tailored for flow of low Reynolds numbers and developed boundary layers, does not seem appropriate for such pulsatile flows and is generally avoided [146, 226]. On the other hand, DNS, LES, or even laminar, which neither resolve nor model turbulence scales, computations are favoured by researchers [19, 47, 146, 245].

In order to assess the required spatial resolution for the computational mesh to accurately capture all the turbulent structures, an estimate of the Kolmogorov scales may be used. The spatial η_k and temporal τ_k Kolmogorov scales can be calculated, based on the dissipation rate

Case ID	Cells	dt Scheme	$\nabla \mathbf{U}$ Scheme	Co_{max}	$dt_{mean}[s]$
2D configuration					
CEU0.5	31k	Euler	Upwind	0.5	$1.6 \cdot 10^{-4}$
MCL1.2	76k	C.-N.	Lin.-Upwind	2. <	$3.3 \cdot 10^{-4}$
MCL0.5	76k	C.-N.	Lin.-Upwind	0.5	$5.5 \cdot 10^{-5}$
MEU1.2	76k	Euler	Upwind	1.4	$3.3 \cdot 10^{-4}$
MEU0.5	76k	Euler	Upwind	0.5	$3.2 \cdot 10^{-5}$
FEU0.5	220k	Euler	Upwind	0.5	$1.4 \cdot 10^{-5}$
3D configuration					
3DCL0.5	1.3M	C.-N.	Lin.-Upwind	0.5	$7.1 \cdot 10^{-5}$

Table C.1: Computational details of the configurations used in the different numerical simulations of the pulsatile flow through bi-leaflet MHV.

ε as below:

$$\varepsilon = \frac{U_p^2}{D} = 21.808 \; m^2/s^3 \tag{C.2a}$$

$$\eta_k = \left(\frac{\nu^3}{\varepsilon}\right)^{1/4} = 3.74 \cdot 10^{-5} \; m \tag{C.2b}$$

$$\tau_k = \sqrt{\frac{\nu}{\varepsilon}} = 4. \cdot 10^{-4} \; s \tag{C.2c}$$

DNS calculations are reported in by Dasi et al. [47] and Borazjani et al. [19]. However there is not a mention or any analysis regarding the resolution of the turbulence scales; for the computational grid only the number of cells per direction is stated. The aforementioned computational domain is discretised by $201 \times 201 \times 241$ nodes, using 10 million hexahedral cells in total. Considering that 201 equidistant nodes are placed along the diameter of the pipes, on the upstream of the valve part the cell edge size is estimated at $dy = 0.127mm$, which yields $dy \approx 3.5\eta_k$.

In the herein presented three-dimensional simulation, the grid is has 74 cells along the diameter of the pipes, 96 along the diameter of the casing and 100 along the diameter of the sinus. The cells in the casing are uniformly spaced while in the pipes and sinus the cells cluster towards the walls, yielding $y^+ < 5$. In the area of interest, in the casing and the sinus bulbs, the edge ratio of the cells ranges from 1.25 to 1.67 and with regards the Kolmogorov scales $dy = 4 - 6\eta_k$ along the diameter.

Regarding the resolution of the temporal scales, the fixed time-step employed in [19, 47], which are assessed herein in the two-dimensional cases as well, with value $dt = 3.3 \times 10^{-4} \; s$, respects the limit set by the temporal Kolmogorov scale. In the case where the time-step varies based on the Courant-Friedrichs-Lewy condition, it is always ensured that $dt \ll \tau_k$, because in addition the maximum value of the time-step is limited at $dt \leq 10^{-4} \; s$.

C.2 Results

2D parametric studies

The simulations' results are primarily assessed based on the induced leaflets' kinematics. Regarding the two-dimensional parametric studies, the influence of mesh resolution on the leaflets' motion is presented in figure C.7 and the impact of the scheme choice and time-step size is illustrated in figure C.8. The different numerical configurations are discussed in terms of flow field with the aid of comparative figures C.9, C.10 and C.11, which present plots of the off-plane vorticity contours for different grids and set-ups.

In figure C.7 it can be seen that the spatial resolution affects significantly the results; while the estimations of the angular position of the leaflets from the medium and fine grids converge, the values from the coarse grid clearly diverge. The same conclusion can be drawn for the temporal resolution, because for both first (Euler, Upwind) and second order (Crank-Nicolson, Linear Upwind) schemes, the results converge when the time-step size is limited by a Courant number bellow 0.5, as seen in figure C.8. From the same plot, it can be extracted that the

second order schemes (Crank-Nicolson, Linear Upwind) offer a more reliable solution as the results exhibit more consistency compared to the results of alternative set-up.

In addition, it can be observed that according to all the aforementioned computations, the motion of the leaflets is not symmetrical, as the one, usually the upper, is closing faster than the other. Only in the cases when second order accurate schemes are used on the medium grid, or when the finer grid is employed, the lower leaflet is the one that closes first. However in the latter this asymmetry is almost negligible. Finally, only in one case (MCL0.5), the lower leaflet bounces once when reaches the casing during the closing face, as it can be seen in figure C.8. Since contact dynamics are neglected and therefore interaction of the IB leaflets with the solid walls does not take place, this bouncing might be caused by a flow induced instability captured by the higher order schemes.
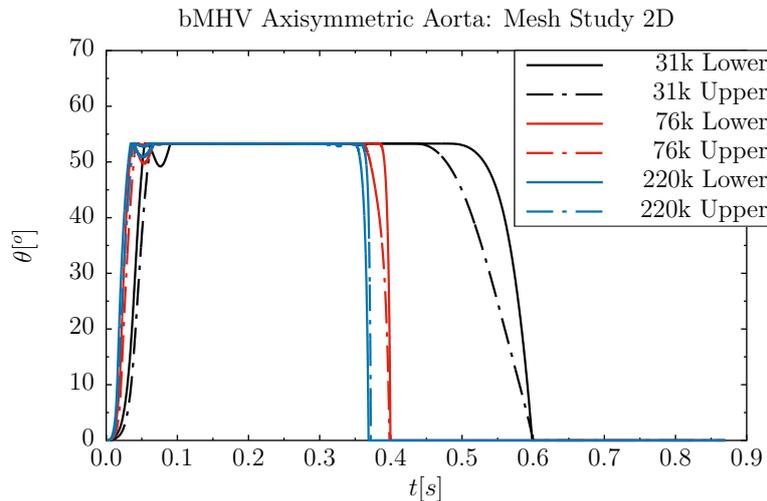
Figure C.7: Axisymmetric bMHV 2D simulation: Mesh influence on leaflet kinematics. The angular position of the two leaflets of the MHV are presented for the three different two-dimensional grids: Coarse (31k cells), Medium (76k cells), Fine (220k cells). The kinematics of upper leaflet are represented by the continuous line and of the lower by the dash-dotted line. The angles are given with respect to the initial, fully closed, position of the leaflets.

137
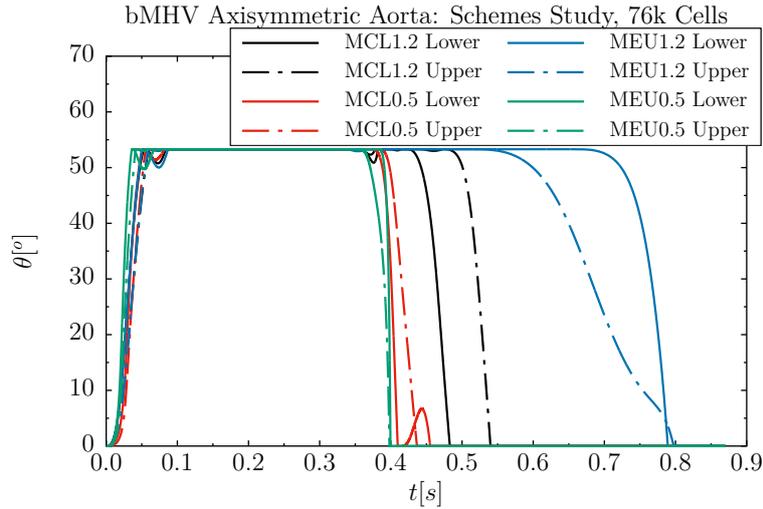
Figure C.8: Axisymmetric bMHV 2D simulation: Time and Space discretisation schemes influence on leaflet kinematics. The angular position of the two leaflets of the MHV are presented for the Medium mesh (76k cells) for different case set-ups from table C.1. The kinematics of upper leaflet are represented by the continuous line and of the lower by the dash-dotted line. The angles are given with respect to the initial, fully closed, position of the leaflets.

The vorticity contour plots of figures C.9, C.10 and C.11 reveal the main characteristics of the flow and shed light in the discrepancies of the leaflets' dynamics between the numerical set-ups. Two counter rotating vortices form over the backward facing step, as the domain expands from the casing to the sinus region, which initially interact with the sinus walls, one on each side. In addition, as the leaflets start to rotate and open, vortices are induced from the tips (50-75 ms) and then a vortex street forms behind the fully opened leaflets until peak systole (200 ms). The initial vortices are captured by all grids, however the coarser the grid, the faster the vortex is diffused. On peak systole, seen in frames C.9d C.9j C.9p, the coarse mesh provides a rather diffused vortex street. In the later stages of the cycle, it becomes more clear that the flow is not symmetrical along the axis of the domain. This lack of symmetry may explain the delay in closing times for the leaflets, as it can be seen in frame C.9k for $t = 395\ ms$, where the asynchronous motion of the two leaflets is visible. By examining the vorticity plots at the same time instance, for the three different grids in frames C.9e C.9k C.9q, it can be seen that while for the fine grid the leaflets are closed, for the medium they are closing asymmetrically, while for the coarse they are still fully open; this illustrates the delay of the closure as the grid coarsens, visible in figure C.7.

On the other hand, the influence of the temporal and spatial schemes is proven more important, both on the opening phase, figure C.10, and the closing phase, figure C.11. The second order schemes provide a sharper and significantly less diffusive representation of the vortices of the opening leaflets, that are sustained for longer and travel further downstream. Moreover, during the closing phase, the second order schemes yield a more chaotic vorticity field, with numerous small structures of various shapes, which differs a lot from the diffused elongated vorticity structures provided by the first order schemes. This may result in a delay of the closure of the leaflets, with regards to the case of the first order schemes, as well as in a more asynchronous motion of the two leaflets, which are also visible in the respective curves of figure C.8.

(a) 50 ms   **(g)** 50 ms   **(m)** 50 ms

(b) 75 ms   **(h)** 75 ms   **(n)** 75 ms

(c) 100 ms   **(i)** 100 ms   **(o)** 100 ms

(d) 200 ms   **(j)** 200 ms   **(p)** 200 ms

(e) 395 ms   **(k)** 395 ms   **(q)** 395 ms

(f) 405 ms   **(l)** 405 ms   **(r)** 405 ms
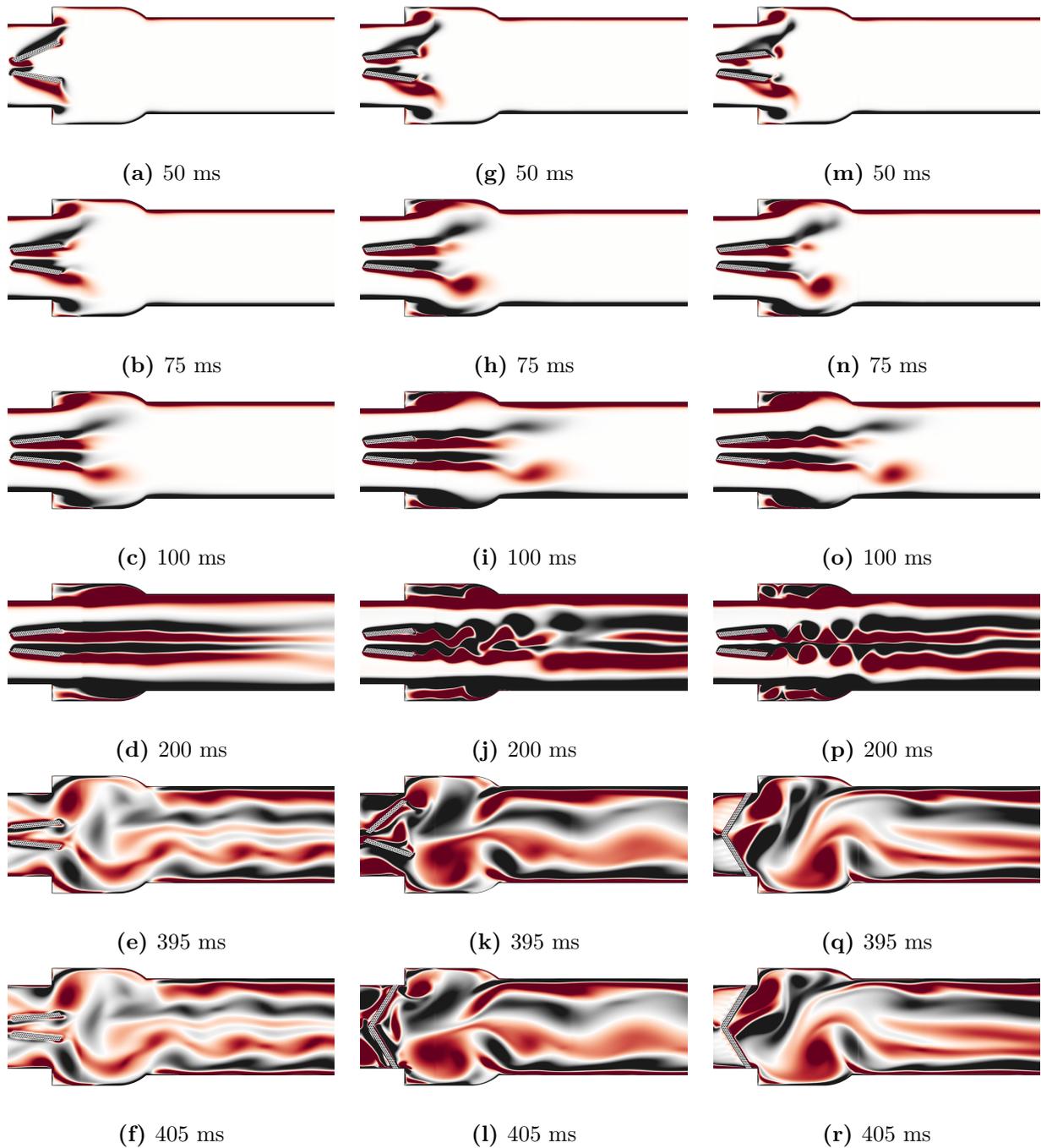
Figure C.9: Axisymmetric bMHV 2D simulation: Off-plane vorticity contours for the 2D Coarse (left), Medium (middle) and Fine (right) mesh, using first order schemes. The plots correspond to cases CEU0.5, MEU0.5 and FEU0.5 respectively. The non-dimensional vorticity is plotted, calculated as $\omega' = \omega \cdot D_o/U_p$ with regards to the inlet tube diameter D_o and inlet peak velocity U_p.

139

(a) 50 ms   **(b)** 100 ms   **(c)** 125 ms

(d) 50 ms   **(e)** 100 ms   **(f)** 125 ms
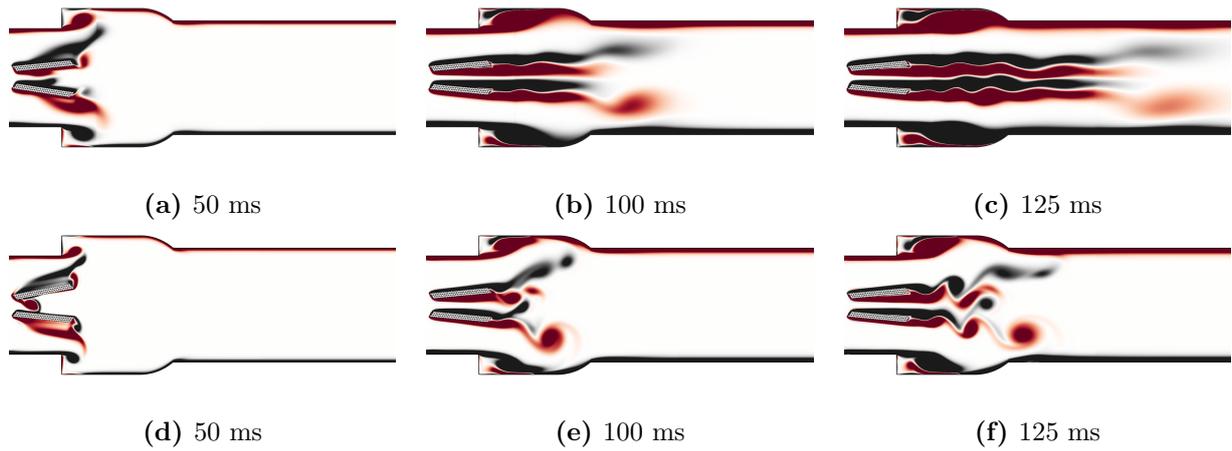
Figure C.10: Axisymmetric bMHV 2D simulation: Off-plane vorticity contours for the 2D Medium mesh, using first order (MEU0.5), on the top, and second order schemes (MCL0.5), at the bottom. The non-dimensional vorticity is plotted, calculated as $\omega' = \omega \cdot D_o/U_p$ with regards to the inlet tube diameter D_o and inlet peak velocity U_p. Valve opening.

(a) 350 ms   **(b)** 405 ms   **(c)** 425 ms

(d) 350 ms   **(e)** 405 ms   **(f)** 425 ms
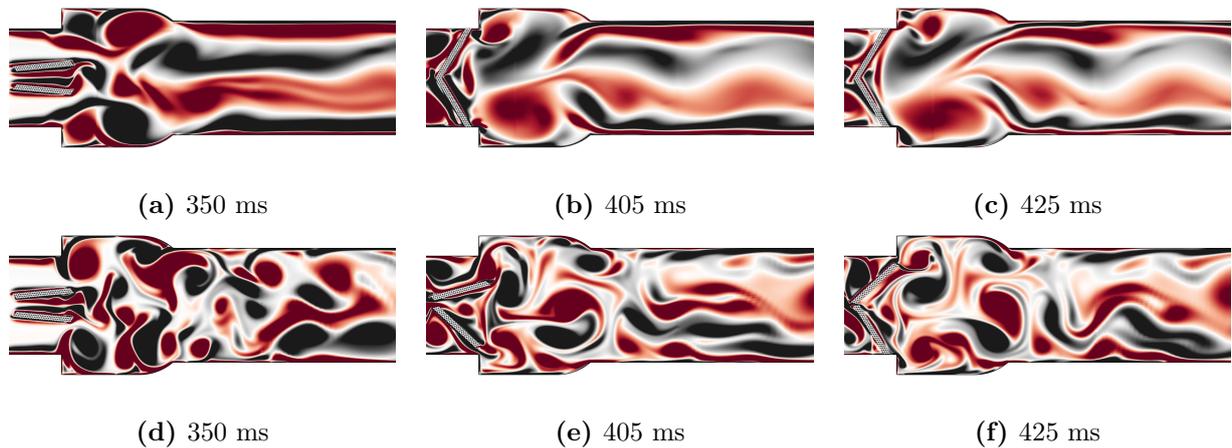
Figure C.11: Axisymmetric bMHV 2D simulation: Off-plane vorticity contours for the 2D Medium mesh, using first order (MEU0.5), on the top, and second order schemes (MCL0.5), at the bottom. The non-dimensional vorticity is plotted, calculated as $\omega' = \omega \cdot D_o/U_p$ with regards to the inlet tube diameter D_o and inlet peak velocity U_p. Valve closing.

3D computation

The plot of figure C.12 validates the numerical computations presented herein against data extracted from the referenced literature and assesses the dimensionality of the problem. The leaflets' kinematics predicted by the 3D computation are found in almost perfect accordance with the experimental measurements from [47] and the simulations of [19]. The predicted motion of the two leaflets is symmetrical as in the references, however a slight deviation is observed during the end of the opening phase. The herein predicted leaflets' motion is more abrupt and the leaflets open quicker, while the curvature of the referenced kinematics indicate a modest deceleration close to the full-open position. In addition, for the sake of comparison, 2D results are also plotted.
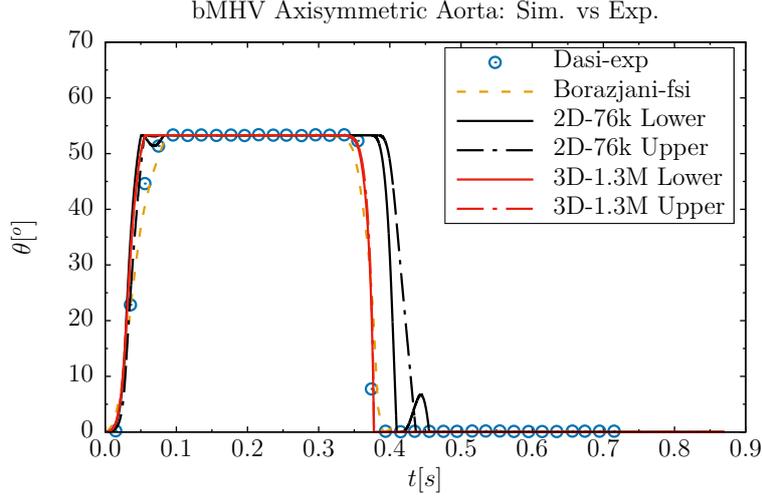
Figure C.12: Axisymmetric bMHV simulation: Leaflet kinematics comparison of the current computational study against FSI numerical results of Borazjani et al. [19] and experimental data of Dasi et al. [47]. The angular position of the two leaflets of the MHV are presented for the 2D Medium mesh (76k cells) and 3D mesh (1.3M cells) with two different lines. The kinematics of upper leaflet are represented by the continuous line and of the lower by the dash-dotted line. These correspond to configurations *MCL0.5* and *3DCL0.5* of table C.1. Numerical results of [19] and the experimental measurements of [47] are presented with a single line for both leaflets, due to symmetry. The angles are given with respect to the initial, fully closed, position of the leaflets.

Furthermore, figure C.13 visualises the vortical structures of the three-dimensional flow, though the use of Q-criterion. According to Q-criterion, the quantity q is calculated by the symmetric and antisymmetric elements of the velocity gradient (let them be S and Ω respectively, see C.3), and denotes the regions where vortical structures appear; $Q > 0$ indicates regions where the rotation rate dominates over the strain rate. The flow is characterised by vortex rings generation over the backward step at the exit of the casing to the sinus region, vortex shedding from the leaflets and chaotic vortical structures developing in the sinus region. The vortical rings initiate on the aorta wall, at the areas of diameter reduction or expansion. At the opening of the leaflets, a vortex ring is shed from the edge of the casing and interacts with the sinus wall. This vortex ring is not axisymmetric, but follows the symmetry of the valve design, which is symmetric with regards to the *Oxz* plane (figure C.4). In addition, vortices are shed over the leaflets, on both sides. The flow inside the sinus is chaotic throughout the cycle.

$$q = \frac{1}{2} \left(\|\Omega\|^2 - \|S\|^2 \right) \tag{C.3}$$

141

(a) 50 ms **(b)** 75 ms **(c)** 100 ms

(d) 150 ms **(e)** 200 ms **(f)** 300 ms

(g) 350 ms **(h)** 375 ms **(i)** 400 ms
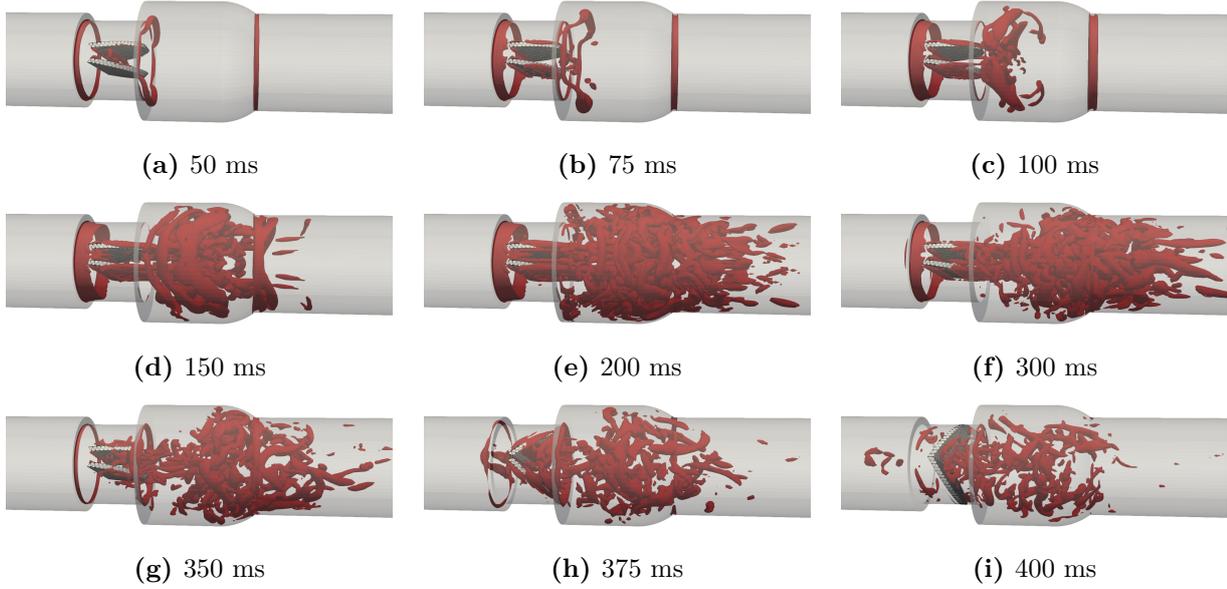
Figure C.13: Axisymmetric bMHV 3D simulation: Vortical structures visualized in terms of iso-surfaces of Q-criterion ($Q = 2 \times 10^4$ $[1/s^2]$) for different time instances during opening and acceleration phase (*a-d*), peak systole (*e*), deceleration and closing phase (*f-i*).

On the other hand, figure C.14 presents the non-dimensional vorticity contours for the three-dimensional simulation, plotted over the vertical mid-plane *AA'*, for the opening and closing phase of the valve. These vorticity contours give an other point of view on the vortical dynamics described by the Q-criterion in figure C.13. The symmetry of the flow is clearly illustrated on the mid-plane; during the opening phase, visible in frames C.14a, C.14b and C.14c, and up until peak systole, seen in frame C.14d, the vortical patterns are in perfect symmetry with respect to the axis of the pipe. The complexity and the chaotic nature of the flow is manifested by the absolute breakdown of this symmetry during the closing phase of the valve, as show in frames C.14e and C.14f.

(a) 50 ms **(b)** 75 ms **(c)** 100 ms

(d) 200 ms **(e)** 395 ms **(f)** 405 ms
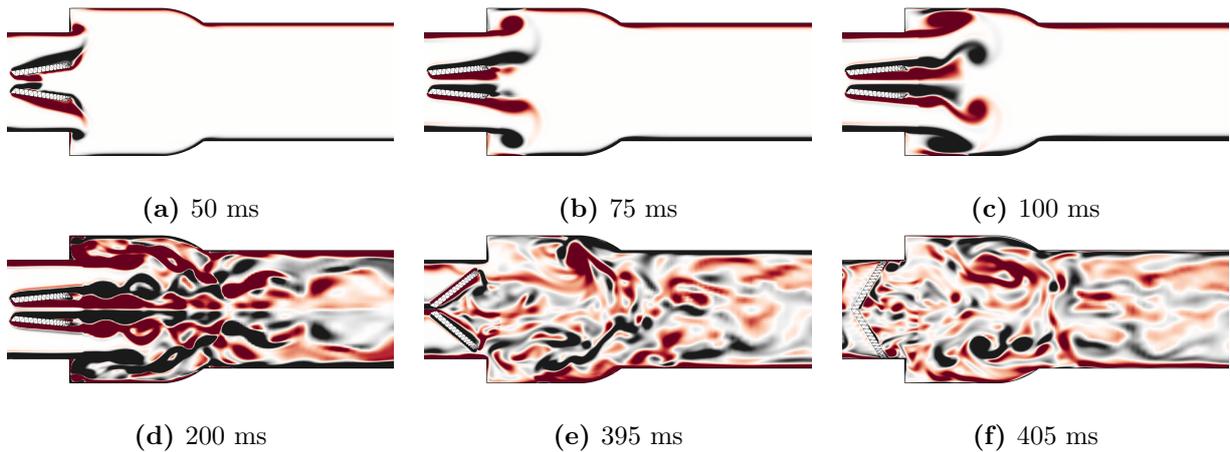
Figure C.14: Axisymmetric bMHV 3D simulation: Off-plane non-dimensional vorticity contours for the 3D simulations. Contours plotted on the mid-plane *AA'*. The non-dimensional vorticity is calculated as $\omega' = \omega \cdot D_o/U_p$ with regards to the inlet tube diameter D_o and inlet peak velocity U_p.

Apart from the quantitative comparison of the leaflet kinematics, a qualitative comparison against the referenced computational results and experimental observations of Borazjani et al. [19] can be performed by the juxtaposition of figures C.15 and C.16.

Figure C.15 presents the calculated and the reconstructed from PIV measurements vorticity contours, on the mid-plane AA'. Figure C.16 presents the vorticity contours on the same plane, as calculated by the current 3D numerical simulation. In both figures the vorticity field is represented in terms of non-dimensional vorticity and although the contours differ, the levels are identical.

It can be seen that the physics is captured by the current simulation, but noticeable deviations are visible between all three data sets. Better agreement amongst all the cases is observed in the early time instances ($110 - 135\ ms$), seen in frames C.15a, C.15b and C.16a, C.16b. Vortices shed over the aorta walls into the sinuses agree in terms of intensity and length; vortex shedding over the leaflets is also similar for all cases, however for the current simulation seems like the vortices detach faster, as two distinct vortices are visible in the sinuses instead of one present in the referenced images. During the later instances ($285 - 374\ ms$), the flow predicted by the current computation is organised in larger and thicker vortical blobs than the referenced flow field. At $285\ ms$, visible in frames C.15c and C.16c, the current simulations exhibit more structured and more symmetrical flow than the referenced data, especially inside the sinus region. At $374\ ms$, visible in frames C.15d and C.16d, the closure of the valve has already commenced and the vortical structures are broken down into random smaller structures, which in the referenced images are more chaotic. However, in both the latter instances, the breakdown in the experimental images is more prominent that both the referenced and current simulations; the simulations predict some longer and more resistant vortical structures. In addition, the FSI computations of Borazjani et al. [19] capture a slight asymmetry on the vorticity field also present in the experimental data, which can be inferred by careful examination of the early times in frames C.15a and C.15b; slight asymmetric leaflet motion is also reported, which is not detectable in the macro-scale of plot C.12. This is thought to be caused by inherent instabilities and the three-dimensional nature of the flow. Such an asymmetry is not captured by the current simulation.

These discrepancies between the herein predicted and the referenced results, may be related to the level of spatial resolution. In the current configuration, the computational grid is refined in an area enclosing the moving leaflets; a finer grid, or at least a constant grid size along the entire sinus region, could improve the results.

(a) $\sim 110\ ms$ **(b)** $\sim 135\ ms$

(c) $\sim 285\ ms$ **(d)** $\sim 374\ ms$
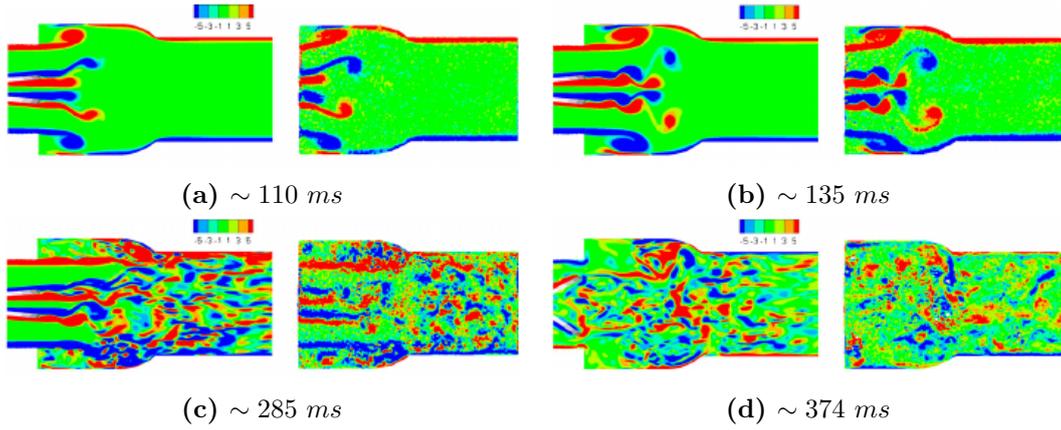
Figure C.15: Instantaneous off-plane (non-dimensional) vorticity contours, from IB FSI simulations (left) and experiments (right), as reported in the work of Borazjani et al. [19]. Times were not explicitly stated but rather reported on (and therefore extracted from) the flow rate pulse diagram.

(a) $110\ ms$ **(b)** $135\ ms$

(c) $285\ ms$ **(d)** $374\ ms$
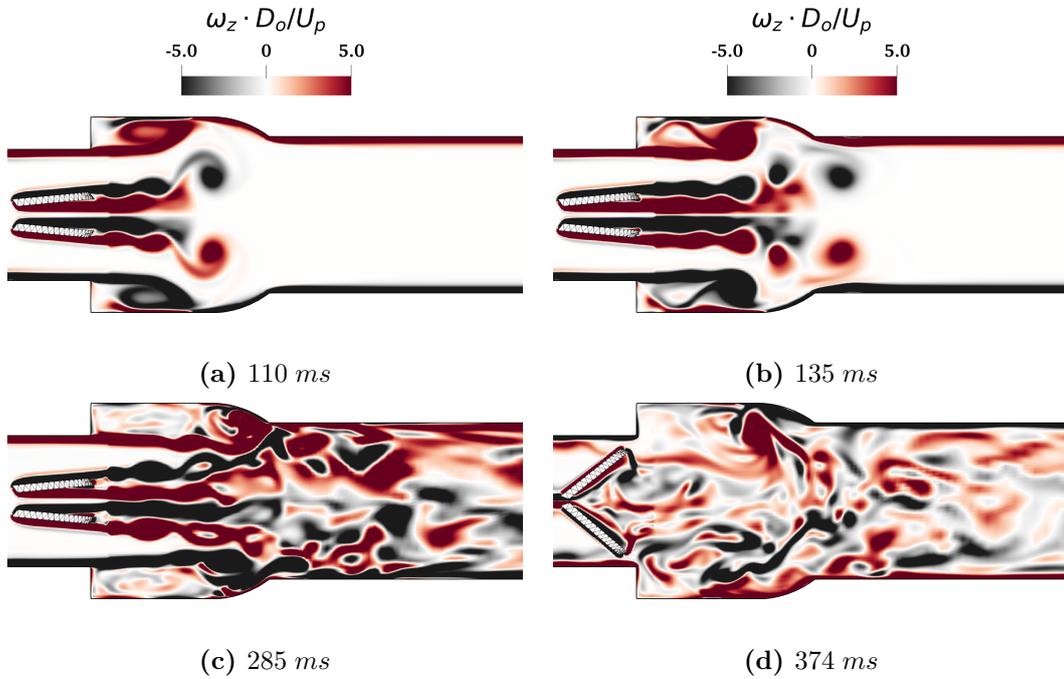
Figure C.16: Instantaneous off-plane vorticity contours, for the 3D simulation, at the same time-instances as reported in the work of Borazjani et al. [19].

Finally, an important feature of the flow, with particular interest to the assessment of cavitation potential in such flows through bi-leaflet MHV, is the *backward* jetting that appears during the closing of the leaflets. Figure C.17 collects four snapshots of the velocity field at the closing moment of the leaflets. The flow is squeezed through the opening between the two leaflets, as well as the gaps between the leaflets and the casing. At the moment that the opening between the two leaflets closes, frame C.17b, a *high-speed* jet is emitted upstream, which travels to the inlet pipe and gets diffused, frame C.17c and C.17d. The length of the jet is comparable to the length scales of the flow, as it can be seen in the diagrams C.18, where

144

the velocity profiles along the diameter of the domain are presented for two locations upstream the leaflets. As it can be seen, the jet velocity may reach values over 1.25 m/s near the leaflets, larger than the peak inlet velocity $U_p = 0.8$ m/s, and retains its strength even upstream the inlet of the casing, into the inlet pipe; at time $t = 370$ ms the jet has a velocity of 1.25 m/s at a location 0.3 mm upstream the leaflets and ~ 0.8 m/s at 0.7 mm upstream the leaflets, which means that the jet at this instance is more than $7mm$ in length. In addition, smaller and weaker jets develop near the points where the leaflets touch the casing, visible at frame C.17c.
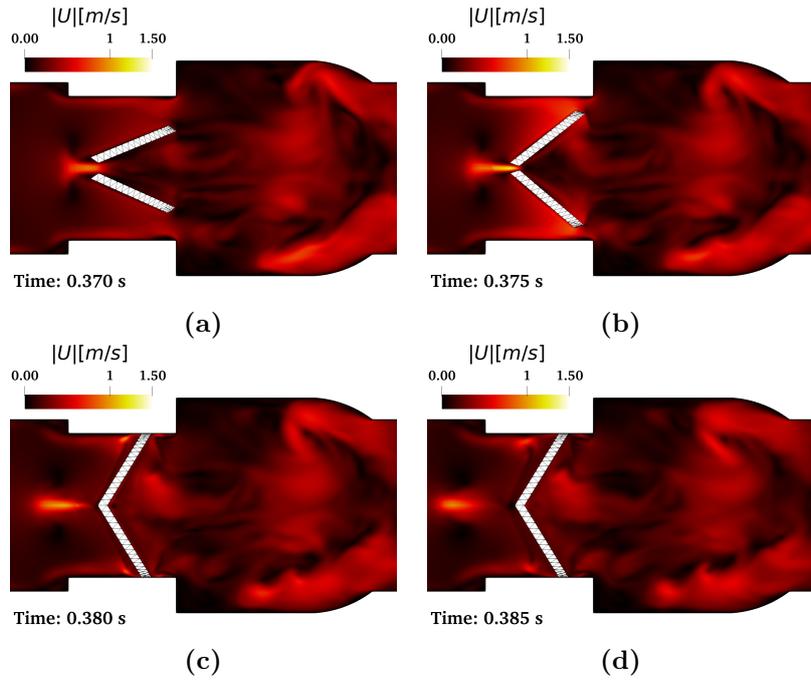
Figure C.17: Axisymmetric bMHV 3D simulation: Magnitude of velocity field in the valve casing, for four different time instanced. Jetting during leaflets' closure. Contours plotted on the mid-plane AA'.
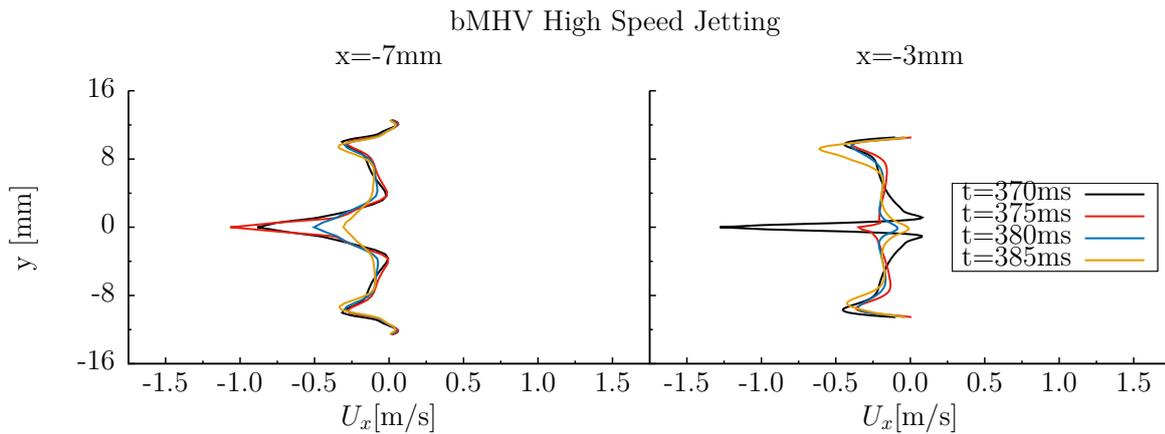
Figure C.18: Axisymmetric bMHV 3D simulation: Velocity profiles on the center plane AA', along the diameter of the domain, at two locations upstream the leaflets, for the four different time-instances of figure C.17. High speed jet at leaflets' closure.

Appendix D

Numerical Implementation Notes

The herein proposed Direct Forcing Immersed Boundary Method was implemented in the platform of `OpenFOAM` [236].

`OpenFOAM` (Open FIELD OPERATION AND MANIPULATION) is an open-source Finite Volume (FV) library, for Computational Fluid Dynamics (CFD), with its own programming pseudo-language that facilitates equation declaration, discretisation and solution. It is written in `C++` and provides a rich library of models and functionalities, which ease the researcher or the engineer to combine different components and develop novel numerical tools. Apart from the model library and the functionalities, numerous solvers (executable programs) are available as well, each one targeting a specific range from a wide spectrum of flow regimes and applications. Since the source-code is open-source and available to anyone, the library and the solvers are highly customisable.

The developed IB method is structured as a functionality library with focus on *portability* and *extensibility*. Since `C++` is a *object-oriented* programming language, the IB library defines a new class object, the `immersedBoundarySource` class, with its private structure, properties and functions, completely independent to the solution algorithm and the solver. The IB library is coded as a standalone dynamic library, so that it can be linked to various solvers (executables). It is comprised by standalone classes so that new functionalities can be added easily without altering the main class of the library, which is linked and called by the solvers. After the update and the new compilation, if the main class is not altered, the executables do not need to be recompiled as well.

Few different versions of `OpenFOAM` exist, as anyone can adapt and reuse it. The main distributions are the `OpenFOAM` from the *OpenFOAM Foundation* [68], the `OpenFOAM+` from *OpenCFD* [166] and community-contribution driven `foam-extend` [41]. In this work the `OpenFOAM` version 2.4.x of OpenFOAM Foundation is used.

Hereafter some technical details are presented.

D.1   The Immersed Boundary library

Following the methodology described in chapter 2, the `immersedBoundarySource` library is designed to calculate a *vector field* for the volumetric forcing term $\mathbf{f}_{IB}$, that can be added to the momentum equations as a source term.

The immersed solid is represented by a closed *triangulated* surface, with N_{IB} faces and

the surface normals **strictly** defined outwards, as illustrated in figure D.1. The *IB surface* is provided as input to the code, in a *stereolithography* (STL) file format. *OpenFOAM* provides the needed functionalities to input/output, modify (translate, rotate, scale) and analyse (determine center of gravity, calculate moments of inertia) such data files.

The IB forcing field is evaluated on each of the N_c cells for the computational domain. The forcing is localised on the area covered by the solid body, using the *mask* α_{IB}. Thus, for each cell j of the N_c cells of the domain, the IB forcing vector is calculated based on the velocity vector $\mathbf{u}_j$ and the *target velocity* $\mathbf{u}_j^t$ (the imposing value) as:

$$\mathbf{f}_{Ib,j} = \alpha_j \frac{\mathbf{u}_j^t - \mathbf{u}_j}{dt}$$

The *target* velocity that the method is trying to impose in a cell, is determined for all the cells of the domain, based on distance vector $\mathbf{r}_j = \overrightarrow{C_s C_j}$ between the IB body center C_s of gravity and the the cell's center C_j and the solid body *translation* and *angular* velocities, $\mathbf{u}_s$ and ω_s respectively:

$$\mathbf{u}_j^t = \mathbf{u}_s + \mathbf{r}_j \times \omega_s$$

The computational cost of calculating the forcing term for all the cells of the domain or estimating the target velocity in cells outside the IB regions (e.i. in pure *fluid* cells), is negligible. The most expensive operation of the method, is the calculation of the mask α_{IB}.

As mentioned on chapter 2, the mask is perceived as the *solid volume fraction*, e.i. the ratio of the cell volume covered by the immersed solid. For each of the N_c cells of the domain, the mask α_j is calculated from the distances of the N_v cell's vertices from the IB surface:

$$\alpha_j = \frac{\displaystyle\sum_{i=1}^{N_v} \mid min(d_{ij}, 0) \mid}{\displaystyle\sum_{i=1}^{N_v} \mid d_{ij} \mid}, \quad j \in [1, N_c]$$

The distance of each vertex from the IB surface, as it is already mentioned in chapter 2, is estimated as the minimum of the distance of the vertex from all of the points of the IB surface:

$$d_{ij} = min(d_n) = min\left(\mathbf{r}_{ij,k} \cdot \mathbf{n}_{IB,k}\right), \quad \mathbf{r}_{ij,k} = \overrightarrow{B_k V_{ij}}, \quad j \in [1, N_c], \ i \in [1, N_v], \ k \in [1, N_{IB}]$$

Therefore, the calculation of the mask field requires $N_c \times N_v \times N_{IB}$ algebraic operations, which increase with the increase of background grid density and the level of complexity or geometric details of the STL.

In order to accelerate this procedure and lower the computational cost, the mask field is calculated only on the grid cells in the immediate vicinity of the IB surface. `OpenFOAM` provides a *Octree* search algorithm, that helps determine which cells' centres lay in the area enclosed by the IB surface. In this way, an initial approximation of the *solid* cells is obtained, which define the *IB Cells* stencil, illustrated in figure D.2a. Then, this stencil is extended to include the neighbour cells that are cut by the IB surface. That way the *IB Cells Extended* stencil is created, that holds all the *internal* or *interface* grid cells, as shown in figure D.2b. Finally the mask field is calculated only for the cells in the latter stencil. For the case of a cylinder, in a

two-dimensional setup, the mask is plotted in D.2c. This way the computational cost of the mask estimation is lowered significantly.

The function that determines the *IB Cells* stencil, using the *octree* search, can be seen in code-listing D.1.

The IB library, is also responsible for the update of the mask field on every time-step, if the immersed body is moving, and of the forcing field with the new velocity field. The function to update the IB in every time-step is explicitly called by the solver (executable), is defined as `updateIb(U)`, accepts as input argument the velocity field and is shown in code-listing D.2. For the motion of the body, three different options are considered:

- prescribed motion, where either the position (angles) or the velocity (angular velocity) is given as a function (linear or sinusoidal) of time

- induced motion, where a 6 d.o.f. motion solver is used to displace the body according to the hydrodynamic or aerodynamic loading excessed by the flow

- tabulated motion, where the position (rotation) of the body is given as a table and at each time-step the position (rotation) is determined by interpolation with respect to time

The IB library is accompanied by a library with modified turbulence models, as explained in chapter 2. A modified wall distance, y'_{wall}, class is included in the turbulence library, which adjusts the wall distance, y_{wall} in the presence of the immersed body:

$$y'_{wall} = min(y_{wall}, y_{wall,Ib})$$

The IB library is responsible for calculating the wall distance, $y_{wall,Ib}$, of the cells' centres from the immersed boundary. If the body is moving, the wall distance has to be updated on every time-step; this is handled by the `updateIb(U)` function as seen in lines 12-15 of code-listing D.2. This operation is also computationally expensive, therefore is limited in an area twice the length of the body (2 times the diagonal of the *bounding box*).

Since all the operations regarding the IB are handled internally by the library, the exposure of the IB algorithm and functions is limited to *creating* the IB object, calling the `updateIB(U)` function to update it, passing the new velocity field, in every time-step, and adding the IB source term in the momentum equations by calling the `ibSourceTerm()` function. An example of linking and using the IB library in a generic solver of `OpenFOAM`, employing a pressure-correction algorithm, is given by code-listing D.3, where an implicit update of the forcing term is also performed by calling the `updateFIb(U)` function in every iteration, which only recalculates the source term $\mathbf{f}_{Ib}$ with the updated velocity.

The definition of multiple immersed bodies is also supported, because of the object oriented nature of the coding platform. Multiple immersed boundary objects can be defined in the beginning of the execution of the solver. Each body has its STL geometry and handles autonomously its functionalities (calculates motion, mask, wall distance, source terms). At every time-step, the forcing terms are summed up to provide a single volumetric source term field to be added to the momentum equations. The solvers have to be adjusted to use the code-snippets to create the immersed boundaries D.4 and sum the forcing terms D.5, provided by the IB library, as seen in code-listing D.6.
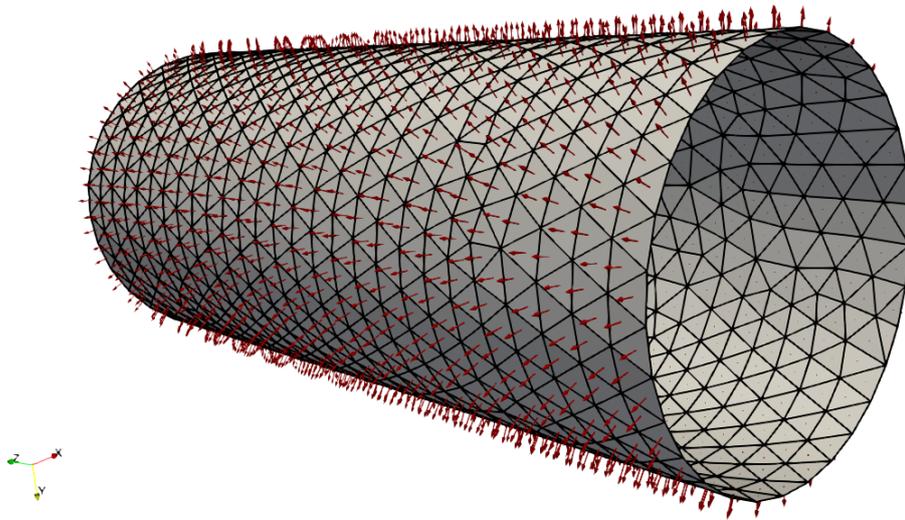
Figure D.1: The triangulated IB surface of a cylinder with the normal vectors.

(a) IB stencil **(b)** IB Extended stencil **(c)** IB Mask
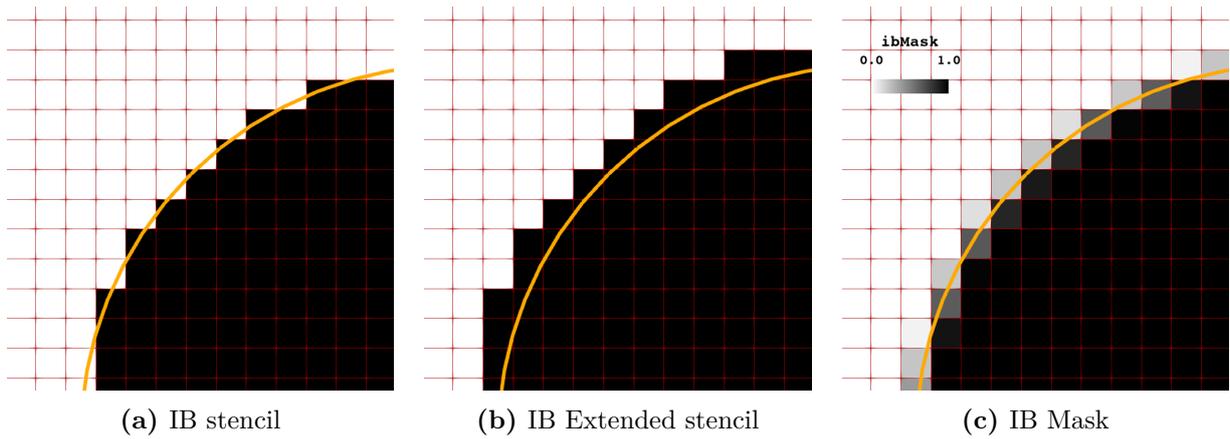
Figure D.2: Immersed Boundary's cell stencils and mask α_{IB} field. *IB cells* have their center laying *inside* the immersed boundary, *IB cells extended* have at least one of their vertices laying *inside* the immersed boundary. The mask represents the *solid volume fraction*.

```cpp
void Foam::immersedBoundarySource::makeIbCells()
{
    scalarField& ibMask_ = ibMask();

    //- TriSurface Search
    triSurface ibTemp( ibSurf_);
    triSurfaceSearch ibTriSurfSearch( ibTemp );

    //- Mark cells inside the TriSurface
    boolList centresInside = ibTriSurfSearch.calcInside( mesh_.cellCentres() );

    labelHashSet ibCellSet;

    forAll(mesh_.C(),cellI)
    {
        if ( centresInside[cellI] )
        {
            ibCellSet.insert(cellI);
            ibMask_[cellI] = 1.;
        }
        else
        {
            ibMask_[cellI] = 0.;
        }
    }

    ibCellsPtr_ = new labelList(ibCellSet.toc());
    sort(*ibCellsPtr_);
}
```

Listing D.1: Use of Octree Search to find cells lying in IB region.

```cpp
void Foam::immersedBoundarySource::updateIb( const volVectorField& UIn )
{
    // Update Stencils if Immersed Boundary is moving
    if ( ibMoving() )
    {
        reInitFields();
        moveIb();
        makeIbCells();
        makeIbCellsExt();
        makeMask();
        makeLayers();
        if (dTurbulent())
        {
            calcWallDistance();
        }
    }
    calcUtarget();
    calcSourceTerms( UIn );
    calcForces();
}
```

Listing D.2: Function to Update IB.

```
1  ...
2  #include "immersedBoundarySource.H"
3  // * * * * * * * * * * * * * * * * * * * * * * * * * * * * * * * * * * * * * * //
4  int main(int argc, char *argv[])
5  {
6      // Create Immersed Boundary
7      immersedBoundarySource ib(mesh);
8      ...
9
10     while (runTime.loop())
11     {
12         ...
13
14         //Calculate IB Masks and Source Terms
15         ib.updateIb(U);
16         Info<<"Immersed Boundary Updated"<<endl;
17         // Pressure-velocity PISO corrector
18         {
19             // Momentum predictor
20             fvVectorMatrix UEqn
21             (
22                 fvm::ddt(U)
23               + fvm::div(phi, U)
24               + turbulence->divDevReff(U)
25               - ib.ibSourceTerm() // IbSource Term
26             );
27             ...
28
29             // --- PISO loop
30             for (int corr=0; corr<nCorr; corr++)
31             {
32                 ...
33
34                 // Pressure corrector
35                 fvScalarMatrix pEqn
36                 (
37                     fvm::laplacian(rAU, p) == fvc::div(phiHbyA)
38                 );
39                 ...
40
41                 U = HbyA - rAU*fvc::grad(p);
42                 U.correctBoundaryConditions();
43                 ib.updateFIb(U);    // Update forcing
44             }
45         }
46         ...
47     }
48 }
```

Listing D.3: Call of IB source term in solver.

```
1  wordList ibNames( immersedBoundaryDict.lookup("Bodies") );
2  PtrList<immersedBoundarySource> ibBodies(ibNames.size());
3
4  Info<<"\nCreating Immersed Boundaries\n"<<endl;
5  forAll (ibNames,counter)
6  {
7      word tmpName(ibNames[counter]);
8      ibBodies.set
9      (
10         counter,
11         new immersedBoundarySource
12         (
13             mesh,
14             immersedBoundaryDict.subDict(tmpName)
15         )
16     );
17 }
```

Listing D.4: Multi-body support: Create IBs.

```
1  volVectorField ibSrc
2  (
3      IOobject
4      (
5          "ibSrc",
6          runTime.timeName(),
7          mesh,
8          IOobject::NO_READ,
9          IOobject::AUTO_WRITE
10     ),
11     mesh,
12     dimensionedVector( "0", dimAcceleration, vector::zero )
13 );
14
15 forAll (ibNames,counter)
16 {
17     ibBodies[counter].updateIb(U);
18     Info<<"Updated Immersed Boundary: "<<ibNames[counter]<<endl;
19     ibSrc += ibBodies[counter].ibSourceTerm();
20 }
```

Listing D.5: Multi-body support: Sum IB forcing.

```
1  ...
2  #include "immersedBoundarySource.H"
3  // * * * * * * * * * * * * * * * * * * * * * * * * * * * * * * * * * * * * //
4  int main(int argc, char *argv[])
5  {
6      //Create Immersed Boundaries
7      #include "createImmersedBoundaries.H"
8      ...
9
10     while (runTime.loop())
11     {
12         //Calculate IB Masks and Source Terms
13         #include "calcIbSourceTerms.H"
14
15         // Pressure-velocity PISO corrector
16         {
17             // Momentum predictor
18             fvVectorMatrix UEqn
19             (
20                 fvm::ddt(U)
21               + fvm::div(phi, U)
22               + turbulence->divDevReff(U)
23               - ibSrc // IbSource Term
24             );
25             ...
26
27         }
28         ...
29     }
30 }
```

Listing D.6: Multi-body support: Multi-body Solver

D.2   Computational Cost

The advantages of the IB methods over the conventional boundary conformal approaches, is qualitatively demonstrated by the ease of grid generation and the ability to undertake computations of moving, internal to the domain, bodies. However, the performance of the herein proposed numerical method can be quantitatively assessed by measuring the computational time of the performed simulations.

Hereafter, numerical details and computational cost of few simulations performed with the presented method are presented. For the simulations, three different computers have been mainly used, according to the computational needs. These computers are:

- *workstation*: Desktop workstation equipped with a Intel Xeon E5-2690 V3 @$2.6GHz$ processor, with 2 sockets of 12 double-threaded cores each, with hyper-threading enabled, increasing the number of available CPUs to 48.

- *arion*: Computer cluster of 4 nodes, each equipped with a processor @$3.3Ghz$, with 2 sockets of 4 single thread cores each.

- *solon*: Computer cluster of many nodes with either 20 or 32 CPUs.

Case of High-Velocity Projectile Impact

In the case of high-velocity projectile impact, presented in Chapter 4, both three- and two-dimensional simulations were carried out.

The importance of the two-dimensional simulations is apparent from the level of detail unveiled in comparison with the three-dimensional simulation. Such fine spatial resolution would not possible to be achieved considering the complete three-dimensional domain, because the computational cost would be prohibiting. This can be seen from table D.1, where the computational cost of the aforementioned computations is presented.

The simulations where carried out mainly on the *workstation* computer, where depending on the total cell count from 4 up to 40 cores have been used. The *solon* cluster computer was also used to accelerate the simulation of the finest 2-D mesh *(5lvl)*, where 96 CPUs have been used.

It can be seen that for the *2D-4lvl* mesh, with far fewer cells, a much higher resolution is achieved, compared to the *3D* mesh, demanding half the computational power. However, further refining the grid, the computational cost gets much higher. The presence of the IB source term in the equations, which receives high values, dictate severe time-step restrictions and for all the simulations, the Courant number is limited below 0.05. This increases the number of iterations/time-steps to complete the simulation and therefore the computational cost, which for the *2D-5lvl* mesh is much higher that for the 3D mesh.

Mesh	Cells	dx_{min} [mm]	dt_{mean} [s]	CPUh	T_{step}^{mean} [s]
3D	2.9M	0.192	5.27e-9	4358	24.92
2D-2lvl	40k	0.250	7.45e-9	18	1.250
2D-3lvl	120k	0.125	3.51e-9	432	4.790
2D-4lvl	375k	0.063	1.33e-9	2621	13.23
2D-5lvl	1.2M	0.031	0.91e-9	31261	20.82

Table D.1: Computational cost (in *CPU-hours*) for the 3D and 2D simulations, along with indicative clock time for completion of one time-step *(T_{step}^{mean})* and characteristic spatial and temporal resolution *(dx_{min} and dt_{mean})*.

Case of bi-leaflet MHV

For the case of bi-leaflet Mechanical Heart Valve (MHV), presented in Appendix C, a parametric study of two-dimensional computations and a three-dimensional simulations were carried out. The *arion* cluster was used and parallel computations were carried out on 2 or 8 CPUs, according to the cell count, except for the case of the coarse 2D mesh that a serial run was performed. The performance details are summarised in table D.2.

It is evident that with larger and finer grids, smaller time-steps are used (based on the CFL condition $C_{o,max} \leq 0.5$) and more computational power is needed. However, for the 2D computations it can be seen that after reaching a certain level of spatial discretisation the (wall-clock) time needed for the implicit pressure-correction algorithm to complete one time-step is stabilised around 30 seconds. On the contrary, for the 3D simulations, the full three-dimensional nature of the flow seems to affect convergence because the (wall-clock) time to achieve convergence and complete one time step increases drastically to 185 seconds, for a spatial and temporal discretisation level equivalent to this of the medium 2D mesh case.

Mesh	Case ID	Cells	dy_{min} [mm]	dt_{min} [s]	dt_{mean} [s]	CPUh	T_{step}^{mean} [s]
2D coarse	CEU0.5	33k	0.237	1.0e-4	1.6e-4	9	10
2D medium	MEU0.5	76k	0.118	2.0e-5	3.2e-5	240	29
2D fine	FEU0.5	220k	0.059	1.9e-6	1.4e-5	1847	31
3D	3DCL0.5	1.3M	0.159	2.7e-5	7.1e-5	2357	185

Table D.2: Computational cost (in *CPU-hours*) for the 3D and 2D simulations of bi-leaflet MHV in straight axisymmetric aorta, along with indicative clock time for completion of one time-step *(T_{step}^{mean})* and characteristic spatial and temporal resolution *(dy_{min} and $dt_{min,mean}$)*.

Also, the computational cost of the cases of pulsatile flow through a model aorta, featuring a 180° bend, with and without a bi-leaflet Mechanical Heart Valve (MHV) mounted on the root of the turn, presented in Chapter 5, is presented here, in table D.3. The simulations without the MHV, are carried out on the *solon* computer cluster, employing 64 (coarse) and 160 (medium, fine) CPUs, while the case with the MHV is ran on the workstation, with 24 CPUs; it was found the optimal number of CPUs for this parallel computation, probably because OpenFOAM could not profit of hyper-threading or because of the architecture of the particular processor was not suitable for parallel numerical computations with that huge amount of data. Although the cases without the MHV, employ a standard incompressible solver provided by OpenFOAM, following a PIMPLE pressure-correction algorithm, without taking into account the Immersed

Boundary proposed in this study, they provide valuable information for qualitative comparison.

It is evident that with increasing spatial resolution, for the cases without the MHV, the total and per time-step computational cost increases significantly. However, the minimum and mean values of the simulation time-step, which is governed by the CFL condition, which remain stable with increasing grid resolution, may be an indication that at least the maxima of the velocity field are well resolved. Also, the influence of the MHV on the flow is implicitly demonstrated by the increase of per time-step computational cost, compared to the coarse mesh simulation without the MHV, despite the similar total number of cells and reduced spatial resolution. The increase is partially a result of the different number and models of the CPUs used (24 with MHV, 64 without MHV), however, ×3 more CPUs seem unlike to cause ×10 acceleration of the computation.

Mesh	Cells	dy_{min} [mm]	dt_{min} [s]	dt_{mean} [s]	CPUh	T_{step}^{mean} [s]
without bi-leaflet MHV						
3D coarse	2M	0.04	1.7e-5	3.7e-5	3531	18
3D medium	8M	0.04	1.6e-5	3.4e-5	41493	77
3D fine	11M	0.02	2.1e-5	3.5e-5	55509	100
with bi-leaflet MHV						
3D coarse	2M	0.20	1.0e-5	2.5e-5	15303	187

Table D.3: Computational cost (in *CPU-hours*) for the 3D simulations of pulsatile flow through a model aorta, for the cases of sections 5.2 and 5.3, along with indicative clock time for completion of one time-step *(T_{step}^{mean})* and characteristic spatial and temporal resolution *(dy_{min} and $dt_{min,mean}$)*.

Despite the particular details of each computation, it is important to highlight that the simulations mentioned above, it is feasible to be performed on an advanced desktop workstation within couple of weeks or a medium size cluster within few days. Given the possible application of studies of such biological flows in real-life medical cases, the required computational means and the completion time are essential for patient-specific solutions.

Case of Flow over NACA0066

For the case of pitching hydrofoil NACA0066, presented in Chapter 3, some computational details are presented here. More precisely, table D.4 compares the computational cost for the cases presented in the aforementioned chapter, for the different turbulent models used. On the other had, table D.5 compares a simulation of the pitching hydrofoil to a simulation of a static hydrofoil, to assess the additional computational burden resulting from the moving Immersed Boundary; the two simulations refer to different cavitating regimes ($\sigma = 1.3$ and $\sigma = 3$) but employ the same mesh, turbulence model and similar total simulated time (~ 0.2 seconds), therefore only the ascending phase of the rotation is considered.

Apart from the fact that all three turbulence models, the single equation Spalart-Allmaras, the two-equations $k-\omega\ SST$ and the four-equations $k-\omega\ SST LM$, perform in a similar way, as seen in table D.4, it can be observed from table D.5 that the motion of the Immersed Boundary do not increase the computational load of the simulation. This is the important advantage of Immersed Boundary techniques over conformal grid approach; since the computational grid does not have to be regenerated or altered in every time-step, the computational cost is similar to the case where the immersed body remains static.

Turb Model	CPUh	T_{write}^{mean} [s]
Sp. Allm.	4099	3900
$k-\omega\ SST$	4398	4184
$k-\omega\ SST-LM$	4598	4374

Table D.4: Computational cost (in *CPU-hours*) for the 3D RANS simulations of turbulent cavitating flow over the pitching hydrofoil *NACA0066*, presented in Chapter 3, for the different turbulent models, along with indicative clock time for results' output every $1.0ms$ (T_{write}^{mean}).

Case	σ	dt_{mean} [s]	CPUh	T_{write}^{mean} [s]	T_{step}^{mean} [s]
Static $\alpha = 6^o$	1.3	1.29e-07	2238	5035	0.7
Pitching $\alpha = 0^o - 15^o$	3.0	1.29e-07	2414	4744	0.6

Table D.5: Computational cost (in *CPU-hours*) for the 3D RANS simulations of turbulent cavitating flow over static and pitching hydrofoil *NACA0066*, using *Spalart Allmaras* turbulent model, along with indicative temporal resolution *(dt_{mean})* and clock time for completion of one time-step *(T_{step}^{mean})* and output results every $1.0ms$ *(T_{write}^{mean})*.

Appendix E

On the Accuracy of the Method

This chapter discusses the numerical accuracy of the developed method. Apart from the validation presented in chapter 3, the present chapter takes a closer look on the numerics of the method, the factors that may affect its accuracy and comments on its diffusive nature as a direct forcing approach.

Among the most widely used benchmark cases for the assessment and the validation of immersed boundary methods are the low Reynolds number incompressible or compressible flows over stationary or moving cylinders [15, 50, 136, 145, 170, 186], for which experimental data also exist, Couette flows that have analytical solutions [15], as well as supersonic flow over cylinders [50, 218] featuring the well-known bow shock; also the development of the boundary layer over a plate can be used to assess the immersed boundary method for turbulence treatment [148], where Blasius solution can provide analytical velocity profiles to compare to. Regarding two-phase flows, a well-known test-case to assess the interaction of an immersed body with liquid-gas interphase is the cylinder exit or entry problem [252]. For fluid-structure interaction problems, vortex-induced-vibrations [19, 40] and particle mitigation or suspension in Couette flow [51] or under the influence of a travelling shock wave [175].

In order to assess an immersed boundary method on cavitating flows, amongst many hydrofoil cases, the case reported by Dular [54], where computational and experimental results exist, serves as a good benchmark. In addition, cavitating flows through step-nozzles, such as the case of Akira Sou et al. [210], who report experimental measurements as well, and the case of Winklhofer nozzle [253], which is widely studied with numerous numerical tools, could also be used. The cavitaing high-speed flow over an underwater projectile [196] or the cavitation initiation form the rotation of a cross [170], could also be an option for validation because of their straightforward configuration. Each of the aforementioned tests may correspond to different cavitation regime, which has to be taken into account during the development of the method.

The simpler the case the more confident conclusions can be drawn upon the characteristics of the method, its accuracy or the influence of spatial and temporal resolution or the discretisation schemes; Kadoch et al. [106] resort into the solution of simple diffusion equations to initially test their penalisation immersed boundary method. On the other hand, if the main interest lays on the application and how the immersed boundary method could ease the simulation of a complex problem, the *ad-hoc* evaluation of the accuracy or a convergence study, on the main case or a simplified version of it, can be more appropriate [59, 149].

E.1   Order of Accuracy

In order to assess the accuracy of the developed Immersed Boundary method, the dependency of the computational error from the spatial resolution is evaluated initially.

As a widely adopted practice, the numerical error of the computed velocity field is estimated for varying spatial resolution, for the cases of an oscillating cylinder in stagnant fluid, presented in chapter 3, as well as of a Taylor-Couette flow developed between two rotating cylinders. Both cases are two-dimensional, assume viscous incompressible fluids and are chosen because of their simplicity.

The *Euclidean* or L_2 norm of the velocity error vector $\mathbf{e} = \mathbf{u} - \mathbf{u}_{ref}$ is used as an indication of the convergence of the computations; it is evaluated as the volume-weighted average of the square of its norm:

$$||e_{\mathbf{u}}|| = ||\mathbf{e}|| = \sqrt{\frac{1}{V_T} \int ||\mathbf{e}||^2 dV} = \sqrt{\frac{1}{V_T} \sum_j^n V_j ||\mathbf{u}_j - \mathbf{u}_{ref,j}||^2} \qquad \text{(E.1)}$$

where V_j and $\mathbf{u}_j$ refer to the volume and velocity, respectively, of the cell j of the discretised computational domain, of total volume V_T and total cell number n. As the reference velocity field, $\mathbf{u}_{ref}$, is chosen in both cases the velocity field of the finest grid, thus the order of convergence rate of the velocity error with increasing spatial resolution is studied.

For the case of the oscillating cylinder, four different canonical homogeneous grids are used, discretising a domain of size $55 d_{cyl} \times 35 d_{cyl}$, where $d_{cyl} = 0.01\ m$ is the diameter of the cylinder, with 60, 120, 240 and 480 cells along the diameter d_{cyl}. Using telescopic refinement, a constant resolution is achieved in an area $4 d_{cyl} \times 4 d_{cyl}$ around the cylinder, where the four grids yield a minimum (square) cell edge of $0.167\ mm$, $0.0833\ mm$, $0.0417 mm$ and $0.0208\ mm$, corresponding to 51k, 67k, 137k and 334k cells in total, respectively. The error of the velocity is estimated with regards to the velocity field of the finest mesh of 480 $cells/d_{cyl}$.

On the other hand, the Taylor-Couette flow developed between two cylinders is studied, with the outer cylinder of radius $R_o = 0.1\ m$ being stationary and the inner cylinder of radius $R_i = 0.025\ m$ rotating counter-clockwise with a constant angular velocity of $\omega_i = 10\ rad/s$. A similar test-case is used by Blais et al. [15]. Both cylinders are modelled as immersed boundaries into a square domain of $2.2 R_o$, discretised with canonical (mainly homogeneous) grids, ranging from 15×15 cells to 200×200 cells, with a corresponding resolution of $dx = 14.667\ mm$ to $dx = 1.1\ mm$. In addition, because the configuration is rather simple, the domain is discretised with conformal grids as well, in order to compare the developed method to standard body conforming solvers. A constant tangential velocity boundary condition is assigned on the inner wall, rather than employing an Arbitrary Lagrangian-Eulerian, rotating frame of reference or sliding mesh method to account for wall motion. The conformal grids follow a canonical polar arrangement, ranging from 16×8 cells along the periphery and the diameter of the circular annulus respectively, to 128×64. The velocity error is calculated relative to the finest grids of 200×200 cells for the IB approach and of 128×64 cells for the body conformal approach.

For the case of the oscillating cylinder, where first order time and spatial schemes are employed, it is clearly shown that the method achieves first order of accuracy. This is in accordance with the findings of Fadlun et al. [59].On the other hand, for the case of Taylor-Couette flow, it can be seen that although for coarser grids the error decreases faster than
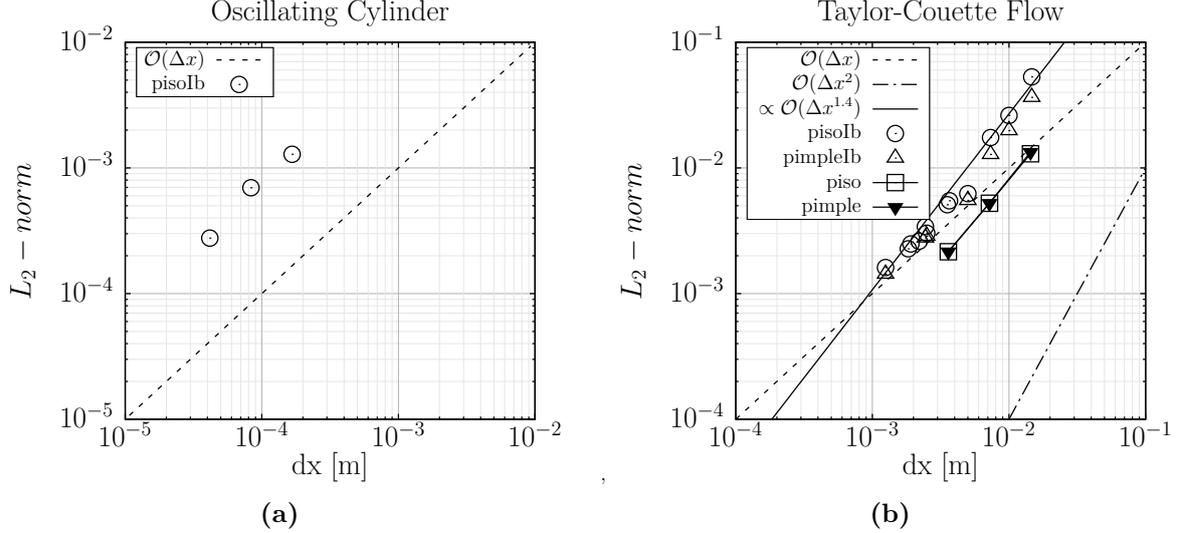
Figure E.1: L_2 error norm of velocity field, of oscillating cylinder in incompressible stagnant fluid *(a)* and for the case of Taylor-Couette flow between two rotating cylinders *(b)*. Grid dependence for the developed forcing IB method coupled with PISO or PIMPLE algorithms is shown; results for standard body-conformal solvers are presented for the Couette flow for comparison.

first order, for denser grids it slows down to first order, for both PISO and PIMPLE pressure-correction algorithms; the overall rate is proportional to an order of convergence of 1.4. It can be seen that computations with conformal mesh exhibit an equivalent convergence rate.

Regarding direct forcing IB methods, Fadlun et al. [59], within the framework of finite-differences, have investigated different interpolation techniques for projecting the body velocity on the background mesh: linear interpolation between the body wall and the grid point, volume weighted interpolation based on *solid* volume fraction, which is similar to the approach employed herein, and direct transfer of the velocity to the closest grid point, which corresponds to a *stepwise* or *stair-case* representation of the body. They have shown that the latter achieves a slower than first order convergence rate, while the solid volume weighting and linear interpolation yield first and second order convergence, respectively. Similar findings, for finite volume solvers, are reported by Mochel et al. [149] who used a stepwise projection of the immersed body and achieved slower than first order convergence, and Blais et al. [15] who developed a direct forcing method employing a volume weighting projection that achieves faster than first order convergence for the case of Taylor-Couette flow; Blais' method employs a less accurate estimation of solid volume fraction based on covered vertices, but also relies on relaxation of the forcing term throughout the PISO iterations.

Moreover, what makes the Taylor-Couette flow an interesting test-case is the fact that an analytical expression for the velocity profile between the two cylinders exists. The velocity of the fully developed flow, when the outer cylinder is static and the inner is rotating with angular velocity ω_i, follows a radial distribution given by:

$$u_\theta(r) = \omega_i \frac{\kappa}{1/\kappa - \kappa} R_o \left(\frac{R_o}{r} - \frac{r}{R_o} \right) \tag{E.2}$$

where $\kappa = R_i/R_o$ the ratio of the cylinders' radii and r the distance from the common centre.

The velocity profile along the radius of the circular annulus is shown in figure E.2a, calculated analytically or extracted from simulations of the proposed IB method coupled with the PISO algorithm, for different grids, as well as from computations with standard conformal grid approach. It can be seen that the no-slip boundary condition is better applied on the outer stationary cylinder, while in the vicinity of the inner rotating immersed body a persistent small underestimation of the velocity can be observed. This probably can be explained by taking into account that for the forcing term to be non-zero, a local small error in the velocity field is needed and therefore a small deviation from the desired value is expected.

The influence of the numerics is quantified in figure E.2b, where the L_2-norm of the velocity error is plotted for different set-ups, using as reference the error of a computation employing the PISO algorithm, 2nd order spatial and temporal discretisation, constant time-step of 1 ms and an implicit treatment of the forcing source term, which is updated in every PISO iteration with the corrected velocity field. It is observed that although the discretisation schemes do not affect the results, the time-step plays an important role, as the use of larger, variable according to the *CFL* condition, time-step, increases significantly the error; all simulations with the PIMPLE algorithm, which can be seen as an implicit PISO, are carried out with adjustable time-step. Thus, the basic advantage of the PIMPLE algorithm over the PISO, which is the ability to use larger stepping, even reaching $Co > 1$, is annulated in the specific test-case, revealing the requirement of the forcing method for controlled time-advancing. Finally, with regards to the representation of the immersed body, it can be seen that a finer surface grid does not affect the result; the projection approach used decouples the computational mesh and the body's triangulated surface resolution, simplifying the pre-processing of the computations. The latter comments can be further discussed.

,

,

(a)   **(b)**
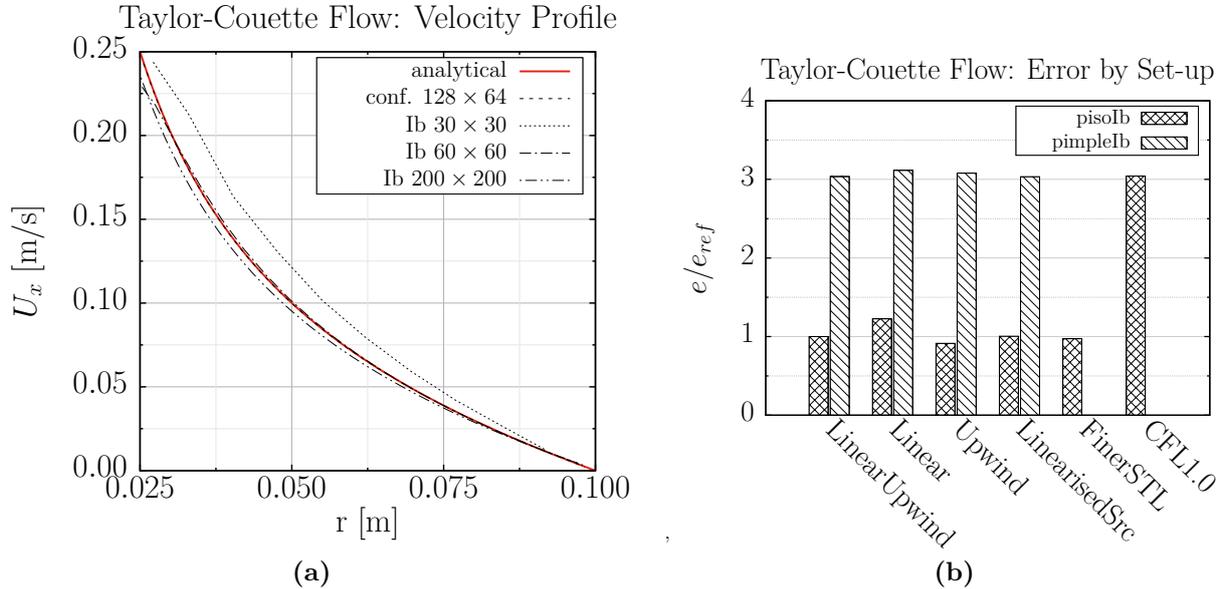
Figure E.2: Velocity profile for different grids compared to the analytical solution *(a)* and Euclidean norm of velocity error for different numerical set-ups *(b)* for the case of Taylor-Couette flow between two rotating cylinders. As reference error is used the error of the *pisoIb* case, with 2nd order *linearUpwind* and *Crank-Nicolson* schemes for velocity's spatial and temporal discretisation, with $dt = 10^{-3}$ s and *implicit* treatment of the forcing source term; $e_{ref} = 2.35 \cdot 10^{-3}$. All computations are carried out on a 88×88 mesh.

E.2 Projection error and Diffusion

The above analysis indicates that the resolution of the triangulated surface that represents the immersed boundary does not play an important role on the computations. This is an characteristic aspect of the method that can be seen as an important advantage. Other methodologies, such as ghost-cell approaches or forcing approaches that employ Lagrangian markers, which may require interpolation of the boundary condition or spreading of the forcing on the Eulerian background grid in the vicinity of the boundary, seem more dependent on the nodes that discretise the body representation. Uhlmann [229] demands that each Lagrangian forcing point should control one Eulerian grid cell, a condition that is equivalent to setting the resolution of the two grids to be of the same order, or the elementary surface area to be equal to the cell's face, that is $dS = dx^2$, where S the immersed surface and dx the Eulerian grid spacing; the least necessary number of Lagrangian markers to discretise the immersed body can be explicitly derived.

For the herein presented IB method, there is not such a requirement, as far as the resolution of the immersed surface is fine enough to capture the characteristics of the geometry and accommodate the geometric features of all the length scales. This is also visualised in figure E.3, where different aspects of the numerical computations are plotted for different ratios of the eulerian grid cell edge over the length of the element discretising the immersed surface. The accuracy of the immersed boundary projection on the background mesh can be estimated by the volume of the discretised cylinder, calculated as the integral of the solid volume fraction. Although the resolution of both the Eulerian and the surface grids determine the accuracy of projection, it is found that the error never exceeds the 3%. Apart from the evident impact of the background grid on the results, shown by the plotted lines, it can be stated that an increase of the number of elements of the triangulated surface, although it affects the immersed boundary projection, it does not increase the accuracy of the computation, as shown by the symbols.

Therefore, the only requirement of the method is a triangulated surface of proper quality. There is not a specific rule for the generation of surface mesh. The points or cell edges should not necessarily be equidistant, but rather the surface should be refined near special or small geometric features or areas of change of curvature; as the projection takes into account the perpendicular distance from the nearest surface point, straight edges could be described even by one element but curves should be explicitly refined or errors would occur. Such errors, although rather small, are visible for the case of under-resolved hydrofoil leading edge of figure E.4.

Another characteristic of forcing methods is their diffusive nature. As continuous or direct forcing methods usually evaluate the forcing on Lagrangian markers or nodes of the immersed boundary representation, the forcing is spread in nearby computational cells [13,77,181,182,186, 229]. Therefore, although the forcing nodes can be accurately tracked and the representation of the boundary would be sharp, the projected forcing would result in a thin diffused interface, sometimes occupying few cells, as required by the discrete forms of Dirac Delta functions $\delta(x)$ (see also figure 1.2). Moreover, if a level-set function is used as a projection of the body on the background computational mesh, the captured fluid-solid interface would be diffused over one or two cells. However, several cut-cell techniques follow a level-set projection and employ a piecewise linear approximation to reconstruct the boundary within the cells and apply the topological changes [102,138,175,198]; this approach would lead to spurious oscillations and is replaced by a more precise representation of the intersection [170].
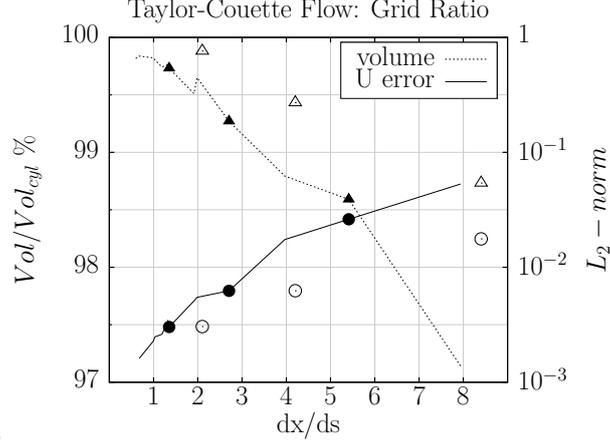
Figure E.3: Influence of ratio of cell edges of background mesh *(dx)* and triangulated immersed surface *(ds)*, on computations is presented, in terms of cylinder's volume and L_2-norm of the velocity field error. The discretised cylinder's volume is presented as a percentage of the actual volume of the cylinder ($V_{cyl} = \pi \cdot R_i^2 \cdot dz$). The lines correspond to cases with constant surface grid (85 points along the circumference) and varying background grid. The symbols indicate cases on constant background resolution but varying surface grid: coarse (85 points) with filled symbols and fine (132 points) with hollow symbols.
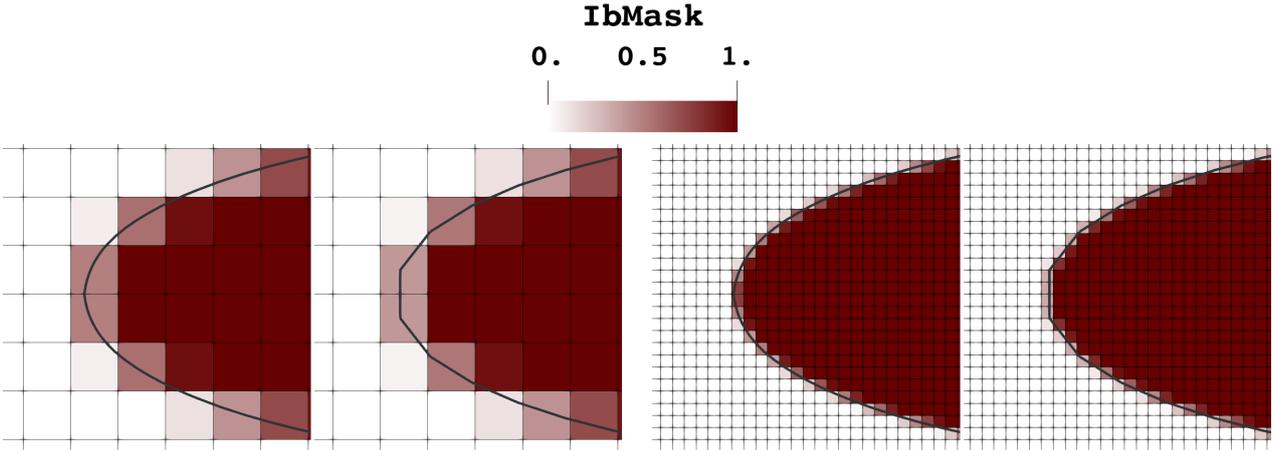
Figure E.4: Influence of the resolution of the triangulated surface representing the immersed boundary, on the *mask* or *solid volume fraction* calculation.

For the herein proposed method the fluid-solid interface has always a width of one cell, those with mask value between 0 and 1; however it is also of diffusive nature, as the exact location inside the cell of the boundary is not known and the forcing is applied on the cell centre, scaled by the mask value. This normally results in low velocity flow in the interface cells, where fraction of the body momentum is imposed, but spurious flow may appear inside the body, in the vicinity of the interface.

The level of this error in the velocity depends mainly on the application, and loosely on the grid resolution. Two examples are given in figure E.5 for an incompressible, low-Re flow, with moving boundary, and a far more complex, high-Re cavitating flow over a static hydrofoil. The error may be judged negligible if we take into account that in the first case, it never exceeds

164

0.6% of the imposed body velocity, and the latter case, velocity values $\leq 0.0008\ m/s$ appear in the body area while the inlet velocity is $13\ m/s$ and the maximum velocity in the channel may reach $\sim 20\ m/s$, due to the blockage or the high-speed re-entrant jets. In addition, this error means the fluid enclosed by a static immersed boundary might be moving slightly, but compared to the bulk flow it cannot produce significant momentum or energy losses and cannot affect significantly the total mass conservation.

Finally, these errors may be tackled by the use of more appropriate numerics, such as the use of relaxation for the forcing term, the use of a predictor step, similar to the fractional-step approach of Fadlun et al. [59] and Uhlmann [229], or pressure correction according to the rationale of Riahi et al. [186].
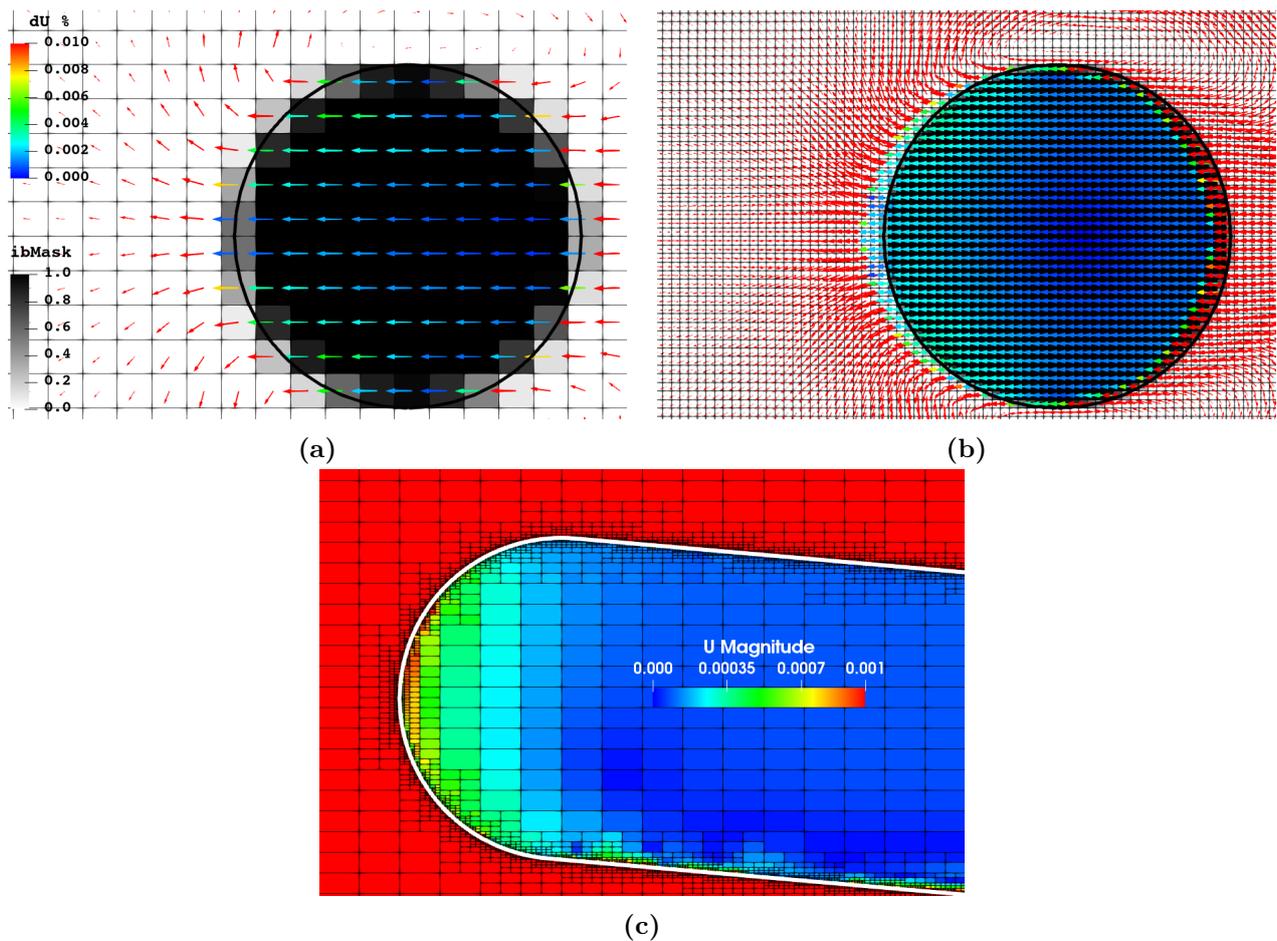
Figure E.5: Examples of erroneous velocity field inside the projected immersed body: *(a,b)* for an oscillating cylinder in incompressible stagnant fluid, presented as the difference of resulting velocity from the instantaneous target body velocity, which is $U_{body} = 0.16\ m/s$; *(c)* for a turbulent cavitating flow over a static hydrofoil in a channel with $U_{in} = 13\ m/s$, presented by means of velocity magnitude, which should be zero inside the immersed body.

Appendix F

List of Publications

Herein are enlisted the publications and the dissemination of the PhD project's progress and results.

Peer-Reviewed Journal Publications

1. Li Q., **Stavropoulos-Vasilakis E.**, Koukouvinis P., Gavaises M. and Bruecker H. C. , March 2020, Micro-pillar wall shear-stress measurements in the aortic arch with CFD-assisted calibration, *In preparation*

2. **Stavropoulos-Vasilakis E.**, Malgarinos I., Koukouvinis P. and Gavaises M., February 2020, A direct forcing Immersed Boundary Method for Cavitating Flows, Computer Methods in Applied Mechanics and Engineering *(Submitted, awaiting editorial decision)*

3. **Stavropoulos-Vasilakis E.**, Kyriazis N., Koukouvinis P., Farhat M. and Gavaises M., 2019, Cavitation induction by projectile impacting on a water jet, International Journal of Multiphase Flow, 114, pp.128-139, doi: 10.1016/j.ijmultiphaseflow.2019.03.001

Conferences Publications

1. **Stavropoulos-Vasilakis E.**, Kyriazis N., Koukouvinis P., Farhat M. and Gavaises M., 2018, Cavitation Induction by Projectile Impacting on a Water Jet, In Proceedings of the 10th International Symposium on Cavitation (CAV2018), ASME Press, doi: 10.1115/1.861851_ch43

Workshop Participation

1. **Stavropoulos-Vasilakis E.**, Malgarinos I., Dr. Koukouvinis P., Prof. Gavaises M., *Coupled simulation of valve motion and cavitation, Validation of Immersed Boundary Method*, 2016, 4$^{\text{rth}}$ Cavitation Workshop, International Institute for Cavitation Research, CIHEAM, Greece, *(poster participation)*

2. **Stavropoulos-Vasilakis E.**, Dr. Koukouvinis P., Prof. Gavaises M., *Immersed Boundary Method for Cavitating Flow Simulation*, 2017, 5$^{\text{th}}$ Cavitation Workshop, International Institute for Cavitation Research, CIHEAM, Greece, *(poster participation)*

3. **Stavropoulos-Vasilakis E.**, Kyriazis N., Dr. Koukouvinis P., Prof. Gavaises M.,*Cavitation During High Speed Impacts*, Dec. 2017, SIG Drop Dynamics Meeting, UK Fluids Network EPSRC, Wadham College, University of Oxford, UK, *(presentation participation)*

4. **Stavropoulos-Vasilakis E.**, Dr. Koukouvinis P., Prof. Gavaises M., *Immersed boundary method for simulation of high-velocity projectile impact on water column*, 2019, 6$^{\text{th}}$ Cavitation Workshop, International Institute for Cavitation Research, CIHEAM, Greece, *(poster and presentation participation)*

Bibliography

[1] I. V. Abalakin, A. P. Duben, N. S. Zhdanova, and T. K. Kozubskaya. Simulating an unsteady turbulent flow around a cylinder by the immersed boundary method. *Mathematical Models and Computer Simulations*, 11(1):74–85, Jan 2019.

[2] Serge Abrate. Soft impacts on aerospace structures. *Progress in Aerospace Sciences*, 81(Supplement C):1–17, 2016. Dynamic Loading Aspects of Composite Materials.

[3] Philippe Angot, Jean-Paul Caltagirone, and Pierre Fabrie. A fast vector penalty-projection method for incompressible non-homogeneous or multiphase navier–stokes problems. *Applied Mathematics Letters*, 25(11):1681–1688, 2012.

[4] M. Arienti and M. Sussman. An embedded level set method for sharp-interface multiphase simulations of diesel injectors. *International Journal of Multiphase Flow*, 59:1–14, 2014.

[5] B. F. Armaly, F. Durst, J. C. F. Pereira, and B. Schönung. Experimental and theoretical investigation of backward-facing step flow. *Journal of Fluid Mechanics*, 127:473–496, Feb 1983.

[6] Elias Balaras. Modeling complex boundaries using an external force field on fixed cartesian grids in large-eddy simulations. *Computers & Fluids*, 33(3):375–404, 2004.

[7] Elias Balaras and Jianming Yang. Nonboundary conforming methods for large-eddy simulations of biological flows. *Journal of Fluids Engineering*, 127(5):851–857, 2005.

[8] Heinz W. Bargmann. The mechanics of erosion by liquid and solid impact. *International Journal of Solids and Structures*, 29(14):1685–1698, 1992.

[9] Michele Battistoni, Qingluan Xue, Sibendu Som, and Eric Pomraning. Effect of off-axis needle motion on internal nozzle and near exit flow in a multi-hole diesel injector. *SAE International Journal of Fuels and Lubricants*, 7(1):167–182, 2014.

[10] Suresh Behara, Iman Borazjani, and Fotis Sotiropoulos. Vortex-induced vibrations of an elastically mounted sphere with three degrees of freedom at re = 300: hysteresis and vortex shedding modes. *Journal of Fluid Mechanics*, 686:426–450, 2011.

[11] Rickard E. Bensow and Göran Bark. Implicit LES Predictions of the Cavitating Flow on a Propeller. *Journal of Fluids Engineering*, 132(4), 04 2010. 041302.

[12] M. Berger. Chapter 1 - cut cells: Meshes and solvers. In Rémi Abgrall and Chi-Wang Shu, editors, *Handbook of Numerical Methods for Hyperbolic ProblemsApplied and Modern Issues*, volume 18 of *Handbook of Numerical Analysis*, pages 1–22. Elsevier, 2017.

[13] R. P. Beyer and R. J. LeVeque. Analysis of a one-dimensional model for the immersed boundary method. *SIAM Journal on Numerical Analysis*, 29(2):332–364, 1992.

[14] Baris Bicer, Ayana Tanaka, Takumi Fukuda, and Akira Sou. Numerical simulation of cavitation phenomena in diesel injector nozzles. In *16 th Annual Conf. ILASS-ASIA, Nagasaki-JAPAN*, pages 58–65, 2013.

[15] Bruno Blais, Manon Lassaigne, Christoph Goniva, Louis Fradette, and François Bertrand. A semi-implicit immersed boundary method and its application to viscous mixing. *Computers & Chemical Engineering*, 85:136–146, 2016.

[16] Jiri Blazek. *Computational fluid dynamics: principles and applications*. Butterworth-Heinemann, 2015.

[17] Iman Borazjani. Fluid–structure interaction, immersed boundary-finite element method simulations of bio-prosthetic heart valves. *Computer Methods in Applied Mechanics and Engineering*, 257:103–116, 2013.

[18] Iman Borazjani, Liang Ge, Trung Le, and Fotis Sotiropoulos. A parallel overset-curvilinear-immersed boundary framework for simulating complex 3d incompressible flows. *Computers & Fluids*, 77(Supplement C):76–96, 2013.

[19] Iman Borazjani, Liang Ge, and Fotis Sotiropoulos. Curvilinear immersed boundary method for simulating fluid structure interaction with complex 3d rigid bodies. *Journal of Computational Physics*, 227(16):7587–7620, 2008.

[20] Iman Borazjani, Liang Ge, and Fotis Sotiropoulos. High-Resolution Fluid–Structure Interaction Simulations of Flow Through a Bi-Leaflet Mechanical Heart Valve in an Anatomic Aorta. *Annals of Biomedical Engineering*, 38(2):326–344, 2010.

[21] Iman Borazjani and Fotis Sotiropoulos. Vortex-induced vibrations of two cylinders in tandem arrangement in the proximity–wake interference region. *Journal of Fluid Mechanics*, 621:321–364, 2009.

[22] Iman Borazjani and Fotis Sotiropoulos. The effect of implantation orientation of a bileaflet mechanical heart valve on kinematics and hemodynamics in an anatomic aorta. *Journal of biomechanical engineering*, 132(11):111005, 2010.

[23] N. K. Bourne, T. Obara, and J. E. Field. The Impact and Penetration of a Water Surface by a Liquid Jet. *Proceedings: Mathematical, Physical and Engineering Sciences*, 452(1949):1497–1502, 1996.

[24] F. P. Bowden and J. H. Brunton. The Deformation of Solids by Liquid Impact at Supersonic Speeds. *Proceedings of the Royal Society of London. Series A, Mathematical and Physical Sciences*, 263(1315):433–450, 1961.

[25] F. P. Bowden and J. E. Field. The Brittle Fracture of Solids by Liquid Impact, by Solid Impact, and by Shock. *Proceedings of the Royal Society of London. Series A, Mathematical and Physical Sciences*, 282(1390):331–352, 1964.

[26] E. Brennen C. *Cavitation and Bubble Dynamics*. 1995.

[27] Martin Brouillette. The richtmyer-meshkov instability. *Annual Review of Fluid Mechanics*, 34(1):445–468, 2002.

[28] Ch Brücker, U Steinseifer, W Schröder, and H Reul. Unsteady flow through a new mechanical heart valve prosthesis analysed by digital particle image velocimetry. *Measurement Science and Technology*, 13(7):1043, 2002.

[29] E.A. Brujan and P.R. Williams. Cavitation Phenomena in Non-Newtonian Liquids. *Chemical Engineering Research and Design*, 84(4):293–299, 2006. Special Issue In Honour of Professor Jack Richardson on the Occasion of his 85th Birthday.

[30] J.H. Brunton. A discussion on deformation of solids by the impact of liquids, and its relation to rain damage in aircraft and missiles, to blade erosion in steam turbines, and to cavitation erosion - High speed liquid impact. *Philosophical Transactions of the Royal Society of London A: Mathematical, Physical and Engineering Sciences*, 260(1110):79–85, 1966.

[31] Erik Burman and Peter Hansbo. Fictitious domain finite element methods using cut elements: Ii. a stabilized nitsche method. *Applied Numerical Mathematics*, 62(4):328–341, 2012. Third Chilean Workshop on Numerical Analysis of Partial Differential Equations (WONAPDE 2010).

[32] Shang-Gui Cai, A Ouahsine, H Smaoui, J Favier, and Y Hoarau. An efficient implicit direct forcing immersed boundary method for incompressible flows. In *3rd International Conference on Mathematical Modeling in Physical Sciences (IC-MSQUARE 2014)*, volume 574. IOP, 2015.

[33] Shang-Gui Cai, Abdellatif Ouahsine, Julien Favier, and Yannick Hoarau. Improved implicit immersed boundary method via operator splitting. In Adnan Ibrahimbegovic, editor, *Computational Methods for Solids and Fluids: Multiscale Analysis, Probability Aspects and Model Reduction*, pages 49–66. Springer International Publishing, Cham, 2016.

[34] Shang-Gui Cai, Abdellatif Ouahsine, Julien Favier, and Yannick Hoarau. Moving immersed boundary method. *International Journal for Numerical Methods in Fluids*, pages n/a–n/a, 2017.

[35] Shang-Gui Cai, Abdellatif Ouahsine, and Philippe Sergent. Modelling wave energy conversion of a semi-submerged heaving cylinder. In Adnan Ibrahimbegovic, editor, *Computational Methods for Solids and Fluids: Multiscale Analysis, Probability Aspects and Model Reduction*, pages 67–79. Springer International Publishing, Cham, 2016.

[36] Francesco Capizzano. Turbulent wall model for immersed boundary methods. *AIAA Journal*, 49(11):2367–2381, 2011.

[37] G. Castiglioni, J.A. Domaradzki, V. Pasquariello, S. Hickel, and M. Grilli. Numerical simulations of separated flows at moderate reynolds numbers appropriate for turbine

blades and unmanned aero vehicles. *International Journal of Heat and Fluid Flow*, 49:91–99, 2014. 8th Symposium on Turbulence & Shear Flow Phenomena (TSFP8).

[38] William M. Chan. Overset grid technology development at NASA Ames Research Center. *Computers & Fluids*, 38(3):496–503, 2009.

[39] Chih-Hao Chang, Xiaolong Deng, and Theo G Theofanous. Direct numerical simulation of interfacial instabilities: a consistent, conservative, all-speed, sharp-interface method. *Journal of Computational Physics*, 242:946–990, 2013.

[40] Ming-Jyh Chern, Yu-Hao Kuan, Giri Nugroho, Guan-Ting Lu, and Tzyy-Leng Horng. Direct-forcing immersed boundary modeling of vortex-induced vibration of a circular cylinder. *Journal of Wind Engineering and Industrial Aerodynamics*, 134:109–121, 2014.

[41] Open-Source Community. foam-extend. http://www.foam-extend.org/.

[42] Eddy Constant, C Li, Julien Favier, M Meldi, P Meliga, and E Serre. Implementation of a discrete immersed boundary method in openfoam. *arXiv preprint arXiv:1609.04364*, 2016.

[43] O Coutier-Delgosha, R Fortes-Patella, and J L Reboud. Simulation of unsteady cavitation with a two-equation turbulence model including compressibility effects. *Journal of Turbulence*, 3:N58, 2002.

[44] O. Coutier-Delgosha, J. L. Reboud, and Y. Delannoy. Numerical simulation of the unsteady behaviour of cavitating flows. *International Journal for Numerical Methods in Fluids*, 42(5):527–548, 2003.

[45] A. Cristallo and R. Verzicco. Numerical Simulations of Blood Flow Inside a Mechanical Heart Valve. volume 762, pages 220–225, 2005.

[46] Antonio Cristallo and Roberto Verzicco. Combined immersed boundary/large-eddy-simulations of incompressible three dimensional complex flows. *Flow, Turbulence and Combustion*, 77(1-4):3, 2006.

[47] L. P. Dasi, L. Ge, H. A. Simon, F. Sotiropoulos, and A. P. Yoganathan. Vorticity dynamics of a bileaflet mechanical heart valve in an axisymmetric aorta. *Physics of Fluids*, 19(6):067105, 2007.

[48] Lee Davison. *Fundamentals of shock wave propagation in solids*. Springer Science & Business Media, 2008.

[49] M. D. de Tullio, G. Pedrizzetti, and R. Verzicco. On the effect of aortic root geometry on the coronary entry-flow after a bileaflet mechanical heart valve implant: a numerical study. *Acta Mechanica*, 216(1):147–163, 2011.

[50] M.D. de Tullio, P. De Palma, G. Iaccarino, G. Pascazio, and M. Napolitano. An immersed boundary method for compressible flows using local grid refinement. *Journal of Computational Physics*, 225(2):2098–2117, 2007.

[51] M.D. de Tullio and G. Pascazio. A moving-least-squares immersed boundary method for simulating the fluid–structure interaction of elastic bodies with arbitrary thickness. *Journal of Computational Physics*, 325:201–225, 2016.

[52] Niels G. Deen, E.A.J.F. Peters, Johan T. Padding, and J.A.M. Kuipers. Review of direct numerical simulation of fluid–particle mass, momentum and heat transfer in dense gas–solid flows. *Chemical Engineering Science*, 116:710–724, 2014.

[53] Antoine Ducoin, Biao Huang, and Yin L. Young. Numerical Modeling of Unsteady Cavitating Flows around a Stationary Hydrofoil. *International Journal of Rotating Machinery*, 2012. Copyright - Copyright © 2012 Antoine Ducoin et al. Antoine Ducoin et al. This is an open access article distributed under the Creative Commons Attribution License, which permits unrestricted use, distribution, and reproduction in any medium, provided the original work is properly cited; Last updated - 2015-04-15.

[54] Matevž Dular and Olivier Coutier-Delgosha. Numerical modelling of cavitation erosion. *International journal for numerical methods in Fluids*, 61(12):1388–1410, 2009.

[55] A. Dullweber, B. Leimkuhler, and R. McLachlan. Symplectic splitting methods for rigid body molecular dynamics. *JOURNAL OF CHEMICAL PHYSICS*, 107(15):5840–5851, 1997.

[56] H. Dütsch, F. Durst, S. Becker, and H. Lienhart. Low-Reynolds-number flow around an oscillating circular cylinder at low Keulegan–Carpenter numbers. *Journal of Fluid Mechanics*, 360:249–271, 4 1998.

[57] Christian P. Egerer, Stefan Hickel, Steffen J. Schmidt, and Nikolaus A. Adams. Large-eddy simulation of turbulent cavitating flow in a micro channel. *Physics of Fluids*, 26(8):085102, 2014.

[58] Peter A. Engel. Chapter 11—Liquid Erosion. In Peter A. Engel, editor, *Impact Wear of Material*, volume 2 of *Tribology Series*, pages 291–319. Elsevier, 1978.

[59] E.A. Fadlun, R. Verzicco, P. Orlandi, and J. Mohd-Yusof. Combined immersed-boundary finite-difference methods for three-dimensional complex flow simulations. *Journal of Computational Physics*, 161(1):35–60, 2000.

[60] Tobias Falkenstein, Seongwon Kang, Marco Davidovic, Mathis Bode, Heinz Pitsch, Toshihiro Kamatsuchi, Junji Nagao, and Toshiyuki Arima. LES of Internal Combustion Engine Flows Using Cartesian Overset Grids. *Oil & Gas Science and Technology - Rev. IFP Energies nouvelles*, 72(6):36, 2017.

[61] P.E. Farrell and J.R. Maddison. Conservative interpolation between volume meshes by local Galerkin projection. *Computer Methods in Applied Mechanics and Engineering*, 200(1):89–100, 2011.

[62] Julien Favier, Alistair Revell, and Alfredo Pinelli. A lattice boltzmann–immersed boundary method to simulate the fluid interaction with moving and slender flexible objects. *Journal of Computational Physics*, 261:145–161, 2014.

[63] Zhi-Gang Feng and Efstathios E. Michaelides. Heat transfer in particulate flows with direct numerical simulation (dns). *International Journal of Heat and Mass Transfer*, 52(3):777–786, 2009.

[64] J. E. Field, M. B. Lesser, and J. P. Dear. Studies of Two-Dimensional Liquid-Wedge Impact and Their Relevance to Liquid-Drop Impact Problems. *Proceedings of the Royal Society of London. Series A, Mathematical and Physical Sciences*, 401(1821):225–249, 1985.

[65] J.E. Field, J.-J. Camus, M. Tinguely, D. Obreschkow, and M. Farhat. Cavitation in impacted drops and jets and the effect on erosion damage thresholds. *Wear*, 290–291:154–160, 2012.

[66] J.E. Field, J.P. Dear, and J.E. Ogren. The effects of target compliance on liquid drop impact. *Journal of Applied Physics*, 65(2):533–540, 1989.

[67] R Fortes-Patella, O Coutier-Delgosha, and J Reboud. Evaluation of the turbulence model influence on the numerical simulations of unsteady cavitation. *J. Fluids Eng*, 125(1):38–45, 2003.

[68] The OpenFOAM Foundation. OpenFOAM. http://www.openfoam.org/.

[69] Jean-Pierre Franc and Jean-Marie 1932 Michel. *Fundamentals of cavitation*, volume 76. Kluwer Academic Publishers, Dordrecht;London;, 2004.

[70] Manolis Gavaises, Fabio Villa, Phoevos Koukouvinis, Marco Marengo, and Jean-Pierre Franc. Visualisation and les simulation of cavitation cloud formation and collapse in an axisymmetric geometry. *International Journal of Multiphase Flow*, 68(Supplement C):14–26, 2015.

[71] Liang Ge, Lakshmi P. Dasi, Fotis Sotiropoulos, and Ajit P. Yoganathan. Characterization of Hemodynamic Forces Induced by Mechanical Heart Valves: Reynolds vs. Viscous Stresses. *Annals of Biomedical Engineering*, 36(2):276–297, Feb 2008.

[72] Liang Ge and Fotis Sotiropoulos. A numerical method for solving the 3d unsteady incompressible navier–stokes equations in curvilinear domains with complex immersed boundaries. *Journal of Computational Physics*, 225(2):1782–1809, 2007.

[73] E. Giannadakis, M. Gavaises, and C. Arcoumanis. Modelling of cavitation in diesel injector nozzles. *Journal of Fluid Mechanics*, 616:153–193, 2008.

[74] A. Gilmanov, F. Sotiropoulos, and E. Balaras. A general reconstruction algorithm for simulating flows with complex 3d immersed boundaries on cartesian grids. *Journal of Computational Physics*, 191(2):660–669, 2003.

[75] Anvar Gilmanov and Fotis Sotiropoulos. A hybrid cartesian/immersed boundary method for simulating flows with 3d, geometrically complex, moving bodies. *Journal of Computational Physics*, 207(2):457–492, 2005.

174

[76] R. Glowinski and Tsorg-Whay Pan. Error estimates for fictitious domain/penalty/finite element methods. *CALCOLO*, 29(1):125–141, Mar 1992.

[77] D. Goldstein, R. Handler, and L. Sirovich. Modeling a no-slip flow boundary with an external force field. *Journal of Computational Physics*, 105(2):354–366, 1993.

[78] D. Goldstein, R. Handler, and L. Sirovich. Direct numerical simulation of turbulent flow over a modeled riblet covered surface. *Journal of Fluid Mechanics*, 302:333–376, Nov 1995.

[79] T Graf, H Reul, C Detlefs, R Wilmes, and G Rau. Causes and formation of cavitation in mechanical heart valves. *The Journal of heart valve disease*, 3:S49–64, 1994.

[80] Boyce E. Griffith, Richard D. Hornung, David M. McQueen, and Charles S. Peskin. An adaptive, formally second order accurate version of the immersed boundary method. *Journal of Computational Physics*, 223(1):10–49, 2007.

[81] Boyce E. Griffith and Charles S. Peskin. On the order of accuracy of the immersed boundary method: Higher order convergence rates for sufficiently smooth problems. *Journal of Computational Physics*, 208(1):75–105, 2005.

[82] Sebastian Grimberg and Charbel Farhat. Fast computation of the wall distance in unsteady eulerian fluid-structure computations. *International Journal for Numerical Methods in Fluids*, 89(4-5):143–161, 2019.

[83] Leopold Grinberg and George Em Karniadakis. Outflow Boundary Conditions for Arterial Networks with Multiple Outlets. *Annals of Biomedical Engineering*, 36(9):1496–1514, Sep 2008.

[84] John W. Grove and Ralph Menikoff. Anomalous reflection of a shock wave at a fluid interface. *Journal of Fluid Mechanics*, 219:313–336, 1990.

[85] L. P. Hackman, G. D. Raithby, and A. B. Strong. Numerical predictions of flows over backward-facing steps. *International Journal for Numerical Methods in Fluids*, 4(8):711–724, 1984.

[86] K. K. Haller, D. Poulikakos, Y. Ventikos, and P. Monkewitz. Shock wave formation in droplet impact on a rigid surface: lateral liquid motion and multiple wave structure in the contact line region. *Journal of Fluid Mechanics*, 490:1–14, 2003.

[87] Francis H. Harlow and John P. Shannon. The Splash of a Liquid Drop. *Journal of Applied Physics*, 38(10):3855–3866, 1967.

[88] Daniel Hartmann, Matthias Meinke, and Wolfgang Schröder. A strictly conservative cartesian cut-cell method for compressible viscous flows on adaptive grids. *Computer Methods in Applied Mechanics and Engineering*, 200(9):1038–1052, 2011.

[89] Dalton J.E. Harvie and David F. Fletcher. A hydrodynamic and thermodynamic simulation of droplet impacts on hot surfaces, Part I: theoretical model. *International Journal of Heat and Mass Transfer*, 44(14):2633–2642, 2001.

[90] N. A. Hawker and Y. Ventikos. Interaction of a strong shockwave with a gas bubble in a liquid medium: a numerical study. *Journal of Fluid Mechanics*, 701:59–97, 2012.

[91] F.J. Heymann. Erosion by liquids. *Machine Design*, 10:118–124, 1970.

[92] Richard L Holmes, Guy Dimonte, Bruce Fryxell, Michael L Gittings, John W Grove, Marilyn Schneider, David H Sharp, Alexander L Velikovich, Robert P Weaver, and Qiang Zhang. Richtmyer–meshkov instability growth: experiment, simulation and theory. *Journal of Fluid Mechanics*, 389:55–79, 1999.

[93] Tobias Holzmann. *Mathematics, numerics, derivations and OpenFOAM®*. 2017.

[94] Martijn Hoogenboom, Dylan Eikelenboom, Martijn H den Brok, Arend Heerschap, Jurgen J Fütterer, and Gosse J Adema. Mechanical high-intensity focused ultrasound destruction of soft tissue: working mechanisms and physiologic effects. *Ultrasound in Medicine and Biology*, 41(6):1500–1517, 2015.

[95] Pierre Horgue, Marc Prat, and Michel Quintard. A penalization technique applied to the "volume-of-fluid" method: Wettability condition on immersed boundaries. *Computers & Fluids*, 100:255–266, 2014.

[96] H Hosseini, S Moosavi-Nejad, H Akiyama, and V Menezes. Shock wave interaction with interfaces between materials having different acoustic impedances. *Applied Physics Letters*, 104(10):103701, 2014.

[97] Biao Huang, Antoine Ducoin, and Yin Lu Young. Physical and numerical investigation of cavitating flows around a pitching hydrofoil. *Physics of Fluids*, 25(10):102109, 2013.

[98] Chenguang Huang, Jian Huang, Yiwei Wang, and Chang Xu. Cloud cavitating flow around an axisymmetric projectile in the shallow water. In *10th International Cavitation Symposium*, 2018.

[99] S. E. Hurlbut, M. L. Spaulding, and F. M. White. Numerical Solution for Laminar Two Dimensional Flow About a Cylinder Oscillating in a Uniform Stream. *Journal of Fluids Engineering*, 104(2):214–220, 1982.

[100] Gianluca Iaccarino and Roberto Verzicco. Immersed boundary technique for turbulent flow simulations. *Applied Mechanics Reviews*, 56(3):331–347, 2003.

[101] R.I Issa. Solution of the implicitly discretised fluid flow equations by operator-splitting. *Journal of Computational Physics*, 62(1):40–65, 1986.

[102] Nicolas James, Emmanuel Maitre, and Iraj Mortazavi. Immersed boundary methods for the numerical simulation of incompressible aerodynamic and fluid-structure interactions. *Annales mathématiques Blaise Pascal*, 20(1):139–173, 2013.

[103] Reza N. Jazar. *Advanced dynamics: rigid body, multibody, and aerospace applications*. Wiley, Hoboken, N.J, 2011.

[104] Mark W. Johnson. A novel cartesian {CFD} cut cell approach. *Computers & Fluids*, 79:105–119, 2013.

[105] Patrick Joly and Leïla Rhaouti. Domaines fictifs, éléments finis h(div) et condition de neumann: le problème de la condition inf-sup. *Comptes Rendus de l'Académie des Sciences - Series I - Mathematics*, 328(12):1225–1230, 1999.

[106] Benjamin Kadoch, Dmitry Kolomenskiy, Philippe Angot, and Kai Schneider. A volume penalization method for incompressible flows and scalar advection–diffusion with moving obstacles. *Journal of Computational Physics*, 231(12):4365–4383, 2012.

[107] Khodor Khadra, Philippe Angot, Sacha Parneix, and Jean-Paul Caltagirone. Fictitious domain approach for numerical modelling of navier–stokes equations. *International Journal for Numerical Methods in Fluids*, 34(8):651–684, 2000.

[108] J. Kim, S. J. Kline, and J. P. Johnston. Investigation of a Reattaching Turbulent Shear Layer: Flow Over a Backward-Facing Step. *Journal of Fluids Engineering*, 102(3):302–308, 09 1980.

[109] V. Kini, C. Bachmann, A. Fontaine, S. Deutsch, and J. M. Tarbell. Flow Visualization in Mechanical Heart Valves: Occluder Rebound and Cavitation Potential. *Annals of Biomedical Engineering*, 28(4):431, 2000.

[110] P. Koukouvinis, M. Gavaises, O. Supponen, and M. Farhat. Simulation of bubble expansion and collapse in the vicinity of a free surface. *Physics of Fluids*, 28(5):052103, 2016.

[111] Phoevos Koukouvinis, Christoph Bruecker, and Manolis Gavaises. Unveiling the physical mechanism behind pistol shrimp cavitation. *Scientific Reports*, 7(1):13994, October 2017.

[112] Phoevos Koukouvinis, Manolis Gavaises, Jason Li, and Lifeng Wang. Large Eddy Simulation of Diesel injector including cavitation effects and correlation to erosion damage . *Fuel*, 175:26–39, 2016.

[113] Phoevos Koukouvinis, Nicholas Mitroglou, Manolis Gavaises, Massimo Lorenzi, and Maurizio Santini. Quantitative predictions of cavitation presence and erosion-prone locations in a high-pressure cavitation test rig. *Journal of Fluid Mechanics*, 819:21–57, 2017.

[114] Phoevos Koukouvinis, Homa Naseri, and Manolis Gavaises. Performance of turbulence and cavitation models in prediction of incipient and developed cavitation. *International Journal of Engine Research*, 18(4):333–350, 2017.

[115] P. O. K. Krehl. *History of Shock Waves, Explosions and Impact.* Springer-Verlag GmbH, 2009.

[116] Akihiro Kubota, Hiroharu Kato, and Hajime Yamaguchi. A new modelling of cavitating flows: a numerical study of unsteady cavitation on a hydrofoil section. *Journal of Fluid Mechanics*, 240:59–96, 1992.

[117] Robert F. Kunz, David A. Boger, David R. Stinebring, Thomas S. Chyczewski, Jules W. Lindau, Howard J. Gibeling, Sankaran Venkateswaran, and T.R. Govindan. A preconditioned Navier–Stokes method for two-phase flows with application to cavitation prediction. *Computers & Fluids*, 29(8):849–875, 2000.

177

[118] Jeong L. Sohn. Numerical analysis of laminar and turbulent incompressible flows using the finite element Fluid Dynamics Analysis Package (FIDAP). 09 1988.

[119] Ming-Chih Lai and Charles S. Peskin. An immersed boundary method with formal second-order accuracy and reduced numerical viscosity. *Journal of Computational Physics*, 160(2):705–719, 2000.

[120] Hung Le, Parviz Moin, and John Kim. Direct numerical simulation of turbulent flow over a backward-facing step. *Journal of Fluid Mechanics*, 330:349–374, 1997.

[121] C.O. Leiber. *Assessment of safety and risk with a microscopic model of detonation.* Elsevier, 2003.

[122] Timothy Leighton. *The acoustic bubble.* Academic press, 2012.

[123] Jean-Baptiste Leroux, Jacques André Astolfi, and Jean Yves Billard. An experimental study of unsteady partial cavitation. *Journal of fluids engineering*, 126(1):94–101, 2004.

[124] Jean-Baptiste Leroux, Olivier Coutier-Delgosha, and Jacques André Astolfi. A joint experimental and numerical study of mechanisms associated to instability of partial cavitation on two-dimensional hydrofoil. *Physics of fluids*, 17(5):052101, 2005.

[125] M. B. Lesser. Analytic Solutions of Liquid-Drop Impact Problems. *Proceedings of the Royal Society of London. Series A, Mathematical and Physical Sciences*, 377(1770):289–308, 1981.

[126] Randall J. LeVeque. Balancing Source Terms and Flux Gradients in High-Resolution Godunov Methods: The Quasi-Steady Wave-Propagation Algorithm. *Journal of Computational Physics*, 146(1):346–365, 1998.

[127] Randall J. Leveque and Zhilin Li. Erratum: The immersed interface method for elliptic equations with discontinuous coefficients and singular sources. *SIAM Journal on Numerical Analysis*, 32(5):1704–1704, 1995.

[128] Qianhui Li, Franziska Hegner, and Christoph Bruecker. Comparative study of wall shear stress at the ascending aorta for different mechanical heart valve prostheses. *Journal of biomechanical engineering*, 2019.

[129] Zhe Li, Julien Favier, Umberto D'Ortona, and Sébastien Poncet. An immersed boundary-lattice boltzmann method for single- and multi-component fluid flows. *Journal of Computational Physics*, 304:424–440, 2016.

[130] Pengzhi Lin. A fixed-grid model for simulation of a moving body in free surface flows. *Computers & Fluids*, 36(3):549–561, 2007.

[131] San-Yih Lin, Yi-Cheng Chen, Fu-Ling Yang, Chuin-Shan Chen, and Shang-Hsien Hsieh. A parallel vof ib pressure-correction method for simulation of multiphase flows. *Applied Mathematical Modelling*, 40(3):1800–1815, 2016.

[132] P. L.-F. Liu, T.-R. Wu, F. Raichlen, C. E. Synolakis, and J. C. Borrero. Runup and rundown generated by three-dimensional sliding masses. *Journal of Fluid Mechanics*, 536:107–144, 2005.

[133] Chi-Wen Lo, Sheng-Fu Chen, Chi-Pei Li, and Po-Chien Lu. Cavitation Phenomena in Mechanical Heart Valves: Studied by Using a Physical Impinging Rod System. *Annals of Biomedical Engineering*, 38(10):3162–3172, 2010.

[134] Henrik Lohrberg, Bernd Stoffel, Regianne Fortes-Patella, O Coutier-Delgosha, and J Reboud. Numerical and experimental investigations on the cavitating flow in a cascade of hydrofoils. *Experiments in fluids*, 33(4):578–586, 2002.

[135] Stjepan Lugomer. Laser generated richtmyer–meshkov instability and nonlinear wave paradigm in turbulent mixing: I. central region of gaussian spot. *Laser and Particle Beams*, 34(4):687–704, 2016.

[136] Kun Luo, Zhenya Zhuang, Jianren Fan, and Nils Erland L. Haugen. A ghost-cell immersed boundary method for simulations of heat transfer in compressible flows under different boundary conditions. *International Journal of Heat and Mass Transfer*, 92:708–717, 2016.

[137] Amir Malvandi, Amirmahdi Ghasemi, Rasoul Nikbakhti, Amirreza Ghasemi, and Faraz Hedayati. Modeling and parallel computation of the non-linear interaction of rigid bodies with incompressible multi-phase flow. *Computers & Mathematics with Applications*, 72(4):1055–1065, 2016.

[138] Matthias Meinke, Lennart Schneiders, Claudia Günther, and Wolfgang Schröder. A cut-cell method for sharp moving boundaries in cartesian grids. *Computers & Fluids*, 85:135–142, 2013. International Workshop on Future of {CFD} and Aerospace Sciences.

[139] Themistoklis Melissaris, Norbert Bulten, and Tom van Terwisga. On Cavitation Aggressiveness and Cavitation Erosion on Marine Propellers using a URANS Method. In *Proceedings of the 10th International Symposium on Cavitation (CAV2018)*. ASME Press, 12 2018.

[140] F. R. Menter, R. Langtry, and S. Völker. Transition Modelling for General Purpose CFD Codes. *Flow, Turbulence and Combustion*, 77(1):277–303, Nov 2006.

[141] Florian R Menter. Two-equation eddy-viscosity turbulence models for engineering applications. *AIAA journal*, 32(8):1598–1605, 1994.

[142] Charles L Merkle, J. Z. Feng, and P. E. O. Buelow. Computational modelling of the dynamics of sheet cavitation. In *Proc. of the 3rd Int. Symp. on Cavitation*, 1998.

[143] Wan Mingxi, Yi Feng, and Gail Ter Haar. *Cavitation in Biomedicine: Principles and Techniques*. Springer, 2015.

[144] Murali-Girija Mithun, Phoevos Koukouvinis, Ioannis K Karathanassis, and Manolis Gavaises. Numerical simulation of three-phase flow in an external gear pump using immersed boundary approach. *Applied Mathematical Modelling*, 72:682–699, 2019.

[145] R. Mittal, H. Dong, M. Bozkurttas, F.M. Najjar, A. Vargas, and A. von Loebbecke. A versatile sharp interface immersed boundary method for incompressible flows with complex boundaries. *Journal of Computational Physics*, 227(10):4825–4852, 2008.

[146] R. Mittal, S. P. Simmons, and F. Najjar. Numerical study of pulsatile flow in a constricted channel. *Journal of Fluid Mechanics*, 485:337–378, 2003.

[147] Rajat Mittal and Gianluca Iaccarino. Immersed boundary methods. *Annual Review of Fluid Mechanics*, 37(1):239–261, 2005.

[148] Loïc Mochel. *Assessment of technological effects with innovative numerical methods on launcher configurations.* Theses, Université Pierre et Marie Curie - Paris VI, March 2015.

[149] Loïc Mochel, Pierre-Élie Weiss, and Sébastien Deck. Zonal immersed boundary conditions: Application to a high-reynolds-number afterbody flow. *AIAA Journal*, 52(12):2782–2794, Jun 2014.

[150] J Mohd-Yusof. Combined immersed boundaries/b-splines methods for simulations of flows in complex geometries. In *Annual Research Briefs*. Center for Turbulence Research, 1997.

[151] J Mohd-Yusof. Development of immersed boundary methods for complex geometries. In *Annual Research Briefs*. Center for Turbulence Research, 1998.

[152] F Moukalled, L Mangani, M Darwish, et al. *The Finite Volume Method in Computational Fluid Dynamics: An Advanced Introduction with OpenFOAM® and Matlab.* Springer, 2016.

[153] Federico Municchi and Stefan Radl. Consistent closures for euler-lagrange models of bi-disperse gas-particle suspensions derived from particle-resolved direct numerical simulations. *International Journal of Heat and Mass Transfer*, 111:171–190, 2017.

[154] Federico Municchi and Stefan Radl. Momentum, heat and mass transfer simulations of bounded dense mono-dispersed gas-particle systems. *International Journal of Heat and Mass Transfer*, 120:1146–1161, 2018.

[155] Langley Research Center NASA. Turbulence Modeling Resource. https://turbmodels.larc.nasa.gov//.

[156] Homa Naseri, Phoevos Koukouvinis, Ilias Malgarinos, and Manolis Gavaises. On viscoelastic cavitating flows: A numerical study. *Physics of Fluids*, 30(3):033102, 2018.

[157] Nikolaos Kyriazis and Phoevos Koukouvinis and Manolis Gavaises. Modelling cavitation during drop impact on solid surfaces. *Advances in Colloid and Interface Science*, 2018.

[158] Hidetoshi Nishida, Souichi Kohashi, and Mitsuru Tanaka. Construction of seamless immersed boundary phase-field method. *Computers & Fluids*, pages –, 2017.

[159] Yang-Yao Niu and Hong-Wei Wang. Simulations of the shock waves and cavitation bubbles during a three-dimensional high-speed droplet impingement based on a two-fluid model. *Computers & Fluids*, 134-135:196–214, 2016.

[160] R.R. Nourgaliev, S.Y. Sushchikh, T.N. Dinh, and T.G. Theofanous. Shock wave refraction patterns at interfaces. *International Journal of Multiphase Flow*, 31(9):969–995, 2005.

[161] Guy S Nusholtz, Lee G Glascoe, and E Benjamin Wylie. Cavitation during head impact. Technical report, SAE Technical Paper, 1997.

[162] Guy S. Nusholtz, E. Benjamin Wylie, and Lee G. Glascoe. Internal cavitation in simple head impact model. *Journal of neurotrauma*, 12(4):707–714, 1995.

[163] T. Obara, N.K. Bourne, and J.E. Field. Liquid-jet impact on liquid and solid surfaces. *Wear*, 186-187(Part 2):388–394, 1995. 8th International Conference on Erosion by Liquid and Solid Impact.

[164] Danail Obreschkow, Nicolas Dorsaz, Philippe Kobel, Aurele de Bosset, Marc Tinguely, John Field, and Mohamed Farhat. Confined shocks inside isolated liquid volumes: A new path of erosion? *Physics of Fluids*, 23(10):101702, 2011.

[165] Daria Ogloblina, Steffen J. Schmidt, and Nikolaus A. Adams. Numerical Simulation of Collapsing Vapor Bubble Clusters Close to a Rigid Wall. In *Proceedings of the 10th International Symposium on Cavitation (CAV2018)*. ASME Press, 12 2018.

[166] OpenCFD. OpenFOAM+. http://www.openfoam.com/.

[167] F Örley, S Hickel, S J Schmidt, and N A Adams. LES of cavitating flow inside a diesel injector including dynamic needle movement. *Journal of Physics: Conference Series*, 656:012097, dec 2015.

[168] F. Örley, T. Trummler, S. Hickel, M. S. Mihatsch, S. J. Schmidt, and N. A. Adams. Large-eddy simulation of cavitating nozzle flow and primary jet break-up. *Physics of Fluids*, 27(8):086101, 2015.

[169] Felix Örley, Stefan Hickel, Steffen J Schmidt, and Nikolaus A Adams. Large-eddy simulation of turbulent, cavitating fuel flow inside a 9-hole diesel injector including needle movement. *International Journal of Engine Research*, 18(3):195–211, 2017.

[170] Felix Örley, Vito Pasquariello, Stefan Hickel, and Nikolaus A. Adams. Cut-element based immersed boundary method for moving geometries in compressible liquid flows with cavitation. *Journal of Computational Physics*, 283:1–22, 2015.

[171] P. De Palma, M.D. de Tullio, G. Pascazio, and M. Napolitano. An immersed-boundary method for compressible viscous flows. *Computers & Fluids*, 35(7):693–702, 2006. Special Issue Dedicated to Professor Stanley G. Rubin on the Occasion of his 65th Birthday.

[172] Konstantinos P. Papadopoulos, Manolis Gavaises, and Chris Atkin. A simplified mathematical model for thrombin generation. *Medical Engineering & Physics*, 36(2):196–204, 2014.

[173] Konstantinos P. Papadopoulos, Manolis Gavaises, Ioannis Pantos, Demosthenes G. Katritsis, and Nicholas Mitroglou. Derivation of flow related risk indices for stenosed left anterior descending coronary arteries with the use of computer simulations. *Medical Engineering & Physics*, 38(9):929–939, 2016.

[174] Sungtaek Park, Jeonghwa Seo, Shin Hyung Rhee, and Sangdon Lee. 6dof motion and cavity dynamics of a ventilated super-cavitating vehicle with control fins. In *Proceedings of the 10th International Symposium on Cavitation (CAV2018)*. ASME Press, 12 2018.

[175] Vito Pasquariello, Georg Hammerl, Felix Örley, Stefan Hickel, Caroline Danowski, Alexander Popp, Wolfgang A. Wall, and Nikolaus A. Adams. A cut-cell finite volume – finite element coupling approach for fluid–structure interaction in compressible flow. *Journal of Computational Physics*, 307:670–695, 2016.

[176] S.V Patankar and D.B Spalding. A calculation procedure for heat, mass and momentum transfer in three-dimensional parabolic flows. *International Journal of Heat and Mass Transfer*, 15(10):1787–1806, 1972.

[177] SN Patek, WL Korff, and RL Caldwell. Biomechanics: deadly strike mechanism of a mantis shrimp. *Nature*, 428(6985):819, 2004.

[178] H.V. Patel, S. Das, J.A.M. Kuipers, J.T. Padding, and E.A.J.F. Peters. A coupled volume of fluid and immersed boundary method for simulating 3d multiphase flows with contact line dynamics in complex geometries. *Chemical Engineering Science*, 166:28–41, 2017.

[179] Wei Peng, Kwang-Ho Lee, and Norimi Mizutani. Application of direct-forcing ib-vof method to the simulation of wave deformation by submerged structures. *Journal of Coastal Research*, 28(3):658–670, 2012.

[180] Marianna Pepona and Julien Favier. A coupled immersed boundary–lattice boltzmann method for incompressible flows through moving porous media. *Journal of Computational Physics*, 321:1170–1184, 2016.

[181] Charles S Peskin. Numerical analysis of blood flow in the heart. *Journal of Computational Physics*, 25(3):220–252, 1977.

[182] A. Pinelli, I.Z. Naqavi, U. Piomelli, and J. Favier. Immersed-boundary methods for general finite-difference and finite-volume navier–stokes solvers. *Journal of Computational Physics*, 229(24):9073–9091, 2010.

[183] T.K. Prasanth, S. Behara, S.P. Singh, R. Kumar, and S. Mittal. Effect of blockage on vortex-induced vibrations at low Reynolds numbers. *Journal of Fluids and Structures*, 22(6–7):865–876, 2006. Bluff Body Wakes and Vortex-Induced Vibrations (BBVIV-4).

[184] Andrea Prosperetti and Grétar Tryggvason. *Computational Methods for Multiphase Flow*. Cambridge University Press, Cambridge, 2007.

[185] Jean-Luc Reboud, Benoit Stutz, and Olivier Coutier. Two phase flow structure of cavitation: experiment and modeling of unsteady effects. In *3rd International Symposium on Cavitation CAV1998*, 1998.

[186] H. Riahi, M. Meldi, J. Favier, E. Serre, and E. Goncalves. A pressure-corrected immersed boundary method for the numerical simulation of compressible flows. *Journal of Computational Physics*, 374:361–383, 2018.

[187] P Roe. Upwind differencing schemes for hyperbolic conservation laws with source terms. *Nonlinear hyperbolic problems*, pages 41–51, 1987.

[188] Ehsan Roohi, Amir Pouyan Zahiri, and Mahmood Passandideh-Fard. Numerical simulation of cavitation around a two-dimensional hydrofoil using VOF method and LES turbulence model. *Applied Mathematical Modelling*, 37(9):6469–6488, 2013.

[189] A Rossetti, G Pavesi, G Ardizzon, and A Santolin. Numerical analyses of cavitating flow in a pelton turbine. *Journal of Fluids Engineering*, 136(8):081304, 2014.

[190] E.M. Saiki and S. Biringen. Numerical simulation of a cylinder in uniform flow: Application of a virtual boundary method. *Journal of Computational Physics*, 123(2):450–465, 1996.

[191] Teluo Sakurai, Katsunori Yoshimatsu, Naoya Okamoto, and Kai Schneider. Volume penalization for inhomogeneous neumann boundary conditions modeling scalar flux in complicated geometry. *Journal of Computational Physics*, 390:452–469, 2019.

[192] Roman Samulyak and Yarema Prykarpatskyy. Richtmyer–meshkov instability in liquid metal flows: influence of cavitation and magnetic fields. *Mathematics and Computers in Simulation*, 65(4):431–446, 2004. Wave Phenomena in Physics and Engineering: New Models, Algorithms, and Applications.

[193] Toshiyuki Sanada, Keita Ando, and Tim Colonius. A computational study of high-speed droplet impact. *Fluid Dynamics & Materials Processing*, 7(4):329–340, 2011.

[194] Jessica Sanders, John E. Dolbow, Peter J. Mucha, and Tod A. Laursen. A new method for simulating rigid body motion in incompressible two-phase flow. *International Journal for Numerical Methods in Fluids*, 67(6):713–732, 2011.

[195] O Saunier, C Benoit, G Jeanfaivre, and A Lerat. Third-order Cartesian overset mesh adaptation method for solving steady compressible flows. *International journal for numerical methods in fluids*, 57(7):811–838, 2008.

[196] Richard Saurel, Jean Pierre Cocchi, and P. Barry Butler. Numerical Study of Cavitation in the Wake of a Hypervelocity Underwater Projectile. *Journal of Propulsion and Power*, 15(4):513–522, 1999.

[197] Richard Saurel, Fabien Petitpas, and Ray A. Berry. Simple and efficient relaxation methods for interfaces separating compressible fluids, cavitating flows and shocks in multiphase mixtures. *Journal of Computational Physics*, 228(5):1678–1712, 2009.

[198] Lennart Schneiders, Daniel Hartmann, Matthias Meinke, and Wolfgang Schröder. An accurate moving boundary formulation in cut-cell methods. *Journal of Computational Physics*, 235:786–809, 2013.

[199] Jung Hee Seo and Rajat Mittal. A sharp-interface immersed boundary method with improved mass conservation and reduced spurious pressure oscillations. *Journal of Computational Physics*, 230(19):7347–7363, 2011.

[200] Gary S Settles and Michael J Hargather. A review of recent developments in schlieren and shadowgraph techniques. *Measurement Science and Technology*, 28(4):042001, 2017.

[201] Linwei Shen and Eng-Soon Chan. Numerical simulation of fluid–structure interaction using a combined volume of fluid and immersed boundary method. *Ocean Engineering*, 35(8–9):939–952, 2008.

[202] Linwei Shen and Eng-Soon Chan. Application of a combined ib–vof model to wave–structure interactions. *Applied Ocean Research*, 32(1):40–48, 2010.

[203] Linwei Shen, Eng-Soon Chan, and Pengzhi Lin. Calculation of hydrodynamic forces acting on a submerged moving object using immersed boundary method. *Computers & Fluids*, 38(3):691–702, 2009.

[204] D. Shirokoff and J.-C. Nave. A sharp-interface active penalty method for the incompressible navier–stokes equations. *Journal of Scientific Computing*, 62(1):53–77, Jan 2015.

[205] A.L.F. Lima E Silva, A. Silveira-Neto, and J.J.R. Damasceno. Numerical simulation of two-dimensional flows over a circular cylinder using the immersed boundary method. *Journal of Computational Physics*, 189(2):351–370, 2003.

[206] SP Singh and S Mittal. Vortex-induced oscillations at low Reynolds numbers: hysteresis and vortex-shedding modes. *Journal of Fluids and Structures*, 20(8):1085–1104, 2005.

[207] Ashok K Singhal, Mahesh M Athavale, Huiying Li, and Yu Jiang. Mathematical Basis and Validation of the Full Cavitation Model. *Journal of Fluids Engineering*, 124(3):617–624, 2002.

[208] Fotis Sotiropoulos and Iman Borazjani. A review of state-of-the-art numerical methods for simulating flow through mechanical heart valves. *Med. Biol. Engineering and Computing*, 47(3):245–256, 2009.

[209] Fotis Sotiropoulos and Xiaolei Yang. Immersed boundary methods for simulating fluid–structure interaction. *Progress in Aerospace Sciences*, 65:1–21, 2014.

[210] Akira Sou, Barış Biçer, and Akio Tomiyama. Numerical simulation of incipient cavitation flow in a nozzle of fuel injector. *Computers & Fluids*, 103:42–48, 2014.

[211] Philippe Spalart and Steven Allmaras. A one-equation turbulence model for aerodynamic flows. In *30th Aerospace Sciences Meeting and Exhibit*, page 439, 1992.

[212] Herbert Städtke. *Gasdynamic aspects of two-phase flow: Hyperbolicity, wave propagation phenomena and related numerical methods.* John Wiley & Sons, 2006.

[213] J. L. Steger, F. C. Dougherty, and J. A. Benek. A chimera grid scheme. In K.N. Ghia and U. Chia, editors, *Advances in Grid Generation*, volume 5, pages 59–69. NASA, ASME, 1983.

[214] J. C. Stettler and A. K. M. Fazle Hussain. On transition of the pulsatile pipe flow. *Journal of Fluid Mechanics*, 170:169–197, 1986.

[215] Xiaosong Sun and Mikio Sakai. Numerical simulation of two-phase flows in complex geometries by using the volume-of-fluid/immersed-boundary method. *Chemical Engineering Science*, 139:221–240, 2016.

[216] Y. Sun, C. Shu, Y. Wang, C.J. Teo, and Z. Chen. An immersed boundary-gas kinetic flux solver for simulation of incompressible flows. *Computers & Fluids*, 142:45–56, 2017. Selected papers of 18th International Conference on Finite Elements in Flow Problems.

[217] Victoria Suponitsky, Aaron Froese, and Sandra Barsky. Richtmyer–meshkov instability of a liquid–gas interface driven by a cylindrical imploding pressure wave. *Computers & Fluids*, 89:1–19, 2014.

[218] Shun Takahashi, Taku Nonomura, and Kota Fukuda. A numerical scheme based on an immersed boundary method for compressible turbulent flows with shocks: Application to two-dimensional flows around cylinders. *Journal of Applied Mathematics*, 2014:1–21, 2014.

[219] H. Tavassoli, S.H.L. Kriebitzsch, M.A. van der Hoef, E.A.J.F. Peters, and J.A.M. Kuipers. Direct numerical simulation of particulate flow with heat transfer. *International Journal of Multiphase Flow*, 57:29–37, 2013.

[220] H. Tavassoli, E.A.J.F. Peters, and J.A.M. Kuipers. Direct numerical simulation of non-isothermal flow through dense bidisperse random arrays of spheres. *Powder Technology*, 314:291–298, 2017. Special Issue on Simulation and Modelling of Particulate Systems.

[221] Ali Thari, Vito Pasquariello, Niels Aage, and Stefan Hickel. Adaptive reduced-order modeling for non-linear fluid-structure interaction. *arXiv preprint arXiv:1702.04332*, 2017.

[222] S. T. Thoroddsen, T. G. Etoh, K. Takehara, and Y. Takano. Impact jetting by a solid sphere. *Journal of Fluid Mechanics*, 499:139–148, 2004.

[223] Eleuterio F Toro. *Riemann solvers and numerical methods for fluid dynamics: a practical introduction.* Springer Science & Business Media, 2013.

[224] Robert Tramel, Robert Nichols, Robert Tramel, and Robert Nichols. A highly efficient numerical method for overset-mesh moving-body problems. In *13th Computational Fluid Dynamics Conference*, page 2040, 1997.

[225] R. Trip, D. J. Kuik, J. Westerweel, and C. Poelma. An experimental study of transitional pulsatile pipe flow. *Physics of Fluids*, 24(1):014103, 2012.

[226] Jiyuan Tu, Kiao Inthavong, and Kelvin K. L. Wong. *Computational hemodynamics: theory, modelling and applications.* Springer, Dordrecht, 2015.

[227] Jiyuan Tu, Kiao Inthavong, and Kelvin Kian Loong Wong. *Fundamentals of Haemodynamics*, pages 67–94. Springer Netherlands, Dordrecht, 2015.

[228] M.D De Tullio, A. Cristallo, E. Balaras, and R. Verzicco. Direct numerical simulation of the pulsatile flow through an aortic bileaflet mechanical heart valve. *Journal of Fluid Mechanics*, 622:259–290, 003 2009.

[229] Markus Uhlmann. An immersed boundary method with direct forcing for the simulation of particulate flows. *Journal of Computational Physics*, 209(2):448–476, 2005.

[230] Yogen Utturkar, Jiongyang Wu, Guoyo Wang, and Wei Shyy. Recent progress in modeling of cryogenic cavitation for liquid rocket propulsion. *Progress in Aerospace Sciences*, 41(7):558–608, 2005.

[231] E. Stavropoulos Vasilakis, N. Kyriazis, P. Koukouvinis, M. Farhat, and M. Gavaises. Cavitation induction by projectile impacting on a water jet. *International Journal of Multiphase Flow*, 114:128–139, 2019.

[232] Stéphane Vincent, Arthur Sarthou, Jean-Paul Caltagirone, Fabien Sonilhac, Pierre Février, Christian Mignot, and Grégoire Pianet. Augmented lagrangian and penalty methods for the simulation of two-phase flows interacting with moving solids. application to hydroplaning flows interacting with real tire tread patterns. *Journal of Computational Physics*, 230(4):956–983, 2011.

[233] A. Viré, J. Spinneken, M.D. Piggott, C.C. Pain, and S.C. Kramer. Application of the immersed-body method to simulate wave–structure interactions. *European Journal of Mechanics - B/Fluids*, 55, Part 2:330–339, 2016. Vortical Structures and Wall Turbulence.

[234] Anthony Wachs, Abdelkader Hammouti, Guillaume Vinay, and Mona Rahmani. Accuracy of finite volume/staggered grid distributed lagrange multiplier/fictitious domain simulations of particulate flows. *Computers & Fluids*, 115:154–172, 2015.

[235] Guoyu Wang, Inanc Senocak, Wei Shyy, Toshiaki Ikohagi, and Shuliang Cao. Dynamics of attached turbulent cavitating flows. *Progress in Aerospace Sciences*, 37(6):551–581, 2001.

[236] H. G. Weller, G. Tabor, H. Jasak, and C. Fureby. A tensorial approach to computational continuum mechanics using object-oriented techniques. *Computers in Physics*, 12(6):620–631, 1998.

[237] David C Wilcox et al. *Turbulence modeling for CFD*, volume 2. DCW industries La Canada, CA, 1998.

[238] CHK Williamson and R Govardhan. Vortex-induced vibrations. *Annu. Rev. Fluid Mech.*, 36:413–455, 2004.

[239] J. R. Womersley. Method for the calculation of velocity, rate of flow and viscous drag in arteries when the pressure gradient is known. *The Journal of Physiology*, 127(3):553–563, 1955.

[240] Tso-Ren Wu, Chia-Ren Chu, Chih-Jung Huang, Chung-Yue Wang, Ssu-Ying Chien, and Meng-Zhi Chen. A two-way coupled simulation of moving solids in free-surface flows. *Computers & Fluids*, 100:347–355, 2014.

[241] Yuan-Ting Wu and Ashfaq Adnan. Effect of Shock-Induced Cavitation Bubble Collapse on the damage in the Simulated Perineuronal Net of the Brain. *Scientific reports*, 7(1):5323, 2017.

[242] Chang Xu, Yiwei Wang, Chenguang Huang, Chao Yu, and Jian Huang. Analysis of near-wall effect on cloud cavitating flow that surrounds an axisymmetric projectile using large eddy simulation with cartesian cut-cell mesh method. *European Journal of Mechanics - B/Fluids*, 67:15–24, 2018.

[243] Chang Xu, Yi wei Wang, Chen guang Huang, Jian Huang, and Chao Yu. The effect of free surface on cloud cavitating flow around a blunt body. *Journal of Hydrodynamics, Ser. B*, 29(6):979–986, 2017.

[244] Duo Xu, Sascha Warnecke, Baofang Song, Xingyu Ma, and Björn Hof. Transition to turbulence in pulsating pipe flow. *Journal of Fluid Mechanics*, 831:418–432, 2017.

[245] Jianming Yang and Elias Balaras. An embedded-boundary formulation for large-eddy simulation of turbulent flows interacting with moving boundaries. *Journal of Computational Physics*, 215(1):12–40, 2006.

[246] Jianming Yang and Frederick Stern. Sharp interface immersed-boundary/level-set method for wave–body interactions. *Journal of Computational Physics*, 228(17):6590–6616, 2009.

[247] Qingchun Yang, Juntao Chang, and Wen Bao. Richtmyer-meshkov instability induced mixing enhancement in the scramjet combustor with a central strut. *Advances in Mechanical Engineering*, 6:614189, 2014.

[248] Ajit P. Yoganathan, K. B. Chandran, and Fotis Sotiropoulos. Flow in Prosthetic Heart Valves: State-of-the-Art and Future Directions. *Annals of Biomedical Engineering*, 33(12):1689–1694, 2005.

[249] Weixing Yuan, Jürgen Sauer, and Günter H Schnerr. Modeling and computation of unsteady cavitation flows in injection nozzles. *Mécanique & industries*, 2(5):383–394, 2001.

[250] M. Zamir. *The physics of pulsatile flow.* AIP Press, New York, 2000.

[251] C J Zeng, Y X Xiao, W Zhu, Y Y Yao, and Z W Wang. Numerical simulation of cavitation flow characteristic on Pelton turbine bucket surface. *IOP Conference Series: Materials Science and Engineering*, 72(4):042043, 2015.

[252] Cheng Zhang, Wei Zhang, Nansheng Lin, Youhong Tang, Chengbi Zhao, Jian Gu, Wei Lin, Xiaoming Chen, and Ang Qiu. A two-phase flow model coupling with volume of fluid and immersed boundary methods for free surface and moving structure problems. *Ocean Engineering*, 74:107–124, 2013.

[253] Hongwu Zhao, Shaoping Quan, Meizhong Dai, Eric Pomraning, P. K. Senecal, Qingluan Xue, Michele Battistoni, and Sibendu Som. Validation of a three-dimensional internal nozzle flow model including automatic mesh generation and cavitation effects. *Journal of Engineering for Gas Turbines and Power*, 136(9), 04 2014. 092603.

[254] Yucheng Zhao and Hamn-Ching Chen. A new coupled level set and volume-of-fluid method to capture free surface on an overset grid system. *International Journal of Multiphase Flow*, 90:144–155, 2017.

[255] Guohua Zhong, Lin Du, and Xiaofeng Sun. Numerical investigation of an oscillating airfoil using immersed boundary method. *Journal of Thermal Science*, 20(5):413, 2011.

[256] Guanyu Zhou. The fictitious domain method with penalty for the parabolic problem in moving-boundary domain: The error estimate of penalty and the finite element approximation. *Applied Numerical Mathematics*, 115:42–67, 2017.

[257] Qulan Zhou, Na Li, Xi Chen, Tongmo Xu, Shien Hui, and Di Zhang. Liquid drop impact on solid surface with application to water drop erosion on turbine blades, Part II: Axisymmetric solution and erosion analysis. *International Journal of Mechanical Sciences*, 50(10):1543–1558, 2008.

[258] Philip J Zwart, Andrew G Gerber, Thabet Belamri, et al. A two-phase flow model for predicting cavitation dynamics. In *Fifth international conference on multiphase flow, Yokohama, Japan*, volume 152, 2004.